

**Multi-Scale Models for the Scale Interaction of Organized
Tropical Convection**

by

Qiu Yang

A dissertation submitted in partial fulfillment
of the requirements for the degree of
Doctor of Philosophy
Department of Mathematics
Center for Atmosphere Ocean Science
Courant Institute of Mathematical Sciences
New York University

May 2017

Professor Andrew J. Majda

© Qiu Yang

All Rights Reserved, 2017

Dedication

To all teachers who have ever taught me; without them I would not be here.

Acknowledgements

First and foremost, I would like to express my special gratitude to my advisor Prof. Andrew J. Majda for his continuous support, patient guidance, and persistent inspiration in the past five years. In the first year as a Ph.D. graduate student, I felt extremely confused when the main goal of my life is supposed to do research independently instead of taking classes and exams. It was him who patiently taught me to do interdisciplinary research in atmosphere sciences and applied math. During the following four years, I made several mistakes such as bad writing, wrong physical interpretation and incorrect model application, which really let me feel depressed. It was him who wisely corrected me and inspired me to improve myself. Sometimes he would give me a hard time when I behaved badly. But it is such strict requirement that stimulates my potential and pushes me to higher levels. As the famous saying goes, “Give a man a fish, and you feed him for a day; teach a man to fish, and you feed him for a lifetime”. For me, Prof. Majda is the one who gives me a fish and also teaches me how to fish.

Besides my advisor, I would also thank the rest of my thesis committee: Prof. Boualem Khouider, Prof. Olivier Pauluis, Prof. Edwin Gerber and Prof. Dimitris Giannakis. Their insightful comments and inspiring suggestions during my seminar talks and thesis committee meeting improve the depth of my thoughts and widen the scope of my research in various perspectives. In particular, I want to thank Prof. Khouider for his kindly help when I need to write a complex Fortran code as a beginner and his continuous support when I met problems in the stages of designing and validating numerical schemes. I would also thank Prof. Olivier Pauluis for his patient guidance when I dealt with observational datasets in the first time. Furthermore, I appreciate the great efforts done by Prof. Andrew Majda, Prof. Boualem Khouider and Prof. Olivier Pauluis to improve this thesis as my thesis readers.

Next, I would like to thank many of my friends in both CAOS and Math department at Courant Institute. I appreciate Sulian Thual (Postdoc) for teaching me how to have a

good write-up when I start to write my first research paper. I also appreciate Nan Chen (Senior student) for his help when I met troubles in research and life. Besides, I had many stimulating discussion with my friends such as Jim Thomas, Noah D. Brenowitz, Yuanxun Bill Bao. Such long-standing communication gives me valuable encouragement and useful ideas in my research.

Last but not the least, I want to thank my parents for bringing me up and supporting me when I decided to pursue research. I always remember their expectation for me to be a good man, whenever and wherever I am.

Abstract

Assessing the upscale impact of organized tropical convection from small spatial and temporal scales is a research imperative, not only for having a better understanding of the multi-scale structures of dynamical and convective fields in the tropics, but also for eventually helping in the design of new parameterization strategies to improve the next-generation global climate models. Here self-consistent multi-scale models are derived systematically by following the multi-scale asymptotic methods and used to describe the hierarchical structures of tropical atmospheric flows. The advantages of using these multi-scale models lie in isolating the essential components of multi-scale interaction and providing assessment of the upscale impact of the small-scale fluctuations onto the large-scale mean flow through eddy flux divergences of momentum and temperature in a transparent fashion. Specifically, this thesis includes three research projects about multi-scale interaction of organized tropical convection, involving tropical flows at different scaling regimes and utilizing different multi-scale models correspondingly. Inspired by the observed variability of tropical convection on multiple temporal scales, including daily and intraseasonal time scales, the goal of the first project is to assess the intraseasonal impact of the diurnal cycle on the planetary-scale circulation such as the Hadley cell. As an extension of the first project, the goal of the second project is to assess the intraseasonal impact of the diurnal cycle over the Maritime Continent on the Madden-Julian Oscillation. In the third project, the goals are to simulate the baroclinic aspects of the ITCZ breakdown and assess its upscale impact on the planetary-scale circulation over the eastern Pacific. These simple multi-scale models should be useful to understand the scale interaction of organized tropical convection and help improve the parameterization of unresolved processes in global climate models.

Contents

Dedication	iv
Acknowledgements	v
Abstract	vii
List of Figures	x
List of Tables	xx
Introduction	1
1 A Multi-Scale Model for the Intraseasonal Impact of the Diurnal Cycle of Tropical Convection	8
1.1 Introduction	8
1.2 Basic Nondimensional Equations and Multi-Scale Asymptotics	12
1.3 A Model for the Diurnal Cycle and Upscale Fluxes	22
1.4 The Intraseasonal Impact of the Diurnal Cycle on the Planetary Scale	31
1.5 Concluding Discussion	43
1.6 Appendix	48
2 A Multi-Scale Model for the Intraseasonal Impact of the Diurnal Cycle over the Maritime Continent on the Madden-Julian Oscillation	62
2.1 Introduction	62
2.2 A model for the diurnal cycle and its upscale fluxes over the Maritime Continent	66

2.3	The planetary-scale circulation response to the intraseasonal impact of the diurnal cycle	73
2.4	The MJO models forced by a moving heat source	78
2.5	The intraseasonal impact of the diurnal cycle over the Maritime Continent on the MJO	92
2.6	Concluding summary and discussion	107
2.7	Appendix	110
3	ITCZ Breakdown and Its Upscale Impact on the Planetary-Scale Circulation over the Eastern Pacific	116
3.1	Introduction	116
3.2	The M-ITCZ Equations and their properties	122
3.3	ITCZ Breakdown in Zonally Symmetric Planetary-Scale Flow	130
3.4	ITCZ Breakdown in Zonally Varying Planetary-Scale Flow	153
3.5	Concluding Discussion	158
3.6	Numerical Scheme	163
	Bibliography	186

List of Figures

1.1	The left figure shows meridional profile $\phi_{m q}, m = 1, 2; q = 1, 2$. The right figure shows heating profile around the equator during equinox at $y = 0$ and $\gamma = 0$. Heating is in units of $4.5K/day^{-1}$.	26
1.2	The upper figure shows eddy flux divergences of momentum and temperature F^u, F^θ during boreal summer. The lower figure is for the equinox case. In each figure, the eight panels show (a) meridional profile of heating; (b) eddy flux divergence of momentum F^u ; (c) its meridional component $-\frac{\partial}{\partial y} \langle \tilde{v}\tilde{u} \rangle$; (d) its vertical component $-\frac{\partial}{\partial z} \langle \tilde{w}\tilde{u} \rangle$; (e) meridional profile of heating; (f) eddy flux divergence of temperature F^θ ; (g) its meridional component $-\frac{\partial}{\partial y} \langle \tilde{v}\tilde{\theta} \rangle$; (h) its vertical component $-\frac{\partial}{\partial z} \langle \tilde{w}\tilde{\theta} \rangle$. One dimensionless unit of F^u is $1m/s/day$ and that of F^θ is $0.45K/day$.	29
1.3	The meridional profile of heating during equinox is shown in the left panel and that during boreal summer is shown in the middle panel. The meridional profile in the middle panel takes its maximum at $y = 1200km, 10.8^\circ N$. The right panel shows the height and time diagram of the diurnal cycle heating. Here red means heating(positive) and blue means cooling(negative). One unit of \tilde{S}_θ is $4.5K/day$.	30

1.4 The upper figure shows eddy flux divergences of momentum and temperature F^u, F^θ during boreal summer ($y_0 = 0$). The lower figure is for an equinox case ($y_0 = 0.8$). In each figure, the six panels show (a) eddy flux divergence of momentum F^u ; (b) its meridional component $-\frac{\partial}{\partial y} \langle \tilde{v} \tilde{u} \rangle$; (c) its vertical component $-\frac{\partial}{\partial z} \langle \tilde{w} \tilde{u} \rangle$; (d) eddy flux divergence of temperature F^θ ; (e) its meridional component $-\frac{\partial}{\partial y} \langle \tilde{v} \tilde{\theta} \rangle$; (f) its vertical component $-\frac{\partial}{\partial z} \langle \tilde{w} \tilde{\theta} \rangle$. One dimensionless unit of F^u is $1m/s/day$ and that of F^θ is $0.45K/day$.	32
1.5 The upper three panels shows the equinox case. The lower three panels are the boreal summer case. (a) zonal momentum forcing; (b) thermal forcing; (c) meridional and vertical flow field. For zonal momentum forcing, blue means westward and red means eastward. For thermal forcing, blue means cooling and red means heating. The units of $\langle \bar{S}_u \rangle, \langle \bar{S}_\theta \rangle, \langle \bar{v} \rangle, \langle \bar{w} \rangle$ are $15m/s/day, 4.5K/day, 5m/s$ and $1.6cm/s$ respectively.	36
1.6 The upper figure shows the large-scale flows induced by upscale flux divergences F^u, F^θ during boreal summer corresponding to the heating in section 1.3.1. The lower figure shows the case corresponding to the heating in section 1.3.2. (a) pressure p ; (b) potential temperature θ ; (c) zonal velocity u ; (d) meridional velocity v ; (e) vertical velocity w ; (f) the meridional and vertical flow field. The units of p, θ, u, v, w are $250m^2/s^2, 1.5 K, 5 m/s, 0.5 m/s, 5 m/s, 0.16 cm/s$ respectively.	40

1.7 The upper figure shows the large-scale flows corresponding to the heating in section 1.3.1. The lower figure shows the case corresponding to the heating in section 1.3.2. (a) pressure p ; (b) potential temperature θ ; (c) zonal velocity u ; (d) meridional velocity v ; (e) vertical velocity w ; (f) the meridional and vertical flow field (v, w) ; (g) color means the meridional velocity of the original Hadley cell, vectors show the flow field in (f); (h) color means the vertical velocity of the original Hadley cell, vectors show the flow field in (f); (i) the modified Hadley cell, $(V + \epsilon v, W + \epsilon w)$. The units of p, θ, u, v, w are $250 \text{ m}^2/\text{s}^2, 1.5 \text{ K}, 5 \text{ m/s}, 0.5 \text{ m/s}, 5 \text{ cm/s}$ and the units of V, W in the Hadley cell are $5 \text{ m/s}, 1.6 \text{ cm/s}$.	44
2.1 The envelope function of the diurnal heating in longitude-latitude diagram during boreal winter. The value here is dimensionless.	69
2.2 The diurnal heating in time-height diagram during boreal winter. The value is dimensionless.	70
2.3 The eddy flux divergences of momentum and temperature F^u, F^θ in the latitude-height diagram during boreal winter. The left panels from top to bottom show (a) eddy flux divergence of momentum F^u , (b) its meridional component $-\frac{\partial}{\partial y} \langle \tilde{v}\tilde{u} \rangle$ and (c) its vertical component $-\frac{\partial}{\partial z} \langle \tilde{w}\tilde{u} \rangle$. The right panels from top to bottom show (d) eddy flux divergence of temperature F^θ , (e) its meridional component $-\frac{\partial}{\partial y} \langle \tilde{v}\tilde{\theta} \rangle$ and (f) its vertical component $-\frac{\partial}{\partial z} \langle \tilde{w}\tilde{\theta} \rangle$. One dimensionless unit of F^u is 1 m/s/day and that of F^θ is 0.45 K/day .	71
2.4 The horizontal flow field (shown by vectors) and pressure perturbation (shown by color) due to the intraseasonal impact of the diurnal cycle. The height in the top panel and bottom panels are 11 km and 5 km, respectively. The unit of pressure perturbation is $250 \text{ m}^2 \text{s}^{-2}$.	75

2.5 The temperature anomaly at the heating center $X = 0$ in the latitude-height diagram due to the intraseasonal impact of the diurnal cycle. The red color means warm and blue color means cold. The unit of temperature anomalies is K.	76
2.6 The mean heating for the Madden-Julian Oscillation. The red color means heating and blue color means cooling. One dimensionless unit of the heating is $4.5Kday^{-1}$	80
2.7 The horizontal flow field (shown by vectors) and pressure perturbation (shown by color) forced by the standard mean heating. The top panel shows the flow field at height $z=11$ km. The bottom panel is for height $z=5$ km. Here one dimensionless unit of pressure perturbation is $250 m^2 s^{-2}$	82
2.8 Contours of synoptic scale heating and vectors of zonal/vertical velocity. One dimensionless unit of heating, zonal velocity and vertical velocity correspond to $4.5Kday^{-1}$, $5ms^{-1}$, $1.6cms^{-1}$	83
2.9 The planetary-scale response to the equatorially symmetric MJO forced by both synoptic-scale heating and mean heating. The color shows pressure perturbation, the flow field is shown by vectors. From top to bottom, these 4 panels show the heights at $z=0$ km, $z=4$ km, $z=8$ km, $z=12$ km. The pressure perturbation is dimensionless and one dimensionless unit corresponds to $250m^2s^{-2}$	85
2.10 The planetary-scale response to the equatorially symmetric MJO forced by both synoptic-scale heating and mean heating. The color shows temperature anomalies, the flow field is shown by vectors. From top to bottom, these 4 panels show the heights at $z=0$ km, $z=4$ km, $z=8$ km, $z=12$ km. The unit of temperature anomalies is K.	87

2.11 Planetary-scale response to equatorially asymmetric synoptic-scale and mean heating centered at 900 km south. The panels shows flow vectors, red means positive pressure perturbation, and blue means negative pressure perturbation at heights (a) 0, (b) 4, (c) 8, (d) 12 km. The pressure perturbation is dimensionless.	89
2.12 Planetary-scale response to equatorially asymmetric synoptic-scale and mean heating centered at 900km south. The panels shows flow vectors, red means positive temperature anomaly, and blue means negative temperature anomaly at heights (a) 0, (b) 4, (c) 8, (d) 12 km. The temperature anomaly is in units of K.	91
2.13 The horizontal flow field and pressure perturbation at $z = 5\text{ km}$ due to the intraseasonal impact of the diurnal cycle and the MJO. The panels from top to bottom show different phases of MJO. The red circles shows the center of mean heating for MJO. The black box shows the regime where diurnal cycle is significant during boreal winter. The winds direction is shown by vectors and their magnitude is shown by the length of vectors. The pressure perturbation is shown in color.	94
2.14 The horizontal flow field and pressure aperturbation at $z = 12\text{ km}$ due to the intraseasonal impact of the diurnal cycle and the MJO. The panels from top to bottom show different phases of MJO. The red circles shows the center of mean heating for MJO. The white box shows the regime where diurnal cycle is significant during boreal winter. The winds direction is shown by vectors and their magnitude is shown by the length of vectors. The pressure perturbation is shown in color.	96

2.15 Contour of vertical motion at the middle troposphere due to the MJO and intraseasonal impact of diurnal cycle. The panels from top to bottom show different phases of MJO. The positive value means rising motion and negative value means sinking motion. The white box shows the location where the diurnal cycle is significant. The red arrow shows the longitude at which the center of MJO convection sits. The unit of vertical velocity is 0.16cm/s	97
2.16 The temperature anomalies associated with the equatorially symmetric MJO and the intraseasonal impact of the diurnal cycle at phase I. The color shows temperature anomalies, the flow field is shown by vectors. From top to bottom, these 4 panels show the heights at $z=0\text{ km}$, $z=4\text{ km}$, $z=8\text{ km}$, $z=12\text{ km}$. The unit of temperature anomaly is K. The red dot shows the center of the MJO convective activities.	100
2.17 The temperature anomalies associated with the equatorially symmetric MJO and the intraseasonal impact of the diurnal cycle at phase II. The color shows temperature anomalies, the flow field is shown by vectors. From top to bottom, these 4 panels show the heights at $z=0\text{ km}$, $z=4\text{ km}$, $z=8\text{ km}$, $z=12\text{ km}$. The unit of temperature anomaly is K. The red dot shows the center of the MJO convective activities.	101
2.18 The temperature anomalies associated with the equatorially symmetric MJO and the intraseasonal impact of the diurnal cycle at phase III. The color shows temperature anomalies, the flow field is shown by vectors. From top to bottom, these 4 panels show the heights at $z=0\text{ km}$, $z=4\text{ km}$, $z=8\text{ km}$, $z=12\text{ km}$. The unit of temperature anomaly is K. The red dot shows the center of the MJO convective activities.	102

3.2 Horizontal profiles of velocity (arrow) and vorticity $\omega = v_x - u_y$ (color) in the longitude (horizontal axis, 10^3 km) and latitude (vertical axis, 10^3 km) diagram in the <i>deep2</i> heating case. The columns from left to right are for different heights from 0 km to 7.85 km to 15.7 km. The first three rows are for different days from Day 1 to Day 2 to Day 4. The last row is for the zonally uniform heating case. The panels in each column share the same color bar at the bottom. The maximum velocity magnitude is shown in the title of each panel and vorticity has units of day^{-1}	137
3.3 Horizontal profiles of velocity (arrow) and vorticity $\omega = v_x - u_y$ (color) in the longitude (horizontal axis, 10^3 km) and latitude (vertical axis, 10^3 km) diagram in the shallow heating case. The left column is for the height 0 km and the right column is for 7.85 km. The middle column is for <i>deep1</i> heating case at the height 0 km. The first three rows are for different days from Day 1 to Day 2 to Day 4. The panels in each column share the same color bar at the bottom. The maximum velocity magnitude is shown in the title of each panel and vorticity has units of day^{-1}	142
3.4 Vertical profiles of zonal velocity, meridional velocity and vorticity at Day 4. The columns from left to right are for zonal velocity, meridional velocity and vorticity. The first row (a-c) shows solutions along the latitude 0.8×10^3 km in the <i>deep2</i> heating case. The third row (g-i) shows solutions along the longitude 0.43×10^3 km in the <i>deep2</i> heating case. The second and fourth rows are the same as the first and third rows but for shallow heating case. The dimensional units of horizontal velocity and vorticity are ms^{-1} and day^{-1} respectively.	144

3.5 Eddy flux divergence of zonal momentum F^U in the latitude-height diagram at day 4. The columns from left to the rights are for <i>deep2</i> , shallow and <i>deep1</i> heating cases. The second column share the same color bar at the bottom with the third column. The three panels from top to bottom are for (a) F^U , (b) its meridional component $-\frac{\partial}{\partial y}(\bar{v}'u')$ (c) its vertical component $-\frac{\partial}{\partial z}(\bar{w}'u')$. The dimensional unit of F^U is $ms^{-1}day^{-1}$.	148
3.6 Mean zonal velocity \bar{u} in the latitude-height diagram at day 4. The left panels from top to bottom show the solutions for (a) zonally localized heating, (b) zonally uniform heating, (c) their difference (a)-(b) in the <i>deep2</i> heating case. The right panels (d-f) show the same fields but for the shallow heating case. The dimensional unit of mean zonal velocity is ms^{-1} .	150
3.7 Acceleration and deceleration of mean zonal velocity due to eddy flux divergence of zonal momentum in the latitude-height diagram at day 4. The color indicates the value of the quantity $F^U\bar{u}$ with positive anomalies for acceleration effects and negative anomalies for deceleration effects. The panels from left to right are for the cases (a) <i>deep2</i> , (b) shallow, (c) <i>deep1</i> . The dimensional unit is $m^2s^{-2}day^{-1}$	152
3.8 A schematic depiction of the multi-scale domain with nested grids. The large red dots are the coarse grids on the planetary scale. Each coarse grid corresponds to a single mesoscale domain characterized by a mesoscale box in thick lines. The fine grids in each mesoscale domain are shown by pink dots.	153
3.9 Cross section of mean zonal velocity anomalies in the center of heating region (longitude $X = 19.51 \times 10^3$ km) at day 4. The left panel is for <i>deep2</i> heating case and the right panel is for shallow heating case. The dimensional unit is ms^{-1} .	155

3.10 Mean zonal velocity anomalies at different heights at day 4 in the longitude-latitude diagram. The left column (a-c) is for <i>deep2</i> heating case and the right column (d-f) is for shallow heating case. The panels from top to bottom are for heights 14.84 km, 7.48 km and 3.62 km respectively. The dimensional unit is ms^{-1} .	157
3.11 A schematic depiction of the essential idea behind the corner transport upwind scheme. The gray box denotes the original copy of the control volume (i, j) , which moves in the direction as indicated by the arrows. This gray box overlaps the neighboring cells and can be divided into as denoted into 4 small rectangles as denoted by A1, A2, A3, A4. Such two-dimensional case can be extended to three-dimensional case with 8 neighboring cells.	171
3.12 The L_∞ norm numerical errors of the horizontal flow field in the logarithmic diagram. The blue line is for zonal velocity and red line is for meridional velocity. The two dashed black lines denote first-order and second-order convergence rate separately. The horizontal axis shows the scaled grid number of these 5 numerical experiments in increasing resolutions and N=1 corresponds to the lowest resolution numerical experiment.	185

List of Tables

1.1	The dimensional units for all physical variables and some constant parameters. Here square brackets mean the value of one unit of the dimensionless variables corresponding to the given scale.	13
2.1	The dimensional units for all physical variables and some constant parameters. Here square brackets mean the value of one unit of the dimensionless variables corresponding to the given scale.	111
3.1	The multi-scale domain with nested grids and grid numbers and time steps in the numerical simulations.	132
3.2	Numerical errors in L_∞ norm in 4 cases with different zonal wavenumber and baroclinic modes. The parameter k denotes zonal wavenumber and q is the vertical index for different baroclinic modes. (U, Θ) are true solutions and $(\tilde{U}, \tilde{\Theta})$ are numerical solutions.	186

Introduction

Tropical convection is organized in a hierarchy of multiple spatial and temporal scales, ranging from cumulus clouds over several kilometers to mesoscale circulation systems (MCSs) (Houze, 2004) to CCEWs (Kiladis et al., 2009) to intraseasonal oscillations on the planetary scale such as the Madden-Julian Oscillation (MJO) (Zhang, 2005). By releasing large amounts of rainfall, tropical convection dramatically impacts local weathers and global atmospheric conditions. The early investigation about mean properties of tropical convection and its variability based on the GARP Atlantic Tropical Experiment (GATE) dates back to 1970s (Houze Jr and Cheng, 1977). Recently, organized tropical convection is documented in the Year of Tropical Convection (YOTC) virtual global field-campaign and further analyzed through diagnostic, theoretical and numerical studies (Moncrieff et al., 2012). In particular, Tropical convection over the Maritime Continent is organized on multiple time scales, ranging from cumulus clouds on the daily time scale to intraseasonal oscillations. On the daily time scale, the diurnal cycle of tropical convection over the Maritime Continent is very significant compared with that over the Indian Ocean and the western Pacific Ocean (Hendon and Woodberry, 1993; Kikuchi and Wang, 2008). On the intraseasonal time scale, the Madden-Julian Oscillation (MJO), the dominant component of the intraseasonal variability in the tropics, typically propagates eastward slowly across the Maritime Continent and can stall or terminate there along with large amounts of rainfall (Zhang, 2005). On the other hand, the intertropical convergence zone (ITCZ) is a narrow band of cloudiness encircling the Earth in the tropics. The eastern Pacific ITCZ remains in the Northern Hemisphere along the latitudes between $5^{\circ}N$ and $15^{\circ}N$ all year round. Instead of being a steady state, the ITCZ over the eastern Pacific is sometimes observed to undulate and break down on the synoptic time scale (Ferreira and Schubert, 1997). Besides, superclusters of cloudiness and rainfall on the synoptic scale are frequently organized by CCEWs that propagate eastward or westward along the equator or the ITCZ (Nakazawa, 1988; Kiladis et al., 2009). Instead

of organizing in a single-scale convective envelope, CCEWs are manifested in a hierarchical structure where numerous mesoscale convective elements are embedded in the synoptic-scale convective envelope.

The morphology of organized tropical convection is similar across multiple scales from the mesoscale to synoptic scale to planetary scale, which is explained by self-similarity principle derived by Majda (2007). One crucial feature of self-similarity is that both dynamical and convective fields during tropical convection exhibit a front-to-rear vertical tilt. By regarding an MCS as a small analogue or prototype of large-scale waves, the self-similarity of cloudiness is explained as a similar progression from shallow to deep convection to stratiform anvils on many time scales (Mapes et al., 2006). Such a trimodal characteristics of tropical convection including cumulus congestus, deep convection and stratiform clouds is also found in a broad spectrum based on shipboard radar data (Johnson et al., 1999). Considering the significant impact of organized tropical convection, capturing its spatial pattern, propagation behaviors and precipitation amounts become a benchmark to examine skills of comprehensive numerical simulations. By parameterizing these three cloud types (congestus, deep, stratiform) and carefully dealing with the transition between different type clouds, the multicloud models successfully reproduce many key features of CCEWs including the spectrum peaks, reduced phase speed and self-similar front-to-rear tilt (Khouider and Majda, 2008a). Besides, the large-scale organization of tropical deep convection is investigated in idealized two-dimensional cloud-resolving simulations (Grabowski and Moncrieff, 2001). Idealized simulations using the weather research and forecast (WRF) model show that traditional cumulus parameterization (CP) tends to destroy both the coherence of the propagating waves and the variability (Khouider and Han, 2013). Therefore, improving the traditional CP to capture coherent multi-scale features of organized tropical convection and self-similar front-to-rear tilt is a research imperative.

Understanding the scale interaction between small-scale disturbances and large-scale wave envelope is crucial, not only for explaining propagation properties and spatial patterns of

CCEWs, but also improving the skills of global climate models (GCMs) for weather and climate forecast. Based on the objective soundings taken during the Tropical Ocean and Global Atmosphere Coupled Ocean-Atmosphere Response Experiment (TOGA COARE) intense observing period (IOP), the momentum budget residual is estimated to study the effects of convective momentum transport (CMT) over the western Pacific warm pool (Tung and Yanai, 2002a,b). In general, CMT not only describes the momentum transport when organized moist convection on smaller scales affects the large-scale flow field, but also involves the process of energy conversion from convective available potential energy to horizontal kinetic energy. In the theoretical directions, simple stochastic models that capture the significant intermittent upscale impact of CMT on the large scales due to organized unresolved convection from squall lines are built and further tested in the column model environment and the organized synoptic-scale CCEWs through an idealized multicloud model (Majda and Stechmann, 2008). Besides, a simple dynamic model is derived by including interactions between a large-scale zonal mean flow and convectively coupled gravity waves and utilized to quantify and parameterize the effects of CMT (Majda and Stechmann, 2009). Furthermore, CMT and its impact on the large-scale organization of convection are diagnostically investigated in the two-dimensional cloud-resolving model (Grabowski and Moncrieff, 2001) and three-dimensional state-of-the-art mesoscale model (Khouider and Han, 2013).

In spite of so much progress, the crucial features of organized tropical convection and its upscale impact on the large-scale circulation and precipitation are still poorly simulated in GCMs, which is mainly related with the fact that the resolution of GCMs is too coarse to explicitly simulate the dynamical and thermal properties of MCSs. In addition, there still exist huge discrepancies in precipitation amounts between the comprehensive numerical simulations and observed tropical convection. For example, the present-day GCMs are still struggling to reproduce the realistic features of the MJO (Jiang et al., 2015). One hypothesis for such huge discrepancies of precipitation amount is the inadequate treatment of organized tropical convection and its missing upscale impact on the large-scale flow field in the GCMs.

The goals of this thesis are as follows: first, using simple multi-scale models to capture the coherent structure of tropical convection across multiple spatial and temporal scales in a multi-scale framework; secondly, assessing the upscale impact of small-scale (short time scale) fluctuations on the large-scale (long time scale) circulation through eddy flux divergence of momentum and temperature; Thirdly, understanding how much of large-scale (long time scale) circulation is induced by upscale impact of small-scale (short time scale) fluctuations rather than mean heating.

In the theoretical directions, the multispace, multitime simplified asymptotic models are derived systematically from the equatorial primitive equations on an equatorial β -plane by following multi-scale asymptotic theory, providing a useful framework to understand the multi-scale phenomenon and describe the hierarchical structures of atmospheric flows in the tropics (Majda and Klein, 2003; Majda, 2007; Yang and Majda, 2014; Majda and Yang, 2016). The advantages of using these multi-scale models lie in isolating the essential components of multi-scale interaction and providing assessment of the upscale impact of the small-scale fluctuations onto the large-scale envelope through eddy flux divergence of momentum and temperature in a transparent fashion. For example, the intraseasonal planetary equatorial synoptic dynamics (IPESD) model (Majda and Klein, 2003) considers the central role of organized vertically tilted synoptic-scale circulations in reproducing key features of the MJO across multiple spatial scales (Majda and Biello, 2004; Biello and Majda, 2005, 2006). The IPESD model involves two spatial scales (synoptic and planetary) but only one temporal scale (intraseasonal). A generalized version of the IPESD model which involves two spatial scales (synoptic and planetary) and two time scales (daily and intraseasonal) is derived in Chapter.1. Besides, the modulation of the ITCZ (M-ITCZ) equations (Biello and Majda, 2013) describe atmospheric flows on both the mesoscale and planetary scale, which interact with each other in a completely nonlinear way. Such complete nonlinearity distinguishes itself from other multi-scale models (Biello and Majda, 2005, 2006; Majda, 2007; Biello and Majda, 2010; Majda et al., 2010; Yang and Majda, 2014; Majda and Yang,

2016), where large-scale mean flow and small-scale fluctuations are typically governed by different groups of equations. The M-ITCZ equations describe atmospheric dynamics on both the mesoscale and planetary scale, which are the typical scales of atmospheric flows in the eastern Pacific ITCZ.

Chapter.1 assesses the intraseasonal impact of planetary-scale inertial oscillations in the diurnal cycle. In nature, one of the crucial features of tropical convection is the observed variability on multiple spatiotemporal scales, ranging from cumulus clouds on the daily time scale over a few kilometers to intraseasonal oscillations over planetary scales. The diurnal cycle of tropical convection is a significant process, but its large-scale impact is not well understood. A self-contained derivation of a multi-scale model governing planetary-scale tropical flows on the daily and intraseasonal time scale is provided in this chapter, by following the derivation of systematic multi-scale models for tropical convection. This derivation demonstrates the analytic tractability of the model. The appeal of the multi-scale model developed here is that it provides assessment of eddy flux divergences of momentum and temperature and their intraseasonal impact on the planetary-scale circulation in a transparent fashion. Here, we use it to study the intraseasonal impact of a model for the diurnal cycle heating with two local phase-lagged baroclinic modes with the congestus, deep, stratiform cloud life cycle. The results show that during boreal summer, the eddy flux divergence of temperature dominates in the northern hemisphere, providing significant heating in the middle troposphere of the northern hemisphere with large-scale ascent and cooling with subsidence surrounding this heating center.

As an extension of Chapter.1, Chapter.2 investigates the intraseasonal impact of the diurnal cycle over the Maritime Continent on the MJO. In reality, the eastward-propagating MJO typically exhibits complex behavior during its passage over the Maritime Continent, sometimes slowly propagating eastward and other times stalling and even terminating there with large amounts of rainfall. This is a huge challenge for present-day numerical models. One possible reason is the inadequate treatment of the diurnal cycle and its scale interaction

with the MJO. Here these two components are incorporated into a simple self-consistent multiscale model that includes one model for the intraseasonal impact of the diurnal cycle and another one for the planetary/intraseasonal circulation. The latter model is forced self-consistently by eddy flux divergences of momentum and temperature from a model for the diurnal cycle with two baroclinic modes, which capture the intraseasonal impact of the diurnal cycle. The MJO is modeled as the planetary-scale circulation response to a moving heat source on the synoptic and planetary scales. The results show that the intraseasonal impact of the diurnal cycle during boreal winter tends to strengthen the westerlies (easterlies) in the lower (upper) troposphere in agreement with the observations. In addition, the temperature anomaly induced by the intraseasonal impact of the diurnal cycle can cancel that from the symmetricasymmetric MJO with convective momentum transfer, yielding stalled or suppressed propagation of the MJO across the Maritime Continent.

Chapter.3 looks at the upscale impact of ITCZ breakdown on the large-scale circulation over the eastern Pacific. The ITCZ over the eastern Pacific is sometimes observed to break down into several vortices on synoptic time scales (Ferreira and Schubert, 1997). It is still a challenge for present-day numerical models to simulate the ITCZ breakdown in the baroclinic modes. Also, the upscale impact of the associated mesoscale fluctuations on the planetary-scale circulation is not well understood. Here a simplified multi-scale model for the modulation of the ITCZ is used to study these issues. A prescribed two-scale heating drives the planetary-scale circulation through both planetary-scale mean heating and eddy flux divergence of zonal momentum, where the latter represents the upscale impact of mesoscale fluctuations. Several key features of the ITCZ breakdown in the baroclinic modes are captured in this multi-scale model. Also, the eddy flux divergence of zonal momentum and the associated acceleration/deceleration effects are discussed in both deep convective heating and shallow congestus heating scenarios.

Studies based on simple multi-scale models have several implications for physical interpretation and for comprehensive numerical models. In particular, the explicit expressions

for eddy flux divergences of momentum and temperature provide a way of assessment of up-scale impact of small-scale (short time scale) fluctuations on the large-scale (long time scale) circulation in a transparent fashion, which should be useful to improve the parameterization of organized tropical convection in GCMs. Meanwhile, these simple multi-scale models can also be generalized in several ways. For example, instead of prescribing the diabatic heating across multiple spatial and temporal scales, an active heating function coupling the multi-scale model with moisture should be useful to model convective instability in the tropics. In addition, coupling equations to the atmospheric boundary layer can further elaborate the multi-scale models and introduce new realistic features of tropical convection.

Chapter 1

A Multi-Scale Model for the Intraseasonal Impact of the Diurnal Cycle of Tropical Convection

1.1 Introduction

The diurnal cycle of solar radiation has a major impact on atmospheric flows. Particularly, it induces significant variability in tropical storms and the associated winds and precipitation over land and ocean areas adjacent to continents. Early investigations of the diurnal variability of tropical precipitation date back to 1920s (Ray, 1928). The development of satellite measurements and computers has triggered more work such as the GARP Atlantic Tropical Experiment (GATE) (McGarry and Reed, 1978; Houze and Betts, 1981; Albright et al., 1981), the European Union Cloud Archive User Service (CLAUS) project (Yang and Slingo, 2001) and the Tropical Rainfall Measuring Mission (TRMM) (Yang and Smith, 2006; Nesbitt and Zipser, 2003; Takayabu, 2002; Sorooshian et al., 2002), leading the community to have a better understanding of the diurnal variability of tropical convection and precipitation over land and oceans. Kikuchi and Wang (2008) confirmed the persistence of the

diurnal variation of tropical precipitation by using empirical orthogonal functions(EOFs) on two complementary TRMM datasets(3B42 and 3G68) for 1998-2006. Their results show that the amplitude of the diurnal variability of tropical precipitation in the continental regime is much stronger than that in the oceanic regime. Meanwhile it was found (Kikuchi and Wang, 2008) that the diurnal range (DR), which is defined as the climatological daily maximum precipitation minus daily minimum precipitation, has different meridional spatial patterns in different seasons. For the annual mean of tropical precipitation, the equatorial continental regime has relatively large DR, such regime is observed at the Indonesian Maritime Continent and South America around the equator. For the June July August(JJA) mean of tropical precipitation, the DR is relatively large on the continents but in the northern hemisphere such as South Asia, the Indonesian Maritime Continent and Mexico.

The representation of the diurnal variability of tropical precipitation is a major unsolved problem and very crucial for global weather forecast and climate models. For example, present-day computer general circulation models (GCM) typically poorly represent the Madden-Julian oscillation (MJO) near the Indonesian Maritime Continent (Sperber et al., 1997). One possible shortcoming is the inadequate treatment of the diurnal cycle and its impact on the intraseasonal variability of atmospheric flow. In fact, current global and regional numerical models of weather and climate have difficulty in reproducing the diurnal variability of tropical precipitation (Randall and Dazlich, 1991; Yang and Slingo, 2001; Dai and Trenberth, 2004; Tian et al., 2004). Nevertheless, both the diurnal cycle of tropical convection and MJO simulation have been improved a lot with superparameterization (Khairoutdinov et al., 2005; Sato et al., 2009; Benedict and Randall, 2011). In a theoretical direction, models utilizing three cloud types (congestus, deep and stratiform) based on the first two baroclinic modes of vertical structure plus a boundary layer mode have been built (Khouider and Majda, 2006a,b,c), successfully reproducing several features of a realistic diurnal cycle of tropical precipitation over land and oceans (Frenkel et al., 2011a,c, 2013).

The goal of this chapter is to build an analytic multi-scale model to assess the intrasea-

sonal impact of the diurnal cycle of tropical convection. Compared with the numerical models, the analytic multi-scale model developed here has the appeal that it is analytically tractable and relatively simple and consistent with several key features of the observations such as the diurnal heating associated with the cloud life cycle. Furthermore, there are eddy flux divergences of momentum and temperature in the planetary/intraseasonal scale equations, which shows that the model is able to assess upscale effects spatially from the synoptic scale to the planetary scale and temporally from the daily time scale to the intraseasonal time scale in an idealized fashion. Several related studies, in the framework of the intraseasonal planetary equatorial synoptic dynamics (IPESD) model (Majda and Klein, 2003), have considered the central role of organized vertically tilted synoptic-scale circulations in reproducing key features of MJO across multiple spatial scales (Majda and Biello, 2004; Biello and Majda, 2005, 2006). The IPESD model involves two spatial scales (the synoptic scale and the planetary scale) but only one temporal scale (the intraseasonal time scale). In contrast, here the analytic multi-scale model is used to assess upscale effects across multiple temporal scales, that is, the intraseasonal impact of the diurnal cycle.

Through systematic multi-scale asymptotics following Majda (2007), four systems of equations involving physical variables on different spatiotemporal scales are derived. The model for the diurnal cycle is one of those systems, involving all physical variables on the planetary scale and daily time scale. Since there is a general heating term in the thermal equation in this model, we prescribe this heating profile to mimic the latent heat which is released during tropical precipitation in the diurnal cycle. Here we utilize the first two baroclinic models of vertical structure to characterize organized tropical convection based on three cloud types (congestus, deep convective and stratiform) in the free troposphere, which was first introduced in a simple multicloud model (Khouider and Majda, 2006a,b,c). The second system of equations derived in the chapter is utilized as a model for the planetary/intraseasonal scale circulation, which includes eddy flux divergences of momentum and temperature from the model for the diurnal cycle. Thus, the resulting circulation response

on the planetary/intraseasonal scales describes the intraseasonal impact of the diurnal cycle. The results show that the eddy flux divergence of temperature during boreal summer is much stronger than that during equinox, which suggests that the significant intraseasonal impact of the diurnal cycle is traced to the meridional asymmetry of the diurnal heating profile in the first two baroclinic modes. In general, the dimensionless magnitude of the eddy flux divergence of temperature due to the diurnal cycle is much larger than that of the eddy flux divergence of momentum. In an ideal zonally symmetric case, the resulting steady state circulation on the planetary/intraseasonal scales during boreal summer is characterized by a circulation cell around the equator. By coupling this system with the model for the Hadley cell, we will see that the intraseasonal impact of the diurnal cycle can strengthen the upper branch of the winter cell of the Hadley circulation but weaken the lower branch of the winter cell of the Hadley circulation.

The rest of this chapter is organized as follows. The basic nondimensional equations and multi-scale asymptotics are summarized in Section 1.2. In that section, we start from the primitive equations and derive four systems on multiple spatiotemporal scales by utilizing the multi-scale asymptotic method. The model for the diurnal cycle is developed in Section 1.3. In that section, we prescribe the diurnal cycle heating in meridionally symmetric and asymmetric profiles to mimic the equinox case and boreal summer case separately. Section 1.4 assesses the intraseasonal impact of the diurnal cycle of tropical convection on the planetary/intraseasonal scales in an ideal zonally symmetric case. There are two planetary/intraseasonal scale circulation systems, which involve meridional and vertical velocity components in different orders. The leading-order system can be used to describe the Hadley cell (Biello and Majda, 2006). The second order system can be understood as the planetary-scale circulation response to the intraseasonal impact of the diurnal cycle, since in this system there are eddy flux divergences of the momentum and temperature from the model of the diurnal cycle in Section 1.3. Here we first consider the intraseasonal impact of the diurnal cycle without the advection effects from the Hadley circulation. Then we consider a fully

coupled system for the planetary/intraseasonal scale circulation advected by the Hadley cell. Finally, a concluding discussion is given in Section 1.5. Technical details for the derivation of the multi-scale model, explicit formulas of eddy flux divergences, and the numerical methods, used for solving the model equations, are summarized in the Appendix.

1.2 Basic Nondimensional Equations and Multi-Scale Asymptotics

Tropical convection is organized on a hierarchy of spatiotemporal scales such as the tropical super clusters within intraseasonal variations over the western Pacific (Nakazawa, 1988; Hendon and Liebmann, 1994; Wheeler and Kiladis, 1999). Here we want to study the effect of the diurnal tropical convection on the large-scale atmospheric flow, by utilizing simplified multiscale asymptotic models. The fundamental model for the dynamical behavior of atmospheric flows consists of the hydrostatic, anelastic Euler equations on an equatorial β -plane, which are the appropriate equations for large-scale phenomena in the tropical troposphere. The governing equations in dimensionless units read as follows,

$$\frac{D}{Dt}u - yv = -p_x + S_u, \quad (1.1a)$$

$$\frac{D}{Dt}v + yu = -p_y + S_v, \quad (1.1b)$$

$$\frac{D}{Dt}\theta + N^2w = S_\theta, \quad (1.1c)$$

$$p_z = \theta, \quad (1.1d)$$

$$(\rho u)_x + (\rho v)_y + (\rho w)_z = 0, \quad (1.1e)$$

where $\frac{D}{Dt} = \frac{\partial}{\partial t} + u\frac{\partial}{\partial x} + v\frac{\partial}{\partial y} + w\frac{\partial}{\partial z}$ is the three dimensional advective derivative. We use the same nondimensionalization as in earlier work (Biello and Majda, 2006; Majda, 2007). Both the density $\rho = \rho(z)$ and the buoyancy frequency $N = N(z)$ are in dimensionless units

Table 1.1: The dimensional units for all physical variables and some constant parameters. Here square brackets mean the value of one unit of the dimensionless variables corresponding to the given scale.

Physical quantity	Mathematical symbol	Value
Froude number	ϵ	0.1
Gravity wave speed	c	50m/s
Brunt-vaisala frequency	N	0.01s ⁻¹
Troposphere height	H_T	16km
Equatorial time scale	T_E	$(c\beta)^{-1/2} = 8.3h$
Equatorial deformation radius	L_E	$(c/\beta)^{1/2} = 1500km$
Synoptic scale	[x, y]	$L_E = 1500km$
vertical scale	[z]	$H_T/\pi = 5km$
Daily scale	[t]	$T_E = 8.3h$
Zonal planetary scale	[X]	$L_P = L_E/\epsilon = 15000km$
Intraseasonal scale	[T]	$T_I = T_E/\epsilon = 3.5day$

and could depend only on the height. The Eqs. (1.1a-1.1e) have been nondimensionalized so that time is measured in units of the equatorial time scale $T_E = (c\beta)^{-1/2} \approx 8.3h$, the horizontal length scale is in units of the equatorial deformation radius $L_E = (c/\beta)^{1/2} = 1500km$, the vertical length scale is in units of the troposphere height divided by π , $H = H_T/\pi \approx 5km$. Here c is defined as the dry Kelvin wave speed and β denotes the Rossby parameter in the Beta plane approximation. The horizontal velocity is scaled to the dry Kelvin/gravity wave speed $c = 50m/s$ and the vertical velocity is scaled to this wave speed c multiplied by the aspect ratio between the vertical length scale and the horizontal length scale, $(H/L_E)c \approx 0.16m/s$. The potential temperature scale is equal to the mean potential temperature difference over one unit of the vertical scale H , $\Theta = N^2\theta_0H/g = 15.3K$, where we assume a constant buoyancy frequency $N = 10^{-2}s^{-1}$ and a mean potential temperature $\theta_0 = 300K$. N^2 has units s^{-2} and is referred as the Brunt-Vaisala frequency. In Eq. 1.1c, θ denotes the potential temperature deviation from the mean potential temperature. The free troposphere occupies the domain $-20 \times 10^3 km \leq x \leq 20 \times 10^3 km$, $-5 \times 10^3 km \leq y \leq 5 \times 10^3 km$, $0 \leq z \leq 16km$. The dimensional units for all physical variables and some constant parameters are summarized in Table 1.1.

In Eqs.1.1a-1.1e, the zonal and meridional momentum forcings S_u, S_v include momentum dissipation. To parameterize the momentum dissipation, we employ a linear drag law closure. The parameter d is the inverse linear damping time scale of the momentum dissipation. Here the dissipation time scale is ascribed to cumulus drag, which has been estimated to be about 5 days from observations of large-scale tropical flows (Lin et al., 2005; Romps, 2014). Since the equatorial time scale is $T_E = (c\beta)^{-\frac{1}{2}} \approx 8.3h \approx \frac{1}{3}day$, the value of the dissipation rate is $d = \frac{1}{15} = 0.07$. Thus we rewrite the horizontal momentum forcings as $-\epsilon du + S_u$ in Eq. (1.1a) and $-\epsilon dv + S_v$ in Eq. (1.1b), where $d = 0.7$ and S_u, S_v account for all extra forcings.

The thermal forcing S_θ includes radiative damping. Here we use a linear Newtonian cooling law $-d_\theta\theta$. Given that the observational estimates for the cooling time scale are of the order 15 days and the equatorial time scale is $T_E = (c\beta)^{-\frac{1}{2}} \approx 8.3h \approx \frac{1}{3}day$, the dimensionless value of the radiative damping rate is $d_\theta = \frac{1}{45} = 0.023$. Thus we rewrite the thermal forcing as $-\epsilon d_\theta\theta + S_\theta$ in Eq. (1.1c), where $d_\theta = 0.23$ and S_θ accounts for all extra forcings such as latent heat release during tropical precipitation.

By incorporating the momentum dissipation and radiative damping terms into the primitive equations (1.1a-1.1e), we can rewrite them as

$$\frac{D}{Dt}u - yv = -p_x - \epsilon du + S_u \quad (1.2a)$$

$$\frac{D}{Dt}v + yu = -p_y - \epsilon dv + S_v \quad (1.2b)$$

$$\frac{D}{Dt}\theta + N^2w = -\epsilon d_\theta\theta + S_\theta \quad (1.2c)$$

$$p_z = \theta \quad (1.2d)$$

$$(\rho u)_x + (\rho v)_y + (\rho w)_z = 0 \quad (1.2e)$$

The derivation of the multi-scale model in this chapter is based on the following three basic assumptions (Majda, 2007):

Assumption 1: Low Froude number. Since the reference flow speed $c = 50m/s$ is much

faster than the real flow speed on the synoptic or larger scales in the tropical troposphere, the Froude number, which is defined as the ratio between the typical horizontal velocity magnitude and the basic wave speed $F_r = U/c = \epsilon$, is assumed to be small. The dimensionless horizontal flow field $\mathbf{u}_h = (u, v)$ is rewritten as $\mathbf{u}_h = \epsilon \mathbf{u}_{h,1}$, where one dimensionless unit of the magnitude of $\mathbf{u}_{h,1}$ means $\epsilon c = 5m/s$.

Assumption 2: Weak potential temperature anomalies. The potential temperature deviation has been nondimensionalized as the temperature scale ($15K$), the mean potential temperature difference over one unit of the vertical length scale. However, the real potential temperature deviation θ , whose value is several Kelvin in the tropical troposphere (Lin and Johnson, 1996; Yanai et al., 2000), is much smaller than that. Thus the dimensionless potential temperature deviation can be rewritten as $\theta = \epsilon \theta_1$, where one dimensionless unit of θ_1 means $\epsilon \Theta = 1.5K$.

Assumption 3: Although the momentum forcing S_u, S_v and the thermal forcing S_θ have been nondimensionalized to $150m/s/day, 45K/day$, the measured atmospheric flow is much weaker than the corresponding dimensional units. For example, the measured heating associated with latent heat release in the tropics on the synoptic and larger scales is only several Kelvin per day. Thus we can rewrite the momentum and thermal forcings as $S_u = \epsilon S_{u,1}, S_\theta = \epsilon S_{\theta,1}$, where one dimensionless unit of $S_{u,1}$ means $15m/s/day$. and that of $S_{\theta,1}$ means $4.5K/day$.

The ansatz we use in this multi-scale model is such that all physical variables can be approximated by functions which vary on two zonal spatial scales and two temporal scales. Specifically, two zonal spatial scales are the synoptic scale ($L_E = 1500km$) and the planetary scale ($L_P = 15000km$). Two temporal scales are the daily time scale ($T_E = 8.3h$) and the intraseasonal time scale ($T_I = 3.5days$). Since ten units of this time scale span more than one month, T_I is an intraseasonal time scale. In general, for an arbitrary function f such as

physical variables u, v, w, p, θ , we can have

$$f(x, t, y, z) = f^\epsilon(x, X, t, T, y, z), \quad (1.3)$$

where we introduce the planetary-scale zonal variable $X = \epsilon x$, and the intraseasonal time scale variable $T = \epsilon t$, and y, z are on the synoptic scale. The implicit meaning in the ansatz (1.3) is that all physical variables can vary an amount of order one but no more than order one if any of the independent variables x, X, t, T, y, z vary an amount of order one, in order to guarantee the validity of the multi-scale asymptotics.

By assuming multi-scale solutions as Eq. (1.3), the zonal and time derivatives are given by chain rule

$$\frac{\partial f^\epsilon}{\partial x} + \epsilon \frac{\partial f^\epsilon}{\partial X}, \quad \frac{\partial f^\epsilon}{\partial t} + \epsilon \frac{\partial f^\epsilon}{\partial T}. \quad (1.4)$$

In order to consider averages of physical variables on the small spatial and temporal scales, we use the following averaging operators

$$\bar{f}(X, t, T, y, z) = \lim_{L \rightarrow \infty} \frac{1}{2L} \int_{-L}^L f(x, X, t, T, y, z) dx, \quad (1.5)$$

$$\langle f \rangle(x, X, T, y, z) = \lim_{T^* \rightarrow \infty} \frac{1}{2T^*} \int_{-T^*}^{T^*} f(x, X, t, T, y, z) dt. \quad (1.6)$$

For an arbitrary function f , we can have its zonal spatial average \bar{f} , therefore $f = \bar{f} + f'$ and f' satisfies $\bar{f}' = 0$. Similarly, we can have its temporal average $\langle f \rangle$, therefore $f = \langle f \rangle + \tilde{f}$ and \tilde{f} satisfies $\langle \tilde{f} \rangle = 0$. In order to guarantee the validity of the multi-scale asymptotics, all physical variables need to satisfy the solvability condition called the sublinear growth condition, which requires that the asymptotic expansion should grow sublinearly in (x, t) to avoid secular terms (Majda, 2003). In general, we have the following conditions for all variables in asymptotic expansion $\overline{\frac{\partial}{\partial x} f} = 0, \langle \frac{\partial}{\partial t} f \rangle = 0$.

With the assumptions of the low Froude number, the weak temperature gradient and that for momentum and thermal forcing magnitude, we are ready to write down the ansatz for all physical variables on multiple spatiotemporal scales (Majda and Klein, 2003; Majda, 2007)

$$g = \epsilon \left[g' (x, X, t, T, y, z) + \bar{g} (X, t, T, y, z) \right] + \epsilon^2 g_2, \quad g \in \{u, v, w, \theta, p, S_u, S_v, S_\theta\} \quad (1.7)$$

Now we can derive the multi-scale model, the detailed steps of the derivation can be found in Appendix 1.6.1.

1.2.1 The planetary-scale system

Substituting the ansatz (1.7) into Eqs. (1.2a-1.2e) and collecting all terms at the leading order yields a linear system. Now we take zonal spatial averaging over the synoptic scale, and get *the planetary-scale system*

$$\bar{u}_t - y\bar{v} = \bar{S}_u, \quad (1.8a)$$

$$\bar{v}_t + y\bar{u} = -\bar{p}_y + \bar{S}_v, \quad (1.8b)$$

$$\bar{\theta}_t + N^2 \bar{w} = \bar{S}_\theta, \quad (1.8c)$$

$$\bar{p}_z = \bar{\theta}, \quad (1.8d)$$

$$\bar{v}_y + \frac{1}{\rho} (\rho \bar{w})_z = 0, \quad (1.8e)$$

which describes the planetary-scale flow field. This system includes the planetary-scale inertial waves on the equatorial β -plane. A crucial property of this system is that it is a linear system without advective effects since the weak advection terms are at the second order. After zonal spatial averaging, this flow field is zonally symmetric on the synoptic scale. In addition, since there is no derivative with respect to the planetary scale X , it can

be regarded as a frozen parameter in the resulting flow field. Also, one dimensionless unit of horizontal velocity corresponds to $5m/s$ and that of potential temperature deviation corresponds to $1.5K$. Therefore, this system allows the momentum forcing to be roughly $15m/s/day$ and the thermal forcing to be roughly $4.5K/day$.

1.2.2 The synoptic-scale system

By subtracting *the planetary-scale system* (1.8a-1.8e) from the leading-order asymptotic equations, we can derive *the synoptic-scale system* (Majda, 2007)

$$u'_t - yv' = -p'_x + S'_u \quad (1.9a)$$

$$v'_t + yu' = -p'_y + S'_v \quad (1.9b)$$

$$\theta'_t + N^2 w' = S'_\theta \quad (1.9c)$$

$$p'_z = \theta' \quad (1.9d)$$

$$u'_x + v'_y + \frac{1}{\rho} (\rho w')_z = 0 \quad (1.9e)$$

which describes the synoptic-scale fluctuations of the flow field. These synoptic-scale fluctuating flows are characterized by linear equations without advective effects. Also, the momentum dissipation and radiative damping do not directly affect these synoptic-scale fluctuating flows since they are at the second order.

1.2.3 The leading-order planetary scale system on the intraseasonal time scale

Since the daily time scale t is the fast time scale compared with the intraseasonal time scale T , it is required that $\langle \partial g / \partial t \rangle = 0$ for any bounded function g to guarantee the validity of the asymptotics. We do time averaging on Eqs. (1.8a,1.8c,1.8e), and get *the leading-order*

planetary scale system on the intraseasonal time scale (Biello and Majda, 2006)

$$-y \langle \bar{v} \rangle = \langle \bar{S}_u \rangle, \quad (1.10a)$$

$$N^2 \langle \bar{w} \rangle = \langle \bar{S}_\theta \rangle, \quad (1.10b)$$

$$(\langle \bar{v} \rangle)_y + \frac{1}{\rho} (\rho \langle \bar{w} \rangle)_z = 0. \quad (1.10c)$$

Since the meridional velocity $\langle \bar{v} \rangle$ on the planetary/intraseasonal scales is directly determined by the zonal momentum forcing $\langle \bar{S}_u \rangle$ and the vertical velocity $\langle \bar{w} \rangle$ on the planetary/intraseasonal scales is directly determined by $\langle \bar{S}_\theta \rangle$, we obtain a constraint when we combine Eqs. (1.10a,1.10b) with the incompressibility condition (1.10c):

$$\left(\frac{\langle \bar{S}_u \rangle}{y} \right)_y = \frac{1}{\rho} \left(\rho \frac{\langle \bar{S}_\theta \rangle}{N^2} \right)_z. \quad (1.11)$$

Intuitively, this is not an unphysical requirement since a steady climatology requires a strict balance between the zonal momentum forcing and the thermal forcing. Also, if we do time averaging on Eqs. (1.8b,1.8d), we get

$$y \langle \bar{u} \rangle = -\langle \bar{p} \rangle_y + \langle \bar{S}_v \rangle, \quad (1.12)$$

$$\langle \bar{p} \rangle_z = \langle \bar{\theta} \rangle, \quad (1.13)$$

which are the geostrophic balance in the meridional direction if $\langle \bar{S}_v \rangle = 0$ and the hydrostatic balance for the leading-order terms $\langle \bar{p} \rangle, \langle \bar{\theta} \rangle$.

1.2.4 The planetary-scale system on the daily time scale

We can further divide each planetary-scale physical variable into a long-time average and a fluctuation variable, that is $\bar{g} = \langle \bar{g} \rangle + \tilde{\bar{g}}$ where $\tilde{\bar{g}}$ satisfies $\langle \tilde{\bar{g}} \rangle = 0$. By subtracting the time mean equations (1.10a-1.10c, 1.12, 1.13) on the planetary/intraseasonal scales from Eqs.

(1.8a-1.8e), we derive *the planetary-scale system on the daily time scale*

$$\tilde{\tilde{u}}_t - y\tilde{\tilde{v}} = \tilde{\tilde{S}}_u \quad (1.14a)$$

$$\tilde{\tilde{v}}_t + y\tilde{\tilde{u}} = -\tilde{\tilde{p}}_y + \tilde{\tilde{S}}_v \quad (1.14b)$$

$$\tilde{\tilde{\theta}}_t + N^2\tilde{\tilde{w}} = \tilde{\tilde{S}}_\theta \quad (1.14c)$$

$$\tilde{\tilde{p}}_z = \tilde{\tilde{\theta}} \quad (1.14d)$$

$$\tilde{\tilde{v}}_y + \frac{1}{\rho} (\rho\tilde{\tilde{w}})_z = 0 \quad (1.14e)$$

which describes the daily time scale fluctuations of the planetary-scale flow. These equations are linear and do not have advection terms. Also, the flow does not depend on the zonal synoptic scale. More importantly, since all physical variables vanish after the time averaging $\langle \tilde{\tilde{g}} \rangle = 0$, this system is a good candidate for the planetary-scale equatorial inertial oscillations to mimic the diurnal cycle of tropical convection. We model the diurnal cycle through this system in section 1.3.

1.2.5 The second-order planetary scale system on the intraseasonal time scale

Now we consider the asymptotic expansion of the primitive equations at the second order following (Majda, 2007). After zonal spatial and temporal averaging on the zonal momentum equation (1.2a), the thermal equation (1.2c), and the mass conservation (1.2e), all terms at the second order are collected and form *the second-order planetary scale system on the*

intraseasonal time scale, when they are combined with Eqs. (1.12-1.13)

$$\begin{aligned} \frac{D}{DT} \langle \bar{u} \rangle - y \langle \bar{v}_2 \rangle &= -\langle \bar{p} \rangle_X - d \langle \bar{u} \rangle - \frac{\partial}{\partial y} \left\langle \overline{v' u'} \right\rangle - \frac{1}{\rho} \frac{\partial}{\partial z} \left(\rho \left\langle \overline{w' u'} \right\rangle \right) \\ &\quad - \frac{\partial}{\partial y} \langle \tilde{v} \tilde{u} \rangle - \frac{1}{\rho} \frac{\partial}{\partial z} (\rho \langle \tilde{w} \tilde{u} \rangle) + \langle \bar{S}_{u,2} \rangle \end{aligned} \quad (1.15a)$$

$$y \langle \bar{u} \rangle = -\langle \bar{p} \rangle_y + \langle \bar{S}_v \rangle \quad (1.15b)$$

$$\begin{aligned} \frac{D}{DT} \langle \bar{\theta} \rangle + N^2 \langle \bar{w}_2 \rangle &= -d_\theta \langle \bar{\theta} \rangle - \frac{\partial}{\partial y} \left\langle \overline{v' \theta'} \right\rangle - \frac{1}{\rho} \frac{\partial}{\partial z} \left(\rho \left\langle \overline{w' \theta'} \right\rangle \right) \\ &\quad - \frac{\partial}{\partial y} \langle \tilde{v} \tilde{\theta} \rangle - \frac{1}{\rho} \frac{\partial}{\partial z} (\rho \langle \tilde{w} \tilde{\theta} \rangle) + \langle \bar{S}_{\theta,2} \rangle \end{aligned} \quad (1.15c)$$

$$\langle \bar{p} \rangle_z = \langle \bar{\theta} \rangle \quad (1.15d)$$

$$\langle \bar{u} \rangle_X + \langle \bar{v}_2 \rangle_y + \frac{1}{\rho} (\rho \langle \bar{w}_2 \rangle)_z = 0 \quad (1.15e)$$

where $\frac{D}{DT} = \frac{\partial}{\partial T} + \langle \bar{v} \rangle \frac{\partial}{\partial y} + \langle \bar{w} \rangle \frac{\partial}{\partial z}$, this system is advected by the leading-order meridional and vertical velocity in section 1.2.3. This system describes the evolution of $\langle \bar{u} \rangle, \langle \bar{p} \rangle, \langle \bar{\theta} \rangle, \langle \bar{v}_2 \rangle, \langle \bar{w}_2 \rangle$ on the planetary/intraseasonal scales. The difference between this system and the leading-order planetary scale system on the intraseasonal time scale (Eqs. 1.10a-1.10c) is that the zonal momentum equation and thermal equation here are forced by eddy flux divergences of momentum and temperature from the synoptic scale and the daily time scale, as shown on the right side of Eqs. (1.15a, 1.15c). There are two pieces of upscale flux divergences in each equation. The first piece corresponds to the spatial upscale feedback from the synoptic scale to the planetary scale and comprises both meridional and vertical components. The second piece corresponds to the temporal upscale feedback from the daily time scale to the intraseasonal time scale and also comprises meridional and vertical components. These two pieces of eddy flux divergence of momentum and temperature force the planetary/intraseasonal scale flows (Eqs. 1.15a-1.15e) in a linear way. According to the physical observation that the dissipation time scales of the momentum damping and the radiative damping are both on the intraseasonal time scale, the planetary/intraseasonal

scale circulation anomalies described here are subject to this momentum dissipation and radiative damping. This system includes not only the eddy flux divergences of momentum and temperature from the synoptic scale, which have already been explored in the IPESD model (Majda and Klein, 2003; Majda and Biello, 2004; Biello and Majda, 2005, 2006), but also those from the daily time scale, providing a more general framework to assess upscale effects.

1.3 A Model for the Diurnal Cycle and Upscale Fluxes

The diurnal variability of tropical precipitation over land and oceans has been documented in Kikuchi and Wang (2008). By applying empirical orthogonal functions (EOF) analysis to two TRMM datasets, they confirmed the persistence of the diurnal cycle of tropical precipitation whose amplitude is relatively large in the continental regime and weak in the oceanic regime. Furthermore, the significant variability of tropical precipitation due to the diurnal cycle of solar heating is examined in the context of simple models for tropical convection (Frenkel et al., 2011a,c, 2013). These models utilize three cloud types (congestus, deep and stratiform) to characterize organized tropical convection. Since the latent heat can drive the atmospheric flow through thermodynamics, the diurnal cycle of tropical precipitation can induce the diurnal variability of the flow field in the tropical troposphere. In this section, we build a model for the diurnal cycle, and discuss the planetary-scale inertial oscillations on the daily time scale as well as the resulting upscale fluxes on the planetary/intraseasonal scale.

We start from *the planetary-scale system on the daily time scale* (1.14a-1.14e) and assume that there is only thermal forcing $\tilde{\tilde{S}}_\theta$ associated with latent heat release, but no momentum forcing $\tilde{\tilde{S}}_u, \tilde{\tilde{S}}_v$. Also, we assume the buoyancy frequency N^2 and the density ρ to be constant so that their dimensionless values are equal to 1 and the Boussinesq approximation is used. Although the density profile in the realistic atmosphere changes dramatically with the height, such distinction does not change the qualitative conclusion and makes for more streamlined

notation.

$$\tilde{u}_t - y\tilde{v} = 0 \quad (1.16a)$$

$$\tilde{v}_t + y\tilde{u} = -\tilde{p}_y \quad (1.16b)$$

$$\tilde{\theta}_t + \tilde{w} = \tilde{S}_\theta \quad (1.16c)$$

$$\tilde{p}_z = \tilde{\theta} \quad (1.16d)$$

$$\tilde{v}_y + \tilde{w}_z = 0 \quad (1.16e)$$

here we assume rigid lid boundary conditions at top and bottom of the troposphere

$$\tilde{w}(x, X, t, T, y, z) |_{z=0,\pi} = 0, \quad (1.17)$$

where in dimensionless form $z = 0$ represents the surface of the earth and $z = \pi$ represents the top of the troposphere.

Since we use the thermal forcing \tilde{S}_θ in Eq. (1.16c) to represent the latent heat release during precipitation from clouds, a good cloud model can provide an appropriate heating profile. For example, the multicloud model convective parameterizations (Khoudier and Majda, 2006a,b,c) based on three cloud types (congestus, deep and stratiform) have been revealed to be very useful in reproducing key features of organized convection and tropical precipitation in the continental regime (Frenkel et al., 2011c). These three cloud types serve to provide the bulk of tropical precipitation and the main source of latent heat in the troposphere. In detail, cumulus congestus clouds heat the lower troposphere through latent heat release and cool the upper troposphere due to detrainment and the high reflectivity at the tops of clouds. Deep convective clouds warm and dry the entire troposphere, and release the majority of tropical precipitation. Stratiform clouds warm the upper troposphere through precipitation and cool the lower troposphere through evaporation of rain from stratiform clouds. To mimic the vertical structure of the three clouds types introduced above, we

assume that the thermal forcing \tilde{S}_θ is based on the first two baroclinic modes in the free troposphere. Earlier examples of models with heating defined by two baroclinic modes include (Haertel and Kiladis, 2004) and (Biello and Majda, 2005). In addition, the figure 3 in (Kikuchi and Wang, 2008) indicates that the principle component time series of the two leading empirical orthogonal functions have dominant diurnal periodicity in sinusoidal variation. In general, we can prescribe this heating forcing as follows

$$\tilde{S}_\theta = H_1(y) \sin(kX + \omega t) (-\sin(z)) + \alpha H_2(y) \sin(kX + \omega t + \beta) (-2 \sin(2z)) \quad (1.18)$$

where both $H_1(y)$ and $H_2(y)$ depend only on y and are used to represent the meridional profile of the heating. The diurnal cycle frequency ω is 2π in units of day^{-1} and the wavenumber k is $\pi/20$ in units of $10^{-3}km^{-1}$. Two specific examples are examined in the following subsections.

1.3.1 A simple heating profile in the first two baroclinic modes

The three cloud types (congestus, deep convective, stratiform) and their life cycle have been investigated through observations of organized tropical convection (Johnson et al., 1999; Mapes et al., 2006). In this cloud life cycle, congestus clouds serve to moisten and precondition the middle troposphere prior to deep convection. Deep convective clouds warm and dry the entire troposphere through large amounts of rainfall. Then stratiform clouds warm and dry the upper troposphere, cool and moisten the lower troposphere after deep convection. Using the multicloud model (Khoudier and Majda, 2006a,b,c), Frenkel et al. (2011c) successfully reproduce several key features of the realistic tropical precipitation over continental regions by building simple multicloud models with the first two baroclinic modes of vertical structure in the free troposphere as well as the bulk atmospheric boundary layer dynamics. By identifying a cycle of five phases for the diurnal cycle of precipitation over land, they explained the underlying physical mechanism and dynamical behaviors in terms of the in-

teractions of the three cloud types with the periodically forcing boundary layer dynamics. Some of the key features are as follows. In the early morning, direct solar heating produces convective activity and detrainment of shallow clouds from the boundary layer. In the late morning/early afternoon, congestus heating slightly warms the lower troposphere and cools the upper troposphere, which delays the reinitiation of deep convection. Meanwhile, the shallow cumulus entrainment and detrainment fluxes moisten the middle atmosphere and precondition deep convection. In the late afternoon, the massive amount of precipitation is released in the explosive afternoon deep convection episode, which warms the entire troposphere through latent heat. After sunset, the moisture recovers quickly and the troposphere nearly reaches a radiative-convective equilibrium (RCE) state by balancing precipitation and the imposed radiative cooling. Here we try to prescribe such thermal forcing which is qualitatively consistent with those key features.

Suppose deep convective clouds in the first baroclinic mode and congestus/stratiform clouds in the second baroclinic mode only have the first two parabolic cylinder functions as their meridional profiles, we can prescribe the heating as follows

$$\tilde{S}_\theta = \sin(kX + \omega t) [\phi_{0|1} + \gamma\phi_{1|1}] (-\sin(z)) + \alpha \sin(kX + \omega t + \beta) [\phi_{0|2} + \gamma\phi_{1|2}] (-2\sin(2z)) \quad (1.19)$$

where $\{\phi_{m|q}\}$ are functions of y , $m = 0, 1$; $q = 1, 2$ as shown in the left panel of Fig. 1.1. The relative strength of the second baroclinic mode $\alpha = \frac{1}{3}$ and the phase draft $\beta = \frac{\pi}{4}$ are two constant parameters which are used to control the spatial pattern of the heating at a specific season without the intraseasonal time scale dependence. We can change the meridional profiles $H_1 = \phi_{0|1} + \gamma\phi_{1|1}$ and $H_2 = \phi_{0|2} + \gamma\phi_{1|2}$ by adjusting the value of parameter γ . For simplicity, here we only choose the leading two meridional modes for each baroclinic mode to mimic different meridional profiles of the heating in different seasons. If $\gamma = 0$, H_1 and H_2 are symmetric about the equator, which can be used to mimic the equinox case. If $\gamma = 1$, H_1 and H_2 reach the maximum value at a positive y value in the northern

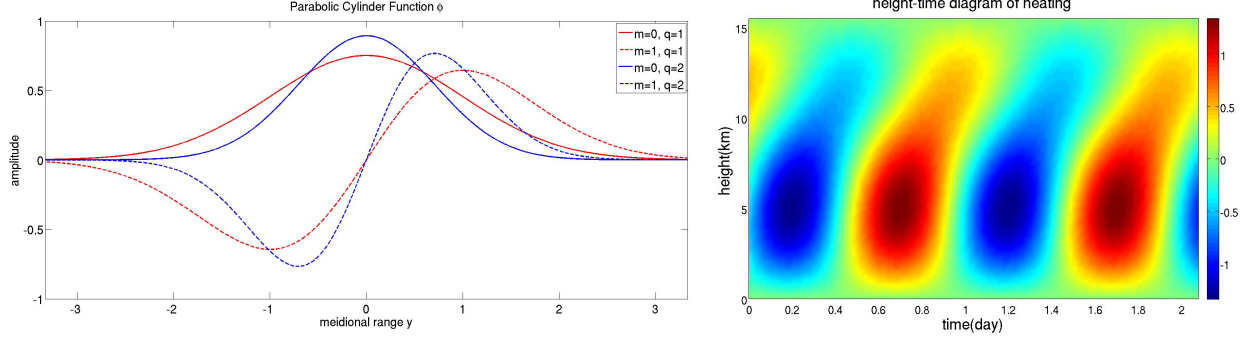


Figure 1.1: The left figure shows meridional profile $\phi_{m|q}$, $m = 1, 2; q = 1, 2$. The right figure shows heating profile around the equator during equinox at $y = 0$ and $\gamma = 0$. Heating is in units of $4.5Kday^{-1}$.

hemisphere. If $\gamma = -1$, H_1 and H_2 reach the maximum value at a negative y value in the southern hemisphere. The time evolution of the heating vertical profile is depicted in the right panel of Fig. 1.1, where the heating center moves from the lower troposphere to the middle troposphere and finally reaches the upper troposphere, consistent with the cloud life cycle, from congestus clouds in the lower troposphere to deep convective clouds throughout the whole troposphere and to stratiform clouds in the upper troposphere. The curves on the left panel show different meridional profiles of heating during equinox and boreal summer, which is consistent with the observation that in annual mean ($\gamma = 0$), the heating mainly centers in the continental regime around the equator and during boreal summer ($\gamma = 1$), the heating reaches the maximum value in the continental regime of the northern hemisphere (Kikuchi and Wang, 2008).

With the explicit solutions (Appendix 1.6.2) for the planetary-scale system on the daily time scale(1.16a-1.16e), we can calculate the inertial oscillations in the diurnal cycle and the eddy flux divergences of momentum and temperature F^u, F^θ that appear in the second-order

planetary scale system on the intraseasonal time scale (1.15a-1.15e)

$$F^u = -\frac{\partial}{\partial y} \langle \tilde{v}\tilde{u} \rangle - \frac{\partial}{\partial z} \langle \tilde{w}\tilde{u} \rangle \quad (1.20)$$

$$F^\theta = -\frac{\partial}{\partial y} \langle \tilde{v}\tilde{\theta} \rangle - \frac{\partial}{\partial z} \langle \tilde{w}\tilde{\theta} \rangle \quad (1.21)$$

Several features of these eddy flux divergences are important. First, F^u, F^θ do not depend on the daily time scale t , but they can still vary on the intraseasonal time scale T in general. Secondly, since upscale flux divergences F^u, F^θ are induced by the diurnal cycle heating in the first and second baroclinic modes, it can be shown that upscale flux divergences F^u, F^θ are in the first and third baroclinic modes (Appendix 1.6.2), and the third baroclinic mode provides extensive vertical structure to capture more realistic features. Thirdly, the magnitudes of F^u, F^θ are proportional to $\alpha \sin(\beta)$. If $\alpha = 0$, the heating \tilde{S}_θ is vertically symmetric with respect to the middle layer of the whole troposphere since there exists only the deep convective clouds in the first baroclinic mode. If $\beta = 0$, the first baroclinic mode for deep convective clouds and the second baroclinic mode for congestus/stratiform clouds are in phase. In both two cases above, F^u, F^θ are zero, meaning that there is no upscale transport of kinetic and thermal energy to the planetary/intraseasonal scales.

Now, we adjust the parameter γ in the expression of \tilde{S}_θ to mimic the equinox case and boreal summer case, calculate the corresponding planetary-scale flow on the daily time scale, and discuss eddy flux divergences of momentum and temperature F^u, F^θ in Fig. 1.2.

During boreal summer, the maximum dimensionless magnitude of F^u is around 0.1 and that of F^θ is around 1, which corresponds to $0.15m/s/day$ for momentum forcing and $0.45K/day$ for thermal forcing on the planetary/intraseasonal scales. Since the thermal forcing is nondimensionalized by $0.45K/day$, there is significant eddy flux divergence of temperature. The maximum dimensionless magnitude of the thermal forcing F^θ is about 10 times that of the momentum forcing F^u . Thus the eddy flux divergence of temperature dominates. Several features of the thermal forcing F^θ are important. First, there is strong

heating in the middle troposphere and cooling in the upper and lower troposphere, in the northern hemisphere, and even the whole troposphere around the equator. The maximum dimensionless magnitude of heating is three times that of cooling, which is intuitively understandable because F^u, F^θ are in the first and third baroclinic modes. Secondly, although the vertical component $-\frac{\partial}{\partial z} \langle \tilde{w}\tilde{\theta} \rangle$ of F^θ is a little stronger than the meridional component $-\frac{\partial}{\partial y} \langle \tilde{v}\tilde{\theta} \rangle$, they are still comparable and form the significant thermal forcing F^θ . However, for momentum forcing F^u , its meridional component $-\frac{\partial}{\partial y} \langle \tilde{v}\tilde{u} \rangle$ is extremely weak and its vertical component $-\frac{\partial}{\partial z} \langle \tilde{w}\tilde{u} \rangle$ dominates but is still weak. Lastly, we can find the unphysical weak heating in the southern hemisphere due to the simplicity of the heating profile (1.19).

During equinox, both F^u, F^θ shown in the lower panels of Fig. 1.2 are quite weak. Thus we conclude that there is quite weak direct intraseasonal impact of the diurnal cycle during equinox, although there is also a possible indirect effect of the diurnal cycle on synoptic and mesoscale dynamics, which in turn may impact the intraseasonal scale dynamics.

1.3.2 A heating profile in the first two baroclinic modes with the same meridional profile

To prescribe a more physical heating profile without loss of generality, we assume that the first baroclinic mode for deep convection clouds and the second baroclinic mode for congestus/stratiform clouds share the same meridional profile, that is $H_1(y) = H_2(y)$ in Eq. (1.18). In detail, the meridional profile of the diurnal cycle heating is prescribed as

$$H(y) = H_0 e^{-a(y-y_0)^2}. \quad (1.22)$$

Fig. 1.3 depicts the heating profile with the meridional profile specified in Eq. (1.22). According to the meridional profile in Eq. (1.22), the diurnal cycle heating is centered at the latitude given by y_0 . By varying the value of y_0 , we are able to mimic different heating

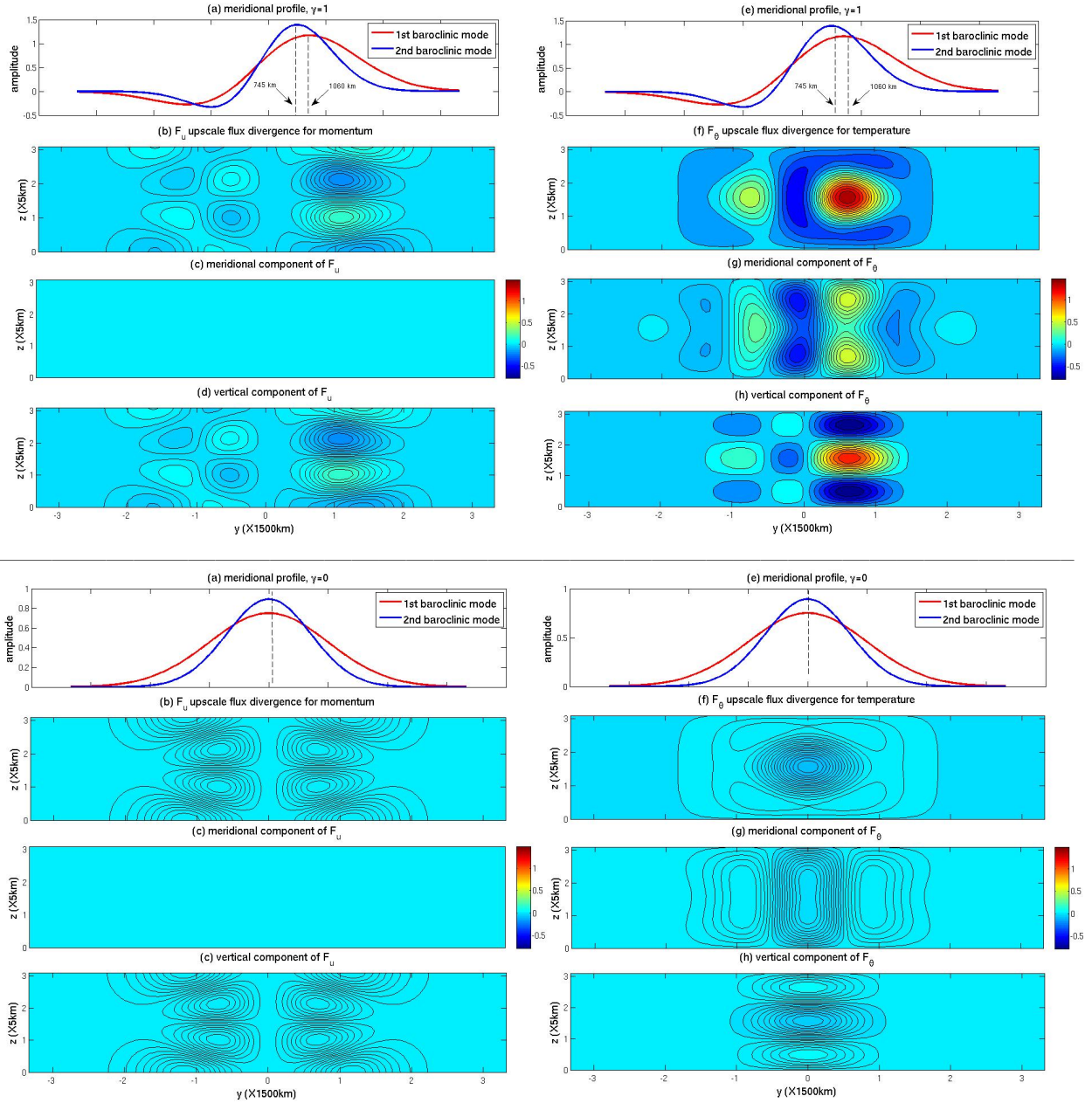


Figure 1.2: The upper figure shows eddy flux divergences of momentum and temperature F^u, F^θ during boreal summer. The lower figure is for the equinox case. In each figure, the eight panels show (a) meridional profile of heating; (b) eddy flux divergence of momentum F^u ; (c) its meridional component $-\frac{\partial}{\partial y} \langle \tilde{v} \tilde{u} \rangle$; (d) its vertical component $-\frac{\partial}{\partial z} \langle \tilde{w} \tilde{u} \rangle$; (e) meridional profile of heating; (f) eddy flux divergence of temperature F^θ ; (g) its meridional component $-\frac{\partial}{\partial y} \langle \tilde{v} \tilde{\theta} \rangle$; (h) its vertical component $-\frac{\partial}{\partial z} \langle \tilde{w} \tilde{\theta} \rangle$. One dimensionless unit of F^u is 1m/s/day and that of F^θ is 0.45K/day .

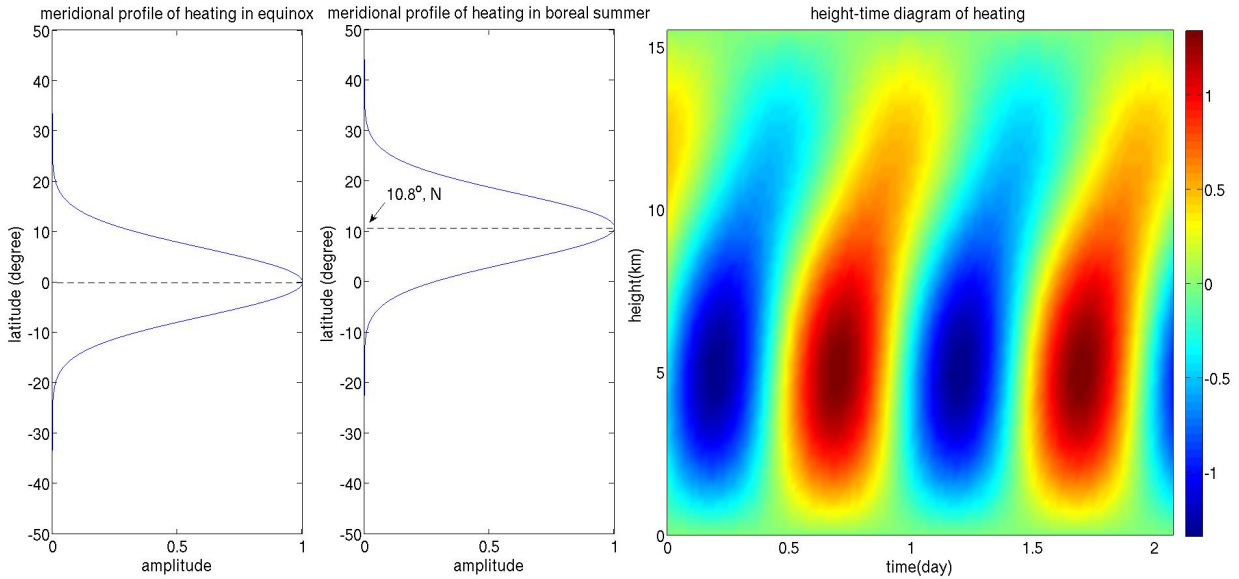


Figure 1.3: The meridional profile of heating during equinox is shown in the left panel and that during boreal summer is shown in the middle panel. The meridional profile in the middle panel takes its maximum at $y = 1200\text{km}$, 10.8°N . The right panel shows the height and time diagram of the diurnal cycle heating. Here red means heating(positive) and blue means cooling(negative). One unit of $\tilde{\bar{S}}_\theta$ is 4.5K/day .

profiles in different seasons, as observed in (Kikuchi and Wang, 2008). During equinox, $y_0 = 0$ means that the heating reaches maximum at the equator. Here we set $a = 2, H_0 = 1$ so that the strength of the heating drops to $1/e$ of its maximum magnitude around latitudes $y = \pm 1000\text{km}$, which qualitatively matches the spatial pattern of diurnal precipitation in the annual mean. During boreal summer, $y_0 = 0.8$ means 1200km away from the equator in the northern hemisphere. Here we set $a = 2, H_0 = 1$ so that the strength of the heating drops to $1/e$ of its maximum magnitude at latitudes $y = 2300\text{km}, y = 140\text{km}$, which also qualitatively matches the spatial pattern of diurnal precipitation during boreal summer. Since the spatial patterns of the diurnal precipitation in different seasons are different, in the following content, we will always discuss the equinox case and the boreal summer case respectively.

Now we adjust the parameter y_0 in the expression of $\tilde{\bar{S}}_\theta$ for the equinox case and boreal

summer case, calculate the corresponding planetary-scale flow on the daily time scale, and discuss eddy flux divergences of momentum and temperature F^u, F^θ (1.20-1.21) in Fig. 1.4.

During boreal summer, the resulting eddy flux divergences of momentum and temperature share many similar properties as the case in Section 1.3.1. The most crucial property is that the thermal forcing F^θ on the planetary/intraseasonal scales is still strong, meaning that there is significant upscale flux feedback of temperature and the eddy flux divergence of temperature F^θ dominates. There is strong heating in the middle troposphere of the northern hemisphere and cooling surrounding the heating center and at higher latitudes of the northern hemisphere. During equinox, both F^u, F^θ are quite weak, so there is weak intraseasonal impact of the diurnal cycle during equinox.

1.4 The Intraseasonal Impact of the Diurnal Cycle on the Planetary Scale

In this section, the planetary-scale circulation on the intraseasonal time scale is studied. According to the multi-scale asymptotic results in section 1.2, there are two systems on the planetary/intraseasonal scales. The first system (Eqs. 1.10a-1.10c) deals with the winds $\langle \bar{v} \rangle, \langle \bar{w} \rangle$, which is derived from the leading-order asymptotic expansion of the primitive equations(1.2a-1.2e). Since the dimensional units of $\langle \bar{v} \rangle, \langle \bar{w} \rangle$ are $5m/s, 1.6cm/s$, respectively, this system can be utilized as a model for the Hadley cell. The second system (Eqs. 1.15a-1.15e) is about $\langle \bar{u} \rangle, \langle \bar{p} \rangle, \langle \bar{\theta} \rangle, \langle \bar{v}_2 \rangle, \langle \bar{w}_2 \rangle$, which is derived from the second-order asymptotic expansion of the primitive equations (1.2a-1.2e). The dimensional units of $\langle \bar{v}_2 \rangle, \langle \bar{w}_2 \rangle$ are $0.5m/s, 0.16cm/s$, thus $\langle \bar{v}_2 \rangle, \langle \bar{w}_2 \rangle$ can be understood as the circulation anomalies on the planetary/intraseasonal scales induced by the diurnal cycle heating driving eddy flux divergences F^u, F^θ . The objective here is to understand the nature of the planetary/intraseasonal scale circulation anomalies that arise from different diurnal cycle heating patterns during

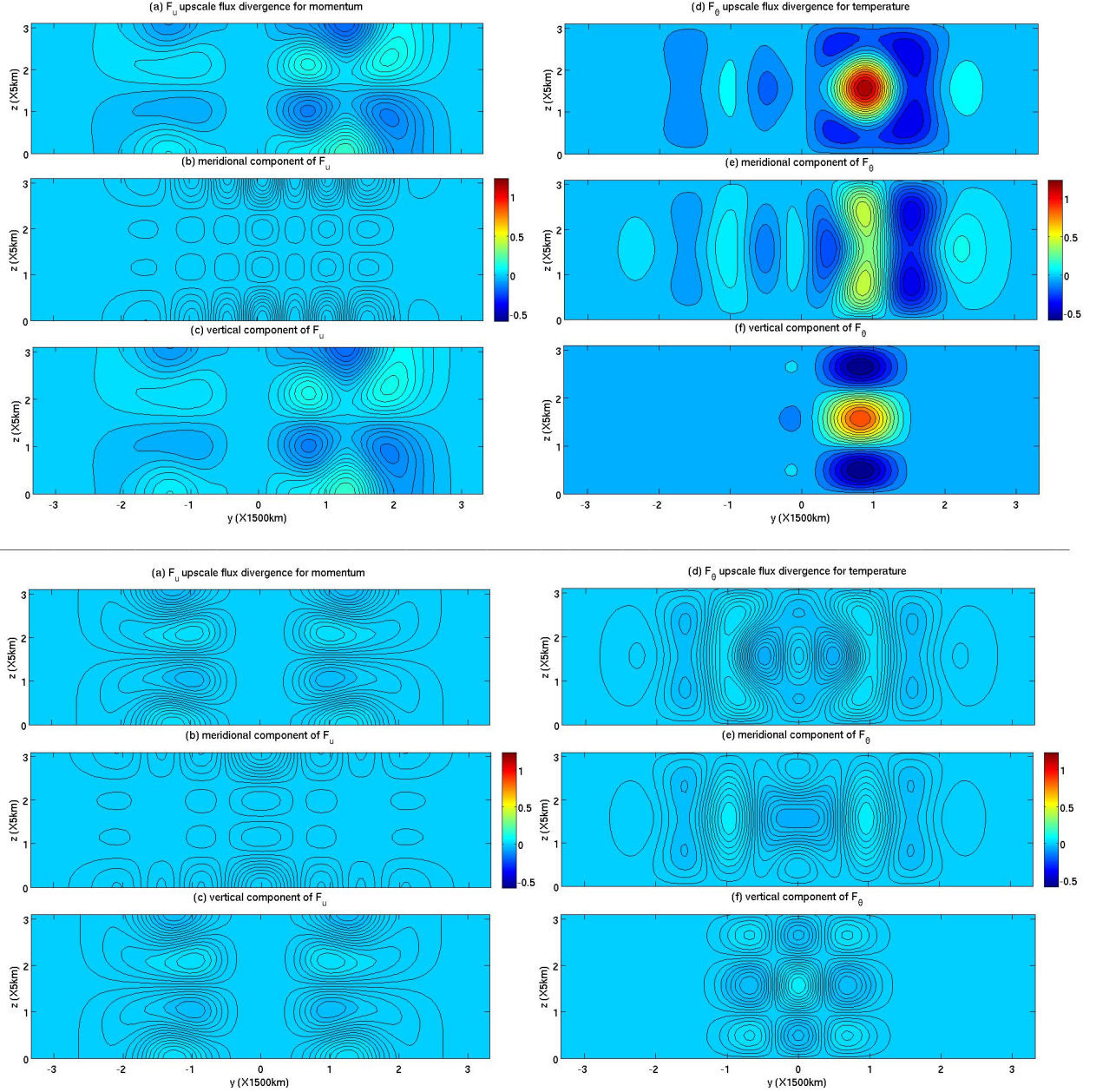


Figure 1.4: The upper figure shows eddy flux divergences of momentum and temperature F^u, F^θ during boreal summer ($y_0 = 0$). The lower figure is for an equinox case ($y_0 = 0.8$). In each figure, the six panels show (a) eddy flux divergence of momentum F^u ; (b) its meridional component $-\frac{\partial}{\partial y} \langle \tilde{v} \tilde{u} \rangle$; (c) its vertical component $-\frac{\partial}{\partial z} \langle \tilde{v} \tilde{u} \rangle$; (d) eddy flux divergence of temperature F^θ ; (e) its meridional component $-\frac{\partial}{\partial y} \langle \tilde{v} \tilde{\theta} \rangle$; (f) its vertical component $-\frac{\partial}{\partial z} \langle \tilde{w} \tilde{\theta} \rangle$. One dimensionless unit of F^u is $1m/s/day$ and that of F^θ is $0.45K/day$.

equinox and boreal summer.

1.4.1 A Model for the Hadley cell

The Hadley circulation consists of two overturning thermally direct cells in the low latitudes of both hemispheres. Observations indicate that two Hadley cells, symmetric about the equator, are rarely observed even in the equinoctial seasons. In boreal summer or winter, the winter hemisphere branch of the Hadley cell is much stronger than the summer hemisphere branch (Holton and Hakim, 2012). In fact, Eqs. (1.23a-1.23c) are derived from the leading-order asymptotic expansion of the primitive equations (1.2a-1.2e), and $\langle \bar{v} \rangle, \langle \bar{w} \rangle, \langle \bar{S}_u \rangle, \langle \bar{S}_\theta \rangle$ are on the planetary/intraseasonal scales. The dimensional units of $\langle \bar{S}_u \rangle, \langle \bar{S}_\theta \rangle$ are $15m/s/day, 4.5K/day$ separately, and the dimensional units of $\langle \bar{v} \rangle, \langle \bar{w} \rangle$ are $5m/s, 1.6cm/s$ separately. Here we assume the buoyancy frequency N^2 and the density ρ to be constant.

$$-y \langle \bar{v} \rangle = \langle \bar{S}_u \rangle \quad (1.23a)$$

$$N^2 \langle \bar{w} \rangle = \langle \bar{S}_\theta \rangle \quad (1.23b)$$

$$(\langle \bar{v} \rangle)_y + \langle \bar{w} \rangle_z = 0 \quad (1.23c)$$

Considering that Eqs. (1.23a-1.23c) describe the leading-order planetary scale flow on the intraseasonal time scale, we can use them to model the Hadley cell. Since the meridional velocity $\langle \bar{v} \rangle$ is directly determined by the momentum forcing $\langle \bar{S}_u \rangle$ and the vertical velocity $\langle \bar{w} \rangle$ is determined by the heating $\langle \bar{S}_\theta \rangle$, there is a strict balance between the momentum forcing $\langle \bar{S}_u \rangle$ and the heating $\langle \bar{S}_\theta \rangle$. If we combine Eqs. (1.23a,1.23b) with the incompressibility condition (1.23c), we obtain

$$\left(\frac{\langle \bar{S}_u \rangle}{y} \right)_y = \left(\frac{\langle \bar{S}_\theta \rangle}{N^2} \right)_z. \quad (1.24)$$

The system (1.23a-1.23c) is independent of other systems and only forced by the leading-order zonal momentum forcing and thermal forcing on the planetary/intraseasonal scales. Unless $\langle \bar{S}_u \rangle, \langle \bar{S}_\theta \rangle$ satisfy the constraint (1.24), these equations can not be solved. Such a constraint is induced in this reduced model satisfying geostrophic balance in zonal direction and weak temperature gradient in the thermal equation. In fact, such a constraint can be relaxed into a group of dynamical equations for trade winds and Hadley circulation by allowing stronger planetary-scale zonal winds, pressure and potential temperature (Biello and Majda, 2010). In general, we can prescribe arbitrary $\langle \bar{S}_u \rangle, \langle \bar{S}_\theta \rangle$ satisfying the constraint(1.24) and get the corresponding leading-order planetary/intraseasonal scale circulation. Here we prescribe the momentum forcing $\langle \bar{S}_u \rangle$ and thermal forcing $\langle \bar{S}_\theta \rangle$ to qualitatively match the key features of the Hadley cell.

During equinox, the Hadley cell is symmetric about the equator. For each cell, there is rising motion near the equator, poleward flow in the upper troposphere, descending motion in the subtropics, and equatorward flow near the surface. The heating and zonal momentum forcing are specified in Eq. 1.25-1.26. The spatial patterns of the forcings and the resulting meridional and vertical flow field are shown in the upper panels of Fig. 1.5.

$$S_\theta = (1 - y^2) e^{-y^2/2} \sin(z), \quad (1.25)$$

$$S_u = y \int_{-\infty}^y (1 - s^2) e^{-s^2/2} ds \cos(z). \quad (1.26)$$

During boreal summer, the winter hemisphere branch of the Hadley cell is much stronger than the summer hemisphere branch. The heating and zonal momentum forcing are specified in Eq. 1.27-1.28. The spatial patterns of the forcings and the resulting meridional and

vertical flow field are shown in the lower panels of Fig. 1.5.

$$S_\theta = \left[ye^{-y^2} - 0.2(y-2)e^{-2(y-2)^2} \right] \sin(z), \quad (1.27)$$

$$S_u = y \int_{-\infty}^y \left[se^{-s^2} - 0.2(s-2)e^{-2(s-2)^2} \right] ds \cos(z). \quad (1.28)$$

1.4.2 A simplified version of the intraseasonal impact of the diurnal cycle

The second-order planetary scale system (1.15a-1.15e) on the intraseasonal time scale describes the planetary/intraseasonal scale dynamic response to the diurnal cycle of tropical convection. It is derived from the second-order asymptotic expansion of the primitive equations (1.2a-1.2e). There are two pieces of eddy flux divergences of momentum in the zonal momentum equation and two pieces of eddy flux divergences of temperature in the thermal equation. In each equation, the first piece corresponds to upscale feedback from the synoptic scale to the planetary scale, which has been utilized to successfully generate key features of MJO (Majda and Biello, 2004; Biello and Majda, 2005, 2006). The second piece corresponds to upscale feedback from the daily time scale to the intraseasonal time scale. In order to consider the intraseasonal impact of the diurnal cycle in a simplified case, we consider the zonally symmetric version of the second-order planetary scale system (Eqs. 1.15a-1.15e), neglect the upscale feedback across multiple spatial scales and just focus on the upscale feedback across multiple temporal scales. All synoptic-scale variables (u' , v' , p' , θ' , w') are set to zero. Also, we assume that there is no extra momentum forcing $\langle \bar{S}_{u,2} \rangle$, $\langle \bar{S}_{v,1} \rangle$ and thermal forcing $\langle \bar{S}_{\theta,2} \rangle$ on the planetary/intraseasonal scales. To consider a simplified version, we assume that there is no leading-order planetary/intraseasonal scale circulation in section (1.4.1), which means there is no advection effects in the system (1.15a-1.15e). Lastly, we assume that the buoyancy frequency N^2 and the density ρ are constants. To be brief, we

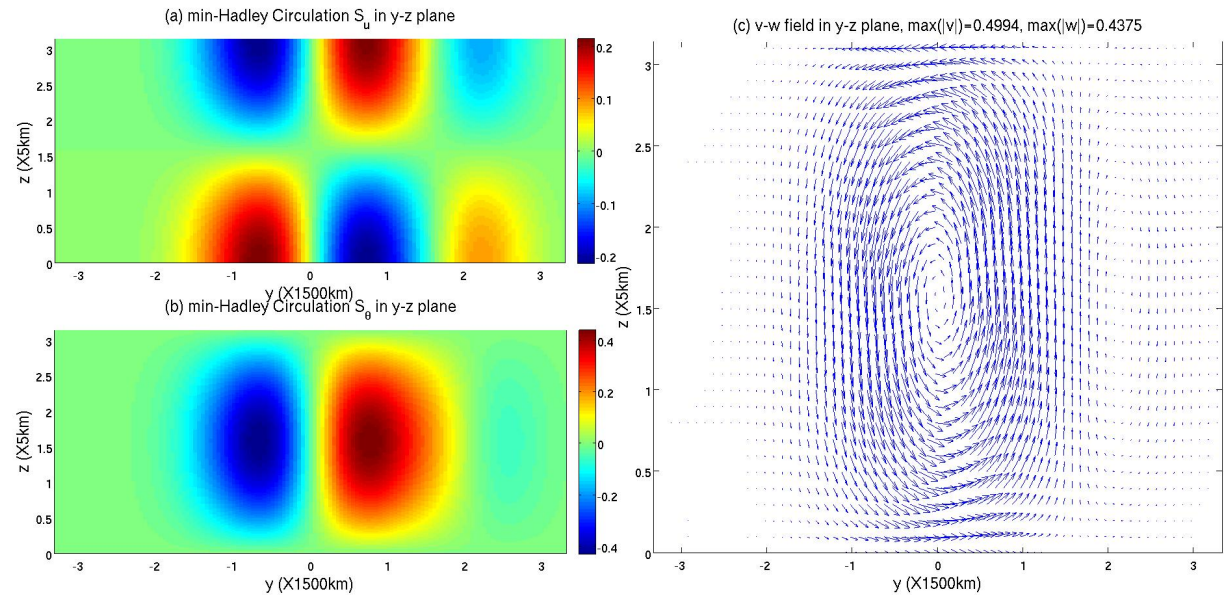
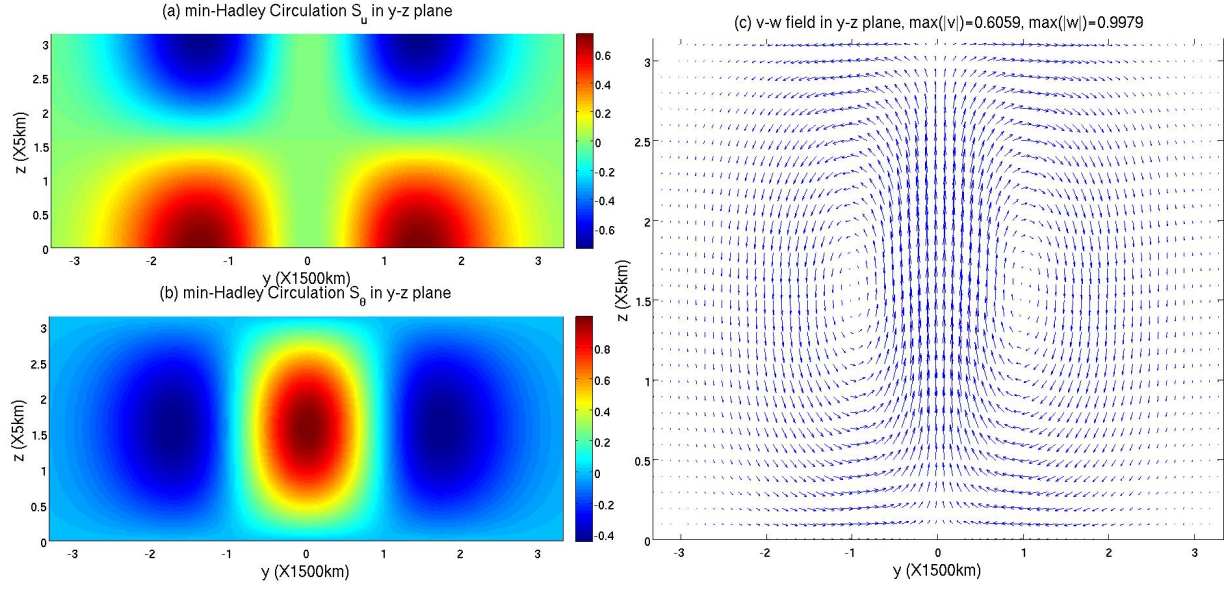


Figure 1.5: The upper three panels shows the equinox case. The lower three panels are the boreal summer case. (a) zonal momentum forcing; (b) thermal forcing; (c) meridional and vertical flow field. For zonal momentum forcing, blue means westward and red means eastward. For thermal forcing, blue means cooling and red means heating. The units of $\langle \bar{S}_u \rangle$, $\langle \bar{S}_\theta \rangle$, $\langle \bar{v} \rangle$, $\langle \bar{w} \rangle$ are $15m/s/day$, $4.5K/day$, $5m/s$ and $1.6cm/s$ respectively.

rename all physical variables $u = \langle \bar{u} \rangle, p = \langle \bar{p} \rangle, \theta = \langle \bar{\theta} \rangle, v = \langle \bar{v}_2 \rangle, w = \langle \bar{w}_2 \rangle$, and we can obtain a simplified version of the second-order planetary scale system on the intraseasonal time scale

$$\frac{\partial}{\partial T} u - yv = -du + F^u, \quad (1.29a)$$

$$yu = -p_y, \quad (1.29b)$$

$$\frac{\partial}{\partial T} \theta + w = -d_\theta \theta + F^\theta, \quad (1.29c)$$

$$p_z = \theta, \quad (1.29d)$$

$$v_y + w_z = 0. \quad (1.29e)$$

We assume rigid lid boundary conditions at top and bottom of the troposphere,

$$w(X, T, y, z) |_{z=0,\pi} = 0, \quad (1.30)$$

where in dimensionless unit $z = 0$ represents the surface of the earth and $z = \pi$ represents the top of the troposphere. The momentum damping coefficient d is $1/5day^{-1}$ and the temperature damping coefficient d_θ is $1/15day^{-1}$. F^u, F^θ represent upscale feedback from the daily scale to the intraseasonal time scale in the zonal momentum equation and the thermal equation respectively

$$F^u = -\frac{\partial}{\partial y} \langle \tilde{v} \tilde{u} \rangle - \frac{\partial}{\partial z} \langle \tilde{w} \tilde{u} \rangle; F^\theta = -\frac{\partial}{\partial y} \langle \tilde{v} \tilde{\theta} \rangle - \frac{\partial}{\partial z} \langle \tilde{w} \tilde{\theta} \rangle. \quad (1.31)$$

This system is driven by eddy flux divergences of momentum and temperature F^u, F^θ , which are associated with the planetary-scale flow on the daily time scale (1.16a-1.16e). The physical variables in this system consist of the leading-order physical variables u, p, θ and the second-order physical variables v, w . The second-order meridional velocity v and vertical velocity w can be understood as the planetary-scale circulation anomalies induced by the

intraseasonal impact of the diurnal cycle of tropical convection. In the following discussion, we consider the different behavior of the planetary/intraseasonal scale dynamics in Eqs. (1.29a-1.29e,1.30) during equinox and boreal summer in an ideal zonally symmetric case.

In order to analyze the intraseasonal impact of the diurnal cycle of tropical convection, we plot and discuss the planetary/intraseasonal scale steady state circulation corresponding to eddy flux divergences F^u, F^θ . The forcings F^u, F^θ can be evaluated explicitly through Eq. (1.31) [see Appendix 1.6.2] and the planetary/intraseasonal scale equations (1.29a-1.29e) can be solved by spectral expansion techniques (Majda, 2003). The numerical method used here follows Biello and Majda (2006).

Since two cases of diurnal cycle heating have been prescribed in section 1.3, here we first consider the case with a simple heating profile utilizing the first two baroclinic modes in section 1.3.1. The corresponding eddy flux divergences of momentum and temperature F^u, F^θ shown in Fig. 1.2 are imposed into Eqs. (1.29a-1.29e). Fig. 1.6 shows all physical variables in the meridional and vertical directions, including pressure p , potential temperature θ as well as velocity components u, v, w .

During boreal summer, the dimensionless maximum magnitudes of all physical variables are larger than 0.1 and that of potential temperature θ even reaches 1, which is intuitively consistent with the significant eddy flux divergence of temperature F^θ shown in Figure 1.2. There are several crucial features of the resulting planetary/intraseasonal scale circulation. First, for the meridional and vertical flow field, a circulation cell forms around the equator, which is characterized by ascent in the northern hemisphere, southward motion in the upper troposphere, descent around the equator and northward motion in the lower troposphere. Secondly, the intraseasonal impact of the diurnal cycle on the planetary scale includes negative potential temperature anomalies in the lower troposphere. In a moist environment, negative potential temperature anomalies in the lower troposphere can increase the convective available potential energy(CAPE) and reduce the convective inhibition(CIN), which enhances the buoyancy of parcels in the free troposphere and provides a favorable condition

for tropical convection; also, the lower temperatures reduce the saturation value of water vapor and promote more convection. Thirdly, there are several zonal jets at different height and latitudes, providing more possible features of the planetary-scale circulation.

During equinox, the planetary/intraseasonal scale circulation response is very weak and much less than 1, which is consistent with the weak eddy flux divergences F^u, F^θ shown in Fig. 1.2. Therefore, we can conclude that there is weak planetary/intraseasonal scale direct circulation response due to the diurnal cycle during equinox.

Now, we consider the heating profile with the first two baroclinic modes sharing the same meridional profile, which is prescribed in section 1.3.2. Basically, during boreal summer, the pressure, p , the potential temperature, θ , and the zonal velocity, u , have similar spatial patterns and magnitudes as the case we discuss above. As for the meridional and vertical flow field, a circulation cell still forms around the equator. Besides, there are two weak circulation cells in the upper and lower troposphere around the equator and a strong downdraft at the higher latitude in the northern hemisphere, providing more possible features of the planetary-scale circulation. The results are shown in lower panels of Fig. 1.6.

1.4.3 A fully coupled version of the intraseasonal impact of the diurnal cycle on the Hadley cell

In section (1.4.2), we neglect the advection effects of the leading-order meridional and vertical flow field from the model for the Hadley cell (1.23a-1.23c) . Such a simplified version of the planetary/intraseasonal scale circulation response can shed some light on the intraseasonal impact of the diurnal cycle through Eqs. (1.29a-1.29e). As demonstrated in section 1.4.1 and Fig. 1.5, the system (1.23a-1.23c) on the planetary/intraseasonal scales is capable of mimicking a Hadley cell by creating two circulation cells with the symmetric spatial pattern during equinox and an asymmetric spatial pattern during boreal summer. Therefore, a fully coupled version of the multi-scale model involving the Hadley cell can be utilized to

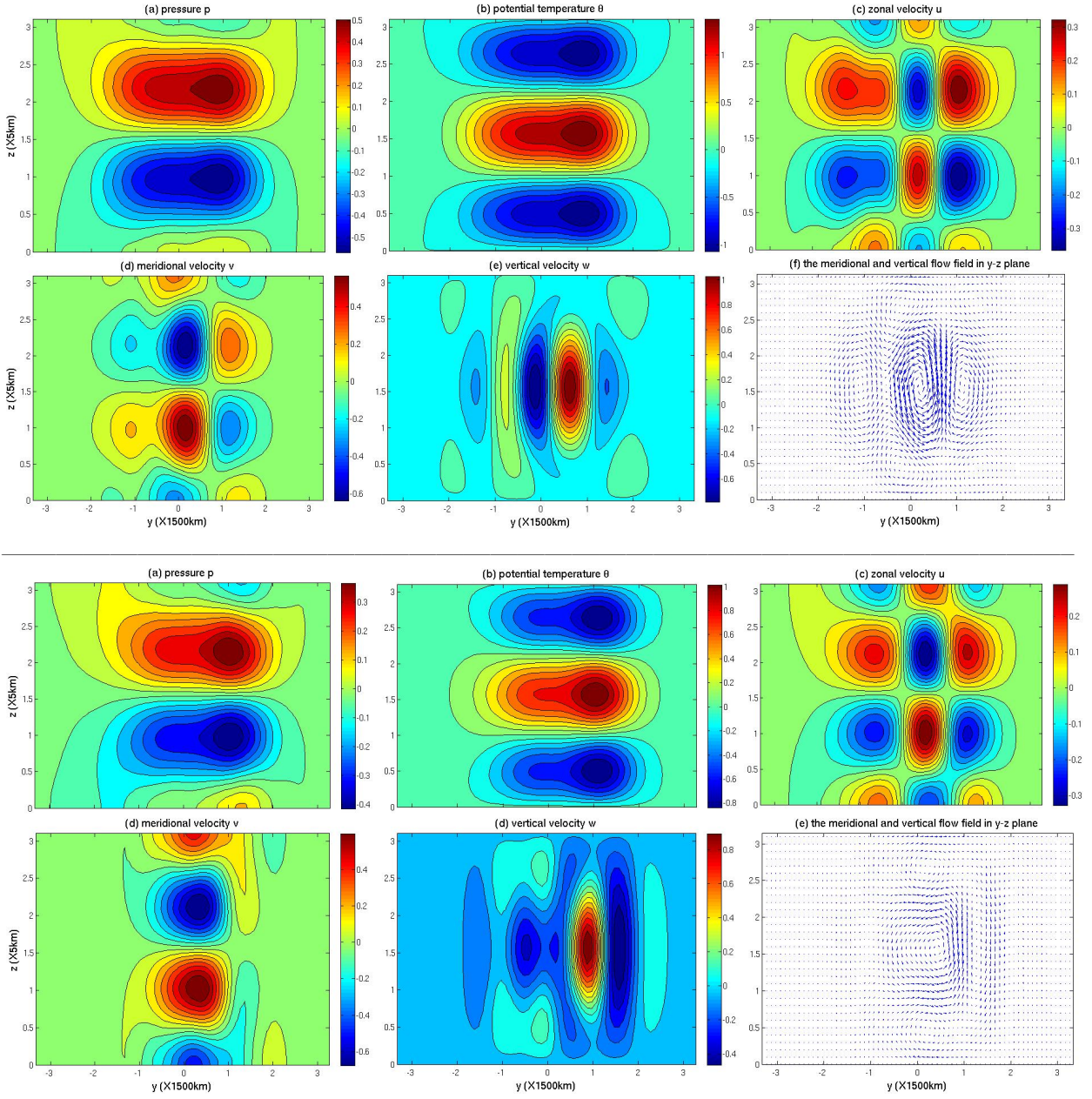


Figure 1.6: The upper figure shows the large-scale flows induced by upscale flux divergences F^u, F^θ during boreal summer corresponding to the heating in section 1.3.1. The lower figure shows the case corresponding to the heating in section 1.3.2. (a) pressure p ; (b) potential temperature θ ; (c) zonal velocity u ; (d) meridional velocity v ; (e) vertical velocity w ; (f) the meridional and vertical flow field in y - z plane. The units of p, θ, u, v, w are $250 m^2/s^2, 1.5 K, 5 m/s, 0.5 m/s, 5 m/s, 0.16 cm/s$ respectively.

model more realistic atmospheric dynamics in the tropics for the intraseasonal impact of the diurnal cycle. In this section, we add the mean flow from the model of the Hadley cell (1.23a-1.23c) and consider how such advection effect from the mean flow can affect the second-order planetary scale system on the intraseasonal time scale (1.15a-1.15e). Here we still consider an ideal zonally symmetric case. All synoptic-scale variables (u' , v' , p' , θ' , w') are set to zero. There is no extra momentum forcing $\langle \bar{S}_{u,2} \rangle$, $\langle \bar{S}_{v,1} \rangle$ and thermal forcing $\langle \bar{S}_{\theta,2} \rangle$ on the planetary/intraseasonal scales. Also, we assume that the buoyancy frequency N^2 and the density ρ are constants. To be brief, we rename all physical variables $u = \langle \bar{u} \rangle$, $p = \langle \bar{p} \rangle$, $\theta = \langle \bar{\theta} \rangle$, $v = \langle \bar{v}_2 \rangle$, $w = \langle \bar{w}_2 \rangle$ and the Hadley cell flow field $V = \langle \bar{v} \rangle$, $W = \langle \bar{w} \rangle$, and obtain a fully coupled version of the second-order planetary scale system on the intraseasonal time scale.

$$\frac{\partial}{\partial T} u + V \frac{\partial}{\partial y} u + W \frac{\partial}{\partial z} u - yv = -du + F^u \quad (1.32a)$$

$$yu = -p_y \quad (1.32b)$$

$$\frac{\partial}{\partial T} \theta + V \frac{\partial}{\partial y} \theta + W \frac{\partial}{\partial z} \theta + w = -d_\theta \theta + F^\theta \quad (1.32c)$$

$$p_z = \theta \quad (1.32d)$$

$$v_y + w_z = 0 \quad (1.32e)$$

We assume rigid lid boundary conditions at top and bottom of the troposphere,

$$w(X, T, y, z) |_{z=0,\pi} = 0 \quad (1.33)$$

where in dimensionless unit $z = 0$ represents the surface of the earth and $z = \pi$ represents the top of the troposphere. This system is advected by the meridional and vertical velocity components V, W from the model for the Hadley cell (1.23a-1.23c). F^u, F^θ (1.31) represent upscale feedback from the daily scale to the intraseasonal time scale in the zonal momentum equation and the thermal equation respectively.

Since the intraseasonal impact of the diurnal cycle of tropical convection during bo-

real summer is much stronger than that during equinox, hereafter we only show the planetary/intraseasonal scale circulation response to the eddy flux divergences F^u, F^θ during boreal summer. The eddy flux divergences of momentum and temperature F^u, F^θ can be evaluated explicitly through Eq. (1.31) (see Appendix 1.6.2). The only difference between the fully coupled version (Eqs. 1.32a-1.32e) and the simplified version (Eqs. 1.29a-1.29e) is that in this case there are advection effects from the model for the Hadley cell in Eqs. (1.32a-1.32e). The planetary/intraseasonal scale equations (1.32a-1.32e) can still be solved numerically by spectral expansion techniques (Majda, 2003) and the Galerkin method. The basic idea behind the numerical method is that since the Hadley cell is in the first baroclinic mode, all the vertical modes in the solutions are coupled with each other due to the advection effects. For each baroclinic mode, we use the Galerkin method and make sure all equations are held for a finite set of basis functions. Instead of solving the problem in each single baroclinic mode, we need to solve the problem by coupling all the vertical modes together, including the baroclinic modes and the barotropic mode. The details for the numerical method can be found at Appendix 1.6.3.

Since two kinds of diurnal cycle heating have been prescribed in section 1.3, we first consider the case with a simple heating profile in the first two baroclinic modes as described in section 1.3.1. The corresponding eddy flux divergences of momentum and temperature F^u, F^θ shown in Fig. 1.2 are imposed into Eqs. (1.32a-1.32e). The upper panels of Fig. 1.7 show all physical variables in the meridional and vertical directions, including pressure p , potential temperature θ , velocity components u, v, w as well as the meridional and vertical components of the velocity field from sec. 1.4.1 and the modified Hadley cell.

There are several new features arising when we couple the model for the Hadley cell with the planetary/intraseasonal scale circulation anomalies induced by the model of the diurnal cycle. First, the maximum magnitude of the pressure p and the potential temperature θ decreases, compared with the simple version shown in Fig. 1.6. Due to the advection effects of the Hadley cell, the spatial patterns of the pressure p and the potential temperature

θ become meridionally tilted. Secondly, the maximum magnitude of the zonal velocity u increases and the spatial pattern of the zonal jets also changes, compared with the simple case without advection effects in Fig. 1.6. In the present case, strong westerly winds form in the middle troposphere of the northern hemisphere and strong easterly winds form in the middle troposphere of the southern hemisphere. Thirdly, there exists a circulation cell at the upper troposphere around the equator. According to the panels (g), (h) of Fig. 1.7, we can find that such a circulation cell can strengthen the upper branch of the winter cell of the Hadley circulation, since this circulation cell moves in the same direction of the Hadley cell. Also, there exists another circulation cell in the lower troposphere around the equator. This circulation cell moves in the opposite direction of the Hadley cell, thus it can weaken the lower branch of the winter cell of the Hadley circulation. Finally, there are strong northward winds in the middle troposphere around the equator where the center of the winter cell of the Hadley circulation is located.

Now we consider the heating profile with the first two baroclinic modes sharing the same meridional profile as prescribed in section 1.3.2. The lower panels of Fig. 1.7 show all physical variables in the meridional and vertical directions, including pressure p , potential temperature θ , velocity components u, v, w as well as the original and modified Hadley cell. Compared with the simple case shown in Fig. 1.6, we can confirm the advection effects of the Hadley cell through the meridionally tilted spatial patterns of the pressure p and the potential temperature θ . The spatial patterns of the velocity components u, v, w share many similar features with the case we discuss above.

1.5 Concluding Discussion

In the present chapter, we have derived a multi-scale model by starting from the hydrostatic, anelastic Euler equations on an equatorial β -plane and following the derivation of systematic multi-scale models for tropical convection (Majda, 2007). Inspired by the observation of the

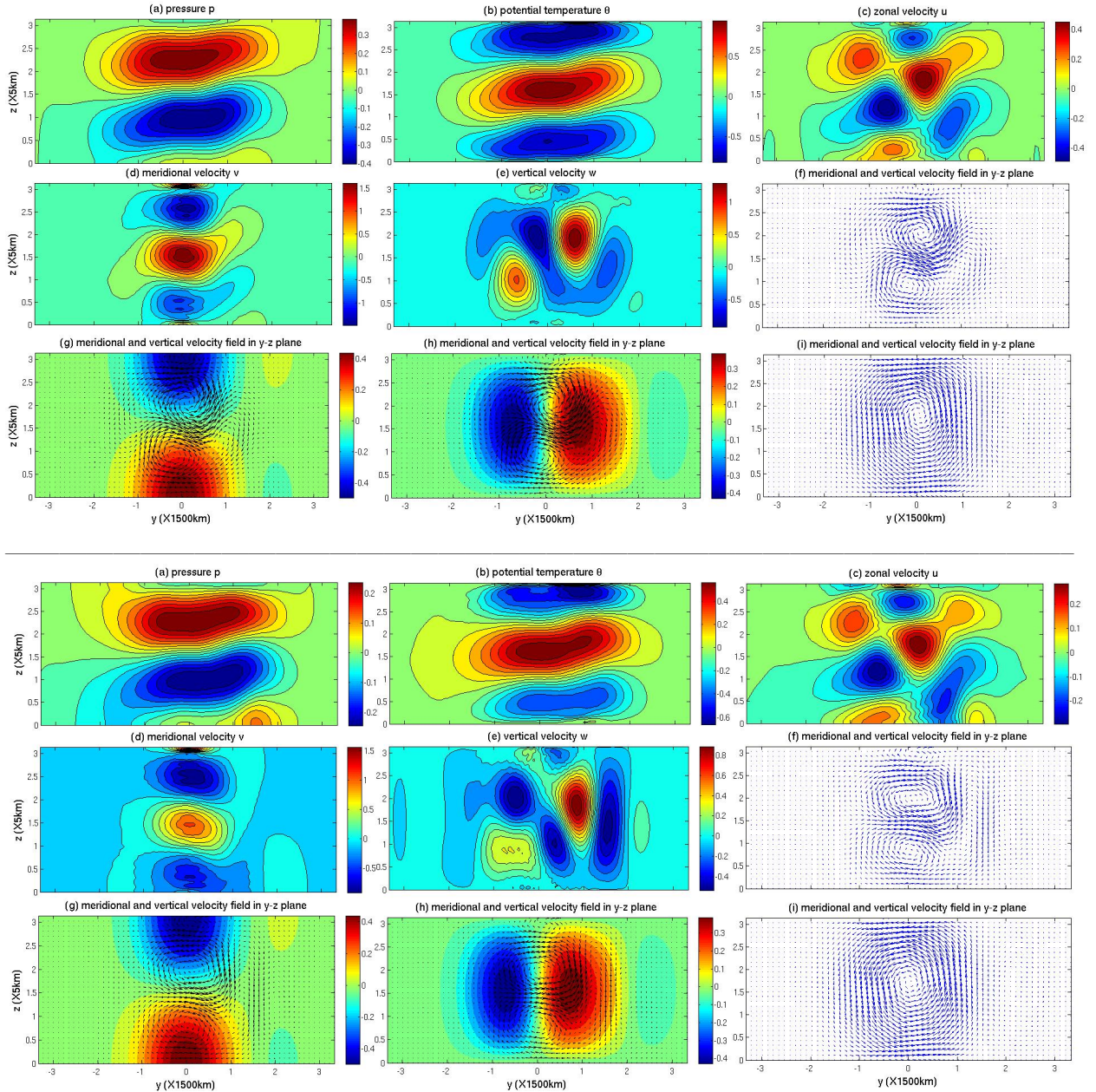


Figure 1.7: The upper figure shows the large-scale flows corresponding to the heating in section 1.3.1. The lower figure shows the case corresponding to the heating in section 1.3.2. (a) pressure p ; (b) potential temperature θ ; (c) zonal velocity u ; (d) meridional velocity v ; (e) vertical velocity w ; (f) the meridional and vertical flow field (v, w); (g) color means the meridional velocity of the original Hadley cell, vectors show the flow field in (f); (h) color means the vertical velocity of the original Hadley cell, vectors show the flow field in (f); (i) the modified Hadley cell, $(V + \epsilon v, W + \epsilon w)$. The units of p, θ, u, v, w are $250 \text{ m}^2/\text{s}^2, 1.5 \text{ K}, 5 \text{ m/s}, 0.5 \text{ m/s}, 5 \text{ m/s}$, and the units of V, W in the Hadley cell are $5 \text{ m/s}, 1.6 \text{ cm/s}$.

diurnal variability of tropical precipitation (Kikuchi and Wang, 2008), we try to assess the intraseasonal impact of planetary-scale inertial oscillations in the diurnal cycle. The appeal of this analytic multi-scale model is that it provides assessment of eddy flux divergences of momentum and temperature and their intraseasonal impact on the planetary-scale circulation in a transparent fashion. Thanks to the multi-scale asymptotics and several essential assumptions, this multi-scale model is capable of reproducing the Hadley cell and its advective effects on the planetary/intraseasonal scale circulation anomalies, allowing us to study large-scale flows in a more general framework. To assess the intraseasonal impact of the diurnal cycle of tropical precipitation on the planetary-scale flow such as the Hadley cell, four systems involving physical variables on different spatiotemporal scales have been separated from the primitive equations by using multi-scale asymptotics. In order to assess the upscale feedback from the daily time scale to the intraseasonal time scale, one system involving physical variables on the planetary scale and daily time scale has been utilized as the model for the diurnal cycle. Since the eddy flux divergences of momentum and temperature involve the planetary-scale flows on the daily time scale from the model for the diurnal cycle, the planetary/intraseasonal scale circulation forced by those eddy flux divergences can be interpreted as the intraseasonal impact of the diurnal cycle.

The model for the diurnal cycle is a linear system with all physical variables on the planetary scale and daily time scale, since the original equations are assumed to be weakly advected and all the resulting equations in the model for the diurnal cycle come from the leading-order asymptotic expansion of the primitive equations. To mimic the latent heat release associated with the diurnal cycle of tropical convection, the model utilizes three cloud types (congestus, deep convective, and stratiform) of organized tropical convection in the free troposphere (Frenkel et al., 2011a,c, 2013). For the eddy flux divergences of momentum and temperature, there are explicit formulas calculated by using spectral expansion techniques (Majda, 2003). The results show that the eddy flux divergence of temperature during boreal summer is much stronger than that during equinox, which suggests that the significant

intraseasonal impact of the diurnal cycle is traced to the meridional asymmetry of the diurnal cycle heating profile in the first two baroclinic modes. During boreal summer, the eddy flux divergence of temperature dominates in the northern hemisphere, providing a significant heating in the middle troposphere of the northern hemisphere with large-scale ascent and cooling surrounding this heating center with large-scale subsidence.

Having recognized the spatial patterns of eddy flux divergences of momentum and temperature during equinox and boreal summer, we can calculate the resulting planetary-scale circulation response on the intraseasonal time scale, which comes from the second-order asymptotic expansion of the primitive equations and indicates the upscale feedback of the diurnal cycle. In an ideal zonally symmetric case, the resulting steady state circulation on the planetary/intraseasonal scales during boreal summer is characterized by ascent in the northern hemisphere, southward motion in the upper troposphere, descent around the equator and northward motion in the lower troposphere. Also, the intraseasonal impact of the diurnal cycle on the planetary scale includes negative potential temperature anomalies in the lower troposphere, which suggests convective triggering in the tropics. The leading-order planetary/intraseasonal scale circulation is utilized as the model for the Hadley cell. Since the planetary/intraseasonal scale circulation system is advected by the Hadley cell, we are able to obtain a fully coupled version of the intraseasonal impact of the diurnal cycle on the Hadley cell. By studying such a fully coupled model, we conclude that the intraseasonal impact of the diurnal cycle can strengthen the upper branch of the winter cell of the Hadley circulation but weaken the lower branch of the winter cell of the Hadley circulation. Meanwhile, there exist strong northward winds in the middle troposphere around the equator, providing extensive features of the intraseasonal impact of the diurnal cycle on the Hadley cell.

The appeal of the multi-scale model developed in this chapter is that there exist explicit formulas for the eddy flux divergences of momentum and temperature for the upscale feedback across multiple spatiotemporal scales, which provides assessment of the intraseasonal

impact of the diurnal cycle in a transparent fashion. In fact, the IPESD model (Majda and Biello, 2004; Majda, 2007; Biello and Majda, 2005, 2006) considers the upscale feedback from the synoptic scale to the planetary scale and successfully generates a planetary-scale circulation resembling the tropical intraseasonal oscillation. In contrast, here we consider the upscale feedback from the daily time scale to the intraseasonal time scale and explore the intraseasonal impact of the diurnal cycle. When it is coupled with the model for the Hadley cell, the multi-scale model developed here provides a clear framework for the modulation and rectification of the Hadley circulation. The framework developed here for the intraseasonal impact of the diurnal cycle may provide insight into the explanation of some tropical phenomena. One promising application of the intraseasonal impact of the diurnal cycle is to better represent the intraseasonal variability in the tropics such as Madden-Julian oscillation (MJO). It may be interesting to include the nonlinear effects of moisture across multiple spatiotemporal scales, as for example in (Biello and Majda, 2010), allowing this multi-scale model to generate more realistic features of tropical phenomena.

This study has some implications for comprehensive numerical models. First, according to the results in sec. 4.2 and 4.3, it can be concluded that the diurnal cycle of tropical convection during boreal summer can induce significant intraseasonal impact on the planetary scale in the tropics. Thus one of the implications of this simple asymptotic model to the comprehensive models is that it emphasizes the significance of the representation of the diurnal variability of tropical precipitation. Specifically, the heating profile utilizing three cloud types (congestus, deep convective and stratiform) on the first two barolinic modes is a good candidate (Khouider and Majda, 2006a,b,c). Secondly, the eddy flux divergences of the momentum and temperature not only allow us to analytically assess the upscale effects from the daily time scale, but also provide the comprehensive numerical models with better intuition for the parameterization associated with the diurnal cycle and its intraseasonal impact. Thirdly, the planetary-scale response to the intraseasonal impact of the diurnal cycle in this model, including the lower level potential temperature anomalies, the multiple zonal

jets and the overturning circulation cells, may provide theoretical predictions and physical mechanisms to improve the simulation of the flow field over the Maritime Continent in the comprehensive numerical models.

1.6 Appendix

1.6.1 Details for the derivation of the multi-scale model

We start from the hydrostatic, anelastic Euler equations on an equatorial β -plane, Eqs. (1.2a-1.2e)

$$u_t + uu_x + vu_y + wu_z - yv = -p_x - \epsilon du + S_u \quad (1.34a)$$

$$v_t + uv_x + vv_y + wv_z + yu = -p_y - \epsilon dv + S_v \quad (1.34b)$$

$$\theta_t + u\theta_x + v\theta_y + w\theta_z + N^2 w = -\epsilon d_\theta \theta + S_\theta \quad (1.34c)$$

$$p_z = \theta \quad (1.34d)$$

$$(\rho u)_x + (\rho v)_y + (\rho w)_z = 0 \quad (1.34e)$$

where $\rho = \rho(z)$ and $N^2 = N^2(z)$ are in dimensionless units and depend only on height.

By assuming multi-scale solutions as the expression (Eq. 1.3) and using the chain rule, the zonal and time derivatives of an arbitrary function f^ϵ are given by

$$\frac{\partial f^\epsilon}{\partial x} + \epsilon \frac{\partial f^\epsilon}{\partial X}, \quad \frac{\partial f^\epsilon}{\partial t} + \epsilon \frac{\partial f^\epsilon}{\partial T} \quad (1.35)$$

Meanwhile, we use the ansatz(1.7)

$$g = \epsilon \left[g' (x, X, t, T, y, z) + \bar{g} (X, t, T, y, z) \right] + \epsilon^2 g_2, \quad g \in \{u, v, w, \theta, p, S_u, S_v, S_\theta\} \quad (1.36)$$

We plug the ansatz into Eqs. (1.34a-1.34e), and collect all terms at the leading order.

For $\mathcal{O}(\epsilon)$:

$$\frac{\partial}{\partial t} (\bar{u} + u') - y(\bar{v} + v') = -\frac{\partial}{\partial x} p' + S'_u + \bar{S}_u, \quad (1.37a)$$

$$\begin{aligned} \frac{\partial}{\partial t} (\bar{v} + v') + y(\bar{u} + u') &= -\frac{\partial}{\partial y} (\bar{p} + p') + S'_v + \bar{S}_v \frac{\partial}{\partial t} (\bar{\theta} + \theta') + N^2 (\bar{w} + w'), \\ &= S'_{\theta} + \bar{S}_{\theta} \frac{\partial}{\partial z} (\bar{p} + p') = \bar{\theta} + \theta' \frac{\partial}{\partial x} u' + \frac{\partial}{\partial y} (\bar{v} + v') + \frac{1}{\rho} \frac{\partial}{\partial z} (\rho (\bar{w} + w')), \\ &= 0. \end{aligned} \quad (1.37b)$$

By doing zonal averaging on Eqs. (1.37a-1.37b), we can get *the planetary-scale system*

$$\frac{\partial}{\partial t} \bar{u} - y \bar{v} = \bar{S}_u, \quad (1.38a)$$

$$\frac{\partial}{\partial t} \bar{v} + y \bar{u} = -\frac{\partial}{\partial y} \bar{p} + \bar{S}_v, \quad (1.38b)$$

$$\frac{\partial}{\partial t} \bar{\theta} + N^2 \bar{w} = \bar{S}_{\theta}, \quad (1.38c)$$

$$\frac{\partial}{\partial z} \bar{p} = \bar{\theta}, \quad (1.38d)$$

$$\frac{\partial}{\partial y} \bar{v} + \frac{1}{\rho} \frac{\partial}{\partial z} (\rho \bar{w}) = 0. \quad (1.38e)$$

By subtracting *the planetary-scale system* (1.38a-1.38e) from Eqs. (1.37a-1.37b), we derive *the synoptic-scale system*

$$\frac{\partial}{\partial t} u' - y v' = -\frac{\partial}{\partial x} p' + S'_u, \quad (1.39a)$$

$$\frac{\partial}{\partial t} v' + y u' = -\frac{\partial}{\partial y} p' + S'_v, \quad (1.39b)$$

$$\frac{\partial}{\partial t} \theta' + N^2 w' = S'_{\theta}, \quad (1.39c)$$

$$\frac{\partial}{\partial z} p' = \theta', \quad (1.39d)$$

$$\frac{\partial}{\partial x} u' + \frac{\partial}{\partial y} v' + \frac{1}{\rho} \frac{\partial}{\partial z} (\rho w') = 0. \quad (1.39e)$$

Since the daily time scale is the fast time scale compared with the intraseasonal time scale, we do time averaging on Eqs. (1.38a-1.38e) and all daily time scale derivatives vanish. In the end, we get *the leading-order planetary scale system on the intraseasonal time scale*

$$-y \langle \bar{v} \rangle = \langle \bar{S}_u \rangle, \quad (1.40a)$$

$$y \langle \bar{u} \rangle = -\frac{\partial}{\partial y} \langle \bar{p} \rangle + \langle \bar{S}_v \rangle, \quad (1.40b)$$

$$N^2 \langle \bar{w} \rangle = \langle \bar{S}_\theta \rangle, \quad (1.40c)$$

$$\frac{\partial}{\partial z} \langle \bar{p} \rangle = \langle \bar{\theta} \rangle, \quad (1.40d)$$

$$\frac{\partial}{\partial y} \langle \bar{v} \rangle + \frac{1}{\rho} \frac{\partial}{\partial z} (\rho \langle \bar{w} \rangle) = 0. \quad (1.40e)$$

By combining Eqs. (1.40a,1.40c,1.40e), we can get a constraint as follows

$$\frac{\partial}{\partial y} \left(\frac{\langle \bar{S}_u \rangle}{y} \right) = \frac{1}{\rho} \frac{\partial}{\partial z} \left(\rho \frac{\langle \bar{S}_\theta \rangle}{N^2} \right). \quad (1.41)$$

For $\mathcal{O}(\epsilon^2)$, we just look at the zonal momentum equation, the thermal equation and the mass conservation equation:

$$\begin{aligned} & \frac{\partial}{\partial T} (\bar{u} + u') + \frac{\partial}{\partial t} u_2 + (\bar{u} + u') \frac{\partial}{\partial x} (\bar{u} + u') + (\bar{v} + v') \frac{\partial}{\partial y} (\bar{u} + u') + (\bar{w} + w') \frac{\partial}{\partial z} (\bar{u} + u') \\ & - yv_2 = -\frac{\partial}{\partial x} p_2 - \frac{\partial}{\partial X} (\bar{p} + p') - d(\bar{u} + u') + S_{u,2} \end{aligned}, \quad (1.42)$$

$$\begin{aligned} & \frac{\partial}{\partial T} (\bar{\theta} + \theta') + \frac{\partial}{\partial t} \theta_2 + (\bar{u} + u') \frac{\partial}{\partial x} (\bar{\theta} + \theta') + (\bar{v} + v') \frac{\partial}{\partial y} (\bar{\theta} + \theta') + (\bar{w} + w') \frac{\partial}{\partial z} (\bar{\theta} + \theta') \\ & + N^2 w_2 = -d_\theta (\bar{\theta} + \theta') + S_{\theta,2} \end{aligned}, \quad (1.43)$$

$$\frac{\partial}{\partial x} u_2 + \frac{\partial}{\partial X} (\bar{u} + u') + \frac{\partial}{\partial y} v_2 + \frac{1}{\rho} \frac{\partial}{\partial z} (\rho w_2) = 0. \quad (1.44)$$

In order to guarantee the validation of multi-scale asymptotics, secular growth on spa-

tiotemporal scales can be avoided and we have $\overline{\frac{\partial}{\partial x} f} = 0, \langle \frac{\partial}{\partial t} f \rangle = 0$.

After doing zonal averaging on the equations above, we can get

$$\frac{\partial}{\partial T} \bar{u} + \frac{\partial}{\partial t} \bar{u}_2 + v' \overline{\frac{\partial}{\partial y} u'} + \bar{v} \overline{\frac{\partial}{\partial y} \bar{u}} + w' \overline{\frac{\partial}{\partial z} u'} + \bar{w} \overline{\frac{\partial}{\partial z} \bar{u}} - y \bar{v}_2 = -\frac{\partial}{\partial X} \bar{p} - d\bar{u} + \overline{S_{u,2}}, \quad (1.45)$$

$$\frac{\partial}{\partial T} \bar{\theta} + \frac{\partial}{\partial t} \bar{\theta}_2 + u' \overline{\frac{\partial}{\partial x} \theta'} + v' \overline{\frac{\partial}{\partial y} \theta'} + \bar{v} \overline{\frac{\partial}{\partial y} \bar{\theta}} + w' \overline{\frac{\partial}{\partial z} \theta'} + \bar{w} \overline{\frac{\partial}{\partial z} \bar{\theta}} + N^2 \bar{w}_2 = -d_\theta \bar{\theta} + \overline{S_{\theta,2}}, \quad (1.46)$$

$$\frac{\partial}{\partial X} \bar{u} + \frac{\partial}{\partial y} \bar{v}_2 + \frac{1}{\rho} \frac{\partial}{\partial z} (\rho \bar{w}_2) = 0. \quad (1.47)$$

By combining the incompressibility condition (1.39e) for $\mathcal{O}(\epsilon)$, we have (Majda, 2007)

$$\overline{u' \frac{\partial}{\partial x} (\rho u')} + \overline{u' \frac{\partial}{\partial y} (\rho v')} + \overline{u' \frac{\partial}{\partial z} (\rho w')} = 0, \quad (1.48)$$

$$\overline{\theta' \frac{\partial}{\partial x} (\rho u')} + \overline{\theta' \frac{\partial}{\partial y} (\rho v')} + \overline{\theta' \frac{\partial}{\partial z} (\rho w')} = 0. \quad (1.49)$$

Similarly, if we use the incompressibility condition (1.40e) for $\mathcal{O}(\epsilon)$, we have (Majda, 2007)

$$\bar{u} \frac{\partial}{\partial y} (\rho \bar{v}) + \bar{u} \frac{\partial}{\partial z} (\rho \bar{w}) = 0, \quad (1.50)$$

$$\bar{\theta} \frac{\partial}{\partial y} (\rho \bar{v}) + \bar{\theta} \frac{\partial}{\partial z} (\rho \bar{w}) = 0. \quad (1.51)$$

Now we can simplify Eqs. (1.45-1.47) by using Eqs. (1.48, 1.49, 1.50, 1.51).

$$\frac{\partial}{\partial T} \bar{u} + \frac{\partial}{\partial t} \bar{u}_2 - y \bar{v}_2 = -\frac{\partial}{\partial X} \bar{p} - d\bar{u} - \overline{\frac{\partial}{\partial y} (v' u')} - \frac{1}{\rho} \overline{\frac{\partial}{\partial z} (\rho w' u')} - \frac{\partial}{\partial y} (\bar{v} \bar{u}) - \frac{1}{\rho} \frac{\partial}{\partial z} (\rho \bar{w} \bar{u}) + \overline{S_{u,2}}, \quad (1.52)$$

$$\frac{\partial}{\partial T} \bar{\theta} + \frac{\partial}{\partial t} \bar{\theta}_2 + N^2 \bar{w}_2 = -d_\theta \bar{\theta} - \overline{\frac{\partial}{\partial y} (v' \theta')} - \frac{1}{\rho} \overline{\frac{\partial}{\partial z} (\rho w' \theta')} - \frac{\partial}{\partial y} (\bar{v} \bar{\theta}) - \frac{1}{\rho} \frac{\partial}{\partial z} (\rho \bar{w} \bar{\theta}) + \overline{S_{\theta,2}}, \quad (1.53)$$

$$\frac{\partial}{\partial X} \bar{u} + \frac{\partial}{\partial y} \bar{v}_2 + \frac{1}{\rho} \frac{\partial}{\partial z} (\rho \bar{w}_2) = 0. \quad (1.54)$$

Similarly, we do time average on the daily time scale t on Eqs. (1.40b, 1.40d, 1.52-1.54). All daily time scale derivatives vanish $\langle \frac{\partial}{\partial t} \bar{u}_2 \rangle = 0; \langle \frac{\partial}{\partial t} \bar{\theta}_2 \rangle = 0$. Also, if we separate each planetary-scale variable into an intraseasonal time scale component and a daily time scale component,

$$\bar{u} = \langle \bar{u} \rangle + \tilde{\bar{u}}; \bar{v} = \langle \bar{v} \rangle + \tilde{\bar{v}}; \bar{w} = \langle \bar{w} \rangle + \tilde{\bar{w}}; \bar{\theta} = \langle \bar{\theta} \rangle + \tilde{\bar{\theta}} \quad (1.55)$$

After time averaging, the eddy flux divergences of momentum and temperature on the planetary scale can be divided into two pieces, one piece can be interpreted as advection effects from the leading-order $\langle \bar{v} \rangle, \langle \bar{w} \rangle$, and the other piece can be understood as eddy flux divergences from the daily time scale to the intraseasonal time scale

$$\begin{aligned} -\frac{\partial}{\partial y} \langle \bar{v} \bar{u} \rangle - \frac{1}{\rho} \frac{\partial}{\partial z} \langle \rho \bar{w} \bar{u} \rangle &= -\frac{\partial}{\partial y} \langle (\langle \bar{v} \rangle + \tilde{\bar{v}}) (\langle \bar{u} \rangle + \tilde{\bar{u}}) \rangle - \frac{1}{\rho} \frac{\partial}{\partial z} \langle \rho (\langle \bar{w} \rangle + \tilde{\bar{w}}) (\langle \bar{u} \rangle + \tilde{\bar{u}}) \rangle, \\ &= -\frac{\partial}{\partial y} \langle \bar{v} \bar{u} \rangle - \frac{1}{\rho} \frac{\partial}{\partial z} \langle \rho \bar{w} \bar{u} \rangle - \frac{\partial}{\partial y} \langle \tilde{\bar{v}} \tilde{\bar{u}} \rangle - \frac{1}{\rho} \frac{\partial}{\partial z} \langle \rho \tilde{\bar{w}} \tilde{\bar{u}} \rangle. \end{aligned} \quad (1.56)$$

If we use Eq. (1.40e) and multiply it by $\langle \bar{u} \rangle$, we can get

$$\langle \bar{u} \rangle \frac{\partial}{\partial y} \langle \bar{v} \rangle + \frac{1}{\rho} \langle \bar{u} \rangle \frac{\partial}{\partial z} \langle \rho \bar{w} \rangle = 0. \quad (1.57)$$

Then we can find that the first two terms in the right hand of Eq. (1.56) can be rewritten as

$$\begin{aligned} -\frac{\partial}{\partial y} \langle \bar{v} \bar{u} \rangle - \frac{1}{\rho} \frac{\partial}{\partial z} \langle \rho \bar{w} \bar{u} \rangle &= -\langle \bar{u} \rangle \frac{\partial}{\partial y} \langle \bar{v} \rangle - \frac{1}{\rho} \langle \bar{u} \rangle \frac{\partial}{\partial z} \langle \rho \bar{w} \rangle - \langle \bar{v} \rangle \frac{\partial}{\partial y} \langle \bar{u} \rangle - \langle \bar{w} \rangle \frac{\partial}{\partial z} \langle \bar{u} \rangle, \\ &\quad -\langle \bar{v} \rangle \frac{\partial}{\partial y} \langle \bar{u} \rangle - \langle \bar{w} \rangle \frac{\partial}{\partial z} \langle \bar{u} \rangle. \end{aligned} \quad (1.58)$$

Similarly, we can rewrite eddy flux divergence of temperature

$$-\frac{\partial}{\partial y} (\bar{v}\bar{\theta}) - \frac{1}{\rho} \frac{\partial}{\partial z} (\rho\bar{w}\bar{\theta}) = -\langle \bar{v} \rangle \frac{\partial}{\partial y} \langle \bar{\theta} \rangle - \langle \bar{w} \rangle \frac{\partial}{\partial z} \langle \bar{\theta} \rangle - \frac{\partial}{\partial y} \langle \tilde{v}\tilde{\theta} \rangle - \frac{1}{\rho} \frac{\partial}{\partial z} \langle \rho\tilde{w}\tilde{\theta} \rangle. \quad (1.59)$$

Finally, we conclude with the planetary/intraseasonal scale system after time averaging on Eqs. (1.52-1.54) plus Eqs. (1.40b, 1.40d)

$$\begin{aligned} \frac{D}{DT} \langle \bar{u} \rangle - y \langle \bar{v}_2 \rangle &= -\langle \bar{p} \rangle_X - d \langle \bar{u} \rangle - \frac{\partial}{\partial y} \langle \bar{v}'u' \rangle - \frac{1}{\rho} \frac{\partial}{\partial z} \left(\rho \langle \bar{w}'u' \rangle \right) \\ &\quad - \frac{\partial}{\partial y} \langle \tilde{v}\tilde{u} \rangle - \frac{1}{\rho} \frac{\partial}{\partial z} (\rho \langle \tilde{w}\tilde{u} \rangle) + \langle \bar{S}_{u,2} \rangle, \end{aligned} \quad (1.60a)$$

$$y \langle \bar{u} \rangle = -\langle \bar{p} \rangle_y + \langle \bar{S}_v \rangle, \quad (1.60b)$$

$$\begin{aligned} \frac{D}{DT} \langle \bar{\theta} \rangle + N^2 \langle \bar{w}_2 \rangle &= -d_\theta \langle \bar{\theta} \rangle - \frac{\partial}{\partial y} \langle \bar{v}'\theta' \rangle - \frac{1}{\rho} \frac{\partial}{\partial z} \left(\rho \langle \bar{w}'\theta' \rangle \right) \\ &\quad - \frac{\partial}{\partial y} \langle \tilde{v}\tilde{\theta} \rangle - \frac{1}{\rho} \frac{\partial}{\partial z} (\rho \langle \tilde{w}\tilde{\theta} \rangle) + \langle \bar{S}_{\theta,2} \rangle, \end{aligned} \quad (1.60c)$$

$$\langle \bar{p} \rangle_z = \langle \bar{\theta} \rangle, \quad (1.60d)$$

$$\langle \bar{u} \rangle_X + \langle \bar{v}_2 \rangle_y + \frac{1}{\rho} (\rho \langle \bar{w}_2 \rangle)_z = 0. \quad (1.60e)$$

where $\frac{D}{DT} = \frac{\partial}{\partial T} + \langle \bar{v} \rangle \frac{\partial}{\partial y} + \langle \bar{w} \rangle \frac{\partial}{\partial z}$, thus this system is advected by the leading-order meridional and vertical velocities on the planetary/intraseasonal scales. Now, the derivation of the multi-scale model is complete.

1.6.2 Explicit formulas for the eddy flux divergences of momentum and temperature

The following formulas are the explicit solutions for Eqs. (1.16a-1.16e) corresponding to the simple heating profile (Eq. 1.19) in the first two baroclinic modes

$$\begin{pmatrix} p \\ u \\ v \\ \theta \\ w \end{pmatrix} = \begin{pmatrix} [\tilde{p}_{0|1}(y) + \gamma\tilde{p}_{1|1}(y)] \cos(kX + \omega t) \cos(z) \\ [\tilde{u}_{0|1}(y) + \gamma\tilde{u}_{1|1}(y)] \cos(kX + \omega t) \cos(z) \\ [\tilde{v}_{0|1}(y) + \gamma\tilde{v}_{1|1}(y)] \sin(kX + \omega t) \cos(z) \\ [\tilde{\theta}_{0|1}(y) + \gamma\tilde{\theta}_{1|1}(y)] \cos(kX + \omega t) \sin(z) \\ [\tilde{w}_{0|1}(y) + \gamma\tilde{w}_{1|1}(y)] \sin(kX + \omega t) \sin(z) \end{pmatrix} \quad (1.61)$$

$$+ \alpha \begin{pmatrix} [\tilde{p}_{0|2}(y) + \gamma\tilde{p}_{1|2}(y)] \cos(kX + \omega t + \beta) \cos(2z) \\ [\tilde{u}_{0|2}(y) + \gamma\tilde{u}_{1|2}(y)] \cos(kX + \omega t + \beta) \cos(2z) \\ [\tilde{v}_{0|2}(y) + \gamma\tilde{v}_{1|2}(y)] \sin(kX + \omega t + \beta) \cos(2z) \\ [\tilde{\theta}_{0|2}(y) + \gamma\tilde{\theta}_{1|2}(y)] \cos(kX + \omega t + \beta) \sin(2z) \\ [\tilde{w}_{0|2}(y) + \gamma\tilde{w}_{1|2}(y)] \sin(kX + \omega t + \beta) \sin(2z) \end{pmatrix}.$$

Since it can be proved that the homogeneous solutions of Eqs. (1.16a-1.16e) do not contribute to eddy flux divergences of momentum and temperature F^u, F^θ , here we only show the particular solutions corresponding to the prescribed heating (Eq. 1.19). For a simple heating profile with the leading two parabolic cylinder functions as its meridional profiles, $\tilde{p}_{0|q}, \tilde{u}_{0|q}, \tilde{v}_{0|q}, \tilde{\theta}_{0|q}, \tilde{w}_{0|q}, \tilde{p}_{1|q}, \tilde{u}_{1|q}, \tilde{v}_{1|q}, \tilde{\theta}_{1|q}, \tilde{w}_{1|q}$ in the expression (1.61) can be rewritten as fol-

lows

$$\begin{pmatrix} \tilde{p}_{0|q} \\ \tilde{u}_{0|q} \\ \tilde{v}_{0|q} \\ \tilde{\theta}_{0|q} \\ \tilde{w}_{0|q} \end{pmatrix} = \begin{pmatrix} \left(-\frac{\sqrt{2}}{6\omega} - \frac{\sqrt{2}\omega}{6(\frac{3N}{q}-\omega^2)} \right) \phi_{2|q} + \left(-\frac{5}{6\omega} + \frac{\omega}{6(\frac{3N}{q}-\omega^2)} \right) \phi_{0|q} \\ \left(-\frac{\sqrt{2}q}{6\omega N} - \frac{\sqrt{2}q\omega}{6N(\frac{3N}{q}-\omega^2)} \right) \phi_{2|q} + \left(-\frac{q}{6\omega N} - \frac{q\omega}{6N(\frac{3N}{q}-\omega^2)} \right) \phi_{0|q} \\ \sqrt{\frac{q}{2N}} \frac{1}{\frac{3N}{q}-\omega^2} \phi_{1|q} \\ \left(\frac{\sqrt{2}q}{6\omega} + \frac{\sqrt{2}q\omega}{6(\frac{3N}{q}-\omega^2)} \right) \phi_{2|q} + \left(\frac{5q}{6\omega} - \frac{q\omega}{6(\frac{3N}{q}-\omega^2)} \right) \phi_{0|q} \\ \left(\frac{q}{3\sqrt{2}N^2} + \frac{q\omega^2}{3\sqrt{2}N^2(\frac{3N}{q}-\omega^2)} \right) \phi_{2|q} + \left(-\frac{q}{6N^2} - \frac{q\omega^2}{6N^2(\frac{3N}{q}-\omega^2)} \right) \phi_{0|q} \end{pmatrix}, \quad (1.62)$$

$$\begin{pmatrix} \tilde{p}_{1|q} \\ \tilde{u}_{1|q} \\ \tilde{v}_{1|q} \\ \tilde{\theta}_{1|q} \\ \tilde{w}_{1|q} \end{pmatrix} = \begin{pmatrix} \left(-\frac{\sqrt{6}}{10\omega} - \frac{\sqrt{6}\omega}{10(\frac{5N}{q}-\omega^2)} \right) \phi_{3|q} + \left(-\frac{3}{10\omega} + \frac{\omega}{5(\frac{5N}{q}-\omega^2)} - \frac{\omega}{2(\omega^2-\frac{N}{q})} \right) \phi_{1|q} \\ \left(-\frac{\sqrt{6}q}{10\omega N} - \frac{\sqrt{6}q\omega}{10N(\frac{5N}{q}-\omega^2)} \right) \phi_{3|q} + \left(\frac{3q}{10\omega N} - \frac{q\omega}{5N(\frac{5N}{q}-\omega^2)} - \frac{q\omega}{2N(\omega^2-\frac{N}{q})} \right) \phi_{1|q} \\ \sqrt{\frac{q}{N}} \frac{1}{\frac{5N}{q}-\omega^2} \phi_{2|q} + \sqrt{\frac{q}{2N}} \frac{1}{\omega^2-\frac{N}{q}} \phi_{0|q} \\ \left(\frac{\sqrt{6}q}{10\omega} + \frac{\sqrt{6}q\omega}{10(\frac{5N}{q}-\omega^2)} \right) \phi_{3|q} + \left(\frac{3q}{10\omega} - \frac{q\omega}{5(\frac{5N}{q}-\omega^2)} + \frac{q\omega}{2(\omega^2-\frac{N}{q})} \right) \phi_{1|q} \\ \left(\frac{\sqrt{6}q}{10N^2} + \frac{\sqrt{6}q\omega^2}{10N^2(\frac{5N}{q}-\omega^2)} \right) \phi_{3|q} + \left(-\frac{7q}{10N^2} - \frac{q\omega^2}{5N^2(\frac{5N}{q}-\omega^2)} + \frac{q\omega^2}{2N^2(\omega^2-\frac{N}{q})} \right) \phi_{1|q} \end{pmatrix}. \quad (1.63)$$

For a more general heating profile \tilde{S}_θ with an arbitrary meridional profile, we need to decompose it into different parabolic cylinder functions $\phi_{m|q}$, $m = 1, 2; q = 1, 2$ and calculate the corresponding solutions.

Since the eddy flux divergences of momentum and temperature F^u, F^θ are product of two physical variables after time averaging on the daily time scale, we need to apply the following facts $\langle \sin^2(\omega t) \rangle = \langle \cos^2(\omega t) \rangle = \frac{1}{2}$. Finally, we can get analytic expressions for F^u, F^θ as follows

$$\begin{aligned}
F^u &= -\frac{\partial}{\partial y} \langle \tilde{v} \tilde{u} \rangle - \frac{1}{\rho} \frac{\partial}{\partial z} (\rho \langle \tilde{w} \tilde{u} \rangle) \\
&= \alpha \sin(\beta) \left\{ -\frac{\partial}{\partial y} \left[\frac{(\tilde{u}_{0|1} + \gamma \tilde{u}_{1|1}) (\tilde{v}_{0|2} + \gamma \tilde{v}_{1|2}) - (\tilde{u}_{0|2} + \gamma \tilde{u}_{1|2}) (\tilde{v}_{0|1} + \gamma \tilde{v}_{1|1})}{4} \right] \right. \\
&\quad \left. - \frac{1}{4} (\tilde{u}_{0|1} + \gamma \tilde{u}_{1|1}) (\tilde{w}_{0|2} + \gamma \tilde{w}_{1|2}) - \frac{1}{4} (\tilde{u}_{0|2} + \gamma \tilde{u}_{1|2}) (\tilde{w}_{0|1} + \gamma \tilde{w}_{1|1}) \right\} \cos(z) \quad (1.64) \\
&\quad + \alpha \sin(\beta) \left\{ -\frac{\partial}{\partial y} \left[\frac{(\tilde{u}_{0|1} + \gamma \tilde{u}_{1|1}) (\tilde{v}_{0|2} + \gamma \tilde{v}_{1|2}) - (\tilde{u}_{0|2} + \gamma \tilde{u}_{1|2}) (\tilde{v}_{0|1} + \gamma \tilde{v}_{1|1})}{4} \right] \right. \\
&\quad \left. - \frac{3}{4} (\tilde{u}_{0|1} + \gamma \tilde{u}_{1|1}) (\tilde{w}_{0|2} + \gamma \tilde{w}_{1|2}) + \frac{3}{4} (\tilde{u}_{0|2} + \gamma \tilde{u}_{1|2}) (\tilde{w}_{0|1} + \gamma \tilde{w}_{1|1}) \right\} \cos(3z)
\end{aligned}$$

$$\begin{aligned}
F^\theta &= -\frac{\partial}{\partial y} \langle \tilde{v} \tilde{\theta} \rangle - \frac{1}{\rho} \frac{\partial}{\partial z} (\rho \langle \tilde{w} \tilde{\theta} \rangle) \\
&= \alpha \sin(\beta) \left\{ \frac{\partial}{\partial y} \left[\frac{(\tilde{v}_{0|1} + \gamma \tilde{v}_{1|1}) (\tilde{\theta}_{0|2} + \gamma \tilde{\theta}_{1|2}) + (\tilde{v}_{0|2} + \gamma \tilde{v}_{1|2}) (\tilde{\theta}_{0|1} + \gamma \tilde{\theta}_{1|1})}{4} \right] \right. \\
&\quad \left. - \frac{1}{4} (\tilde{w}_{0|1} + \gamma \tilde{w}_{1|1}) (\tilde{\theta}_{0|2} + \gamma \tilde{\theta}_{1|2}) + \frac{1}{4} (\tilde{w}_{0|2} + \gamma \tilde{w}_{1|2}) (\tilde{\theta}_{0|1} + \gamma \tilde{\theta}_{1|1}) \right\} \sin(z) \quad (1.65) \\
&\quad + \alpha \sin(\beta) \left\{ \frac{\partial}{\partial y} \left[\frac{(\tilde{v}_{0|1} + \gamma \tilde{v}_{1|1}) (\tilde{\theta}_{0|2} + \gamma \tilde{\theta}_{1|2}) - (\tilde{v}_{0|2} + \gamma \tilde{v}_{1|2}) (\tilde{\theta}_{0|1} + \gamma \tilde{\theta}_{1|1})}{4} \right] \right. \\
&\quad \left. + \frac{3}{4} (\tilde{w}_{0|1} + \gamma \tilde{w}_{1|1}) (\tilde{\theta}_{0|2} + \gamma \tilde{\theta}_{1|2}) - \frac{3}{4} (\tilde{w}_{0|2} + \gamma \tilde{w}_{1|2}) (\tilde{\theta}_{0|1} + \gamma \tilde{\theta}_{1|1}) \right\} \sin(3z)
\end{aligned}$$

1.6.3 The numerical method to solve the fully coupled planetary/intraseasonal scale system

In section (1.4.3), we need to solve the planetary/intraseasonal scale system advected by the Hadley cell. To be brief, we rename all physical variables $u = \langle \bar{u} \rangle, p = \langle \bar{p} \rangle, \theta = \langle \bar{\theta} \rangle, v = \langle \bar{v}_2 \rangle, w = \langle \bar{w}_2 \rangle$ and the Hadley cell flow field $V = \langle \bar{v} \rangle, W = \langle \bar{w} \rangle$. The equations are as

follows

$$\frac{\partial}{\partial T}u + V \frac{\partial}{\partial y}u + W \frac{\partial}{\partial z}u - yv = -du + F^u \quad (1.66a)$$

$$yu = -p_y \quad (1.66b)$$

$$\frac{\partial}{\partial T}\theta + V \frac{\partial}{\partial y}\theta + W \frac{\partial}{\partial z}\theta + N^2w = -d_\theta\theta + F^\theta \quad (1.66c)$$

$$p_z = \theta \quad (1.66d)$$

$$v_y + \frac{1}{\rho} (\rho w)_z = 0 \quad (1.66e)$$

This system is advected by the meridional and vertical velocity $\langle \bar{v} \rangle, \langle \bar{w} \rangle$ in the model for the Hadley cell (1.23a-1.23c). We assume rigid lid boundary conditions at top and bottom of the troposphere,

$$w(X, T, y, z) |_{z=0,\pi} = 0 \quad (1.67)$$

where in dimensionless unit $z = 0$ represents the surface of the earth and $z = \pi$ represents the top of the troposphere.

Since we want to get the solutions in equilibrium, we can neglect the time derivatives and only solve time-independent equations. We utilize a very crucial property that both the meridional velocity and vertical velocity $\langle \bar{v} \rangle, \langle \bar{w} \rangle$ of the Hadley cell are in the first baroclinic mode, as prescribed in Eqs.1.25-1.26 and Eqs.1.27-1.28. Therefore, we can still use the ansatz that the solution can be represented by the sum of different baroclinic modes and the barotropic mode. The basic idea follows the numerical method used in (Biello and Majda, 2006). However, due to the advection terms in this system, different vertical modes are coupled to each other. After doing vertical decomposition to separate all physical variables into different vertical modes, we use the Galerkin method to guarantee that all the equations are satisfied for a finite set of parabolic cylinder functions.

First, we do vertical decomposition and use the following ansatz

$$\left\{ \begin{array}{ll} u = \sum_{q=0}^N U_q \cos(qz); & V = H(y) \cos(z) \\ p = \sum_{q=0}^N P_q \cos(qz); & W = K(y) [-\sin(z)] \\ v = \sum_{q=0}^N V_q \cos(qz); & d = 0.7; d_\theta = 0.23 \\ \theta = \sum_{q=1}^N \Theta_q [-q \sin(qz)]; & F^u = S_1^u(y) \cos(z) + S_3^u(y) \cos(3z) \\ w = \sum_{q=1}^N W_q [-q \sin(qz)]; & F^\theta = S_1^\theta(y) [-\sin(z)] + S_3^\theta(y) [-3 \sin(3z)] \end{array} \right. \quad (1.68)$$

here $H(y), K(y), S_1^u(y), S_3^u(y), S_1^\theta(y), S_3^\theta(y)$ are all known functions of y . Then we can derive equations for the coefficients of all vertical modes. Here we just list equations for the q^{th} baroclinic mode, we omit the equations for the barotropic mode, the first baroclinic mode and the last baroclinic mode for simplicity. If $q \geq 2$ and $q \leq N$, the q^{th} baroclinic mode

$$\frac{1}{2}H \frac{\partial}{\partial y} U_{q-1} + \frac{1}{2}H \frac{\partial}{\partial y} U_{q+1} - \frac{q-1}{2}KU_{q-1} + \frac{q+1}{2}KU_{q+1} - yV_q = -dU_q + S_q^u \quad (1.69)$$

$$yU_q = -\frac{\partial}{\partial y} P_q \quad (1.70)$$

$$\frac{q-1}{2}H \frac{\partial}{\partial y} \Theta_{q-1} + \frac{q+1}{2}H \frac{\partial}{\partial y} \Theta_{q+1} - \frac{(q-1)^2}{2}K\Theta_{q-1} + \frac{(q+1)^2}{2}K\Theta_{q+1} + qW_q = -d_\theta q\Theta_q + qS_q^\theta \quad (1.71)$$

$$P_q = \Theta_q \quad (1.72)$$

$$\frac{\partial}{\partial y} V_q - q^2 W_q = 0 \quad (1.73)$$

Now we do the meridional decomposition. Remembering that Eqs. (1.69-1.73) can be reduced to three equations for each baroclinic mode, we only need to do meridional decomposition for $U_q, P_q, V_q; q \geq 1$ as follows

$$\left\{ \begin{array}{l} U_q = \sum_{m=0}^{M-1} U_{m|q} \phi_{m|q}(y); \quad S_q^u = \sum_{m=0}^{M-1} S_{m|q}^u \phi_{m|q}(y) \\ P_q = \sum_{m=0}^{M-1} P_{m|q} \phi_{m|q}(y); \quad S_q^\theta = \sum_{m=0}^{M-1} S_{m|q}^\theta \phi_{m|q}(y) \\ V_q = \sum_{m=0}^{M-1} V_{m|q} \phi_{m|q}(y); \\ \Theta_q = P_q; \\ W_q = \frac{1}{q^2} \frac{\partial}{\partial y} V_q; \end{array} \right. \quad (1.74)$$

We can notice that different baroclinic modes are interacted with each other in Eqs. (1.69-1.73). In order to use the spectrum expansion techniques (Biello and Majda, 2006), we need to use the parabolic cylinder functions corresponding to the same baroclinic mode. Therefore, to a good approximation, we introduce the notation $\langle \cdot, \cdot \rangle$ to represent the integral from $-\infty$ to ∞ and do Galerkin projection

$$\langle f(y), g(y) \rangle = \int_{-\infty}^{\infty} f(y) g(y) dy. \quad (1.75)$$

What we do next is to solve the equations and guarantee that the coefficients before parabolic cylinder functions are zero in each equation. Ideally, with more meridional modes, the solutions are more accurate. Here we truncate the series of the parabolic cylinder functions and choose the number of the basic functions to be large ($M = 30$). Similarly, we just list equations for the q^{th} baroclinic mode, we omit the equations for the barotropic mode, the first baroclinic mode and the last baroclinic mode for simplicity.

If $q \geq 2$ and $q \leq N$, the q^{th} baroclinic mode

$$\begin{aligned}
& \sum_{s=0}^{M-1} P_{s|q-1} \left\langle \frac{q-1}{2} H \frac{\partial}{\partial y} \phi_{s|q-1}, \phi_{m|q} \right\rangle + \sum_{s=0}^{M-1} P_{s|q+1} \left\langle \frac{q+1}{2} H \frac{\partial}{\partial y} \phi_{s|q+1}, \phi_{m|q} \right\rangle + \\
& \sum_{s=0}^{M-1} P_{s|q-1} \left\langle -\frac{(q-1)^2}{2} K \phi_{s|q-1}, \phi_{m|q} \right\rangle + \sum_{s=0}^{M-1} P_{s|q+1} \left\langle \frac{(q+1)^2}{2} K \phi_{s|q+1}, \phi_{m|q} \right\rangle + \\
& \sum_{s=0}^{M-1} U_{s|q-1} \left\langle \frac{1}{2} H \frac{\partial}{\partial y} \phi_{s|q-1}, \phi_{m|q} \right\rangle + \sum_{s=0}^{M-1} U_{s|q+1} \left\langle \frac{1}{2} H \frac{\partial}{\partial y} \phi_{s|q+1}, \phi_{m|q} \right\rangle + \quad (1.76) \\
& \sum_{s=0}^{M-1} U_{s|q-1} \left\langle -\frac{q-1}{2} K \phi_{s|q-1}, \phi_{m|q} \right\rangle + \sum_{s=0}^{M-1} U_{s|q+1} \left\langle \frac{q+1}{2} K \phi_{s|q+1}, \phi_{m|q} \right\rangle + \\
& \frac{1}{q} V_{m-1|q} (-\sqrt{2qm}) + d_\theta q P_{m|q} + dU_{m|q} = \\
& q S_{m|q}^\theta + S_{m|q}^u,
\end{aligned}$$

$$\begin{aligned}
& \sum_{s=0}^{M-1} P_{s|q-1} \left\langle \frac{q-1}{2} H \frac{\partial}{\partial y} \phi_{s|q-1}, \phi_{m|q} \right\rangle + \sum_{s=0}^{M-1} P_{s|q+1} \left\langle \frac{q+1}{2} H \frac{\partial}{\partial y} \phi_{s|q+1}, \phi_{m|q} \right\rangle + \\
& \sum_{s=0}^{M-1} P_{s|q-1} \left\langle -\frac{(q-1)^2}{2} K \phi_{s|q-1}, \phi_{m|q} \right\rangle + \sum_{s=0}^{M-1} P_{s|q+1} \left\langle \frac{(q+1)^2}{2} K \phi_{s|q+1}, \phi_{m|q} \right\rangle + \\
& \sum_{s=0}^{M-1} U_{s|q-1} \left\langle -\frac{1}{2} H \frac{\partial}{\partial y} \phi_{s|q-1}, \phi_{m|q} \right\rangle + \sum_{s=0}^{M-1} U_{s|q+1} \left\langle -\frac{1}{2} H \frac{\partial}{\partial y} \phi_{s|q+1}, \phi_{m|q} \right\rangle + \quad (1.77) \\
& \sum_{s=0}^{M-1} U_{s|q-1} \left\langle \frac{q-1}{2} K \phi_{s|q-1}, \phi_{m|q} \right\rangle + \sum_{s=0}^{M-1} U_{s|q+1} \left\langle -\frac{q+1}{2} K \phi_{s|q+1}, \phi_{m|q} \right\rangle + \\
& \frac{1}{q} V_{m+1|q} (\sqrt{2q(m+1)}) + d_\theta q P_{m|q} - dU_{m|q} = \\
& q S_{m|q}^\theta - S_{m|q}^u,
\end{aligned}$$

$$(qP_{m+1|q} + U_{m+1|q}) \sqrt{2q(m+1)} - (qP_{m-1|q} - U_{m-1|q}) \sqrt{2qm} = 0.$$

Finally, we can get a linear equation with a matrix A involving all the coefficients $U_{m|q}, P_{m|q}, V_{m|q}$ for the physical variables, and a vector B involving all the coefficients

$S_{m|q}^\theta, S_{m|q}^u$ for the forcings. Then we just solve this linear equation

$$AX = B \quad (1.78)$$

By using the ansatz for meridional and vertical decomposition (1.68,1.74), we can recover all the physical variables to be functions of y and z by using the vector X for all coefficients.

Chapter 2

A Multi-Scale Model for the Intraseasonal Impact of the Diurnal Cycle over the Maritime Continent on the Madden-Julian Oscillation

2.1 Introduction

The Maritime Continent is a region in the tropical warm pool, consisting of islands, peninsulas and shallow seas. Due to strong insolation near the equator and low heat capacity of the land surface, tropical convection prevails over the Maritime Continent and releases a huge amount of latent heat to the atmosphere. Thus the Maritime Continent is considered as an important energy source region for the global circulation (Ramage, 1968; Neale and Slingo, 2003). Tropical convection over the Maritime Continent is organized on multiple time scales, ranging from cumulus clouds on the daily time scale to intraseasonal oscillations. In particular, on the daily time scale, the diurnal cycle of tropical convection over the Maritime Continent is very significant compared with that over the Indian Ocean and the

western Pacific Ocean (Hendon and Woodberry, 1993; Kikuchi and Wang, 2008). On the intraseasonal time scale, the Madden-Julian Oscillation (MJO), the dominant component of the intraseasonal variability in the tropics, typically propagates eastward slowly across the Maritime Continent and can stall or terminate there releasing large amounts of rainfall (Zhang, 2005).

The contemporary general circulation models (GCMs) still do a poor job of resolving tropical convection over the Maritime Continent. One of the significant errors is that the GCMs cannot correctly simulate the precipitation over the Maritime Continent. For instance, obvious discrepancies of the diurnal amplitude in precipitation over the islands of the Maritime Continent during boreal winter have been noticed in the present-day GCM (Yang and Slingo, 2001; Stratton and Stirling, 2012). Another one of the significant errors is that the GCMs typically poorly represent the eastward propagating MJO over the Maritime Continent (Sperber et al., 1997; Inness and Slingo, 2003). One possible reason is the inadequate treatment of the diurnal cycle and its impact on the intraseasonal variability of atmospheric flow. In fact, current numerical models have difficulty in reproducing the diurnal variability of tropical precipitation (Randall and Dazlich, 1991; Dai and Trenberth, 2004; Tian et al., 2004), although superparameterization has enhanced fidelity (Khairoutdinov et al., 2005; Benedict and Randall, 2011). In order to improve comprehensive numerical simulations with more realistic features, it is important to have a better understanding of the intraseasonal impact of the diurnal cycle and whether such upscale impact from the diurnal cycle can influence the MJO.

In fact, many observational studies focus on the scale interaction between the diurnal cycle of precipitation and the MJO over the Maritime Continent (Chen and Houze, 1997; Slingo et al., 2003; Rauniar and Walsh, 2011; Peatman et al., 2014). Among the previous studies, the modulation of the diurnal cycle of tropical convection by the MJO has been investigated by evaluating the difference in magnitude and phase of the diurnal cycle between the convectively active and suppressed phases of the MJO (Sui and Lau, 1992; Sui et al., 1997;

Tian et al., 2006). However, the upscale impact of the diurnal cycle of tropical convection on the MJO is not well understood. In the theoretical direction, the resonant nonlinear interactions between equatorial waves in the barotropic mode and the first baroclinic mode have been studied in the presence of a diurnally varying heat source, but the effect of the second baroclinic mode is not considered there (Raupp and Silva Dias, 2009, 2010). In contrast to that, the multicloud models based on the first and second baroclinic modes for the three type clouds (congestus, deep and stratiform) have been built (Khouider and Majda, 2006c,a,b, 2007, 2008b,a) and reproduce several realistic features of the diurnal cycle of tropical convection (Frenkel et al., 2011b,d, 2013).

The goal of this chapter is to provide a framework for modelling the passage of the MJO over the Maritime Continent where the diurnal cycle of tropical convection is significant and assess how the intraseasonal impact of the diurnal cycle of tropical convection will modify the kinematic and thermodynamic characteristics of the MJO. Indeed, a self-consistent multi-scale model with two time scales (the daily/intraseasonal time scales) has been built to assess the intraseasonal impact of the diurnal cycle of tropical convection (Yang and Majda, 2014). This multi-scale model provides two sets of equations governing planetary-scale tropical flow on the daily and intraseasonal time scales separately. It turns out that the planetary-scale circulation response on the intraseasonal time scale is forced by eddy flux divergences of zonal momentum and temperature from the daily time scale. These eddy flux divergence terms provide us with assessment of upscale transfer of kinetic and thermal energy across multiple time scales in a transparent fashion.

According to this multi-scale model (Yang and Majda, 2014), the planetary-scale tropical flow on the daily time scale is governed by a set of linear equations, which can be thermally forced by a heat source. Here we prescribe a diurnally varying heat source within a standing convective envelope to mimic the latent heat release over the Maritime Continent. In detail, we utilize the vertical structure in the first and second baroclinic modes for the heat source to characterize the diurnal cycle (Frenkel et al., 2011b,d, 2013) and the organized tropical

convection with three type clouds (congestus, deep and stratiform) life cycle, which was first introduced in the multicloud models (Khouider and Majda, 2006c,a,b, 2007, 2008b,a).

The planetary-scale tropical flow on the intraseasonal time scale is governed by another set of Gill-type equations in long wave approximation (Matsuno, 1966; Gill, 1980), which can be forced by the spatially upscale transfer from the synoptic scale to the planetary scale and the temporally upscale transfer from the daily time scale to the intraseasonal time scale as well as a mean heat source. In fact, the upscale transfer from the synoptic scale to the planetary scale from wave trains of thermally driven equatorial synoptic-scale circulations in a moving convective envelope and the direct mean heating have been studied previously in a multi-scale model for the MJO (Majda and Biello, 2004; Biello and Majda, 2005, 2006). In the similar model setup here, we consider three different scenarios of the MJO induced by synoptic-scale heating and planetary-scale heating, and all of them show some key features of the MJO such as the horizontal quadrupole structure and upward/westward tilted vertical structure. Then, by considering the upscale impact of the diurnal cycle from the daily time scale to the intraseasonal time scale, we are able to obtain the planetary-scale circulation response during the passage of the MJO over the Maritime Continent where the diurnal cycle of tropical convection is typically significant. The resulting flow field and temperature anomalies resemble some realistic features of the MJO behavior over the Maritime Continent including stalling or termination.

The rest of this chapter is organized as follows. The model for the diurnal cycle and its upscale fluxes over the Maritime Continent are summarized in section 2.2. The planetary-scale circulation response to the intraseasonal impact of the diurnal cycle is shown in section 2.3. Section 2.4 describes three different scenarios for the MJO induced by synoptic-scale heating and planetary-scale heating. In section 2.5, we discuss the intraseasonal impact of the diurnal cycle on the MJO over the Maritime Continent and compare the resulting flow fields and temperature anomalies with the observations. The chapter ends with concluding summary and discussion. The detailed description for notations, dimensional units,

parameters in the moving heat source for the MJO and the synoptic-scale equatorial weak temperature gradient equations (Majda and Biello, 2004; Biello and Majda, 2005, 2006) can be found in the appendix.

2.2 A model for the diurnal cycle and its upscale fluxes over the Maritime Continent

The diurnal variability of tropical convection has attracted attention of the scientific community in a long history. Early investigations of the diurnal variability of tropical precipitation can date back to the 1920s (Ray, 1928). Due to the development of satellite measurements and computers, more global datasets in higher resolutions such as the Tropical Rainfall Measuring Mission (TRMM) are available for the scientific community to study convection in the tropics. In fact, the TRMM dataset has already been utilized to study the diurnal variability of the global tropical precipitation over land and oceans (Nesbitt and Zipser, 2003; Kikuchi and Wang, 2008). By applying empirical orthogonal function (EOF) analysis to two complementary TRMM datasets (3B42 and 3G68) for 1998-2006, Kikuchi and Wang (2008) concluded the persistence of the diurnal cycle of tropical precipitation with strong amplitude in the continental regime and weak amplitude in the oceanic regime. According to the figure 2 in the paper (Kikuchi and Wang, 2008), the diurnal cycle of tropical convection over the Maritime Continent is more significant than that over the Indian Ocean and the western Pacific Ocean during boreal winter.

In the theoretical direction, the significant diurnal variability of tropical precipitation is examined in some simple models for tropical convection by considering three types cloud (congestus, deep and stratiform) to characterize organized tropical convection (Frenkel et al., 2011b,d, 2013). Since latent heat released in tropical convection can drive the tropical flow through thermodynamics (Hartmann et al., 1984; Larson and Hartmann, 2003a,b), the

diurnal cycle of tropical precipitation can induce the diurnal variability of the flow field. By following this underlying physical mechanism, the multi-scale model (Yang and Majda, 2014) provides a set of equations governing the tropical flow associated with the diurnal cycle. In this section, we use this set of equations for the diurnal cycle and discuss the corresponding upscale fluxes on the planetary/intraseasonal time scale. The equations in dimensionless units appropriate for the daily time scale read as follows,

$$\tilde{u}_t - y\tilde{v} = 0 \quad (2.1a)$$

$$\tilde{v}_t + y\tilde{u} = -\tilde{p}_y \quad (2.1b)$$

$$\tilde{\theta}_t + \tilde{w} = \tilde{S}_\theta \quad (2.1c)$$

$$\tilde{p}_z = \tilde{\theta} \quad (2.1d)$$

$$\tilde{v}_y + \tilde{w}_z = 0 \quad (2.1e)$$

where all physical variables such as velocity $\tilde{u}, \tilde{v}, \tilde{w}$ and potential temperature $\tilde{\theta}$ have zero mean on the daily time scale. More details about the notations and the dimensional units can be found at Appendix A and the papers (Majda, 2007; Yang and Majda, 2014). Here we assume rigid-lid boundary conditions at the surface and top of the troposphere, $\tilde{w}|_{z=0,\pi} = 0$ where $z = 0, \pi$ represent the surface and top of the troposphere separately.

The large-scale tropical flow can be modelled as atmospheric circulation response to diabatic heating (Gill, 1980). Here the thermal forcing \tilde{S}_θ on the right side of Eq.2.1c is used to represent latent heat release during tropical precipitation, thus a good cloud model can help to provide an appropriate heating profile. On the other hand, the multicloud model convective parameterizations (Khouider and Majda, 2006c,a,b, 2007, 2008b,a) based on three cloud types (congestus, deep and stratiform) have successfully reproduced some crucial features of organized convection and tropical precipitation. In the multicloud models, the three types of clouds are highlighted and they serve to provide the bulk of tropical precipitation and

the main source of latent heat in the troposphere. In detail, the cumulus congestus clouds heat the lower troposphere by latent heat release and cool the upper troposphere due to the detrainment and high reflectivity of the clouds top. Deep convective clouds, which are responsible for the majority of tropical precipitation, produce warming throughout the entire troposphere. The stratiform clouds can heat the upper troposphere through deposition and growth of precipitation particles and cool the bottom due to the evaporation of rainfall and melting of ice precipitation. Therefore, the heating and cooling effects associated with these three clouds types exhibit the first and second baroclinic modes of vertical structure and here we incorporate these two baroclinic modes into the heating profile in dimensionless units to mimic diurnal variability (Frenkel et al., 2011b,d, 2013) as follows,

$$\tilde{S}_\theta = F(X) H(y) [\sin(kX + \omega t) \sin(z) + \alpha \sin(kX + \omega t + \beta) \sin(2z)] \quad (2.2)$$

$$F(X) = A_0 \cos \left[\frac{\pi X}{2L} \right]^+; H(y) = H_0 e^{-a(y-y_0)^2}. \quad (2.3)$$

Here $F(X)$ is large-scale convective envelope function, which only depends on the planetary scale X in the zonal direction, while $H(y)$ is the meridional profile of the heat source. At each location with specific longitude and latitude, we utilize the first baroclinic mode for deep convective heating and the second baroclinic mode for congestus and stratiform heating. Both these two baroclinic modes are harmonically oscillating to mimic the diurnal cycle. The phase shift between these two modes β and the relative strength of the second baroclinic mode to the first baroclinic mode α are key parameters here. The exact expressions for the envelope function and parameter values can be found in Appendix B.

According to the main conclusion in (Yang and Majda, 2014), the diurnal cycle of tropical convection has significant intraseasonal impact through eddy flux divergence of potential temperature associated with Eqs.2.1a-2.1e only during the solstices (boreal summer/boreal winter). Meanwhile, the eastward propagating MJO typically occurs during boreal winter. Therefore, we mainly focus on the case during boreal winter by setting the heating center

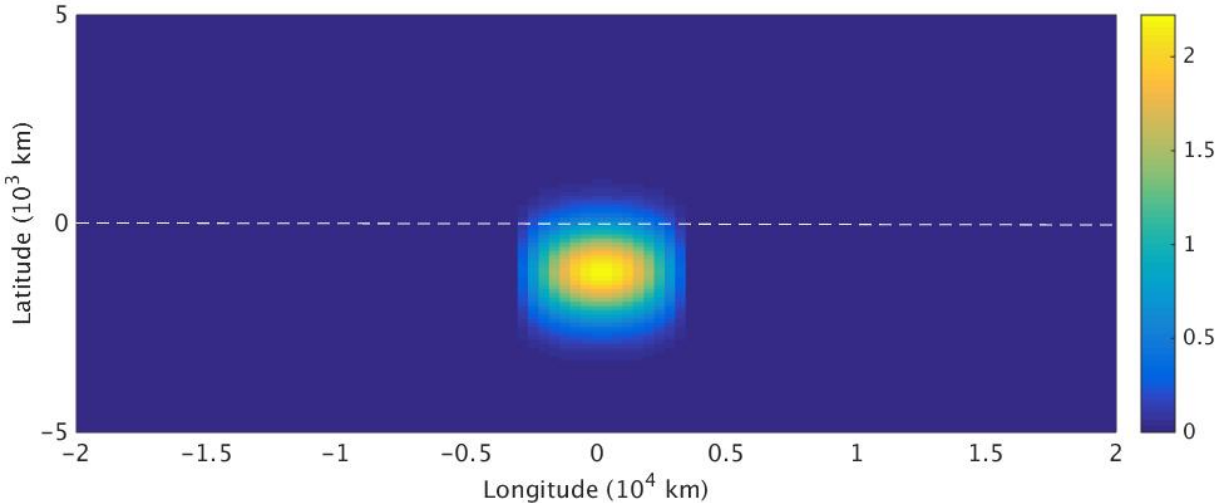


Figure 2.1: The envelope function of the diurnal heating in longitude-latitude diagram during boreal winter. The value here is dimensionless.

of the envelope function south of the equator. Fig.2.1 shows the envelope function of the diurnal heating in longitude-latitude diagram during boreal winter, that is, $F(X)H(y)$ in Eq.2.2. This envelope function reaches maximum value at 1200 km south of the equator with about 6600 km width in zonal direction, which resembles the observation such as the figure 2(c) in (Kikuchi and Wang, 2008). This envelope profile mimics the localized effect of the Maritime Continent in the model here.

Fig.2.2 shows the diurnal heating in time-height diagram for a given place with specific X, y , that is, $\sin(kX + \omega t)\sin(z) + \alpha\sin(kX + \omega t + \beta)\sin(2z)$. The alternating heating and cooling at a given height is due to the opposite thermal effects by congestus clouds and stratiform clouds as well as the intensification and diminishment of deep convective clouds. In particular, the upward movement of the heating center can be used to describe three clouds type (congestus, deep and stratiform) life cycle and mimic key features of the diurnal cycle (Frenkel et al., 2011b,d, 2013).

Based on several essential assumptions and systematic multi-scale asymptotics, the multi-scale model (Yang and Majda, 2014) shows that the resulting flow field forced by the diurnal

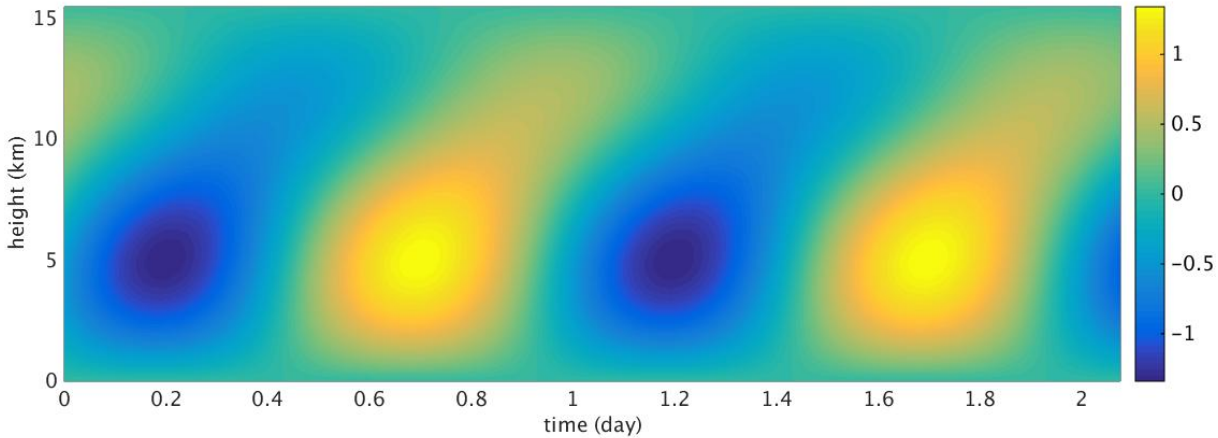


Figure 2.2: The diurnal heating in time-height diagram during boreal winter. The value is dimensionless.

heating model can generate eddy flux divergences of zonal momentum and temperature on the intraseasonal time scale,

$$F^u = -\frac{\partial}{\partial y} \langle \tilde{v}\tilde{u} \rangle - \frac{\partial}{\partial z} \langle \tilde{w}\tilde{u} \rangle; F^\theta = -\frac{\partial}{\partial y} \langle \tilde{v}\tilde{\theta} \rangle - \frac{\partial}{\partial z} \langle \tilde{w}\tilde{\theta} \rangle \quad (2.4)$$

which can further drive the planetary-scale circulation response on the intraseasonal time scale.

It has been shown in the appendix of (Yang and Majda, 2014) that the existence of the second baroclinic mode for congestus/stratiform heating α and its phase shift from the first baroclinic mode β are essential for the intraseasonal impact of the diurnal cycle, which highlights the importance of the congestus and stratiform cloud heating during tropical convection for the large-scale tropical circulation, besides deep convection. However, the exact eddy flux divergences of zonal momentum and temperature are less sensitive to these two parameters α, β in the sense that their magnitudes are determined by the product $\alpha \sin(\beta)$ while their spatial patterns are independent of α and β . Fig.2.3 shows the eddy flux divergences of momentum and temperature in the latitude-height diagram during boreal winter.

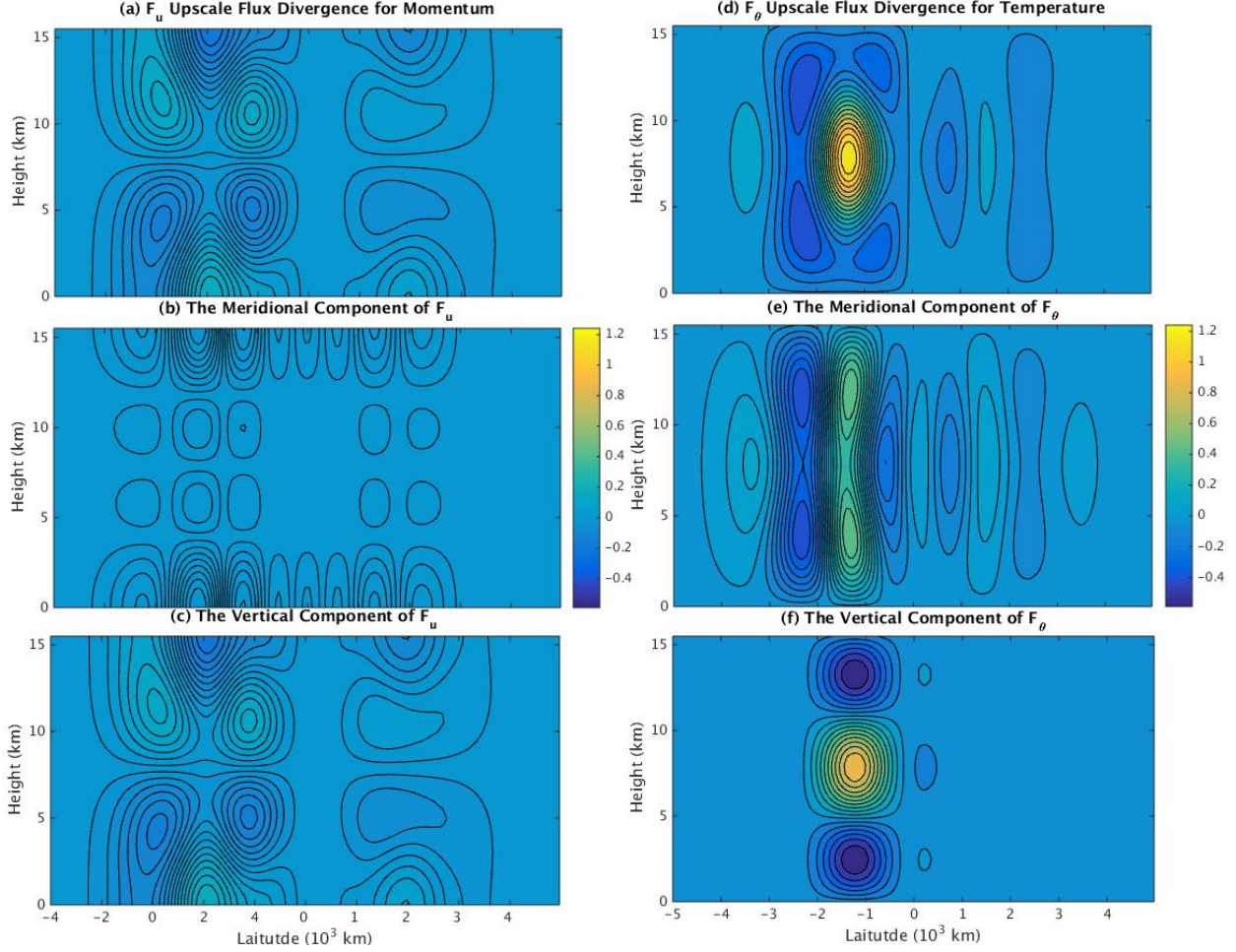


Figure 2.3: The eddy flux divergences of momentum and temperature F^u, F^θ in the latitude-height diagram during boreal winter. The left panels from top to bottom show (a) eddy flux divergence of momentum F^u , (b) its meridional component $-\frac{\partial}{\partial y} \langle \tilde{v}\tilde{u} \rangle$ and (c) its vertical component $-\frac{\partial}{\partial z} \langle \tilde{w}\tilde{u} \rangle$. The right panels from top to bottom show (d) eddy flux divergence of temperature F^θ , (e) its meridional component $-\frac{\partial}{\partial y} \langle \tilde{v}\tilde{\theta} \rangle$ and (f) its vertical component $-\frac{\partial}{\partial z} \langle \tilde{w}\tilde{\theta} \rangle$. One dimensionless unit of F^u is $1m/s/day$ and that of F^θ is $0.45K/day$.

According to Fig.2.3a and Fig.2.3d, the dimensionless eddy flux divergence of zonal momentum from the diurnal cycle is weak and the eddy flux divergence of temperature provides dominating intraseasonal impact on the planetary-scale circulation off the equator at the southern hemisphere. There is a significant heating center in the middle troposphere of the southern hemisphere and cooling surrounding this heating center shown in Fig.2.3d. In addition, the magnitude of the heating in the middle troposphere is about two times as large as that of the cooling in upper and lower troposphere, which indicates that the first and third baroclinic modes are both significant in the intraseasonal impact of the diurnal cycle. Fig.2.3b and Fig.2.3c show the meridional and vertical components of the eddy flux divergence of momentum F^u , and both of them have small magnitudes. Fig.2.3e shows the meridional component of the eddy flux divergence of temperature F^θ , which consists of alternate heating and cooling at different latitudes. Fig.2.3f shows the dominating vertical component of the eddy flux divergence of temperature F^θ with heating in the middle troposphere of the southern hemisphere and cooling in the upper and lower troposphere.

2.3 The planetary-scale circulation response to the intraseasonal impact of the diurnal cycle

The planetary-scale tropical flow can be modelled by the large-scale circulation response to a heat source such as latent heat release during tropical precipitation (Gill, 1980; Sobel et al., 2001). In these studies, the long wave approximation and weak temperature gradient approximation are discussed to further simplify the models. According to the multi-scale model (Majda, 2007; Yang and Majda, 2014), it turns out that the governing equations for the planetary-scale circulation response on the intraseasonal time scale are similar to the Gill-type model but also forced by upscale flux divergences of momentum and temperature from the daily time scale to the intraseasonal time scale. Due to the essential scaling assumptions for large-scale tropical flow, this set of equations is also in long wave approximation (Majda and Klein, 2003; Majda and Biello, 2004) and thus the eastward flow is in geostrophic balance with the pressure gradient. Furthermore, the zonal momentum damping and the radiative cooling have dissipation on the intraseasonal time scale (Mapes and Houze Jr, 1995; Lin et al., 2005; Romps, 2014) and thus they can play a role here. The equations in dimensionless units read as follows,

$$U_T - yV = -P_X - dU + F^u, \quad (2.5a)$$

$$yU = -P_y, \quad (2.5b)$$

$$\Theta_T + W = -d_\theta\Theta + F^\theta, \quad (2.5c)$$

$$P_z = \Theta, \quad (2.5d)$$

$$U_X + V_y + W_z = 0. \quad (2.5e)$$

Here all physical variables represent daily time scale mean and depend on the intraseasonal time scale T . The meridional circulation (V, W) is the secondary flow compared with that

on the daily time scale. More details about the notations and the dimensional units can be found at Appendix A and the paper (Yang and Majda, 2014). Here we assume rigid-lid boundary conditions at the surface and top of the troposphere, $W|_{z=0,\pi} = 0$ where $z = 0, \pi$ represent the surface and top of the troposphere, separately. On the right side of Eqs.2.5a and 2.5c, F^u, F^θ represent eddy flux divergences of zonal momentum and temperature from the daily time scale to the intraseasonal time scale respectively,

$$F^u = -\frac{\partial}{\partial y} \langle \tilde{v}\tilde{u} \rangle - \frac{\partial}{\partial z} \langle \tilde{w}\tilde{u} \rangle; F^\theta = -\frac{\partial}{\partial y} \langle \tilde{v}\tilde{\theta} \rangle - \frac{\partial}{\partial z} \langle \tilde{w}\tilde{\theta} \rangle. \quad (2.6)$$

Here all these daily fluctuation components $\tilde{u}, \tilde{v}, \tilde{w}, \tilde{\theta}$ are from the model for the diurnal cycle in Sec.2.2.

Since the forcing terms F^u, F^θ only involve the daily fluctuation components $(\tilde{u}, \tilde{v}, \tilde{w}, \tilde{\theta})$, the planetary-scale circulation is driven by the upscale feedback from the daily time scale to the intraseasonal time scale, as shown in the zonal momentum equation (Eq.2.5a) and the thermal equation (Eq.2.5c). After solving Eqs.2.1a-2.1e to obtain the daily fluctuation components $(\tilde{u}, \tilde{v}, \tilde{w}, \tilde{\theta})$, we can calculate the forcing terms F^u, F^θ based on the expression (Eq.2.6) and their spatial patterns are shown in Fig.2.3. The resulting planetary-scale circulation response governed by Eqs.2.5a-2.5e can be inferred with the forcing terms F^u, F^θ . Fig.2.4 shows the horizontal flow field and pressure perturbation due to the intraseasonal impact of the diurnal cycle at the upper troposphere ($z = 11km$) and lower troposphere ($z = 5km$). The main feature is that there is a cyclone (anticyclone) at the lower (upper) troposphere along with negative (positive) pressure perturbation in the southern hemisphere. The minimum (maximum) pressure perturbation in the lower (upper) troposphere is located south of the equator and slightly west of the diurnal heating center (the diurnal heating center is at $X = 0$ shown in Fig.2.1). Such longitude difference between the pressure perturbation and diurnal heating can be explained by the westward propagating Rossby waves off the equator.

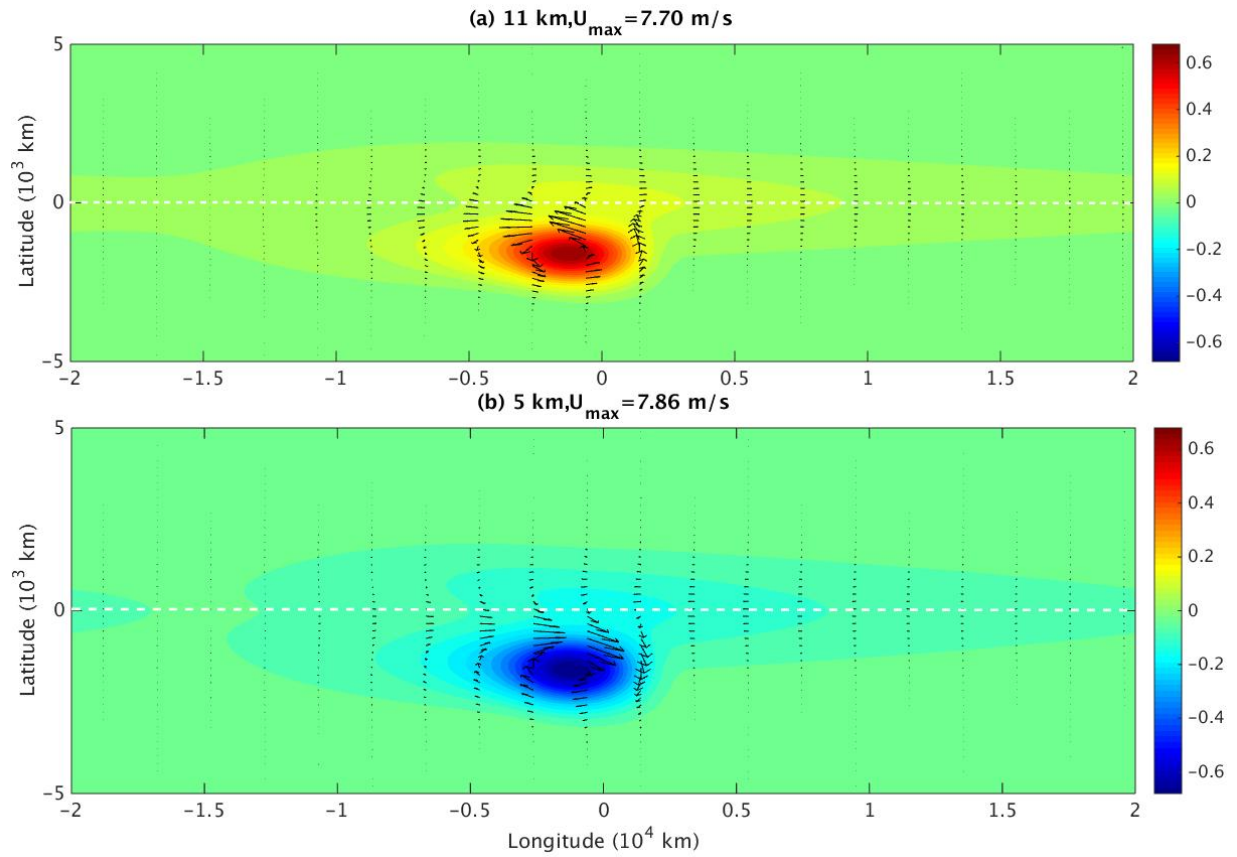


Figure 2.4: The horizontal flow field (shown by vectors) and pressure perturbation (shown by color) due to the intraseasonal impact of the diurnal cycle. The height in the top panel and bottom panels are 11 km and 5 km, respectively. The unit of pressure perturbation is $250 \text{ m}^2 \text{s}^{-2}$.

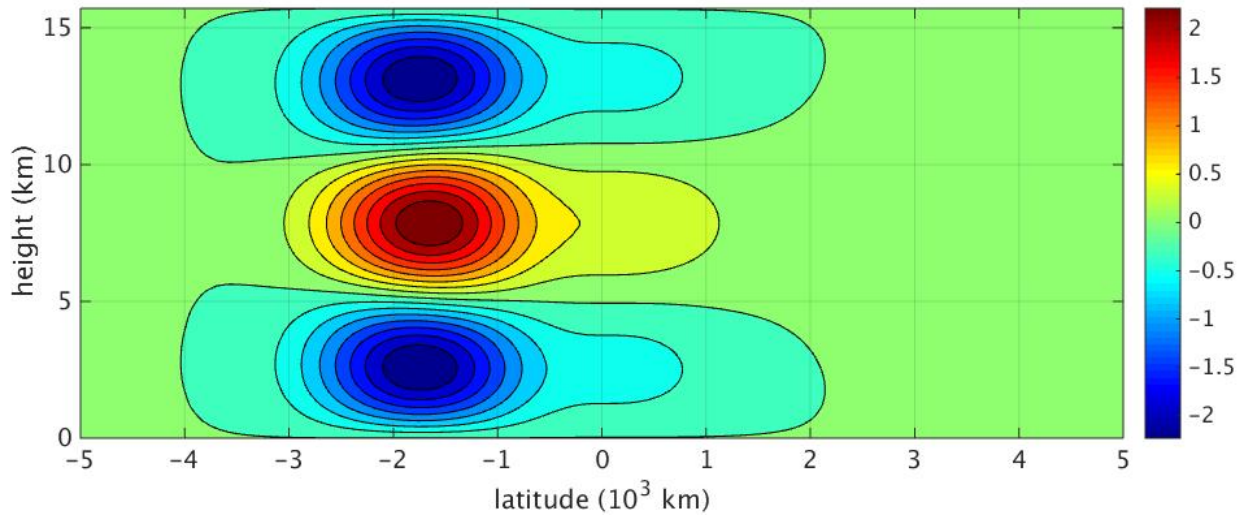


Figure 2.5: The temperature anomaly at the heating center $X = 0$ in the latitude-height diagram due to the intraseasonal impact of the diurnal cycle. The red color means warm and blue color means cold. The unit of temperature anomalies is K.

In addition, thermodynamic characteristics of the planetary-scale circulation response on the intraseasonal time scale are crucial properties since they are related with cloudiness and precipitation in tropical convection. Fig.2.5 shows the temperature anomalies at the latitude-height diagram due to the intraseasonal impact of the diurnal cycle during boreal winter. The main feature is that in the southern hemisphere, there is a positive temperature anomaly in the middle troposphere and negative temperature anomaly in the upper and lower troposphere. The comparable magnitudes of positive and negative temperature anomalies at different heights indicate that the third baroclinic mode is quite significant here. Also, such temperature anomalies even extend to the northern hemisphere but in much weaker magnitude. In a moist environment, negative potential temperature anomalies in the lower troposphere can increase the convective available potential energy(CAPE) and reduce the convective inhibition(CIN), which enhances the buoyancy of parcels in the free troposphere and provides a favorable condition for tropical convection. Meanwhile, the negative temperature anomaly reduces the saturation value of water vapor and promotes more convection in

the lower troposphere. In contrast to that, the positive temperature anomaly in the middle troposphere can suppresses deep convection in the opposite way.

2.4 The MJO models forced by a moving heat source

On the intraseasonal time scale (30 – 90 days), the eastward propagating MJO is the most significant large-scale phenomenon in the tropical atmosphere, which typically initializes over Equatorial Africa, intensifies over the Indian Ocean, gets weakened over the Maritime Continent, sometimes redevelops over the western Pacific and dissipates near the date line (Rui and Wang, 1990; Zhang, 2005). The MJO is organized on multiple spatial scales and consists of coupled patterns of wind field and tropical convection.

Although individual MJO events may vary in the magnitude of convection and the spatial patterns of atmospheric circulation in reality, the majority of MJO events share several key features in the kinematic and thermodynamic characteristics, which should become an important criterion for model validation. First of all, the velocity field exhibits horizontal quadrupole structure with flow convergence in the lower troposphere and divergence in the upper troposphere (Hendon and Salby, 1994). In the lower troposphere, the easterly winds near the equator are accompanied by anticyclones to the east of the convection center. The westerly winds near the equator are accompanied by cyclones to the west of the convection center. In the upper troposphere, the horizontal quadrupole structure has opposite signs for wind directions and pressure perturbation. Secondly, the westerly wind burst has a distinct upward/westward tilt, meaning that the onset region of the westerly winds at the lower troposphere is located to the west of that at the surface (Lin and Johnson, 1996; Yanai et al., 2000).

In the theoretical direction, several mechanisms have been proposed to improve our understanding of the MJO and a lot of numerical modelling has been done to capture the primary observed features of the MJO (Zhang, 2005). Having noticed that the planetary-scale circulation associated with the MJO also lives on the intraseasonal time scale, we can use the same equations (Eqs.2.5a-2.5e) from Sec.2.3 to model the MJO in an eastward propagating convective envelope. In fact, besides the upscale flux divergences of zonal momentum

and temperature from the daily time scale, these equations in the full multi-scale model (Yang and Majda, 2014) are also forced by the upscale flux divergences of zonal momentum and temperature from the synoptic scale (Majda and Biello, 2004; Biello and Majda, 2005). The latter has been interpreted as upscale transfer from synoptic to planetary scales of momentum and temperature and used to construct a multi-scale model for the MJO (Biello and Majda, 2005). Here we build three such MJO models in different scenarios forced by the planetary-scale mean heating and the synoptic-scale heating in a moving convective envelope, which exhibit several key features of the MJO as mentioned above.

2.4.1 The symmetric MJO with horizontal quadrupole structure induced by the planetary-scale heating

Although individual MJO events may behave differently from each other, the statistical composites of reanalysis data provide insight into the horizontal structure of the MJO envelope with key features (Hendon and Salby, 1994). One of the significant features of the MJO is its horizontal quadrupole structure with cyclone/anticyclone pairs at both the lower troposphere and upper troposphere.

In a long period with multiple MJO events, the overall convection field intensifies and diminishes with changing rainfall at each specific location, which corresponds to the alternating active and suppressed phases of the MJO. Here we prescribe the planetary-scale heating for latent heat release during tropical convection as follows

$$\langle S^\theta \rangle = F(X - st) H(y) [\sin(z) + \alpha \sin(2z)], \quad (2.7)$$

$$F(X) = A_0(a^2 - X^2)e^{-a_0 X^2}; H(y) = H_0 e^{-(y-y_0)^2}. \quad (2.8)$$

The envelope function $F(X - st)$ is used to mimic the eastward moving convective envelope in Eq.2.7 and below. The MJO phase speed is prescribed by $s = 5ms^{-1}$. Different from the

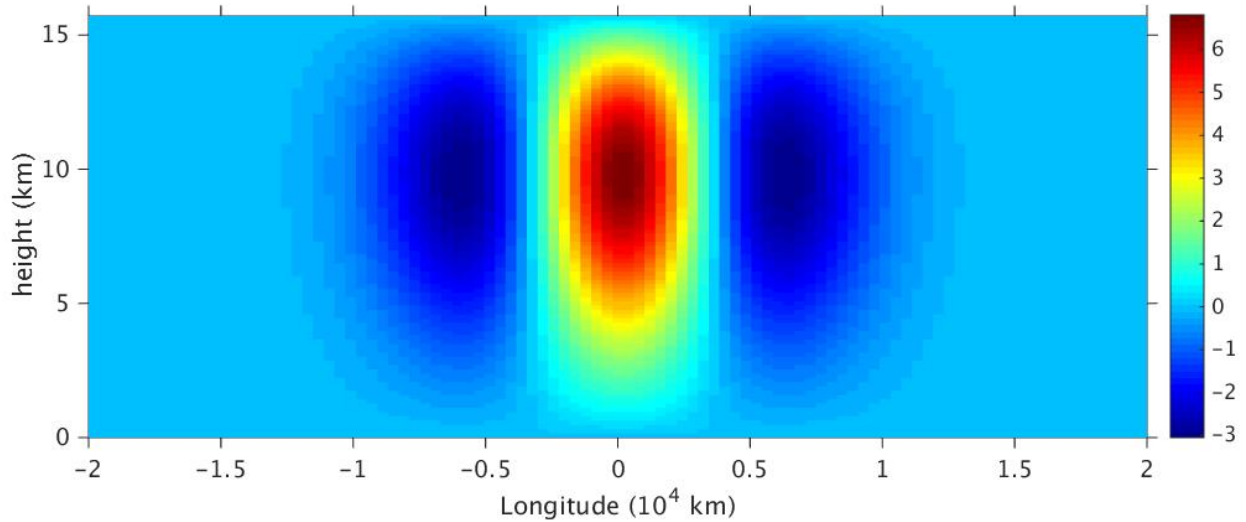


Figure 2.6: The mean heating for the Madden-Julian Oscillation. The red color means heating and blue color means cooling. One dimensionless unit of the heating is $4.5 K day^{-1}$

standard mean heating used by Biello and Majda (2005), the envelope function $F(X)$ used here is positive in the middle and negative on both sides, which resembles the active phase of the MJO in the middle and suppressed phases on the two sides. In fact, such an envelope function is crucial for the quadrupole structure of the resulting circulation response. The meridional profile $H(y)$ is a Gaussian shape function, symmetric about the equator. The relative strength of the second baroclinic mode $\alpha = -0.25$ is a parameter to adjust the heating center in height. The exact expressions for the heating profile and parameter values can be found in Appendix B.

As for the vertical structure of the heating in Eq.2.7, the first baroclinic mode represents deep convection with maximum latent heat release in the middle troposphere. The second baroclinic mode with negative strength coefficient α can be interpreted as stratiform precipitation with latent heat in the upper troposphere and cooling in the lower troposphere due to rain evaporation. The combination of these two baroclinic modes leads to the top-heavy heating profile as shown in Kiladis et al. (2005). Fig.2.6 shows the longitude-height diagram for the planetary-scale heating at the equator. There is top-heavy heating in the middle

of the convection envelope and cooling to the east and west of the convection region. The planetary-scale heating decays as the latitude increases.

After prescribing such planetary-scale heating as shown in Fig.2.6, we can obtain the planetary-scale circulation response on the intraseasonal time scale by letting this heating to thermally force the Eqs.2.5a-2.5e. Fig.2.7 shows the horizontal flow fields with pressure perturbation at the lower troposphere ($z = 5\text{km}$) and upper troposphere ($z = 11\text{km}$). The horizontal quadrupole structure is clear at both levels. In addition, the pressure perturbation is quite weak in the sense that its magnitude is much less than 1 in dimensionless units. Meanwhile, the zonal winds at the lower and upper troposphere are out of phase, which is consistent with the low-level flow convergence and upper-level flow divergence.

2.4.2 The symmetric MJO with westerly winds burst induced by synoptic-scale heating and planetary-scale heating

A multi-scale model for the MJO with two spatial scales (the synoptic scale and planetary scale) has been developed by (Majda and Biello, 2004; Biello and Majda, 2005, 2006). This model accounts for both the upscale transfer from the synoptic scale to the planetary scale of momentum and temperature from wave trains of thermally driven equatorial synoptic-scale circulations in a moving convective envelope as well as direct mean heating on the planetary scale. In addition, the model prescribes the heat source with dominant low-level congestus convection to the east of the moving convective envelope and dominant upper-level supercluster activity to the west.

Here we construct the two-scale MJO model driven by both the synoptic-scale heating and planetary-scale heating in a similar way. The planetary-scale mean heating is similar to that in Eq.2.7 but with $\alpha = 0$ and $A_0 = 44.8$ in Eq.2.7-2.8, which is used to mimic deep convection at the alternating active and suppressed phases of MJO on the planetary scale. On the synoptic scale, there are equatorial synoptic-scale heating in a eastward moving

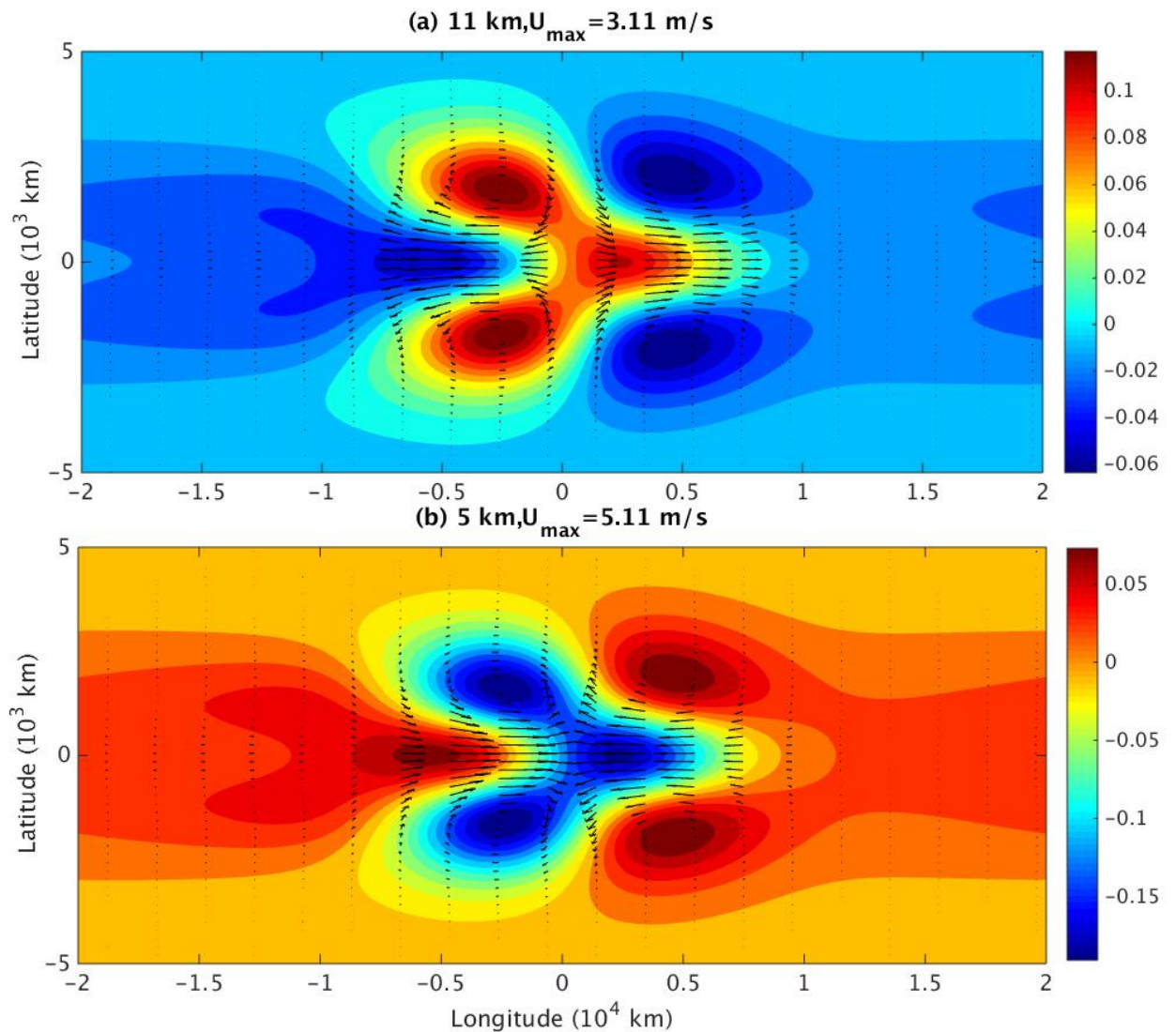


Figure 2.7: The horizontal flow field (shown by vectors) and pressure perturbation (shown by color) forced by the standard mean heating. The top panel shows the flow field at height $z=11$ km. The bottom panel is for height $z=5$ km. Here one dimensionless unit of pressure perturbation is $250 \text{ m}^2 \text{s}^{-2}$.

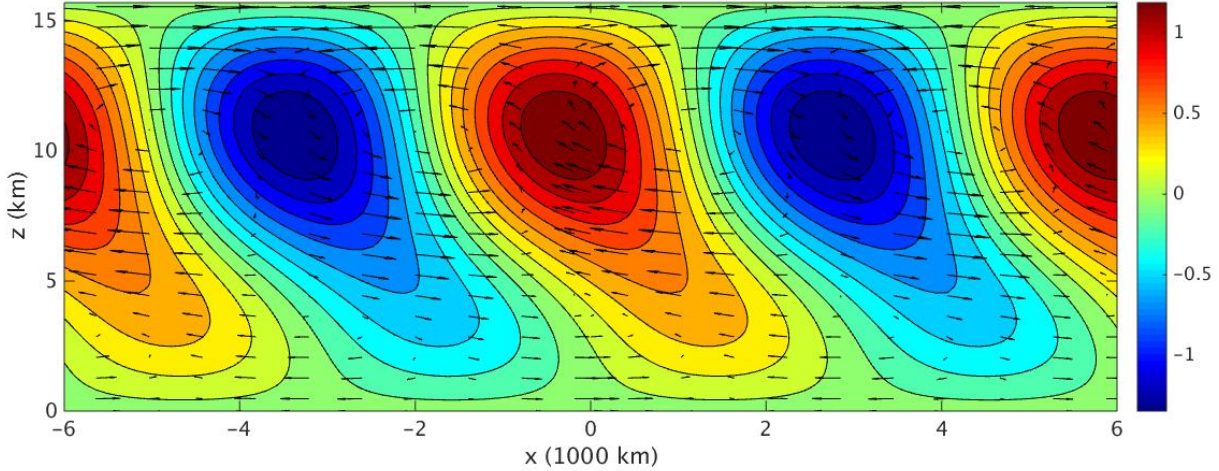


Figure 2.8: Contours of synoptic scale heating and vectors of zonal/vertical velocity. One dimensionless unit of heating, zonal velocity and vertical velocity correspond to $4.5Kday^{-1}$, $5ms^{-1}$, $1.6cms^{-1}$.

planetary-scale convective envelope. The synoptic-scale heating, in dimensionless units, reads as follows,

$$S'_\theta = F(X - sT) H(y) \left\{ \cos\left(\frac{x}{\lambda} - \phi(T)\right) \sin(z) - \alpha(X - sT) \cos\left(\frac{x + x_0}{\lambda} - \phi(T)\right) \sin(2z) \right\}, \quad (2.9)$$

$$F(X - sT) = A_0 \cos\left[\frac{\pi(X - sT)}{2L_F}\right]^+; H(y) = H_0 e^{-a_0(y - y_0)^2}; \alpha(X - sT) = -\frac{8(X - st)}{3L_F}. \quad (2.10)$$

Here $F(X - st)$ is the moving envelope function where $s = 0.1$ corresponds to $5ms^{-1}$. The magnitude of the convective envelope $A_0 = 1$ is chosen to yield realistic magnitudes of wind. The meridional profile $H(y)$ is a Gaussian shape function, symmetric about the equator. The first and second baroclinic modes are modulated by wave trains on the synoptic scale. All the parameter values and their interpretation can be found in Appendix B and Biello and Majda (2005).

In general, the synoptic-scale heating for the MJO can be on both the daily time scale and

the intraseasonal time scale. For simplicity, here we only consider the case where the MJO is driven by the heating across multiple spatial scales on the intraseasonal time scale and discuss how the diurnal cycle on the daily time scale can impact the behavior of the MJO. Through the assumption that the synoptic-scale heating only depends on the intraseasonal time scale T instead of the daily time scale t , the synoptic-scale fluctuation components of all physical variables satisfy the synoptic-scale equatorial weak temperature gradient (SEWTG) equations (shown in Appendix C), which has been discussed in (Majda and Biello, 2004; Biello and Majda, 2005, 2006). In the SEWTG equations, the momentum and thermal damping do not play a role because of their longer time scale. Fig.2.8 shows the contours of synoptic scale heating on the synoptic scale longitude-height diagram with the maximum heating and cooling in the upper troposphere, which resembles the diabatic heating observed in reality (Kiladis et al., 2005). The heating is upward/westward tilted with consistent rising and sinking motions, which is used to characterize organized convective superclusters in the convective envelope.

According to the full multi-scale model (Yang and Majda, 2014), the planetary-scale circulation response can also be forced by the spatially upscale transfer from the synoptic scale to the planetary scale, besides the temporally upscale transfer from the daily time scale to the intraseasonal time scale. This spatially upscale transfer from the synoptic scale of zonal momentum and temperature can be expressed as follows,

$$F^u = -\overline{(u'v')}_y - \overline{(u'w')}_z; F^\theta = -\overline{(\theta'v')}_y - \overline{(\theta'w')}_z. \quad (2.11)$$

Here u' , v' , w' , θ' are the fluctuation components with zero mean on the synoptic scale. The bar represents spatial averaging on the synoptic scale and its exact definition can be found at Appendix A.

Then we can consider the superimposition effect of the planetary-scale heating (Eq.2.7) and the upscale transfer from the synoptic scale of zonal momentum and temperature

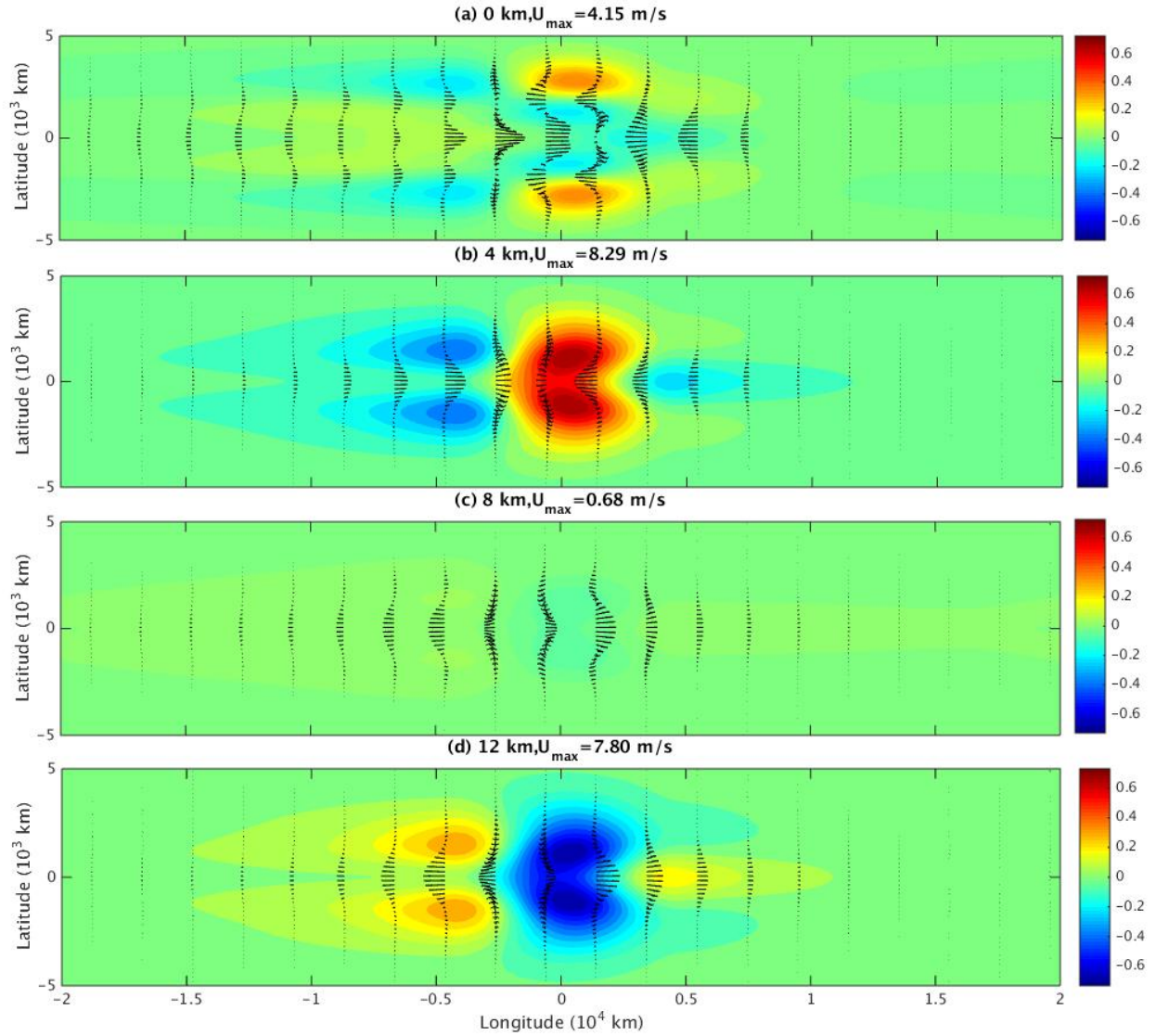


Figure 2.9: The planetary-scale response to the equatorially symmetric MJO forced by both synoptic-scale heating and mean heating. The color shows pressure perturbation, the flow field is shown by vectors. From top to bottom, these 4 panels show the heights at $z=0 \text{ km}$, $z=4 \text{ km}$, $z=8 \text{ km}$, $z=12 \text{ km}$. The pressure perturbation is dimensionless and one dimensionless unit corresponds to $250 \text{ m}^2 \text{s}^{-2}$.

(Eqs.2.11), and let the combined forcing drive the planetary-scale circulation response on the intraseasonal time scale (Eqs.2.5a-2.5e). Here for clear display, we reduce the magnitude of the planetary-scale heating to $\frac{4}{5}$ of its original value. Fig.2.9 shows the horizontal flow field with pressure perturbation from this MJO model. The horizontal quadruple structure can be found clearly at the surface, the lower and upper troposphere. In addition, the horizontal flow field indicates flow convergence at the lower troposphere with upward/westward tilted westerlies .

On the other hand, the potential temperature anomaly field is one of the crucial thermodynamic characteristics of the MJO. Fig.2.10 shows the horizontal flow field and temperature anomalies from the same MJO model above. One of the significant features is that there is very significant third baroclinic mode with a cold temperature anomaly at height 8 km (Fig.2.10.c) and warm temperature anomalies at height 4 km (Fig.2.10.b) and height 12 km (Fig.2.10.d) around the center of the convective envelope, which is intuitively consistent with the hydrostatic balance assumption. The magnitude of the cold temperature anomaly at the middle troposphere is larger than those of warm temperature anomalies at both the upper and lower troposphere, which also indicates the significance of the first baroclinic mode for the deep convection.

2.4.3 The asymmetric MJO with upward/westward tilt induced by synoptic-scale heating and planetary-scale heating

Some MJO observations indicate that seasonal variations in convective activity can also affect the planetary-scale atmospheric flow (Lin and Johnson, 1996). On the other hand, the zonal winds and temperature anomalies associated with the MJO exhibit upward/westward tilted vertical structure according to the observations (Lin and Johnson, 1996; Kiladis et al., 2005). Therefore, it is interesting to construct a model for the MJO in tilted vertical structure of easterlies and temperature anomalies, which also propagates eastward off the equator,

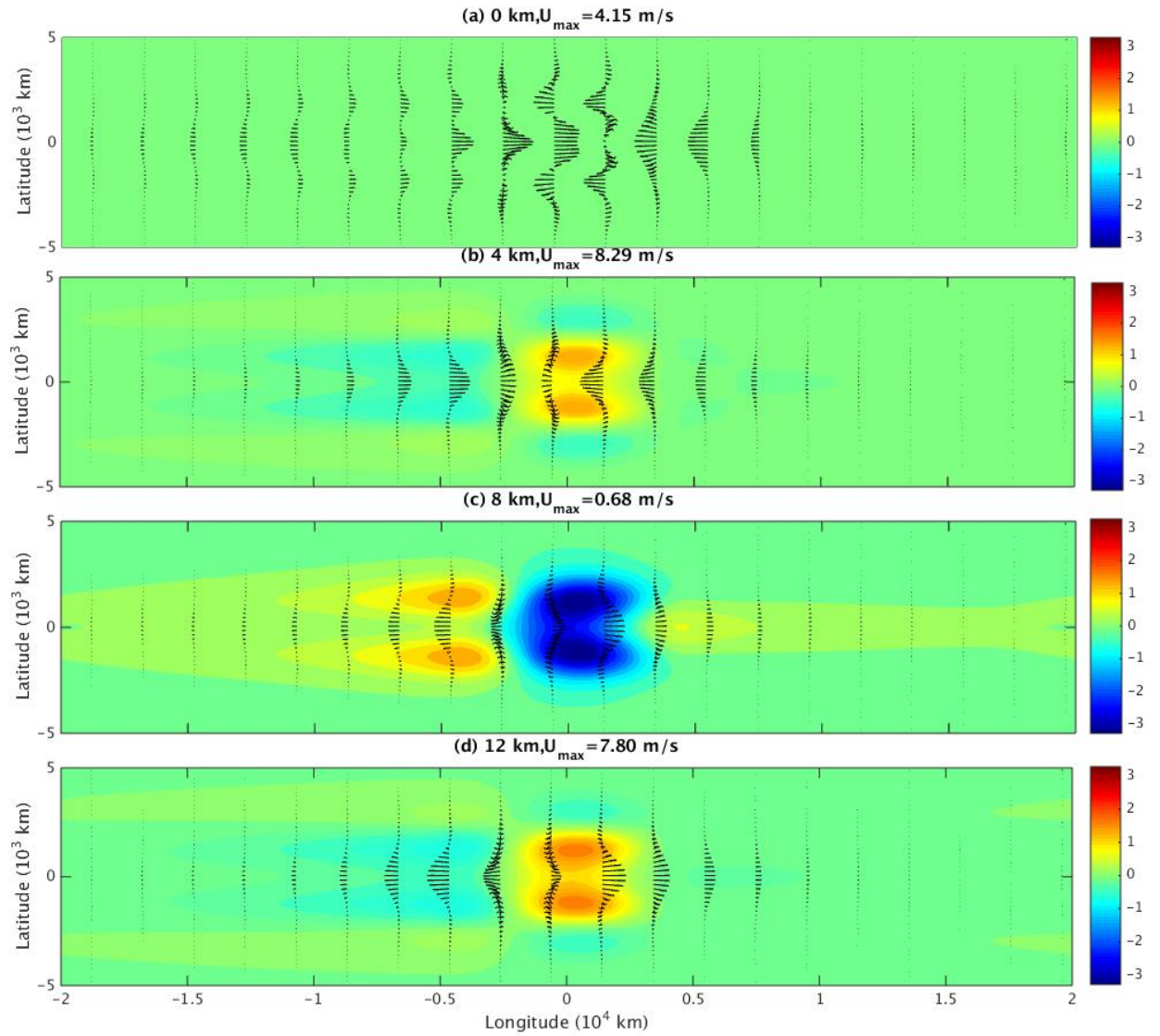


Figure 2.10: The planetary-scale response to the equatorially symmetric MJO forced by both synoptic-scale heating and mean heating. The color shows temperature anomalies, the flow field is shown by vectors. From top to bottom, these 4 panels show the heights at $z=0 \text{ km}$, $z=4 \text{ km}$, $z=8 \text{ km}$, $z=12 \text{ km}$. The unit of temperature anomalies is K.

following (Biello and Majda, 2005).

Here we consider a meridionally asymmetric MJO model forced by both the synoptic-scale heating and planetary-scale heating in a moving convective envelope off the equator. Meanwhile, both the heating on the synoptic and planetary scales are upward/westward tilted, which reflects the similarity of tropical convection across multiple scales. The synoptic-scale heating can be expressed by Eq.2.9 except that the maximum heating is located at 900 km south of the equator. In contrast to the planetary-scale heating with constant relative strength of the second baroclinic mode (Eq.2.7), here we vary the relative strength of the second baroclinic mode α so that the heating center is located at the lower troposphere to the east and the upper troposphere to the west. Such planetary-scale heating can be used to characterize the low-level congestus heating to the east of the convection envelope and upper troposphere supercluster heating to the west. The planetary-scale heating, in dimensionless units, reads as follows

$$\overline{S^\theta} = F(X - st)H(y) \left[\sin(z) + \frac{3(X - sT)}{2L_F} \sin(2z) \right], \quad (2.12)$$

$$F(X - sT) = A_0 \cos \left[\frac{\pi(X - sT)}{2L_F} \right]^+; H(y) = H_0 e^{-(y-y_0)^2}, \quad (2.13)$$

where the envelope function $F(X - st)$ is used to mimic the eastward moving convective envelope. Compared with the planetary-scale heating in Eq.2.7 with constant relative strength of the second baroclinic mode, the heating in Eq.2.12 has a relative strength coefficient in a linear function so that the vertical profiles of the heating are different within the convective envelope. The meridional profile $H(y)$ is a Gaussian shape function which is asymmetric about the equator. The exact expression for the heating profile and parameter values can be found in Appendix B.

Similarly, we can consider the superimposition effect of the planetary-scale heating (Eq.2.12) and the upscale transfer from the synoptic scale of zonal momentum and tempera-

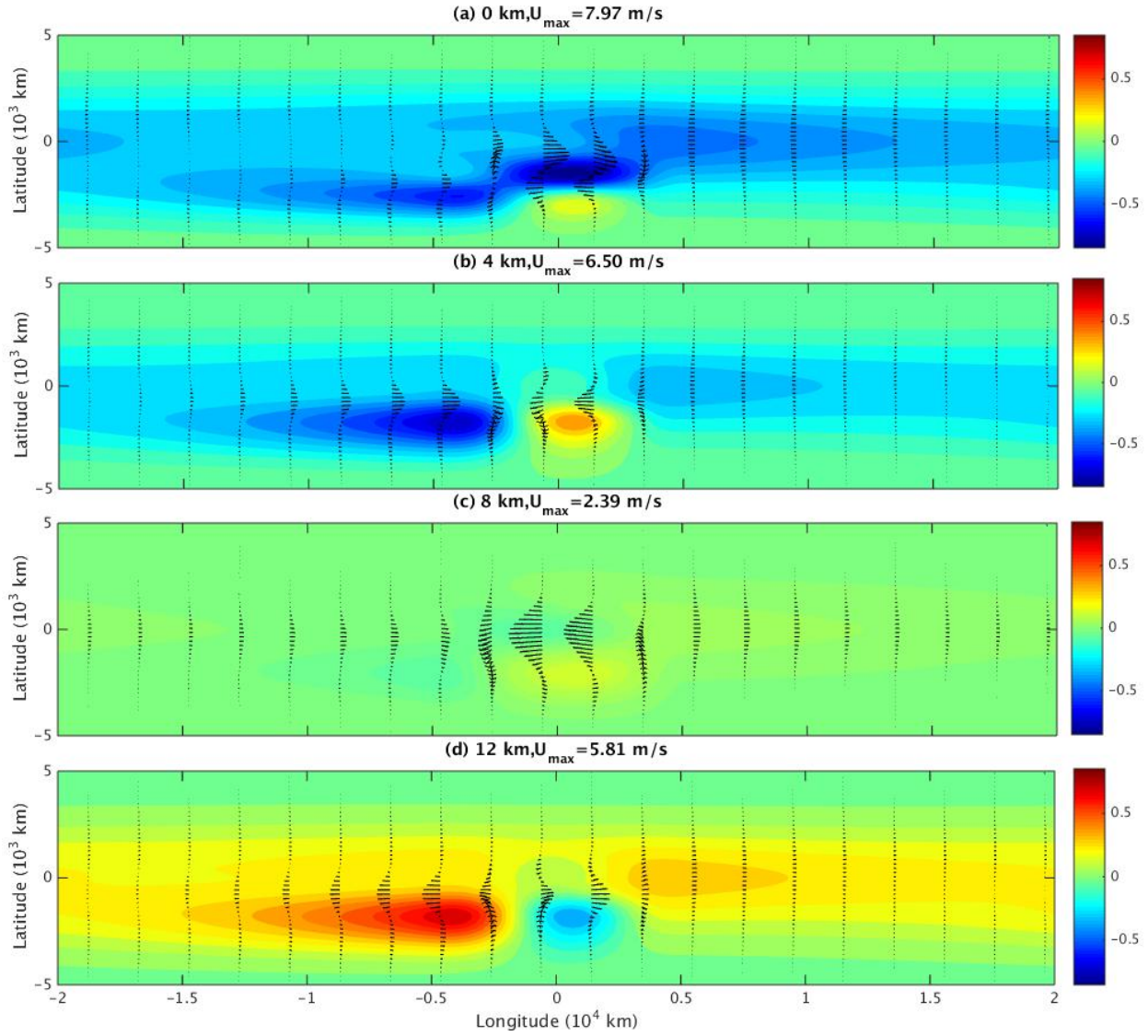


Figure 2.11: Planetary-scale response to equatorially asymmetric synoptic-scale and mean heating centered at 900 km south. The panels show flow vectors, red means positive pressure perturbation, and blue means negative pressure perturbation at heights (a) 0, (b) 4, (c) 8, (d) 12 km. The pressure perturbation is dimensionless.

ture (Eqs.2.11) with the off-equator meridional profile, and let the combined forcing drive the planetary-scale circulation response on the intraseasonal time scale (Eqs.2.5a-2.5e). Fig.2.11 shows the horizontal flow field and pressure perturbation from the meridionally asymmetric MJO model with the synoptic-scale and planetary-scale heating centered at 900 km south. At the equator, there are flow convergence in the lower troposphere and flow divergence in the upper troposphere. The horizontal profiles of flow field and pressure perturbation exhibit strong asymmetry with only one anticyclonic/cyclonic pair of gyres south of the equator.

Again, the potential temperature anomaly field is one of the crucial thermodynamic characteristics of the MJO. Fig.2.12 shows the horizontal flow field and temperature anomalies in the meridionally asymmetric MJO model with the synoptic-scale and planetary-scale heating at 900 km south. One of significant features is that the temperature anomalies exhibit significantly the first and third baroclinic modes with a cold temperature anomaly in the middle troposphere and warm temperature anomalies in both the upper and lower troposphere.

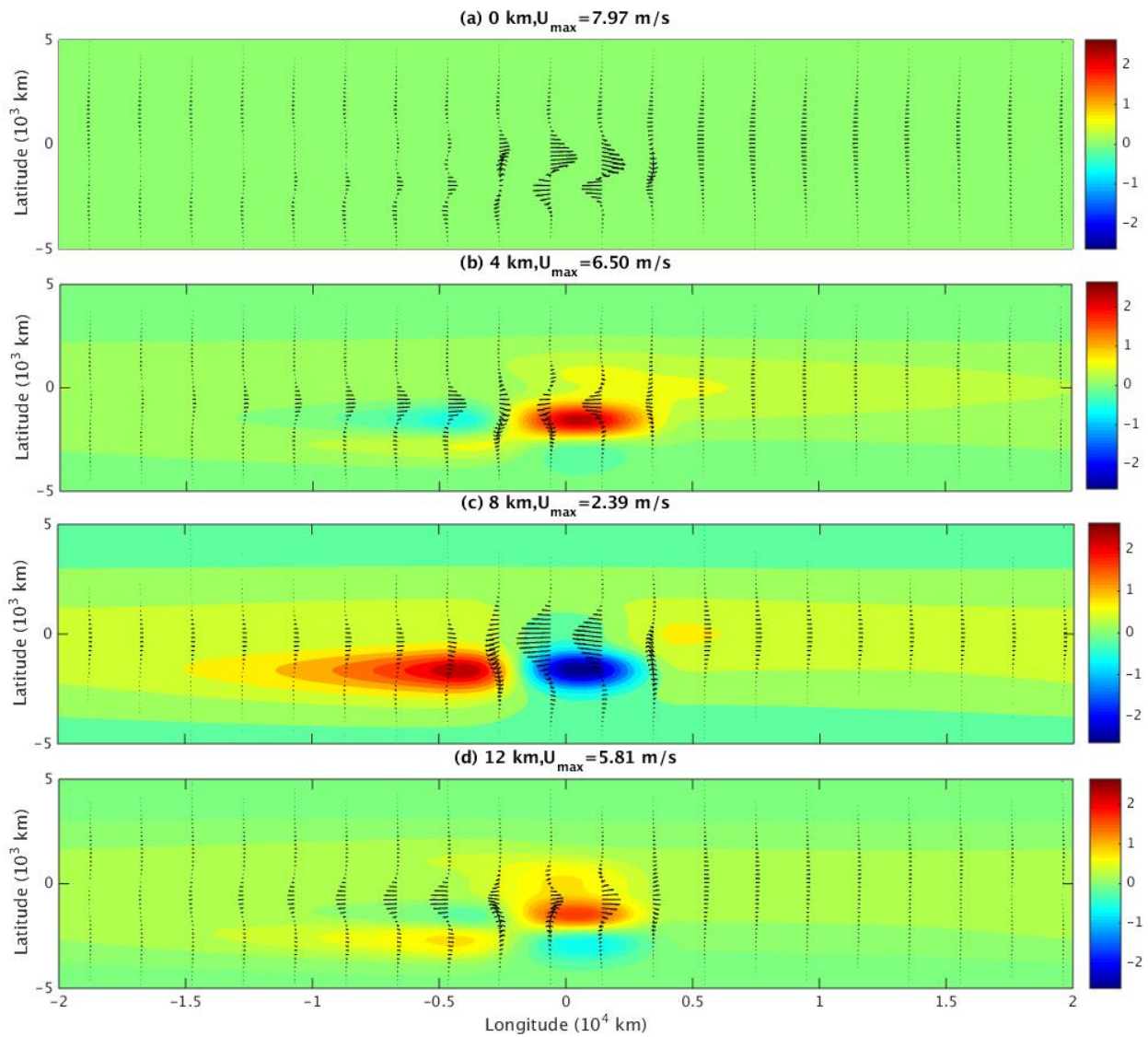


Figure 2.12: Planetary-scale response to equatorially asymmetric synoptic-scale and mean heating centered at 900km south. The panels shows flow vectors, red means positive temperature anomaly, and blue means negative temperature anomaly at heights (a) 0, (b) 4, (c) 8, (d) 12 km. The temperature anomaly is in units of K.

2.5 The intraseasonal impact of the diurnal cycle over the Maritime Continent on the MJO

The MJO consists of large-scale dynamic field and tropical convection field in a coherent structure and typically propagates eastward from the Indian Ocean to the Maritime Continent to the western Pacific Ocean (Zhang, 2005). Due to complex topography and tropical convection over the Maritime Continent, the MJO exhibits quite different velocity and thermodynamic characteristics there from those over other regions (Wu and Hsu, 2009). For example, the convection field associated with the MJO usually gets weakened during its passage over the Maritime Continent (Rui and Wang, 1990). Furthermore, when the MJO is over the Indian Ocean, its convective center sits in the region with flow convergence at the surface. After the MJO goes across the Maritime Continent, the dynamic field has faster propagation speed than the convection field so that the upper-level easterlies and low-level westerlies include the convection center (Rui and Wang, 1990).

As we already know the fact that the diurnal cycle of tropical convection is very significant over the Maritime Continent (Kikuchi and Wang, 2008), one possible reason for the complex MJO behavior is its scale interaction with the diurnal cycle of precipitation based on the observational evidence (Peatman et al., 2014). In the theoretical direction, based on the multi-scale model (Yang and Majda, 2014), we concluded in Sec.2.2-2.3 that the diurnal cycle has significant impact on both the atmospheric circulation and temperature anomalies during boreal winter. By adding the intraseasonal impact of the diurnal cycle during the passage of the MJO over the Maritime Continent, we can investigate how the intraseasonal impact of the diurnal cycle will modify the velocity and thermodynamic characteristics of the MJO and get intuition and mechanisms for the complicated behavior of the MJO. Since we have already built three different models with some key features of the MJO in Sec.2.4, in this section, we will discuss the intraseasonal impact of the diurnal cycle on these different

MJOs separately.

2.5.1 the symmetric MJO with horizontal quadrupole structure induced by the planetary-scale heating

The relative phase between the surface winds and convection center varies during the eastward propagation of the MJO from the Indian Ocean to the western Pacific Ocean. When the MJO intensifies in the Indian Ocean, the convective center matches the surface flow convergence. During the passage of the MJO over the Maritime Continent, however, the westerlies dominates and thus the convection center is situated in low-level westerly winds, as suggested by several observational studies. For example, Sui and Lau (1992) studied multiscale variability of the atmosphere during the boreal winter in 1979 and identified two intraseasonal oscillations (ISOs) within the equatorial belt. They found that persistent westerly winds are established in the region between 120° and 180° throughout the northern winter season. Such persistent westerly winds are also observed in the monsoon intraseasonal variability of 1987/1988 between 105° and 150° in the southern hemisphere (Waliser and Lau, 2005). In addition, Rui and Wang (1990) investigated the development and dynamical structure of intraseasonal low-frequency convection anomalies in the equatorial region with 200 and 850 mb wind data and found that there are strong westerlies over the convection region when the convection anomaly reaches the Maritime Continent.

If we assume that the eastward propagating MJO can keep the coupled structure of atmospheric circulation and convection as the one in the Indian Ocean, there are easterly winds to the east of the convection center and westerly winds to the west. However, as the observation shows, there are persistent westerly winds during the passage of the MJO over the Maritime Continent. The significant diurnal cycle over the Maritime Continent can be the essential reason. Due to the intraseasonal impact of the diurnal cycle of tropical convection, the resulting cyclone dominates in the lower troposphere of the southern hemisphere and

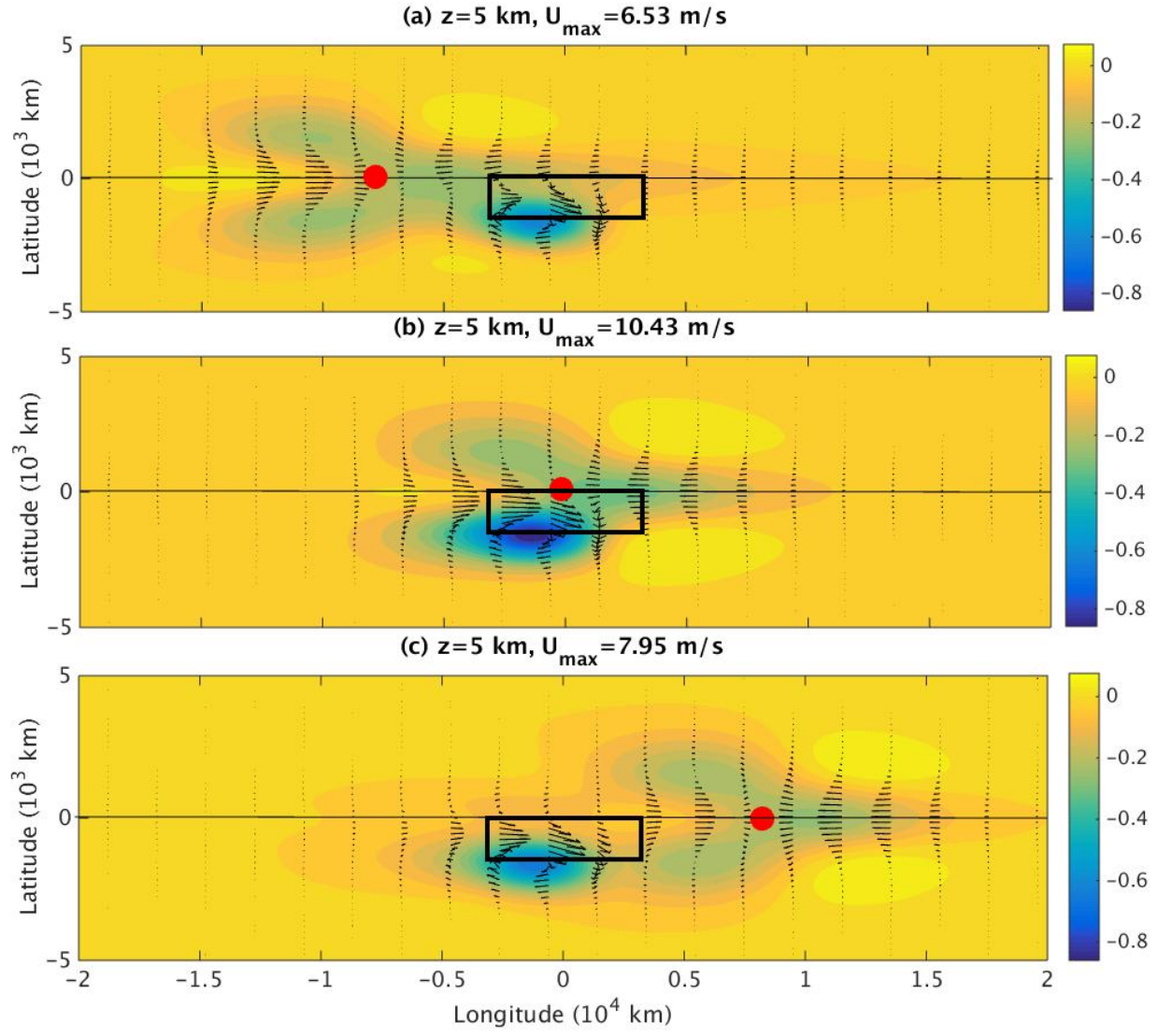


Figure 2.13: The horizontal flow field and pressure perturbation at $z = 5 \text{ km}$ due to the intraseasonal impact of the diurnal cycle and the MJO. The panels from top to bottom show different phases of MJO. The red circles shows the center of mean heating for MJO. The black box shows the regime where diurnal cycle is significant during boreal winter. The winds direction is shown by vectors and their magnitude is shown by the length of vectors. The pressure perturbation is shown in color.

generates westerlies at low latitudes of the southern hemisphere as shown in Fig.2.4, which can explain the persistent lower-level westerly winds over the Maritime Continent. If the strong westerlies due to the intraseasonal impact of the diurnal cycle can dominate over the Maritime Continent in the southern hemisphere, the resulting low-latitude westerlies can be significant during the passage of the MJO. Here we consider both the MJO with horizontal quadrupole structure (Sec.refsubsec4.1B) and the intraseasonal impact of the diurnal cycle in Sec.2.3. Fig.2.13 shows the horizontal velocity field under the impact of both MJO and diurnal cycle at 5 km. The black box denotes the region between $15^{\circ}S \sim 0^{\circ}$ over the Maritime Continent where the diurnal cycle is significant during boreal winter. One crucial feature is that during the passage of the MJO, there are persistent westerly winds in the region denoted by the black box in Fig.2.13, which matches well with the observation mentioned earlier.

As for the upper troposphere, the convection center is situated in upper-level easterlies during the passage of the MJO across the Maritime Continent (Rui and Wang, 1990). If we assume that the eastward propagating MJO can keep the coupled structure of atmospheric circulation and convection as the one in the Indian Ocean, there are westerly winds to the east of the convection center and easterly winds to the west at the upper troposphere, which does not match the observation described above. One of the reasons is the intraseasonal impact of the diurnal cycle. Due to the anticyclone in the upper troposphere of the southern hemisphere induced by the diurnal cycle (shown in Fig.2.4), the resulting upper-level easterlies at low latitudes of the southern hemisphere can explain the persistent upper-level easterly winds over the Maritime Continent. Here we consider both the MJO with horizontal quadrupole structure (Sec.2.4.1) and the intraseasonal impact of the diurnal cycle in Sec.2.3. Fig.2.14 shows the horizontal velocity field under the impact of both MJO and diurnal cycle at 12 km. The white box denotes the region where the diurnal cycle is significant during boreal winter. There are strong easterly winds over the region denoted by the white box when the convection center moves to Maritime Continent, which matches the observation well.

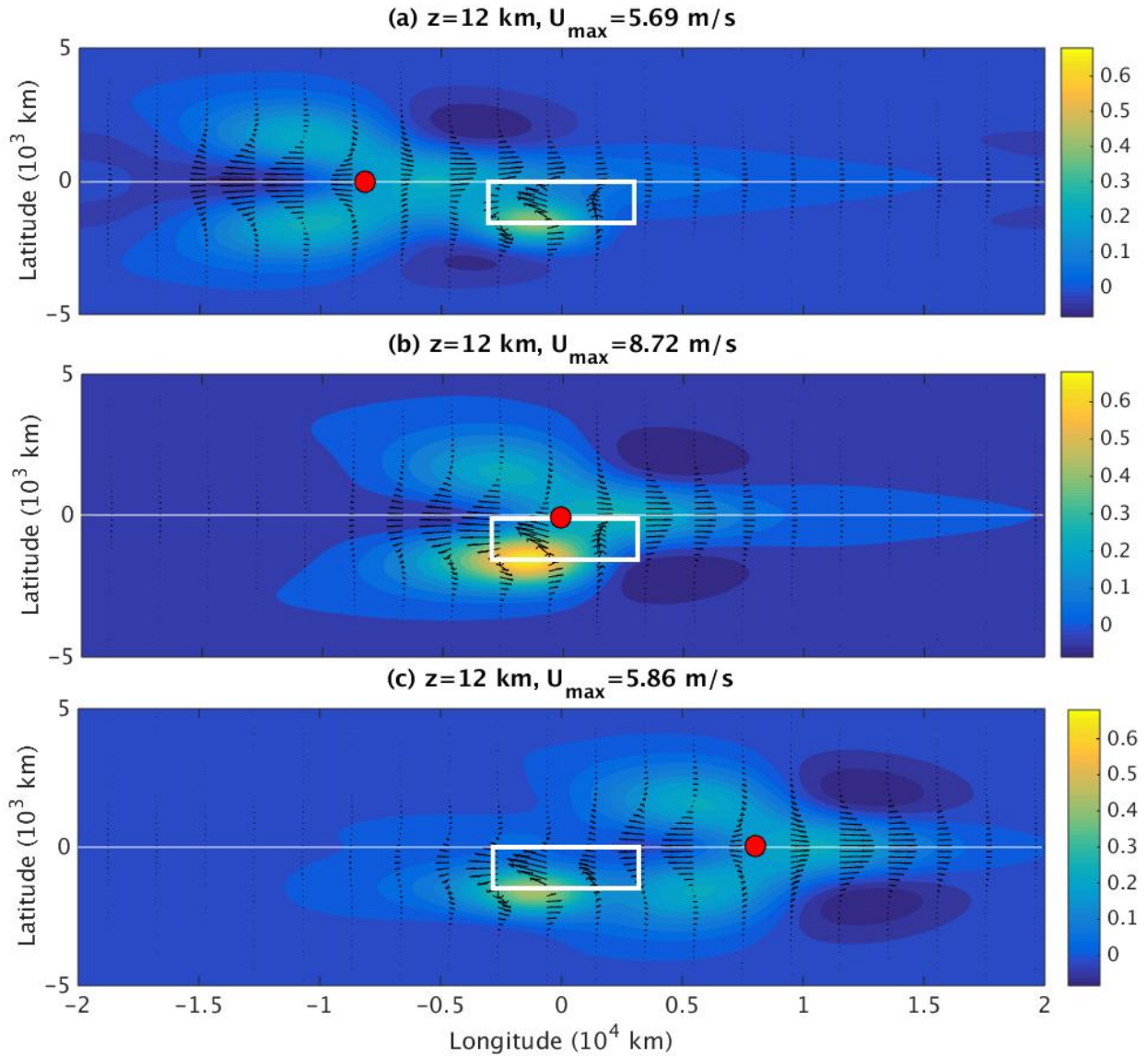


Figure 2.14: The horizontal flow field and pressure aperturbation at $z = 12 \text{ km}$ due to the intraseasonal impact of the diurnal cycle and the MJO. The panels from top to bottom show different phases of MJO. The red circles shows the center of mean heating for MJO. The white box shows the regime where diurnal cycle is significant during boreal winter. The winds direction is shown by vectors and their magnitude is shown by the length of vectors. The pressure perturbation is shown in color.

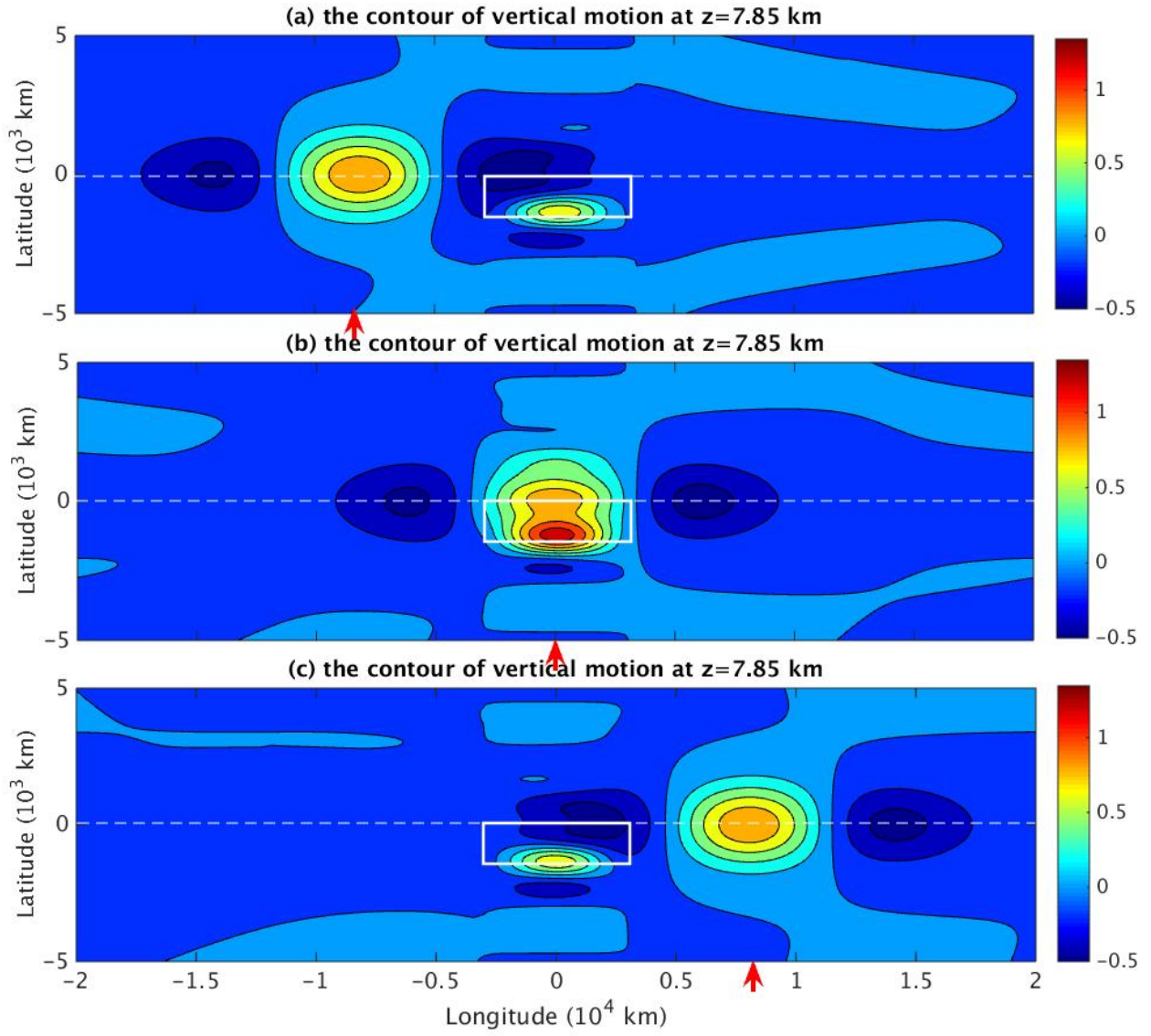


Figure 2.15: Contour of vertical motion at the middle troposphere due to the MJO and intraseasonal impact of diurnal cycle. The panels from top to bottom show different phases of MJO. The positive value means rising motion and negative value means sinking motion. The white box shows the location where the diurnal cycle is significant. The red arrow shows the longitude at which the center of MJO convection sits. The unit of vertical velocity is 0.16cm/s

In order to explore the primary structure of the vertical motion, Rui and Wang (1990) also calculate the differential divergence $D_{200} - D_{850}$, which can be considered as an estimate of the vertical motion at middle troposphere. One significant feature is that at the period when the convection center reaches the Maritime Continent, the large differential divergence anomaly also moves into the Maritime Continent and reaches its maximum magnitude at the low latitude of the southern hemisphere, meaning the intensifying rising motion in the middle troposphere. On the other hand, the intraseasonal impact of the diurnal cycle induces a heating center in the middle troposphere of southern hemisphere and cooling in the upper and lower troposphere (shown in Fig.2.3). Correspondingly, there is rising motion dominating in the middle troposphere of the southern hemisphere. Thus one possible reason for the intensifying rising motion in the middle troposphere is due to the diurnal cycle. Here we use the same model setup as above and Fig.2.15 shows the contour of vertical motion at the middle troposphere ($z = 7.85$ km) associated with both the MJO and the intraseasonal impact of diurnal cycle. The white box denotes the region where the diurnal cycle is significant during boreal winter. One significant feature in this figure is that when the MJO moves to the region denoted by the white box, the rising motion associated with the MJO is doubled due to the intraseasonal impact of diurnal cycle, which resembles the observation described above.

2.5.2 the symmetric MJO with westerly winds burst induced by synoptic-scale heating and planetary-scale heating

Although individual MJO events vary in the propagation extent and convection strength, some common features of the MJO events can be obtained by using composite MJO based on a longer time period of observational satellite data. By focusing on the composite MJO using 10 years of outgoing longwave radiation (OLR) and 7 years of wind data, Rui and Wang (1990) found that the eastward propagating convective anomaly typically gets weakened over

the Maritime Continent (Rui and Wang, 1990). One of the explanations for such weakening convection anomaly is attributed to the direct topographic effect such as blocking and wave-making effects (Wu and Hsu, 2009). Alternatively, here we try to explain the weakening MJO convection by the intraseasonal impact of the diurnal cycle of tropical convection over the Maritime Continent, which can be interpreted as the indirect topographic effect since the significant diurnal cycle is associated with the low heat capacity of the land (Frenkel et al., 2011b,d, 2013).

Here we consider both the symmetric MJO with westerly winds burst in Sec.2.4.2 and the intraseasonal impact of the diurnal cycle in Sec.2.3. The relative strength of the diurnal cycle is adjusted to $\frac{3}{4}$ so that the magnitude of its temperature anomaly is comparable with that from the MJO. In order to fully discuss the intraseasonal impact of the diurnal cycle on the MJO, it is interesting to consider different phases of the MJO during its passage over the Maritime Continent. Here we use three phases (phase I, phase II, phase III) to denote different longitudes where the MJO convective center is located. Phase I corresponds to the case when the MJO convective center is 8.1×10^3 km to the west of the diurnal cycle heating center. In phase II, the MJO convective center is 2.4×10^3 km to the west and phase III is the case with the MJO convective center 3.2×10^3 km to the east. Fig.2.16-2.18 show the total planetary-scale circulation response with temperature anomalies as the MJO propagates across the Maritime Continent. The center of the diurnal cycle heating is set at $X = 0$. One important feature is that at Phase II, the temperature anomaly south of the equator associated with the MJO is weakened by the intraseasonal impact of the diurnal cycle. In fact, the intraseasonal impact of the diurnal cycle introduces temperature anomalies in the first and third baroclinic modes in opposite sign with those from the MJO model, which is quite clear at Phase I (shown in Fig.2.16) and Phase III (shown in Fig.2.18). Such temperature anomaly cancellation can potentially explain the fact that the MJO convection field gets weakened and even stalls during its passage over the Maritime Continent.

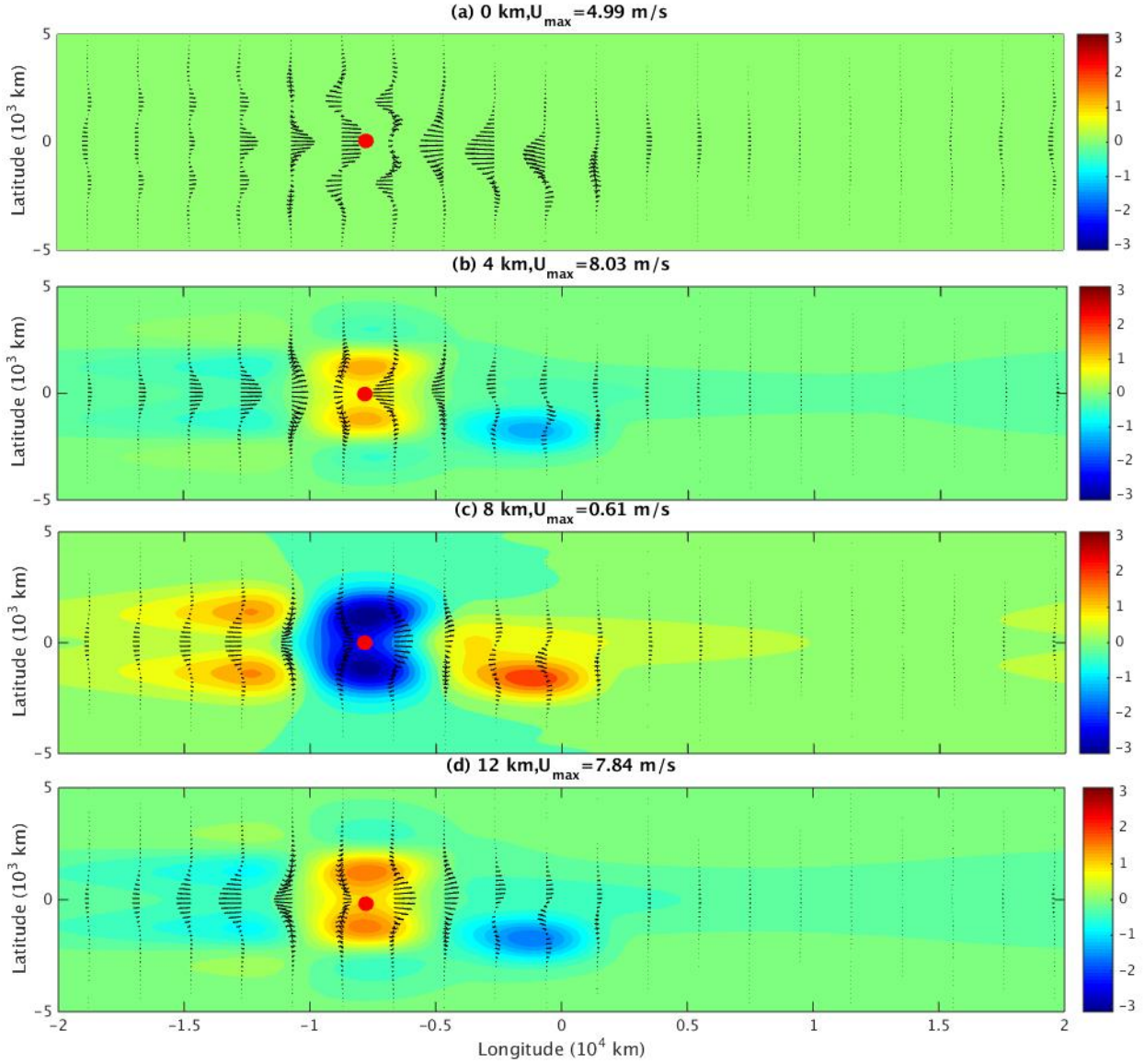


Figure 2.16: The temperature anomalies associated with the equatorially symmetric MJO and the intraseasonal impact of the diurnal cycle at phase I. The color shows temperature anomalies, the flow field is shown by vectors. From top to bottom, these 4 panels show the heights at $z=0 \text{ km}$, $z=4 \text{ km}$, $z=8 \text{ km}$, $z=12 \text{ km}$. The unit of temperature anomaly is K. The red dot shows the center of the MJO convective activities.

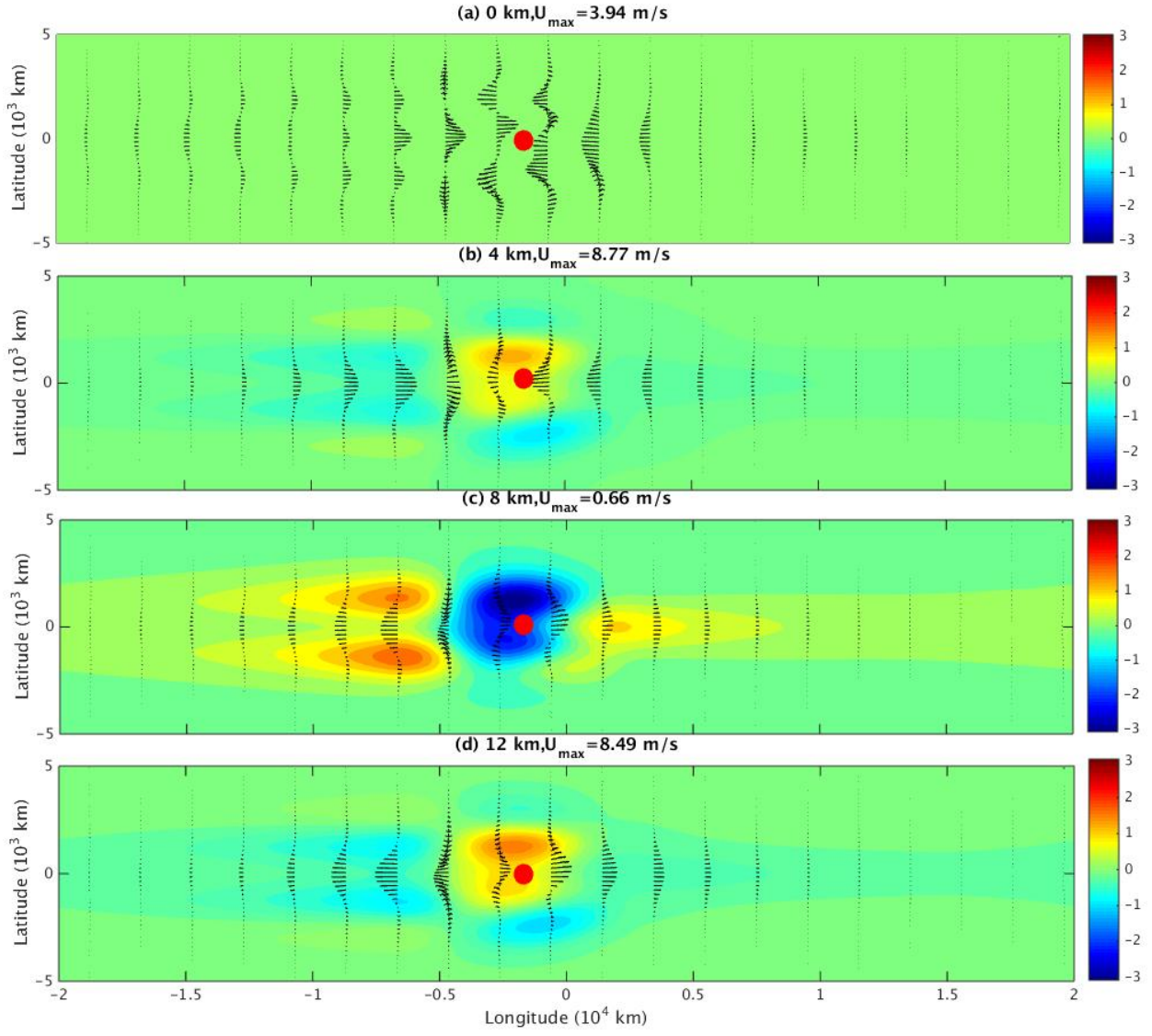


Figure 2.17: The temperature anomalies associated with the equatorially symmetric MJO and the intraseasonal impact of the diurnal cycle at phase II. The color shows temperature anomalies, the flow field is shown by vectors. From top to bottom, these 4 panels show the heights at $z=0 \text{ km}$, $z=4 \text{ km}$, $z=8 \text{ km}$, $z=12 \text{ km}$. The unit of temperature anomaly is K. The red dot shows the center of the MJO convective activities.

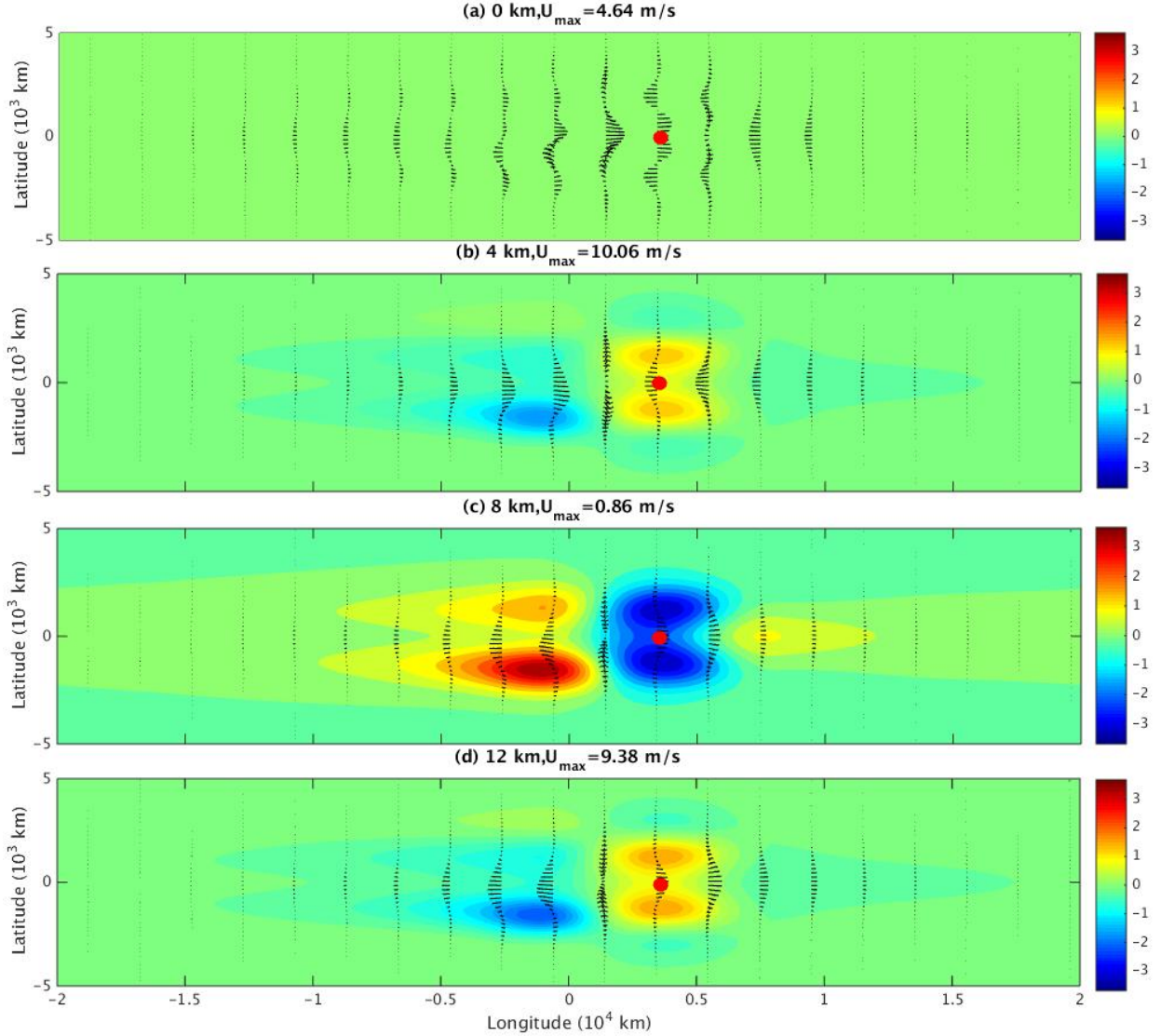


Figure 2.18: The temperature anomalies associated with the equatorially symmetric MJO and the intraseasonal impact of the diurnal cycle at phase III. The color shows temperature anomalies, the flow field is shown by vectors. From top to bottom, these 4 panels show the heights at $z=0 \text{ km}$, $z=4 \text{ km}$, $z=8 \text{ km}$, $z=12 \text{ km}$. The unit of temperature anomaly is K. The red dot shows the center of the MJO convective activities.

2.5.3 the asymmetric MJO with upward/westward tilt induced by synoptic-scale heating and planetary-scale heating

It is also interesting to consider the asymmetric MJO with upward/westward tilt when the MJO convective center located south of the equator. Here we consider both the asymmetric MJO with westerly winds burst in Sec.2.4.3 and the intraseasonal impact of the diurnal cycle in Sec.2.3. The relative strength of the diurnal cycle is adjusted to its 0.8 so that the magnitude of its temperature anomaly is comparable with that from the MJO. Also, we consider the three phases (phase I, phase II, phase III) as Sec.refsubsec5.2B. Fig.2.19-2.21 shows the temperature anomaly under the intraseasonal impact of the diurnal cycle during the passage of the asymmetric MJO at Phase I, II and III. The intraseasonal impact of the diurnal cycle introduces temperature anomalies in the first and third baroclinic mode in opposite sign with those from the MJO model, which is quite clear at phase I (shown in Fig.2.19) and Phase III (shown in Fig.2.21). During the phase II, the temperature anomaly in the active phase of the MJO is cancelled by that from the intraseasonal impact of the diurnal cycle. Such weakening temperature anomaly can potentially explain the fact that some MJOs gets weakened and even stalls during its passage over the Maritime Continent.

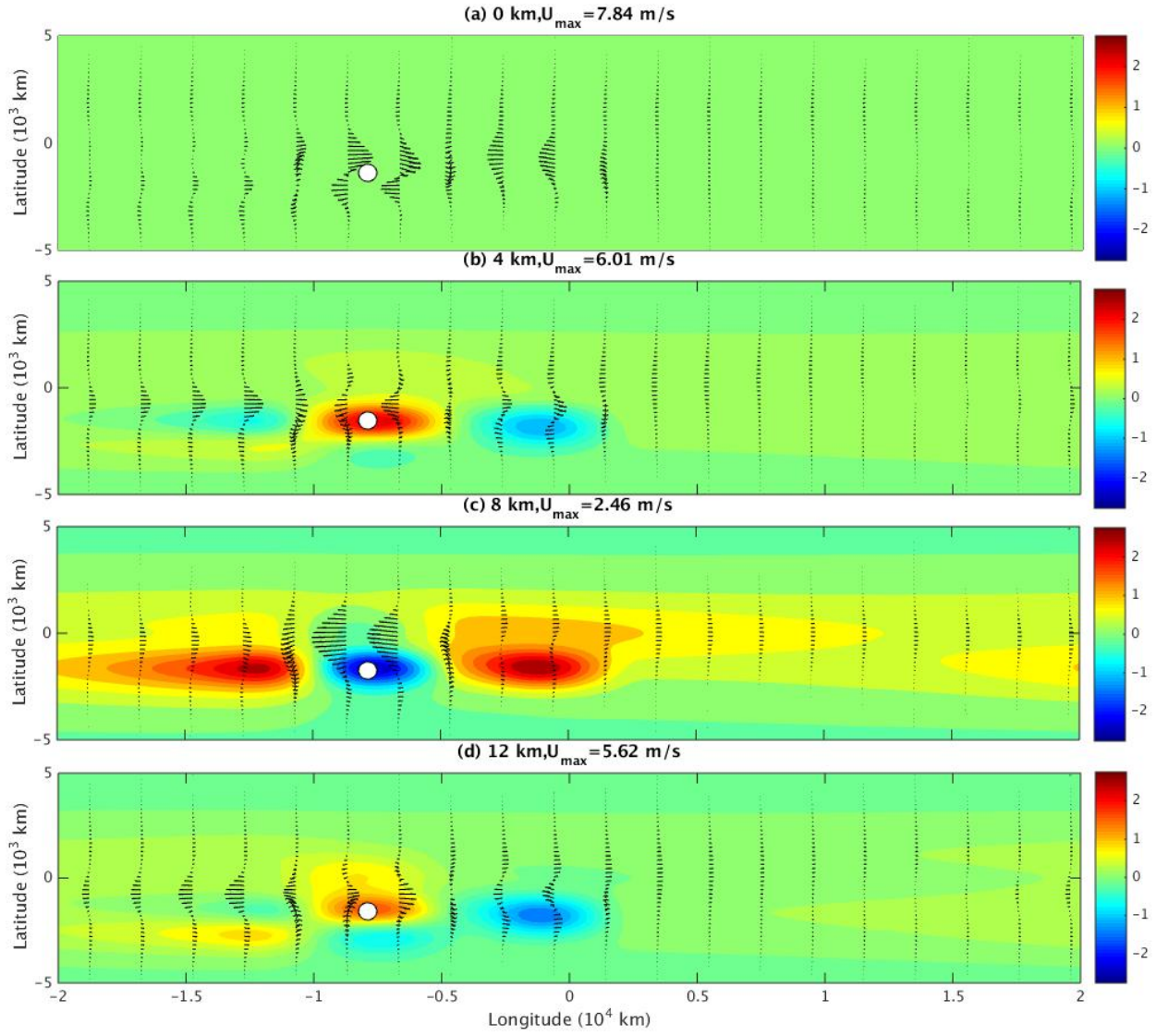


Figure 2.19: The temperature anomaly under the intraseasonal impact of the diurnal cycle during the passage of the asymmetric MJO at Phase I. The panels shows flow vectors, red means positive temperature anomaly, and blue means negative temperature anomaly at heights (a) 0, (b) 4, (c) 8, (d) 12 km. The temperature anomaly is in units of K. The white dot shows the heating center.

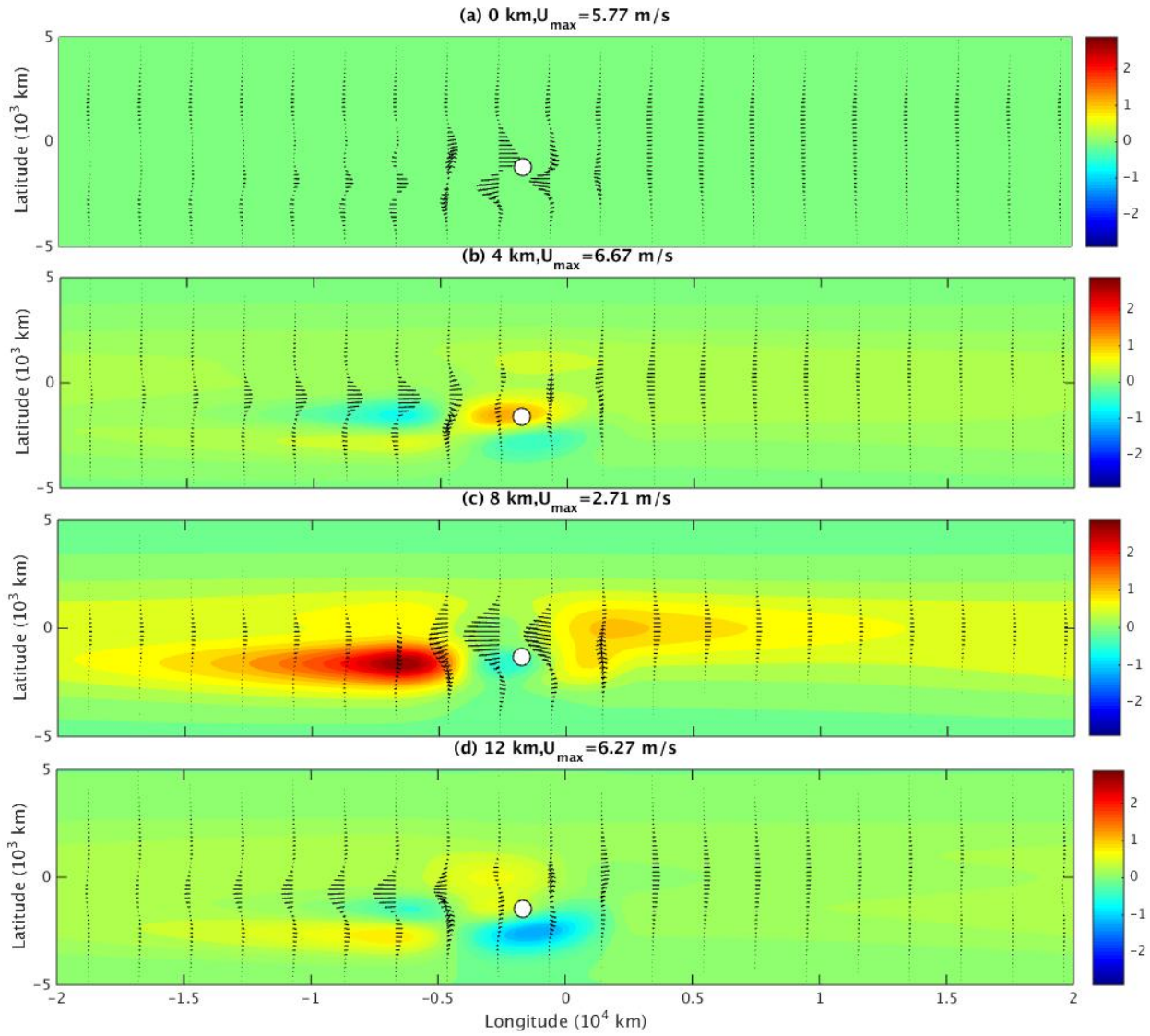


Figure 2.20: The temperature anomaly under the intraseasonal impact of the diurnal cycle during the passage of the asymmetric MJO at Phase II. The panels shows flow vectors, red means positive temperature anomaly, and blue means negative temperature anomaly at heights (a) 0, (b) 4, (c) 8, (d) 12 km. The temperature anomaly is in units of K. The white dot shows the heating center.

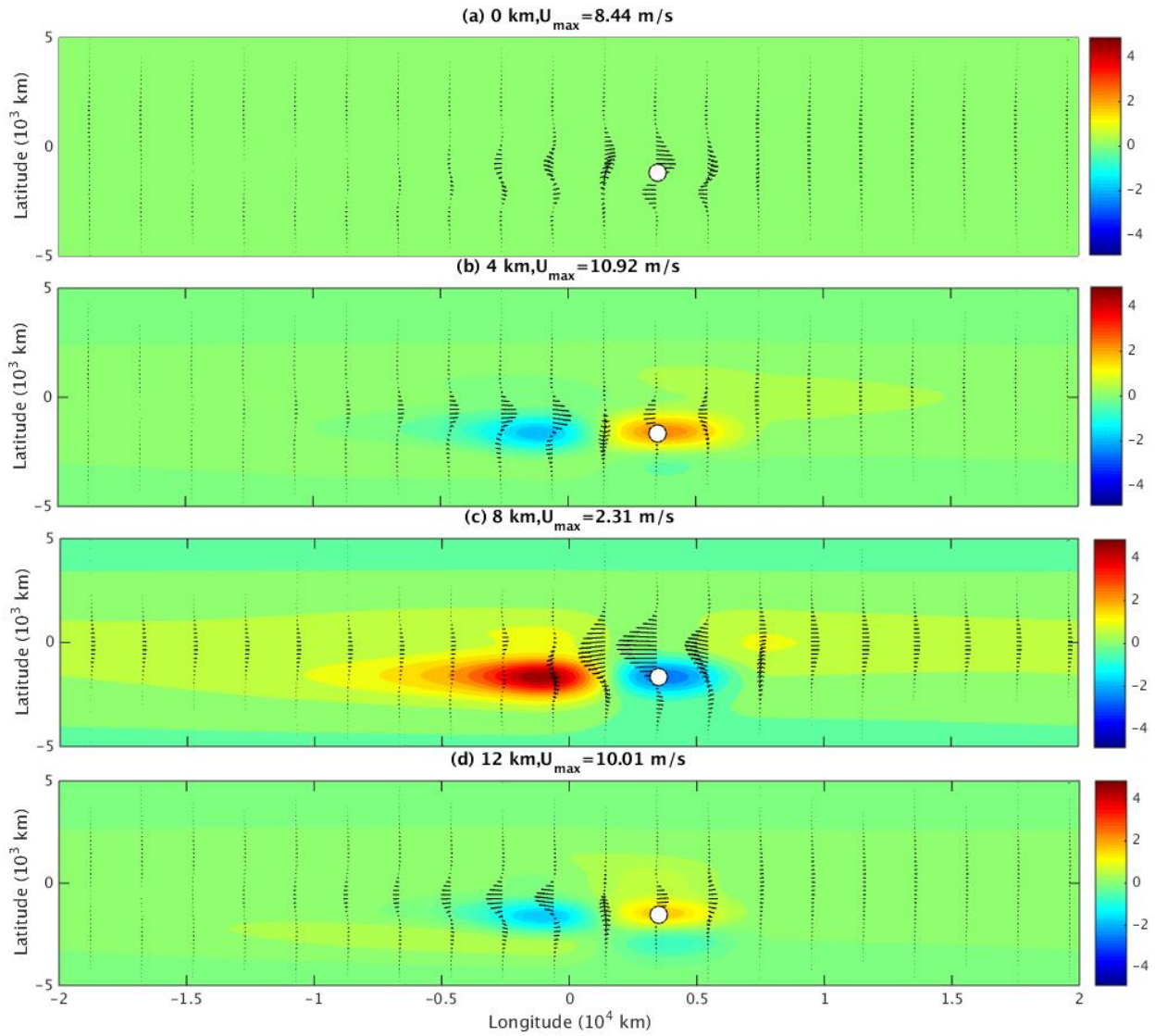


Figure 2.21: The temperature anomaly under the intraseasonal impact of the diurnal cycle during the passage of the asymmetric MJO at Phase III. The panels shows flow vectors, red means positive temperature anomaly, and blue means negative temperature anomaly at heights (a) 0, (b) 4, (c) 8, (d) 12 km. The temperature anomaly is in units of K. The white dot shows the heating center.

2.6 Concluding summary and discussion

Tropical convection over the Maritime Continent is organized on multiple spatiotemporal scales, ranging from cumulus clouds on the daily time scale over a few kilometers to intraseasonal oscillations over planetary scales. The diurnal cycle, the significant process on the daily time scale, has stronger magnitude over the Maritime Continent than that over the Indian Ocean and the western Pacific Ocean. On the other hand, the MJO, the significant component of the intraseasonal variability of tropical convection, typically propagates eastward across the Maritime Continent during boreal winter. To improve the present-day comprehensive numerical simulations for tropical convection over the Maritime Continent, a better understanding about the scale interaction between the diurnal cycle and the MJO is necessarily required. In this chapter, we focused on the intraseasonal impact of the diurnal cycle over the Maritime Continent on the MJO during boreal winter.

In the theoretical direction, the multi-scale analytic model with two time scales (daily/intraseasonal) provides assessment of the intraseasonal impact of planetary-scale inertial oscillations in the diurnal cycle (Yang and Majda, 2014). In detail, this multi-scale model provides two sets of equations governing planetary-scale tropical flow on the daily and intraseasonal time scale separately. Here we use the set of equations on the daily time scale to model the diurnal cycle and that on the intraseasonal time scale for the planetary-scale circulation response on the intraseasonal time scale. The latter is forced by eddy flux divergences of zonal momentum and temperature from the daily time scale. Furthermore, the full multi-scale model considers two spatial scales (synoptic/planetary) and two time scales(daily/intraseasonal), and thus the planetary-scale circulation response is also forced by eddy flux divergences of zonal momentum and temperature from the synoptic scale to the planetary scale. In fact, the upscale transfer from the synoptic scale to the planetary scale of momentum and temperature has been applied to successfully model the MJO based on its multi-scale features (Majda and Biello, 2004; Biello and Majda, 2005, 2006).

In the model for the diurnal cycle, diurnal heating in the first and second baroclinic mode is prescribed to mimic latent heat release associated with three cloud types (congestus, deep and stratiform) life cycle (Frenkel et al., 2011b,d, 2013). Such organized tropical flow in the diurnal cycle can generate eddy flux divergences of momentum and temperature, which further drives the planetary-scale circulation response on the intraseasonal time scale (Yang and Majda, 2014). In particular, here we consider the diurnal heating during boreal winter with the heating center sitting to the south of the equator. The resulting upscale flux divergence of temperature has the dominating impact on the circulation response and exhibits a heating center in the middle troposphere of the southern hemisphere and cooling at both the upper and lower troposphere surrounding the heating center. The corresponding planetary-scale circulation response on the intraseasonal time scale shows that such intraseasonal impact of the diurnal cycle can induce a cyclone (anticyclone) in the lower (upper) troposphere as well as significant temperature anomalies in the tropics. In a moist environment, particularly, the negative potential temperature anomaly in the lower troposphere can increase the convective available potential energy(CAPE) and reduce the convective inhibition(CIN), which enhances the buoyancy of parcels in the free troposphere and provides a favorable condition for tropical convection. Meanwhile, the negative temperature anomaly reduces the saturation value of water vapor and promotes more convection in the lower troposphere. A positive temperature anomaly in the middle troposphere has the opposite effect and can suppress deep convection.

By using the planetary-scale equations on the intraseasonal time scale, we model the original MJO by the circulation response in a moving heat source without the impact of the diurnal cycle. Since the real individual MJO events may differ in convection magnitude and circulation pattern to each other, we consider MJO models forced by three different types of the synoptic/planetary heating in a moving heat source. Each MJO model can capture several key features of the MJO such as the horizontal quadrupole structure and upward/westward tilt. Then, by considering the diurnal cycle during the passage of the

MJO over the Maritime Continent, we try to answer the questions how the intraseasonal impact of the diurnal cycle will modify the behavior of the original MJO and whether the resulting velocity and thermodynamic characteristics match the observations.

The results are as follows. For the MJO with the horizontal quadrupole structure induced by the planetary-scale heating, the intraseasonal impact of the diurnal cycle tends to strengthen westerly winds in the lower troposphere and easterly winds in the upper troposphere during the passage of the MJO over the Maritime Continent, which explains the fact that the MJO convection center typically sits in the westerlies in the lower troposphere and easterlies in the upper troposphere there. In addition, the intraseasonal impact of the diurnal cycle can also strengthen the vertical motion in the middle troposphere. As for the symmetric MJO with westerly wind burst induced by the synoptic-scale and planetary-scale heating, the temperature anomaly associated with the MJO tends to get cancelled by that from the intraseasonal impact of the diurnal cycle, which can explain the fact that MJO events typically get weakened across the Maritime Continent. In fact, such temperature anomaly cancellation is also significant in the asymmetric MJO with upward/westward tilt induced by the synoptic-scale and planetary-scale heating. Tung et al. (2014) found that during the passage of the MJO over the Maritime Continent, the symmetric MJO signals such as the heating and drying signals diminish entirely and the corresponding off-equatorial signals propagates with weakening strength. In contrast, the off-equatorial convection in the asymmetric MJO convection passes the Maritime Continent without inhibition. One possible factor developed here to support the asymmetric MJO propagating off the equator is the negative temperature anomaly induced by the intraseasonal impact of the diurnal cycle, which provides a favorable condition for tropical convection off the equator.

This study has several important implications for physical interpretation and model prediction. First, the diurnal cycle of tropical convection has significant upscale transfer of temperature from the daily time scale to the intraseasonal time scale through eddy flux divergence of temperature, which leads to another mechanism about the upscale impact of

tropical convection from small spatiotemporal scales, besides convective momentum transport (Majda and Biello, 2004; Biello and Majda, 2005). Secondly, the intraseasonal impact of the diurnal cycle can significantly modify the MJO during its passage over the Maritime Continent, which helps to explain the complex behavior of the MJO over the Maritime Continent and its scale interaction with the diurnal cycle. Thirdly, it emphasizes the significance of the representation of the diurnal variability of tropical precipitation for comprehensive numerical simulations. The present model can also be elaborated in several ways. For example, the diurnal heating prescribed here is assumed to have zero mean on the daily time scale. The diurnal heating with nonzero daily mean can generalize the framework and may be more realistic for the tropical convection over the Maritime Continent. In addition, we only consider the diurnal cycle of tropical convection on the planetary scale here. The diurnal cycle on the synoptic scale or even smaller scales can be interesting for modelling individual tropical convection events such as cumulus clouds.

2.7 Appendix

2.7.1 the dimensional units and notations in the multi-scale model

The full multi-scale model for the intraseasonal impact of the diurnal cycle of tropical convection (Yang and Majda, 2014) is derived from the hydrostatic, anelastic Euler equations on an equatorial β -plane, which are the appropriate equations for large-scale phenomenon in the tropical troposphere. This derivation follows using multiple-scale techniques developed in (Majda and Klein, 2003; Majda, 2007). These equations have been nondimensionalized first so that time scale is measured in units of the equatorial time scale $T_E = (c\beta)^{-1/2} \approx 8.3h$, the horizontal length scale is in units of the equatorial deformation radius $L_E = (c/\beta)^{1/2} = 1500km$, the vertical length scale is in units of the troposphere height divided by π , $H = H_T/\pi \approx 5km$. Here c is defined as the dry Kelvin wave speed

Physical quantity	Mathematical symbol	Value
Froude number	ϵ	0.1
Gravity wave speed	c	$50m/s$
Brunt-vaisala frequency	N	$0.01s^{-1}$
Troposphere height	H_T	$16km$
Equatorial time scale	T_E	$(c\beta)^{-1/2} = 8.3h$
Equatorial deformation radius	L_E	$(c/\beta)^{1/2} = 1500km$
Synoptic scale	$[x, y]$	$L_E = 1500km$
Vertical scale	$[z]$	$H_T/\pi = 5km$
Daily scale	$[t]$	$T_E = 8.3h$
Zonal planetary scale	$[X]$	$L_P = L_E/\epsilon = 15000km$
Intraseasonal scale	$[T]$	$T_I = T_E/\epsilon = 3.5day$
Horizontal velocity	\tilde{u}, \tilde{v}	$5ms^{-1}$
Vertical velocity	\tilde{w}	$1.6cms^{-1}$
Potential temperature anomaly	$\tilde{\theta}$	$1.53K$
Zonal velocity on the intraseasonal time scale	U	$5ms^{-1}$
Meridional velocity on the intraseasonal time scale	V	$0.5ms^{-1}$
Vertical velocity on the intraseasonal time scale	W	$0.16cms^{-1}$
Potential temperature anomaly on the intraseasonal time scale	Θ	$1.53K$
Momentum dissipation coefficient	d	$1/7days$
Radiative cooling coefficient	d_θ	$1/7 days$

Table 2.1: The dimensional units for all physical variables and some constant parameters. Here square brackets mean the value of one unit of the dimensionless variables corresponding to the given scale.

and β denotes the Rossby parameter in the Beta plane approximation. The free troposphere occupies the domain $-20 * 10^3 km \leq x \leq 20 * 10^3 km$, $-5 * 10^3 km \leq y \leq 5 * 10^3 km$, $0km \leq z \leq 16km$. The dimensional units for all physical variables and some constant parameters are summarized in Table 2.1.

In order to consider the large-scale quantities after averaging about the small scales, two averaging operators on the synoptic scale and daily time scale have been defined as follows

$$\bar{f}(X, t, T, y, z) = \lim_{L \rightarrow \infty} \frac{1}{2L} \int_{-L}^L f(x, X, t, T, y, z) dx \quad (2.14)$$

$$\langle f \rangle(x, X, T, y, z) = \lim_{T^* \rightarrow \infty} \frac{1}{2T^*} \int_{-T^*}^{T^*} f(x, X, t, T, y, z) dt \quad (2.15)$$

For all physical variables f , we can have its planetary-scale mean and synoptic-scale fluctuation decomposition $f = \bar{f} + f'$ and f' satisfies $\bar{f}' = 0$. Similarly, we can also have the intraseasonal time mean and daily fluctuation decomposition $f = \langle f \rangle + \tilde{f}$ and \tilde{f} satisfies $\langle \tilde{f} \rangle = 0$.

By using the averaging operator on the daily time scale, we can define the daily time mean for all physical variables as follows, $U = \langle u \rangle$, $V = \langle v_2 \rangle$, $W = \langle w_2 \rangle$, $\Theta = \langle \theta \rangle$, $P = \langle u \rangle$. Here v_2 and w_2 are at the second order and u, p, θ are at the first order in the asymptotic expansion.

2.7.2 the expressions and parameters in the heating profile for the diurnal cycle and MJO

2.7.2.1 the heating profile for the diurnal cycle

In the heating profile for the diurnal cycle in Eq.2.2, the envelope function $F(X)$ and the meridional profile $H(y)$ are chosen as follows,

$$F(X) = A_0 \cos \left[\frac{\pi X}{2L} \right]^+ ; H(y) = H_0 e^{-a(y-y_0)^2} \quad (2.16)$$

here $F(X)$ is chosen to be half cosine function to mimic the Maritime Continent in about 6600km longitude width ($L = \frac{2}{9}$), and its magnitude is $A_0 = \sqrt{5}$. The symbol for half cosine function used in the following context has the same meaning. The meridional profile is chosen to be a Gaussian shape function for simplicity. $y_0 = -0.8$ is chosen to mimic the case for boreal winter so that the latitude with maximum magnitude is at $10.8^\circ S$, $H_0 = 1$, $a = 2$. The dimensionless parameters $\alpha = 2/3$, $\beta = \pi/4$ are chosen to be physically consistent with the three type clouds (congestus, deep and stratiform) life cycle. The dimensionless k is chosen to be wavenumber 1 and ω corresponds to 1 day frequency for the diurnal cycle.

2.7.2.2 the heating profile in the MJO model at the section 2.4.1

In the MJO model in Eq.2.7, the envelope function of the heating $F(X)$ and the meridional profile $H(y)$ are chosen as follows,

$$F(X) = A_0(a^2 - X^2)e^{-a_0X^2}; H(y) = H_0e^{-(y-y_0)^2} \quad (2.17)$$

here we choose the parameters in the envelope function $A_0 = 56$, $a = 0.2357$, $a_0 = 9$ so that the zonal average of $F(X)$ around the equator is zero. Such envelope function can mimic the planetary-scale convection with the active phase in the middle and suppressed phases on the two sides. Also, the circulation response to the planetary-scale heating is not sensitive to the damping coefficients due to the zero zonal mean. As for the meridional profile, we choose $H_0 = 2$, $y_0 = 0$ to mimic the MJO when it propagates along the equator and the convection is trapped around equatorial regions. In order to mimic the deep convection and stratiform cloud heating, we choose $\alpha = -\frac{1}{4}$.

2.7.2.3 the heating profile in the MJO model at the section 2.4.2

In the MJO model in Eq.2.9, the envelope function of the heating $F(X - sT)$ and the meridional profile $H(y)$ are chosen as follows,

$$F(X - sT) = A_0 \cos \left[\frac{\pi(X - sT)}{2L_F} \right]^+; H(y) = H_0 e^{-a_0(y-y_0)^2}; \alpha(X - sT) = -\frac{8(X - st)}{3L_F} \quad (2.18)$$

here $L_F = 1/3$ represents 5000 km half width of the envelope, $A_0 = 1$. y_0 can be adjusted for different seasons, $H_0 = 2\sqrt{2}$, $a_0 = 0.6$. It has been shown that the upscale flux divergence is insensitive to many details of the wave train (Biello and Majda, 2005). Thus we pick the cosine function for the wavelike structure for the synoptic scale fluctuations. $\lambda = 0.65$ measures the typical length scale of the wave packet and $\phi(T)$ is for the time varying phases of the convective supercluster. α is the ratio of stratiform to deep convective heating and

$x_0 = 0.5$ is phase difference between the stratiform and deep convective heating.

2.7.2.4 the heating profile in the MJO model at the section 2.4 and 2.4.3

In the MJO model in Eq.2.12, the envelope function of the heating $F(X - sT)$, the meridional profile $H(y)$ and the relative strength of the second baroclinic mode are chosen as follows,

$$F(X - sT) = A_0 \cos \left[\frac{\pi (X - sT)}{2L_F} \right]^+; H(y) = H_0 e^{-(y-y_0)^2}; \alpha (X - sT) = \frac{3 (X - sT)}{2L_F} \quad (2.19)$$

here $A_0 = 1.08$ is the magnitude of the convective envelope. $L = 1/3$ represents 5000 km half width of the envelope. $s = 0.1$ corresponds to $5ms^{-1}$, $H_0 = 2$. The maximum value for the meridional profile $y_0 = -0.8$ is chosen so that the heating reaches maximum value south of the equator to mimic the boreal winter case. The envelope function is nonzero only in the domain $-L < X - st < L$, thus the relative strength coefficient α varies in the range $[-3/2, 3/2]$.

2.7.3 the SEWTG equations

The synoptic-scale equatorial weak temperature gradient (SEWTG) equations were first established based on the systematic derivation of the intraseasonal planetary equatorial synoptic dynamics(IPESD) model from the primitive equations (Majda and Klein, 2003). Then they are utilized for wave trains of thermally driven equatorial synoptic-scale circulations in a multi-scale model for the MJO (Majda and Biello, 2004; Biello and Majda, 2005, 2006).

The equations, in dimensionless units, read as follows,

$$-yv' + p'_x = 0, \quad (2.20a)$$

$$yu' + p'_y = 0, \quad (2.20b)$$

$$w' = S'_\theta, \quad (2.20c)$$

$$p'_z = \theta', \quad (2.20d)$$

$$u'_x + v'_y + w'_z = 0. \quad (2.20e)$$

Here all physical variables including the synoptic heating has zero mean on the synoptic scale.

Chapter 3

ITCZ Breakdown and Its Upscale Impact on the Planetary-Scale Circulation over the Eastern Pacific

3.1 Introduction

The ITCZ is a narrow band of cloudiness encircling the Earth in the tropics. Due to the low heat capacity of the continental regions, a large portion of the energy that originally comes from insolation is released back to the troposphere in the form of longwave radiation, providing favorable conditions for tropical convection in the ITCZ (Ramage, 1968). Over the oceanic regions, convective activity in the ITCZ is accompanied by warm sea surface temperatures, which increases evaporation and heat influx through the atmospheric boundary layer (Zhang, 2001). Besides, low pressure in the ITCZ induces wind convergence in the lower troposphere with the northeasterly trade winds to its north and southeasterly trade winds to its south (Toma and Webster, 2010a). The early observational studies based on satellite imagery can date back to the 1960s, where the variation of the visible brightness field affected by all cloud types is used to estimate the convective field with cloudiness (Hanson et al.,

1967; Hubert et al., 1969; Winston, 1971; Gruber, 1972). With the development of satellite measurement in higher spatiotemporal resolutions, global-scale analysis for the ITCZ has been done based on long-record satellite datasets, providing the community with concise descriptions of global ITCZ climatology (Waliser and Gautier, 1993). In general, the ITCZ in the continental regions such as Africa and South America and most of the oceanic regions such as the Indian Ocean, the western Pacific and Atlantic Ocean migrates between the Northern and Southern Hemispheres with the seasonal cycle. However, the eastern Pacific ITCZ remains in the Northern Hemisphere along the latitudes between $5^{\circ}N$ and $15^{\circ}N$ all year round. Such persistent location of the eastern Pacific ITCZ in the Northern Hemisphere has attracted attention of the community, and many theoretical and numerical studies have been undertaken to illustrate the underlying mechanism (Philander et al., 1996). Climate models fail to capture this Northern Hemisphere persistence of the ITCZ, which is associated with the so-called double ITCZ problem (Hubert et al., 1969; Zhang, 2001; Lin, 2007).

Instead of being a steady state, the ITCZ over the eastern Pacific is sometimes observed to undulate and break down on the synoptic time scale (Ferreira and Schubert, 1997). In details, the ITCZ first undulates and breaks down into several disturbances in the form of displaced cloud clusters at different locations. Among these disturbances, some grow to become tropical cyclones and others dissipate in the following several days. As tropical cyclones move to high latitudes, a new ITCZ band of cloudiness reforms in the original place. This whole process is referred to as the ITCZ breakdown. Since most of tropical cyclones forming near the ITCZ (Gray, 1979) can significantly impact the local weather and global atmospheric conditions, many physical mechanisms have been proposed to explain the ITCZ breakdown. For instance, easterly waves are frequently observed in the Atlantic Ocean, West Africa and the Pacific (Toma and Webster, 2010a,b), which can be an external reason for the ITCZ breakdown as the westward moving synoptic-scale disturbances propagate to the eastern Pacific and disturb the ITCZ flow field (Gu and Zhang, 2002). In addition, internal instability such as the vortex roll-up mechanism (Hack et al., 1989; Ferreira and

Schubert, 1997) involving a reversed meridional potential vorticity gradient field is proposed to explain the ITCZ breakdown. As the ITCZ undulates and breaks down into disturbances, the atmospheric flows get disturbed with cyclonic flows, which further impact the large-scale circulation over the eastern Pacific (Wang and Magnusdottir, 2006).

In spite of many observational studies based on satellite measurement, understanding the essential mechanism for the ITCZ breakdown and its upscale impact on the planetary-scale circulation is still an unsolved problem. For example, the barotropic aspects of the ITCZ breakdown are examined through a nonlinear shallow water model on the sphere (Ferreira and Schubert, 1997). After prescribing a zonally elongated mass sink near the equator, a potential vorticity strip with a reversed meridional gradient appears on the poleward side of the mass sink, which is unstable with weak disturbances and resembles the ITCZ breakdown. However, since the eastern Pacific ITCZ is characterized as a narrow band of cloudiness, air parcels gain buoyancy and arise into the upper troposphere. Such baroclinic aspects of the ITCZ breakdown are not captured by the shallow water model in Ferreira and Schubert (1997). On the other hand, three-dimensional simulations using a primitive equation model have been used to model the atmospheric flows during the ITCZ breakdown (Wang and Magnusdottir, 2005). In that work, a positive potential vorticity strip is generated in the lower troposphere of the Northern Hemisphere with a reversed meridional gradient, while the potential vorticity in the upper troposphere is negative with a broader meridional extent. As the potential vorticity strip undulates and breaks down, the resulting vorticity anomalies resemble tropical cyclones over several hundred kilometers in the eastern Pacific ITCZ. However, the upscale impact of the atmospheric flows associated with the ITCZ breakdown on the planetary-scale circulation is still unclear (Wang and Magnusdottir, 2005). The goal of this chapter is to use a simple multi-scale model to address those issues including the baroclinic aspects of the ITCZ breakdown and the upscale impact of mesoscale fluctuations on the planetary-scale circulation through eddy flux divergence of zonal momentum.

In the theoretical directions, self-consistent multi-scale models based on multi-scale

asymptotic methods were derived systematically and used to describe such hierarchical structures of atmospheric flows in the tropics (Majda and Klein, 2003; Majda, 2007). The advantages of using these multi-scale models lie in isolating the essential components of multi-scale interaction and providing assessment of the upscale impact of the small-scale fluctuations onto the large-scale mean flow through eddy flux divergence of momentum and temperature in a transparent fashion. In particular, the modulation of the ITCZ (M-ITCZ) equations (Biello and Majda, 2013) describe atmospheric flows on both the mesoscale and planetary scale, which interact with each other in a completely nonlinear way. Such complete nonlinearity distinguishes itself from other multi-scale models (Biello and Majda, 2005, 2006; Majda, 2007; Biello and Majda, 2010; Majda et al., 2010; Yang and Majda, 2014; Majda and Yang, 2016), where large-scale mean flow and small-scale fluctuations are typically governed by different groups of equations. Here a specific numerical scheme is designed to achieve satisfactory accuracy without violating the asymptotic assumptions after the discretization of the multi-scale system.

The M-ITCZ equations describe atmospheric dynamics on both the mesoscale and planetary scale, which are the typical scales of atmospheric flows in the eastern Pacific ITCZ. On the one hand, a single tropical cyclone and the associated cyclonic flows during the ITCZ breakdown have a comparable size as the mesoscale components in the M-ITCZ equations, and they are driven by latent heat release during precipitation of cloud clusters. On the other hand, the planetary-scale velocity and temperature fields in the M-ITCZ equations can be used to mimic the large-scale circulation pattern over the eastern Pacific, which is characterized by a strong overturning circulation cell around the equator. Here the M-ITCZ equations are used to simulate the ITCZ breakdown and its upscale impact of the disturbed atmospheric flows associated with tropical cyclones on the planetary-scale circulation. To begin with, an idealized scenario with zonal symmetry on the planetary scale is considered so that the planetary-scale gravity wave is suppressed. On the mesoscale, zonally localized heating is prescribed in the Northern Hemisphere to mimic diabatic heating associated with

a single cloud cluster in the eastern Pacific ITCZ. Outside this heating region, horizontally uniform cooling is prescribed to mimic radiative cooling and subsiding motion in the cold and dry region such as the whole Southern Hemisphere (Toma and Webster, 2010a). Besides deep meridional circulation in the eastern Pacific ITCZ, shallow meridional circulation with northerly returning flows just above the atmospheric boundary layer is observed by satellite measurement and dropsondes and wind profilers (Zhang et al., 2004; Nolan et al., 2007; Zhang et al., 2008). Since the large-scale meridional circulation can be regarded as a response to convective heating (Schneider and Lindzen, 1977; Gill, 1980; Wu, 2003), the resulting mesoscale solutions in the M-ITCZ equations driven by deep convective heating and shallow congestus heating are compared in terms of their different upscale impact. In fact, the deep and shallow ITCZ breakdown classified by convection depth have been observed and studied in Wang and Magnusdottir (2006). Then a more realistic scenario including both mesoscale and planetary-scale dynamics is considered with the diabatic heating modulated by a convective envelope to mimic the eastern Pacific ITCZ. The upscale impact of mesoscale fluctuations during the ITCZ breakdown can induce rectification of the planetary-scale circulation over the eastern Pacific.

After prescribing the diabatic heating for latent heat release in the eastern Pacific ITCZ, the M-ITCZ equations are initialized from a background state of rest and numerically integrated when forced by the diabatic heating. Several crucial results are obtained by diagnostically calculating eddy flux divergence of zonal momentum and comparing the flow fields with mesoscale zonally localized and uniform heating in the first scenario. First, a positive vorticity strip is generated in the northern side of the deep diabatic heating region in the lower troposphere and undulates in the first two days, followed by the formation of a strong vortex, which resembles the ITCZ breakdown as seen in observations (Ferreira and Schubert, 1997). In the middle troposphere, a pair of vorticity dipoles form at low latitudes of the Northern Hemisphere. The baroclinic aspects of the ITCZ breakdown is examined here, including the vertical structure of vorticity and flow fields. Secondly, in the

deep heating case, the eddy flux divergence of zonal momentum is characterized by mid-level (low-level) eastward (westward) momentum forcing at high latitudes of the Northern Hemisphere and alternate mid-level momentum forcing at low latitudes. As far as kinetic energy is concerned, such eddy impact of the mesoscale dynamics accelerate mid-level zonal jets at both low and high latitudes, and decelerate low-level zonal jets at high latitudes. Thirdly, compared with deep convective heating, shallow congestus heating efficiently drives stronger vorticity anomalies and induces more significant eddy flux divergence of zonal momentum and acceleration/deceleration effects in the Northern Hemisphere, although the flow fields are confined in the shallower levels. In the more realistic scenario where the mesoscale fluctuations are coupled to the planetary-scale gravity waves, it is found that the most significant zonal velocity anomalies are confined to the diabatic heating region while small zonal velocity anomalies are transported away by the planetary-scale gravity waves. As for the rectification of the planetary-scale circulation in the Northern Hemisphere, westerly wind anomalies are induced at high latitudes of the lower and middle troposphere and low latitudes of the upper troposphere, while easterly wind anomalies are induced around the equator in the middle troposphere.

The rest of this chapter is organized as follows. The properties of the M-ITCZ equations for mesoscale barotropic Rossby waves and planetary-scale gravity waves and conservation of potential vorticity and kinetic energy are discussed in Sec.3.2. Sec.3.3 presents numerical solutions for the ITCZ breakdown in zonally symmetric planetary-scale flow. Both deep convective heating and shallow congestus heating cases are considered in the same model setup and compared in terms of vorticity field, eddy flux divergence of zonal momentum and acceleration/deceleration effects on the mean flow. Sec.3.4 considers the general case where the diabatic heating is modulated by a planetary-scale convective envelope, explaining the rectification of the planetary-scale circulation due to the ITCZ breakdown over the eastern Pacific. This chapter ends with a concluding discussion. The numerical scheme for solving the M-ITCZ equations is summarized in the Appendix.

3.2 The M-ITCZ Equations and their properties

3.2.1 The governing equations

Inspired by the multi-scale features of tropical convection, the multi-scale asymptotic methods were used to derive reduced models across multiple spatiotemporal scales (Majda and Klein, 2003; Majda, 2007). In particular, the M-ITCZ equations, derived in Biello and Majda (2013), describe the multi-scale dynamics of the ITCZ from the diurnal to monthly time scales in which mesoscale convectively coupled Rossby waves are modulated by large-scale gravity waves. The M-ITCZ equations in dimensionless units read as follows,

$$\frac{Du}{Dt} - yv = -\frac{\partial p}{\partial x} - \frac{\partial \Pi}{\partial X} - du, \quad (3.1a)$$

$$\frac{Dv}{Dt} + yu = -\frac{\partial p}{\partial y} - dv, \quad (3.1b)$$

$$w = S^\theta, \quad (3.1c)$$

$$\frac{\partial u}{\partial x} + \frac{\partial v}{\partial y} + \frac{\partial w}{\partial z} = 0, \quad (3.1d)$$

$$\frac{\partial \Pi}{\partial x} = \frac{\partial \Pi}{\partial y} = 0, \quad \frac{\partial \Pi}{\partial z} = \Theta, \quad (3.1e)$$

$$\frac{\partial \Theta}{\partial t} + \langle \bar{w} \rangle \frac{\partial \Theta}{\partial z} + W = 0, \quad (3.1f)$$

$$\frac{\partial}{\partial X} [\langle \bar{u} \rangle - U] + \frac{\partial W}{\partial z} = 0, \quad (3.1g)$$

where $\frac{D}{Dt} = \frac{\partial}{\partial t} + u \frac{\partial}{\partial x} + v \frac{\partial}{\partial y} + w \frac{\partial}{\partial z}$ is the advection derivative due to the three-dimensional flow.

The M-ITCZ equations describe multi-scale flow fields in the tropical belt across two zonal spatial scales (planetary-scale X , mesoscale x). Except for the large-scale pressure gradient $-\Pi_X$ in Eq.3.1a, the first four equations in Eqs.3.1a-3.1d govern tropical flows on the mesoscale, where one dimensionless unit of (x, y) corresponds to 500 km and those of horizontal and vertical velocity correspond to 5 ms^{-1} and 0.05 ms^{-1} respectively. The

diabatic heating S_θ measured in units of 33 K day^{-1} directly drives the mesoscale dynamics in weak temperature gradient balance. The remaining three equations in Eqs.3.1e-3.1g describes the zonal modulation of tropical flows on the planetary scale, where one dimensionless unit of X corresponds to 5000 km. Such planetary-scale tropical flows are governed by hydrostatic balance with potential temperature anomalies measured Θ in units of 3.3 K in Eq.3.1e, thermal equation in Eq.3.1f and incompressibility constraint between the baroclinic mode of large-scale zonal velocity and secondary vertical velocity W (in dimensional units of 0.005 ms^{-1}) in Eq.3.1g. When coupled with the mesoscale mean zonal velocity and planetary-scale pressure gradient in Eq.3.1a, the last three equations describe planetary-scale gravity waves propagating zonally in the tropics. In order to obtain the mesoscale mean flow fields, mesoscale zonal and meridional averaging operators defined for an arbitrary function f are as follows.

$$\bar{f}(X, y, z, t) = \lim_{L \rightarrow \infty} \frac{1}{2L} \int_{-L}^L f(x, X, y, z, t) dx, \quad (3.2)$$

$$\langle f \rangle(x, X, z, t) = \frac{1}{2L_*} \int_{-L_*}^{L_*} f(x, X, y, z, t) dy, \quad (3.3)$$

where L is the mesoscale zonal length of the domain in the asymptotic limit and L_* measures the finite poleward extent of the domain on the equatorial β plane. Besides, U denotes the barotropic mode of mean zonal velocity $\langle \bar{u} \rangle$.

3.2.2 Mesoscale barotropic Rossby waves and planetary-scale gravity waves

One crucial feature of the M-ITCZ equations is that the planetary-scale and mesoscale dynamics are nonlinearly coupled with each other. As already mentioned, such a model with complete nonlinearity is quite different from multi-scale models where the flow fields on different scales are governed by different groups of equations. For example, the intraseasonal

planetary equatorial synoptic dynamics (IPESD) model consists of two groups of equations (Majda and Biello, 2004; Biello and Majda, 2005, 2006). One of them describes equatorial synoptic-scale fluctuations and the other one is for the planetary-scale circulations. In the IPESD model, the planetary-scale equations are forced by upscale transfer of momentum and temperature from synoptic-scale fluctuations. In contrast, the M-ITCZ equations consists of only one group of equations, which involve zonal variation on both the planetary scale and mesoscale in a single time scale.

Although both the planetary-scale and mesoscale dynamics in the M-ITCZ equations are completely coupled to each other, the mesoscale dynamics still can be isolated by assuming zonal symmetry of the planetary-scale dynamics. Consequently, the planetary-scale pressure perturbation term $-\Pi_X$ in Eq.3.1a vanishes, Eqs.3.1a-3.1d decouple from Eqs.3.1e-3.1g , and the equations for the mesoscale dynamics in dimensionless units become,

$$\frac{Du}{Dt} - yv = -\frac{\partial p}{\partial x} - du, \quad (3.4a)$$

$$\frac{Dv}{Dt} + yu = -\frac{\partial p}{\partial y} - dv, \quad (3.4b)$$

$$w = S^\theta, \quad (3.4c)$$

$$\frac{\partial u}{\partial x} + \frac{\partial v}{\partial y} + \frac{\partial w}{\partial z} = 0. \quad (3.4d)$$

Eqs.3.4a-3.4d are called Mesoscale Equatorial Weak Temperature Gradient (MEWTG) equations (Majda and Klein, 2003), which consist of three-dimensional velocity field (u, v, w) and pressure perturbation p . The nonlinear horizontal momentum equations on an equatorial β -plane come with a linear momentum damping term, which is used to mimic cumulus drag in large-scale tropical flows (Lin et al., 2005). Due to the Weak Temperature Gradient (WTG) approximation (Sobel et al., 2001), the vertical velocity w is directly determined by the diabatic heating S^θ . The conservation of mass is guaranteed by the divergence-free constraint and constant density in the Boussinesq approximation. The MEWTG equations have been

applied to model a variety of physical phenomena in the tropical circulation. For example, through a combination of exact solutions and simple numerics, some elementary exact solutions and an exact nonlinear stability analysis about a model similar to the MEWTG equations but on smaller scales and the f -plane are obtained in Majda et al. (2008). The elementary solutions including the evolution of radial eddies to represent hot towers in a hurricane embryo are studied in a suitable radial preconditioned background. Meanwhile, similar equations to the MEWTG equations also appear in the balanced hot tower model and balanced mesoscale vortex model as dynamical core, which are utilized successfully to illustrate key mechanisms in the hurricane embryo (Majda et al., 2010).

By plugging the ansatz of plane waves into the linear MEWTG equations without thermal forcing and momentum damping, the dispersion relation of barotropic Rossby waves can be obtained (Majda and Klein, 2003),

$$\omega = -\frac{k}{k^2 + l^2}, \quad (3.5)$$

where ω is the frequency and k, l are the wavenumber in the zonal and meridional directions. Such linear solutions with the dispersion relation of barotropic Rossby waves can have arbitrary vertical structure including both barotropic and baroclinic modes.

As for the planetary-scale dynamics of the M-ITCZ equations, the planetary-scale equations can be obtained by applying the zonal averaging operators defined in Eq.3.2. In order to guarantee the multi-scale asymptotic assumptions and avoid secular growth, all terms involving mesoscale zonal derivative are assumed to be zero after taking mesoscale zonal averaging. The resulting equations for the planetary-scale gravity wave in dimensionless units

read as follows.

$$\frac{\partial \bar{u}}{\partial t} + \frac{\partial}{\partial y} (\bar{v}\bar{u}) + \frac{\partial}{\partial z} (\bar{w}\bar{u}) - y\bar{v} = -\frac{\partial \Pi}{\partial X} - d\bar{u} - \frac{\partial}{\partial y} (\bar{v}'\bar{u}') - \frac{\partial}{\partial z} (\bar{w}'\bar{u}'), \quad (3.6a)$$

$$\bar{w} = \bar{S}^\theta, \quad (3.6b)$$

$$\frac{\partial \bar{v}}{\partial y} + \frac{\partial \bar{w}}{\partial z} = 0, \quad (3.6c)$$

$$\frac{\partial \Pi}{\partial x} = \frac{\partial \Pi}{\partial y} = 0, \quad \frac{\partial \Pi}{\partial z} = \Theta, \quad (3.6d)$$

$$\frac{\partial \Theta}{\partial t} + \langle \bar{w} \rangle \frac{\partial \Theta}{\partial z} + W = 0, \quad (3.6e)$$

$$\frac{\partial}{\partial X} [\langle \bar{u} \rangle - U] + \frac{\partial W}{\partial z} = 0, \quad (3.6f)$$

where $\langle \bar{w} \rangle$ in Eq.3.6e vanishes if the rigid boundary condition for meridional velocity \bar{v} is imposed for no inflow and outflow in the meridional boundaries. The prime notation denotes mesoscale zonal fluctuations $f = \bar{f} + f'$, satisfying $\bar{f}' = 0$.

Eqs.3.6a-3.6f describe zonally propagating gravity waves on the planetary scale. The meridional circulation (\bar{v}, \bar{w}) is directly determined by the diabatic heating \bar{S}^θ with some suitable boundary conditions. The zonal velocity \bar{u} is forced by advection effects of the meridional circulation (\bar{v}, \bar{w}) , the Coriolis force $y\bar{v}$, planetary-scale zonal gradient of pressure perturbation $-\Pi_X$, momentum damping $-d\bar{u}$ and eddy flux divergence of zonal momentum $-(\bar{v}'\bar{u}')_y - (\bar{w}'\bar{u}')_z$. The meridional mean of zonal velocity in the baroclinic mode and the secondary vertical velocity W have zero divergence. The equations are closed with the hydrostatic balance in Eq.3.6d and thermal equation in Eq.3.6e. In fact, the planetary-scale gravity wave equations without upscale fluxes have been studied in Biello and Majda (2013). By prescribing the diabatic heating in the first baroclinic mode within a zonally localized envelope, planetary-scale gravity waves are generated and propagate in both eastward and westward directions. The planetary-scale gravity waves tend to equalize the meridional mean of the vertical shear of zonal wind at all longitudes in the tropics. Meanwhile, they carry cold temperature anomalies and upward velocity to the west, warm temperature anomalies

and downward velocity to the east. In a moist environment, the cold temperature anomalies and upward velocity provide favorable conditions for convection to the west and unfavorable conditions for convection to the east.

3.2.3 Conservation of potential vorticity and kinetic energy

Here the conservation of potential vorticity (PV) and kinetic energy in the M-ITCZ equations are discussed.

PV is a useful quantity to understand the generation of vorticity in cyclogenesis, which is materially invariant in flows and can only be changed by diabatic and frictional processes. In the M-ITCZ equations, planetary-scale quantities such as the large-scale pressure perturbation Π_X do not depend on the mesoscale zonal and meridional coordinates (x, y) , thus the planetary-scale gravity wave does not directly modify vorticity and PV on the mesoscale except for the advection of the mean zonal velocity. After taking the meridional derivative of Eq.3.1a and the zonal derivative of Eq.3.1b along with the thermal equation in Eq.3.1c and the continuity equation in Eq.3.1d, the equations for PV can be derived. We have,

$$\frac{DQ}{Dt} = Q \frac{\partial S^\theta}{\partial z} - \frac{\partial v}{\partial z} \frac{\partial S^\theta}{\partial x} + \frac{\partial u}{\partial z} \frac{\partial S^\theta}{\partial y} - d\omega, \quad (3.7)$$

where $Q = \omega + y$, is the summation of relative vorticity, $\omega = v_x - u_y$, and the vorticity due to earth rotation, y , on an equatorial β -plane.

One simple scenario is that both diabatic heating S^θ and momentum dissipation d are assumed to be zero. Then all terms on the right hand side of Eq.3.7 vanish and Q is materially invariant. In general, both diabatic heating S^θ and momentum dissipation d are nonzero so that potential vorticity Q is also modified by several terms on the right hand side of Eq.3.7. The first term $QS_z^\theta = Qw_z$ represents vortex stretching. The second and third terms $-v_z S_x^\theta + u_z S_y^\theta = -v_z w_x + u_z w_y$ give rise to vortex tilting. The fourth term $-d\omega$ describes damping effect that has the same dissipation time as the zonal momentum, and its value is

proportional to the vorticity ω instead of PV.

On the mesoscale, the vertical velocity w is directly balanced by the diabatic heating S^θ in the M-ITCZ equations, whose vertical gradient also means wind divergence and convergence due to the conservation of volume in Eq.3.1d. Meanwhile, the momentum damping d in Eqs.3.1a-3.1b for cumulus drag has increasing dissipation time scale as height increases (Romps, 2014), which tends to decelerate winds and restore the forced flows into equilibrium. Therefore, the M-ITCZ equations with the prescribed diabatic heating profile is a forced and damped model.

The conservation of kinetic energy can provide a better understanding of the dynamical field, especially the acceleration/deceleration effects due to the upscale impact of the mesoscale fluctuations. In details, the conservation of kinetic energy on the mesoscale can be derived by multiplying the zonal momentum equation in Eq.3.1a by u and the meridional momentum equations in Eq.3.1b by v and adding these two equations together as follows,

$$\frac{\partial K_m}{\partial t} + \nabla \cdot (K_m \mathbf{v} + p \mathbf{u}) = -pw_z - \frac{\partial \Pi}{\partial X} u - 2dK_m, \quad (3.8)$$

where $\mathbf{v} = (u, v, w)$ represents three-dimensional velocity field and $\mathbf{u} = (u, v, 0)$ represents horizontal velocity field. $K_m = \frac{u^2+v^2}{2}$ denotes kinetic energy of horizontal flow field on the mesoscale. Eq.3.8 is in the general form of the conservation of energy, which includes the time tendency of kinetic energy, the kinetic energy fluxes and some source terms on the right hand side. Specially, the kinetic energy flux term $K_m \mathbf{v}$ involves the three-dimensional flow field, while only horizontal flows do work against pressure force in the term $p \mathbf{u}$. The first term $-pw_z$ at the right hand side of Eq.3.8 involves the vertical stretching of upward motion against pressure, which is thermally driven by the diabatic heating. The second term $-\Pi_X u$ represents the acceleration/deceleration effects of the planetary-scale pressure perturbation in the zonal direction. The third term $-2dK_m$ represents the energy dissipation due to cumulus drag, which has half dissipation time scale as momentum dissipation.

On the planetary scale, after multiplying Eq.3.6a by \bar{u} , the equation for kinetic energy of zonal winds can be obtained as follows,

$$\frac{\partial}{\partial t} \left(\frac{\bar{u}^2}{2} \right) + \frac{\partial}{\partial y} \left(\bar{v} \frac{\bar{u}^2}{2} \right) + \frac{\partial}{\partial z} \left(\bar{w} \frac{\bar{u}^2}{2} \right) = y \bar{v} \bar{u} - \frac{\partial \Pi}{\partial X} \bar{u} - d\bar{u}^2 + F^u \bar{u}, \quad (3.9)$$

where $F^u = -(\bar{v}' \bar{u}')_y - (\bar{w}' \bar{u}')_z$ is the eddy flux divergence of zonal momentum from the mesoscale fluctuations. Similarly, the equation for kinetic energy of meridional winds can also be obtained by using Eq.3.1b and multiplying \bar{v} ,

$$\frac{\partial}{\partial t} \left(\frac{\bar{v}^2}{2} \right) + \frac{\partial}{\partial y} \left(\bar{v} \frac{\bar{v}^2}{2} \right) + \frac{\partial}{\partial z} \left(\bar{w} \frac{\bar{v}^2}{2} \right) = -y \bar{v} \bar{u} - \frac{\partial \bar{p}}{\partial y} \bar{v} - d\bar{v}^2 + F^v \bar{v}, \quad (3.10)$$

where $F^v = -(\bar{v}' \bar{v}')_y - (\bar{w}' \bar{v}')_z$ is the eddy flux divergence of meridional momentum from the mesoscale fluctuations. By adding Eq.3.9-3.10 together, the equation for the total kinetic energy reads as follows,

$$\frac{\partial K}{\partial t} + \frac{\partial}{\partial y} (\bar{v} K) + \frac{\partial}{\partial z} (\bar{w} K) = -\frac{\partial \Pi}{\partial X} \bar{u} - \frac{\partial \bar{p}}{\partial y} \bar{v} - 2dK + F^u \bar{u} + F^v \bar{v}, \quad (3.11)$$

where $K = \frac{\bar{u}^2 + \bar{v}^2}{2}$ represents the kinetic energy of horizontal flow.

Eq.3.11 describes the budget of horizontal kinetic energy on the planetary scale, including the time tendency of kinetic energy and the kinetic energy fluxes in the meridional/vertical directions on the left hand side, and some source terms on the right hand side. The kinetic energy flux term $(\bar{v} K)_y + (\bar{w} K)_z$ represents the advection effect of the planetary-scale meridional/vertical circulation (\bar{v}, \bar{w}) . On the right hand side, the first term $-\Pi_X \bar{u}$ represents the acceleration/deceleration effects of large-scale pressure gradient in zonal direction. The second term $-\bar{p}_y \bar{v}$ represents the acceleration/deceleration effects of pressure gradient in meridional direction. The third term $-2dK$ describes the energy dissipation due to cumulus drag, which has half dissipation time scale as momentum dissipation. The last two terms, $F^u \bar{u} + F^v \bar{v}$, denote the acceleration/deceleration effects due to mesoscale eddy flux diver-

gence of zonal and meridional momentum. Furthermore, the first terms $\mp y\bar{v}\bar{u}$ on the right hand side of Eq.3.9-3.10 cancel each other and do not show up in the kinetic energy equation in Eq.3.11. In fact, these two terms represent energy transfer between the planetary-scale zonal and meridional velocity due to the Coriolis force.

3.3 ITCZ Breakdown in Zonally Symmetric Planetary-Scale Flow

The eastern Pacific ITCZ turns out to be an unstable environment where many tropical cyclones are generated (Gray, 1979). One case of the ITCZ breakdown in the eastern Pacific is observed in July of 1988 (Ferreira and Schubert, 1997), based on geostationary operational environmental satellites (GOES) infrared (IR) images. In that case, the ITCZ was first seen as an elongated zonal band of cloudiness off the equator in the eastern Pacific. After two days, the ITCZ started undulating and breaking down into several tropical cyclones, which moved into high latitudes, followed by the reforming of the ITCZ cloud band in its original location. The atmospheric flows over the eastern Pacific are organized into a hierarchical structure across multiple spatiotemporal scales. Such hierarchical structure of convective and dynamical fields is a suitable scenario to use multi-scale models (Majda, 2007).

After the ITCZ breakdown, the resulting tropical cyclones are typically accompanied by upward motion and cloud clusters over several hundred kilometers (Mapes and Houze Jr, 1993). Meanwhile, the large-scale meridional circulation including Pacific easterly waves over the eastern Pacific has zonal extent of several thousand kilometers (Serra et al., 2008). On the other hand, the M-ITCZ equations describe such multi-scale features across two zonal spatial scales (planetary-scale $L_p = 5000$ km, mesoscale $L_m = 500$ km), which match well with the typical length scale of small-scale tropical cyclones and the large-scale meridional circulation, justifying the appropriateness of using the M-ITCZ equations to model the ITCZ breakdown

and its upscale impact on the planetary-scale circulation. Over the eastern Pacific, the large-scale meridional circulation has zonal variation due to boundary conditions such as sea surface temperature gradient and atmospheric disturbance such as easterly waves (Toma and Webster, 2010a,b). In order to model ITCZ breakdown in a simple scenario, the solutions of the M-ITCZ equations are assumed to be zonally symmetric on the planetary scale so that all derivatives about planetary-scale X vanish. Then the M-ITCZ equations in Eqs.3.1a-3.1g are reduced to the MEWTG equations in Eqs.3.4a-3.4d, where S^θ stands for thermal forcing such as diabatic heating in cloud clusters and radiative cooling effects.

For simplicity, local periodicity is imposed in mesoscale zonal direction and rigid-lid boundary conditions are imposed in meridional and vertical boundaries. By taking both zonal and meridional averaging and enforcing the boundary conditions in these two directions, Eq.3.4d reduces to $\langle \bar{w} \rangle_z = \langle \bar{S}^\theta \rangle_z = 0$, which means conservation of volume at each level. Since vertical velocity vanishes in the rigid-lid vertical boundaries, an implicit constraint for diabatic heating can be derived as follows,

$$\langle \bar{S}^\theta \rangle = 0, \quad (3.12)$$

where the notation bar and angle bracket stand for mesoscale zonal and meridional averaging as defined in Eqs.3.2-3.3.

The momentum dissipation for cumulus drag in the convective region is described by a linear damping law in Eqs.3.4a-3.4b. The coefficient d in units of $1/day$ sets the time scale for momentum dissipation on the mesoscale. According to the observation, momentum damping time scale at the surface of the Pacific ocean could be as strong as 1 day (Deser, 1993) while that at the upper troposphere is much longer. In general, the momentum damping of large-scale circulation occurs on a time scale of $\mathcal{O}(1 - 10)$ days, and also depends on the vertical wavelength of the wind profile (Romps, 2014). For simplicity, the momentum damping coefficient d is assumed to be a linear function of height $d(z)$, which has 1 day damping time

Name	Symbol	Length of Domain	Grid Number	Resolution
planetary-scale zonal	X	$L_p = 4 \times 10^3 km$	41	$\Delta X = 0.976 \times 10^3 km$
mesoscale zonal	x	$L_m = 0.976 \times 10^3 km$	81	$\Delta x = 12.045 km$
meridional	y	$L_y = 3 \times 10^3 km$	241	$\Delta y = 12.5 km$
vertical	z	$L_z = 15.7 km$	127	$\Delta z = 0.125 km$
temporal	t	$T = 4 days$	1200	$\Delta t = 4.8 min$

Table 3.1: The multi-scale domain with nested grids and grid numbers and time steps in the numerical simulations.

scale at surface and 10 days damping time scale at top of the troposphere.

Eqs.3.4a-3.4d are solved numerically by using a new method based on the Helmholtz decomposition and a second-order corner transport upwind scheme to effectively resolve the non-linear eddies. The details of the numerical scheme are summarized in the Appendix.

For the numerical simulations in Sec.3.4, the banded region from $15^\circ S$ to $15^\circ N$ circling the globe in the tropics is chosen as the full domain with zonal extent $0 \leq X \leq 40 \times 10^3 km$. As summarized in the Appendix, the coarse grid number N_{xp} is fixed and the zonal extent of each mesoscale box is $0.976 \times 10^3 km$, which is in the same order as the mesoscale length, $L_m = 500 km$. In the numerical scheme with nested grids, each coarse cell corresponds to a single mesoscale box with horizontal extent $0 \leq x \leq 0.976 \times 10^3 km$, $-1.5 \times 10^3 km \leq y \leq 1.5 \times 10^3 km$ and the vertical extent $0 \leq z \leq 15.7 km$. Besides, the planetary-scale domain and all mesoscale domains share the same vertical grids. The details about grid numbers and grid spacing in the numerical simulations are summarized in Table.3.1 and Sec.3.4. Here the planetary-scale variations are ignored and a relatively high spatial resolution for a single mesoscale domain is chosen to resolve mesoscale eddies in the MEWTG equations. A short time step is used for numerical accuracy and stability.

3.3.1 Deep and shallow heating profile

The dominating meridional circulation over the eastern Pacific consists of a strong overturning circulation cell around the equator and a weak one at high latitudes of the Northern Hemisphere. The strong overturning cell around the equator expands over the whole tropo-

sphere with southerly winds in its lower branch near the surface and northerly winds in its upper branch near the tropopause, which is referred to deep meridional circulation. Such deep overturning cell can be explained as the response of the large-scale circulation to deep convective heating in the ITCZ (Schneider and Lindzen, 1977; Wu, 2003). The deep convective heating in the ITCZ comes from latent heat release during precipitation associated with cloudiness such as deep convective cumulonimbus clouds, which tends to warm and dry the entire troposphere and produce amounts of rainfall.

Here the deep convective heating S^θ for a single cloud cluster in dimensionless units is prescribed as follows,

$$S^\theta = cH(x, y)G(z)\phi(t), \quad (3.13)$$

where heating magnitude coefficient $c = 2$ corresponds to the maximum heating rate $66K \cdot day^{-1}$. $H(x, y)$ is the horizontal envelope function shown in Fig.3.1a. The vertical heating profile is the first baroclinic mode $G(z) = \sin(z)$, as shown in Fig.3.1c. $\phi(t)$ is the time dependent heating magnitude, which linearly increases from 0 to 1 at day 1 and remains constant afterwards. Since the typical life time of cloud clusters is between several hours to several days (Mapes and Houze Jr, 1993), here 1 day in duration is set as initialization time when the deep convective heating increases from zero to its maximum magnitude. The prescribed diabatic heating S^θ is used to mimic convective heating associated with a single deep cloud cluster in the ITCZ. As shown in Fig.3.1a, the deep heating is located at the latitudes between $y = 0km$ and $y = 1.2 \times 10^3 km$ of the Northern Hemisphere and zonally localized in the center of the mesoscale domain. Outside of the convective heating region such as the Southern Hemisphere and high latitudes of the Northern Hemisphere, there is horizontally uniform cooling in much weaker magnitude, which is used to mimic radiative cooling in the troposphere.

The shallow meridional circulation is also significant in the meridional circulation over the eastern Pacific, besides the deep meridional circulation. The existence of shallow meridional

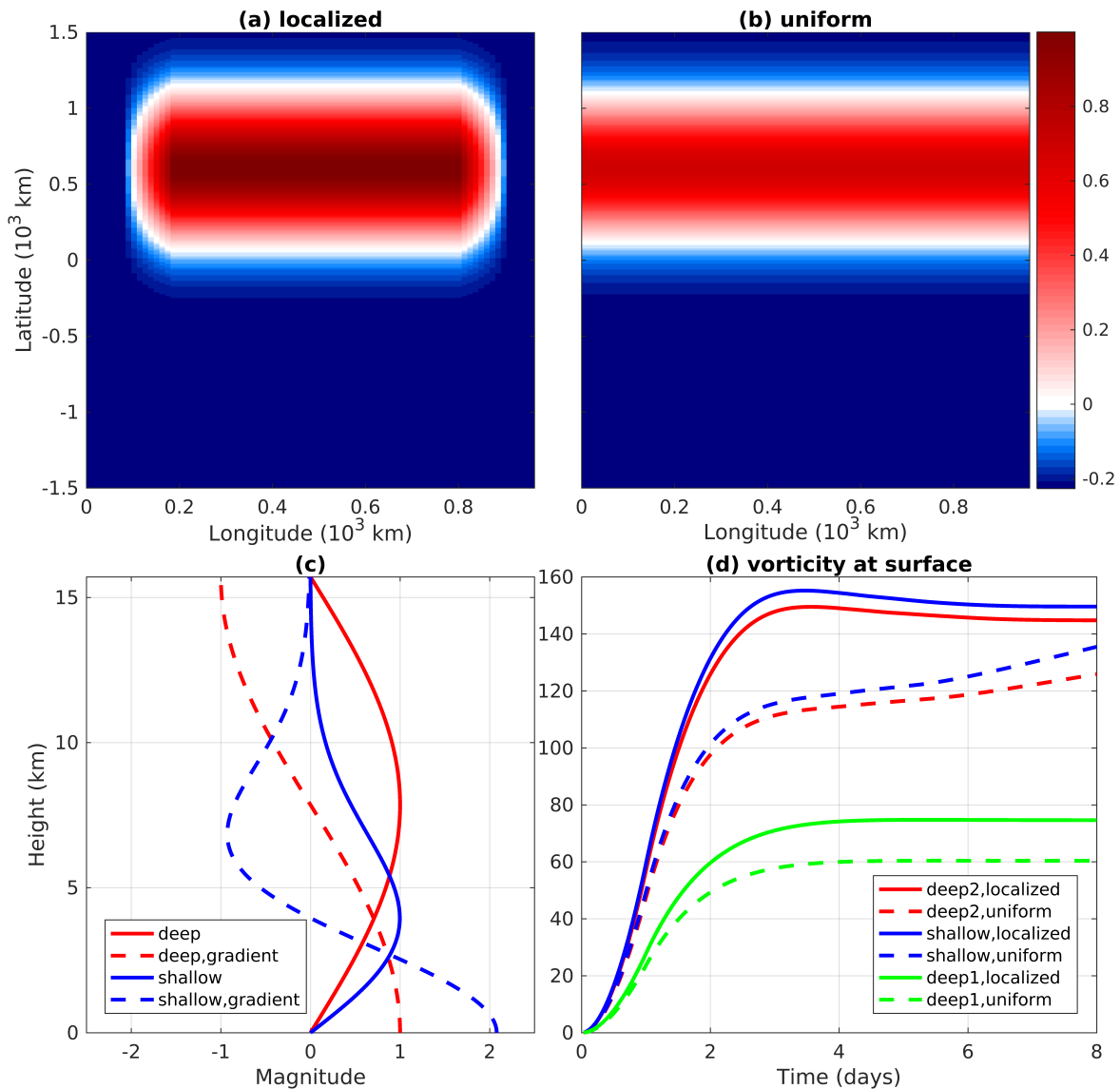


Figure 3.1: Horizontal and vertical properties of heating profiles in all scenarios. (a) horizontal profile of zonally localized heating. (b) horizontal profile of zonally uniform heating. (c) vertical profiles of heating and its gradient. (d) time series of the vorticity at the surface in the Frobenius norm. The value is in dimensionless units.

circulation is beyond the classic theory of the Hadley circulation over the eastern Pacific, where deep convection typically dominates and drives meridional circulation with deep vertical extent. By analyzing observational data from upper-air soundings, aircraft dropsondes and wind profilers (Zhang et al., 2004), the shallow meridional circulation is identified as a circulation cell with its northerly cross-equatorial return flow above the atmospheric boundary layer from the ITCZ into the Southern Hemisphere. The causes and dynamics of the shallow meridional circulation are explained by a large-scale sea-breeze circulation theory and an idealized Hadley circulation simulation driven by moist convection in a tropical channel (Nolan et al., 2007).

As suggested by many theoretical studies (Schneider and Lindzen, 1977; Gill, 1980; Wu, 2003), the large-scale tropical circulation can be regarded as the response to convective heating associated with tropical precipitation. Correspondingly, the diabatic heating associated with the shallow meridional circulation has shallower vertical extent than that of deep convective heating. Here the shallow congestus heating S^θ in dimensionless units is prescribed in the same general expression in Eq.3.13, and heating magnitude coefficient c_s is 1 (maximum heating rate $33K \cdot day^{-1}$). The horizontal profile $H(x, y)$ and time series $\phi(t)$ are the same as Eq.3.13. The vertical profile of shallow congestus heating $G(z)$ is prescribed in Fig.3.1c and reaches its maximum value around the height $z = 4$ km, while that of deep convective heating reaches maximum value at the height $z = 7.8$ km. According to the conservation of volume in Eq.3.4d, horizontal wind divergence is proportional to the gradient of $G(z)$ as shown in Fig.3.1c. Firstly, the magnitude of wind convergence at the surface in the shallow congestus heating case is more than twice as much as that in the deep convective heating case. Secondly, compared with the deep convective heating case, the maximum wind divergence in the shallow heating case is near the height $z = 6$ km, which qualitatively matches well with the returning flows above the atmospheric boundary layer in the shallow meridional circulation (Zhang et al., 2004).

In the following discussion, two deep heating cases are considered. The strong deep

heating case (*deep2*: magnitude coefficient $c = 2$) indicates the significant baroclinic aspects of ITCZ breakdown. The relatively weak deep heating case (*deep1*: magnitude coefficient $c = 1$) in the same maximum heating magnitude as the shallow heating is used for comparison with the shallow heating case. According to Fig.3.1d, the spin up time for all the scenarios is around 3 days, here the numerical solutions at day 4 are mainly chosen for discussion.

3.3.2 Formation and undulation of a positive vorticity strip

In the ITCZ, convective activities occur with large amounts of rainfall, which release latent heat and lift air parcels to higher levels. Due to the conservation of mass, such upward motion of air leads to wind convergence (divergence) in the lower (upper) troposphere. Under the Coriolis force, the southerly (northerly) winds to the south (north) of the ITCZ in the Northern Hemisphere deflect to the right side and generate westerly (easterly) winds, resulting in meridional shear of zonal winds in the lower troposphere. Such meridional shear of zonal winds is characterized by a positive vorticity strip in the Northern Hemisphere. Therefore, the ITCZ breakdown can be visualized through the vorticity strip dynamics from its formation and undulation in the early stage to its breakdown into several vortices later. In this section, such a scenario involving a positive vorticity strip is captured.

Fig.3.2a-c shows the horizontal profile of velocity and vorticity fields at the surface during the first 4 days in the *deep2* heating case. At day 1 in Fig.3.2a when the magnitude of diabatic heating reaches its maximum, a positive low-level vorticity strip develops on the poleward side of the diabatic heating region. It is centered at the latitude $y = 750\text{km}$. As explained above, such a positive vorticity strip with meridional shear of zonal winds is related to wind convergence in the low troposphere and meridional wind deflection due to the Coriolis force. Meanwhile, the positive vorticity has nearly zonally uniform strength along all longitudes of the diabatic heating region. At the lower latitudes of the Northern Hemisphere, southerly winds deflect to the right side due to the Coriolis force and generate westerly wind anomalies.

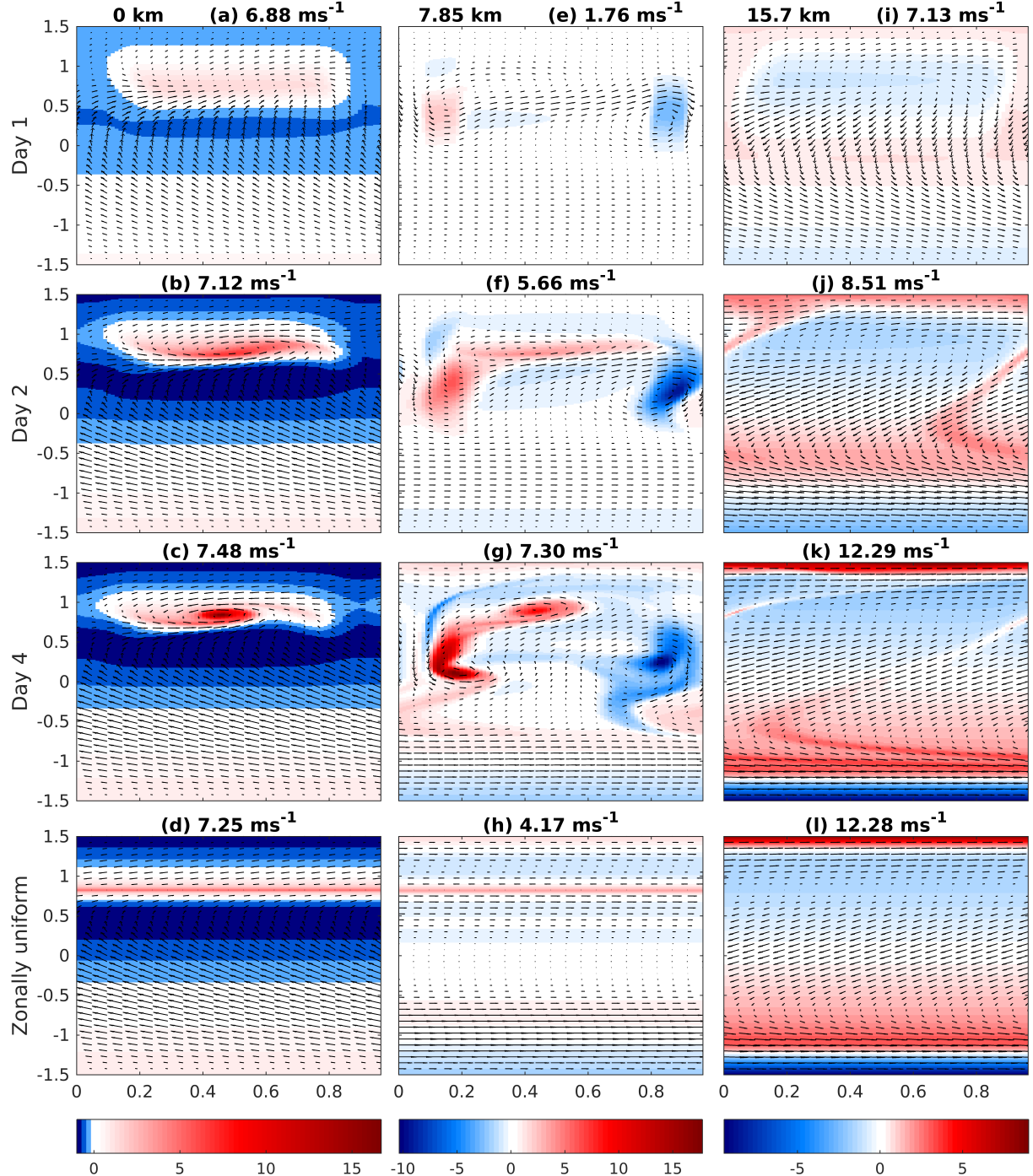


Figure 3.2: Horizontal profiles of velocity (arrow) and vorticity $\omega = v_x - u_y$ (color) in the longitude (horizontal axis, 10^3 km) and latitude (vertical axis, 10^3 km) diagram in the deep2 heating case. The columns from left to right are for different heights from 0 km to 7.85 km to 15.7 km. The first three rows are for different days from Day 1 to Day 2 to Day 4. The last row is for the zonally uniform heating case. The panels in each column share the same color bar at the bottom. The maximum velocity magnitude is shown in the title of each panel and vorticity has units of day^{-1} .

Stronger westerly winds are generated as the Coriolis coefficient increases on the equatorial β -plane. Therefore, such positive meridional shear of zonal velocity induces negative vorticity anomalies at low latitudes of the Northern Hemisphere. Besides, winds in the Southern Hemisphere blow from the southeast, which has similar wind direction and magnitude as the trade winds (Wyrtki and Meyers, 1976). At day 2 in Fig.3.2b, the magnitude of the positive vorticity strip in the Northern Hemisphere gets strengthened. The zonally elongated vorticity strip starts to undulate with its eastern end moving northward and western end moving southward, which is reminiscent of the undulation process of cloudiness during the ITCZ breakdown. Besides, negative vorticity anomalies at low latitudes of the Northern Hemisphere have stronger magnitude and broader zonal extent. The horizontal flow field has increasing maximum wind magnitude but its horizontal spatial pattern is similar to Fig.3.2a. At day 4 in Fig.3.2c, the magnitude of the positive vorticity strip continuously increases and its maximum value reaches about $16\text{day}^{-1} \approx 1.85 \times 10^{-4}\text{s}^{-1}$, which is comparable with the observational data as well as numerical simulations (Ferreira and Schubert, 1997). As both ends of the positive vorticity strip undulate in weak magnitude, a strong positive vortex forms in the middle, resembling the formation of tropical cyclones. In addition, such a positive vorticity strip is surrounded by negative vorticity anomalies in both its northern and southern sides. Although the maximum wind strength still increases, the spatial pattern of horizontal flow field is quite similar to that in the early stage.

One interesting phenomenon with regard to the numerical solutions in Fig.3.2a-c is that the zonally elongated positive vorticity strip is located in the northern side of the diabatic heating region. The underlying mechanism can be explained as follows. First, as far as the mesoscale zonal mean flow is concerned, the conservation of volume is guaranteed through the divergence-free meridional circulation in Eq.3.4d,

$$\frac{\partial \bar{v}}{\partial y} + \frac{\partial \bar{w}}{\partial z} = 0, \quad (3.14)$$

Considering the fact that there are a strong circulation cell around the equator and a weak circulation cell in the Northern Hemisphere, the southerly winds in the lower branch of the strong circulation cell are prevailing in the Southern Hemisphere and low latitudes of the Northern Hemisphere, and vanishing at the latitude where upward and downward motion to its south exactly cancel by each other. Since downward motion to the south of the diabatic heating region occurs in much broader area than that to the north, the latitude where meridional winds vanish is located in the northern side of the diabatic heating region, generating negative meridional shear of zonal winds (positive vorticity anomalies $\omega = v_x - u_y$). Secondly, PV ($Q = \omega + y$) is advected by three-dimensional flow and forced by several terms involving gradient of diabatic heating as well as damping in Eq.3.7. Since meridional winds converge in the Northern Hemisphere, the vorticity ω decreases (increases) due to the increasing (decreasing) mean PV y to the south (north), resulting in poleward displacement of positive vorticity anomalies.

The other interesting phenomenon arising in the numerical solutions in Fig.3.2a-c is the undulation of the positive vorticity strip and the resulting strong positive vortex in its middle, which describes a similar scenario for the ITCZ breakdown. According to the conservation of volume in Eq.3.4d, horizontal wind convergence is induced by the accelerating upward motion in the lower troposphere in the heating region. Due to the Coriolis force, the southerly (northerly) winds to the south (north) of the ITCZ deflect to the right side, which then become southwesterly (northeasterly) winds. The overall flow field near the diabatic heating region tends to rotate counterclockwise, and advect the eastern (western) end of the positive vorticity strip poleward (equatorward) as shown in Fig.3.2b-c. Such undulation of the positive vorticity strip in the rotational flows due to the zonal asymmetry and the Coriolis force is related with the ‘vortex roll-up’ mechanism, which is one of the main mechanisms used to explain the eastern Pacific ITCZ breakdown (Hack et al., 1989; Ferreira and Schubert, 1997; Wang and Magnusdottir, 2005).

The vertical structure of the deep heating in Fig.3.1c reaches maximum value in the

middle troposphere at height $z = 7.48$ km. Fig.3.2e-g shows the horizontal profile of velocity and vorticity field in the middle troposphere during the first 4 days in the *deep2* heating case. A positive vorticity strip is generated in the northern side of the diabatic heating region, gets strengthened at day 2 in Fig.3.2f, undulates and breaks down into a strong vortex in the middle at day 4 in Fig.3.2g. Besides, a pair of vortex dipoles form at low latitudes of the Northern Hemisphere with negative (positive) vorticity anomalies to the east (west). Such vortex dipoles can be explained through the PV equation in Eq.3.7, where PV anomalies are forced by the vorticity tilting term $-v_z S_x^\theta$. The low latitudes of the Northern Hemisphere are dominated by southerly winds in the lower troposphere and northerly winds in the upper troposphere, indicating negative vertical shear of meridional velocity. On the other hand, zonal gradient of diabatic heating is negative (positive) to its eastern (western) end. Therefore, the product term $-v_z S_x^\theta$ has a negative (positive) value to the eastern (western) end of the diabatic heating region, resulting in a pair of vortex dipoles with negative (positive) anomalies to the east (west) of the heating maximum. As far as the velocity field is concerned, the strong positive vortex in the northern side of the diabatic heating and the western vortex dipole come along with cyclonic flows, while the eastern vortex dipole comes along with anticyclonic flows. In the Southern Hemisphere, the prevailing westerly winds in gradually increasing wind strength, and the maximum westerly wind occurs at the latitude $y = -10^3$ km.

Horizontal flows at the top diverge over the deep heating region and move northward and southward afterwards. Fig.3.2i-k shows the horizontal profile of velocity and vorticity fields near the top of the troposphere during the first 4 days in the *deep2* heating case. As a counterpart of the positive vorticity strip at surface, a negative vorticity strip is generated in the Northern Hemisphere. Since PV is advected by the three-dimensional flow in Eq.3.7, this negative vorticity strip has broader meridional extent and weaker magnitude due to the advection effects of meridionally divergent winds. As far as the velocity field is concerned, the strong meridional shear of westerly winds at high latitudes of the Southern Hemisphere

results in strong vorticity anomalies near the southern boundary. Since the momentum damping strength at the top of the domain is only 1/10 of that at surface, the maximum wind magnitude at the top is much stronger than those at lower levels.

Compared with the deep convective heating in Fig.3.1c, shallow congestus heating has stronger vertical gradient near the surface when the maximum heating magnitudes are the same. Such large vertical gradient of upward motion also means stronger horizontal wind convergence at the surface, which can accelerate the ITCZ breakdown as shown in the other study (Wang and Magnusdottir, 2005).

Fig.3.3a-c shows the horizontal profile of velocity and vorticity fields at the surface in the first 4 days in the shallow heating case. The velocity and vorticity fields share many similar features with those in the deep convective heating case in Fig.3.2a-c, including the formation and undulation of a positive vorticity strip. In spite of the similarity, a direct comparison is not appropriate since the maximum shallow congestus heating is $33Kday^{-1}$ while the maximum deep convective heating is $66Kday^{-1}$. Fig.3.3d-f shows the horizontal profile of velocity and vorticity fields at the surface in the *deep1* heating case with maximum heating magnitude $33Kday^{-1}$. In contrast, there are no significant positive vorticity anomalies in the middle of the positive strip after 4 days. As for the horizontal wind field, both cases with deep/shallow heating share similar spatial patterns with cyclonic flows in the Northern Hemisphere, southerly winds around the equator and southeasterly winds in the whole Southern Hemisphere, but the maximum wind strength in the *deep1* heating case in Fig.3.3d-f is about half that in the shallow heating case in Fig.3.3a-c. In fact, such stronger horizontal velocity and vorticity fields in the shallow heating case have been emphasized in a model for hot towers in the hurricane embryo (Majda et al., 2008) and the ITCZ breakdown in three-dimensional flows (Wang and Magnusdottir, 2005).

Different from the deep convective heating case, the velocity and vorticity fields in the shallow heating case are confined in the lower troposphere. Fig.3.3g-i shows the horizontal profile of velocity and vorticity field at height $z = 7.48$ km in the shallow heating case.

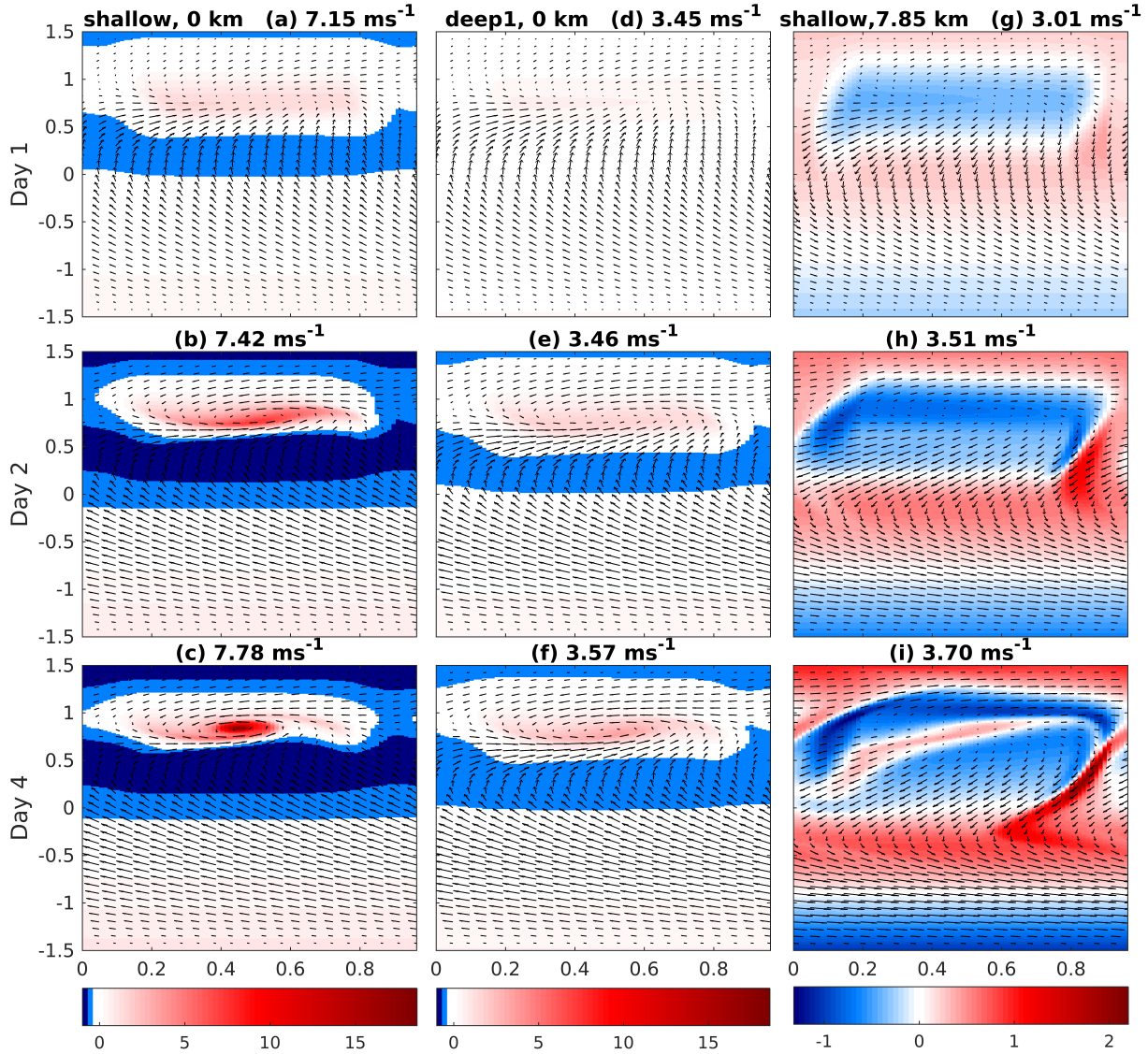


Figure 3.3: Horizontal profiles of velocity (arrow) and vorticity $\omega = v_x - u_y$ (color) in the longitude (horizontal axis, 10^3 km) and latitude (vertical axis, 10^3 km) diagram in the shallow heating case. The left column is for the height 0 km and the right column is for 7.85 km. The middle column is for *deep1* heating case at the height 0 km. The first three rows are for different days from Day 1 to Day 2 to Day 4. The panels in each column share the same color bar at the bottom. The maximum velocity magnitude is shown in the title of each panel and vorticity has units of day^{-1} .

Again, the overall spatial pattern of the velocity and vorticity fields is quite similar to that in the deep convective heating case with doubled magnitude in Fig.3.2i-k. Over the diabatic heating region in the Northern Hemisphere, divergent winds prevail and negative vorticity anomalies have broader meridional extent. The whole Southern Hemisphere is dominated by zonally uniform westerly winds with the maximum wind magnitude at $y = 10^3$ km, resulting in positive meridional shear of zonal winds (negative vorticity) near the southern boundary.

3.3.3 Vertical stretching of wind and vorticity fields

Deep clouds such as cumulonimbus have vertical extent throughout the whole troposphere, warm and dry the entire troposphere, contributing the majority of tropical rainfall (Khouider and Majda, 2008b). During convective periods associated with deep clouds in the ITCZ, warm and moist air parcels have enough buoyancy to get lifted up from the atmospheric boundary layer to the upper troposphere. Besides, the upward motion in the ITCZ has significant wind strength in the free troposphere, and it serves to transport energy and moisture from the lower troposphere to the upper troposphere. In contrast, shallow meridional circulation is characterized by a northerly return flow just above the atmospheric boundary layer (Zhang et al., 2004). In the northern branch of the overturning circulation cell, the upward motion over the eastern Pacific ITCZ is driven by shallow congestus heating, which is confined in the lower troposphere. On the other hand, the MEWTG equations in Eqs.3.4a-3.4d are fully nonlinear with the three-dimensional advection effects. Considering that vertical velocity is directly balanced by diabatic heating in Eq.3.4c, persistent upward motion exists in the diabatic heating regions, advecting both horizontal velocity and vorticity field upward and resulting in the vertical stretching of these fields.

Fig.3.4a-c shows the vertical profile of horizontal velocity and vorticity fields along the latitude $y = 0.8 \times 10^3$ km at day 4 in the *deep2* heating case. As shown in Fig.3.4c, a positive vorticity disturbance is located in the middle longitude of the mesoscale domain

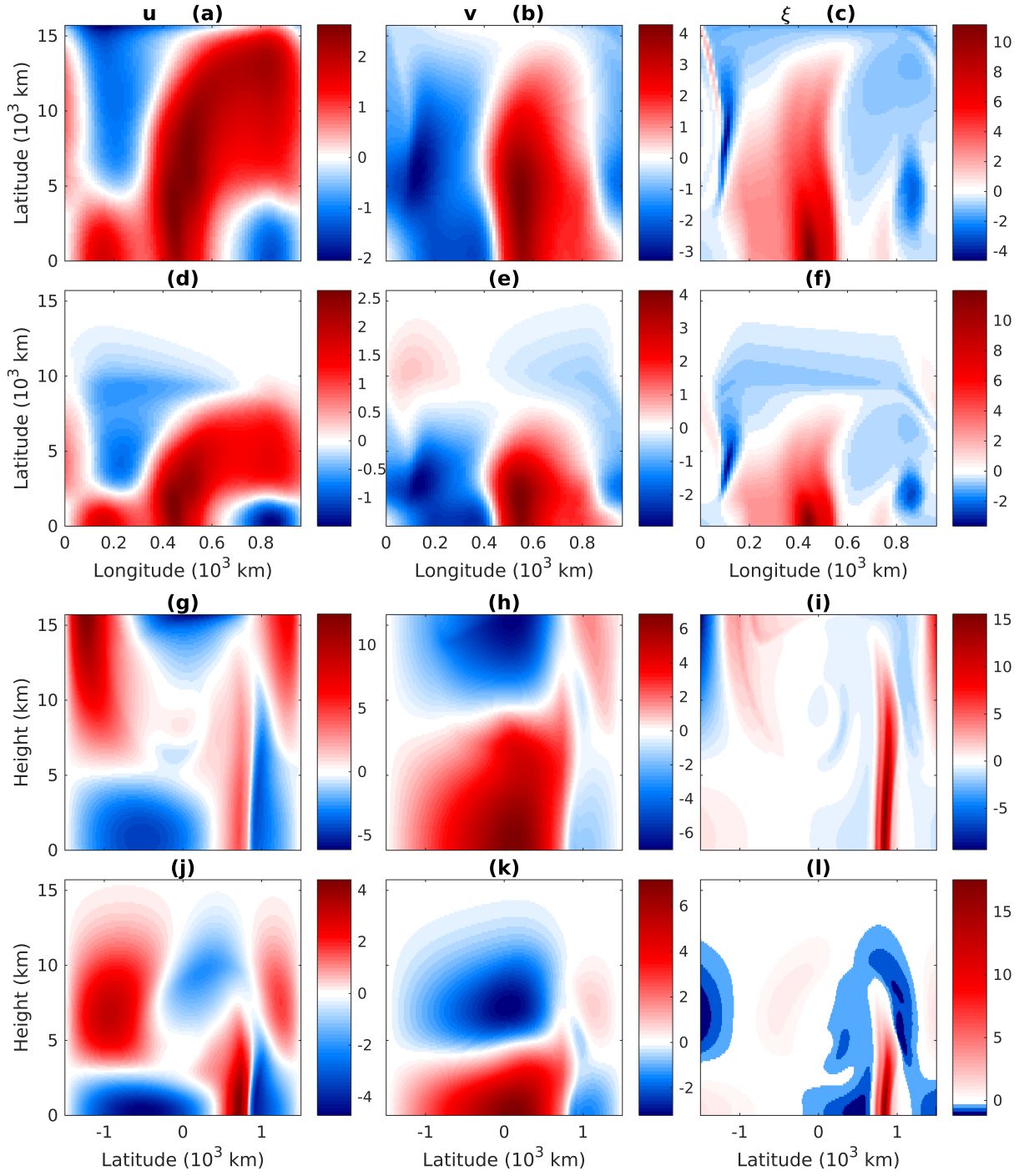


Figure 3.4: Vertical profiles of zonal velocity, meridional velocity and vorticity at Day 4. The columns from left to right are for zonal velocity, meridional velocity and vorticity. The first row (a-c) shows solutions along the latitude 0.8×10^3 km in the *deep2* heating case. The third row (g-i) shows solutions along the longitude 0.43×10^3 km in the *deep2* heating case. The second and fourth rows are the same as the first and third rows but for shallow heating case. The dimensional units of horizontal velocity and vorticity are $m s^{-1}$ and day^{-1} respectively.

with its maximum magnitude at the surface. Due to persistent upward motion in the diabatic heating region, the positive vorticity, which characterizes cyclonic flows following the ITCZ breakdown, extends to the upper troposphere. As far as the horizontal flow field in Fig.3.4a-b is concerned, the cyclonic flows associated with the positive vortex also stretch vertically over the whole troposphere and their vertical structure becomes dominated by the barotropic mode. Fig.3.4d-f shows the same fields in the shallow heating case. Both velocity and vorticity fields are confined to the much shallower levels compared with those in the deep heating case. Since the positive vorticity anomalies are accompanied by cyclonic flows, southerly winds to the east of the positive vortex and northerly winds to the west can be found in Fig.3.4e. Besides, the positive vorticity anomalies in the middle are surrounded by weak negative vorticity anomalies to both the east and west as well as the top.

Along with the vertical stretching of positive vorticity anomalies, winds diverge in the upper levels and go along the upper branches of the overturning circulation cells. Fig.3.4g-i shows the vertical profile of horizontal velocity and vorticity field along the longitude $x = 0.43 \times 10^3 km$ at day 4 in the *deep2* heating case. As indicated by Fig.3.4i, positive vorticity anomalies have very narrow meridional extent but deep vertical extent, which are accompanied by horizontal cyclonic flows, including westerly winds to the south of the positive vortex and easterly winds to the north as shown in Fig.3.4g. A strong circulation cell forms around the equator and a weak one forms at high latitudes of the Northern Hemisphere, whose upper and lower branches of meridional winds are shown in Fig.3.4h. Fig.3.4j-l shows the same fields in the shallow heating case. The overall spatial pattern of velocity and vorticity fields is similar to those in deep convective heating case, except that the vertical extent is much shallower. As shown by Fig.3.4l, the positive vorticity vortex is located to the north of the diabatic heating region and surrounded by weak negative vorticity anomalies. The shallow congestus heating can also drive a strong overturning circulation cell around the equator and a weak circulation cell at high latitudes of the Northern Hemisphere. The corresponding lower and upper branches of these overturning circulation cells are shown in

Fig.3.4k. Due to the strong momentum dissipation in lower levels, the resulting maximum zonal winds in the shallow heating case are much weaker than those in the deep convective heating case.

3.3.4 Eddy flux divergence of zonal momentum and mean flow acceleration/deceleration

The M-ITCZ equations are a multi-scale model with two spatial zonal scales (planetary-scale $L_p = 5000$ km, mesoscale $L_m = 500$ km). This scale selection is a good approximation for the hierarchical structure of tropical convection across multiple spatiotemporal scales in the ITCZ (Majda and Klein, 2003; Majda, 2007). Eddy flux divergence of zonal momentum arising from the mesoscale dynamics forces the planetary-scale circulation, while the large-scale flow field provides the background mean flow for the mesoscale dynamics. Specifically, the planetary-scale zonal momentum equation is derived by taking mesoscale zonal averaging on Eq.3.4a as follows,

$$\frac{\partial \bar{u}}{\partial t} + \bar{v} \frac{\partial \bar{u}}{\partial y} + \bar{w} \frac{\partial \bar{u}}{\partial z} - y\bar{v} = -d\bar{u} - \frac{\partial}{\partial y} (\bar{v}'u') - \frac{\partial}{\partial z} (\bar{w}'u'), \quad (3.15)$$

where the notation bar is defined in Eq.3.2 and the prime denotes mesoscale fluctuations. Eq.3.15 describes zonal momentum dynamics on the planetary-scale, which can be used to model zonal jets associated with the meridional circulation over the eastern Pacific. In detail, the planetary-scale zonal velocity is advected by the two-dimensional planetary-scale meridional circulation (\bar{v}, \bar{w}) and forced by the Coriolis force and linear momentum damping. Besides, the eddy flux divergence of zonal momentum that involves mesoscale fluctuations appears on the right hand side of Eq.3.15 and represents upscale impact of mesoscale fluctuations on the planetary-scale circulation. In fact, the eddy flux divergence of zonal momentum is referred to convective momentum transport (CMT), which has been studied from different perspectives to highlight its significance such as stochastic models (Majda and Stechmann,

2008; Khouider et al., 2012) and dynamical models with cloud parameterization (Majda and Stechmann, 2009). This eddy flux divergence of zonal momentum in dimensionless units reads as follows,

$$F^U = -\frac{\partial}{\partial y} (\overline{v'u'}) - \frac{\partial}{\partial z} (\overline{w'u'}), \quad (3.16)$$

The eddy flux divergence of zonal momentum F^U in Eq.3.16 constitutes an upscale zonal momentum forcing on the planetary scale that can have a significant impact on the planetary-scale flow. Specifically, positive (negative) anomalies of eddy flux divergence of zonal momentum F^U represent eastward (westward) momentum forcing. Fig.3.5a-c shows eddy flux divergence of zonal momentum F^U in the latitude-height diagram at day 4 in the *deep2* heating case. Along the latitude where the positive vortex located (see Fig.3.4i), eastward momentum forcing is induced by eddy flux divergence of zonal momentum F^U with deep vertical extent, which is mainly contributed by the meridional component of F^U in Fig.3.5b. In addition, meridionally alternating eastward and westward momentum forcing exists at low latitudes and the middle troposphere of the Northern Hemisphere in Fig.3.5a, which is directly related to the vorticity dipoles as shown in Fig.3.2g. Lastly, the maximum magnitudes of both the meridional and vertical components of F^U are comparable to each other, providing significant contributions to the total eddy flux divergence of zonal momentum. Fig.3.5d-f shows the same fields in the shallow heating case. The most significant F^U anomalies are similar to those in the *deep2* heating case but confined in the lower troposphere. Besides the positive anomalies at high latitudes of the Northern Hemisphere, there are also significant negative anomalies to the south of the positive anomalies near the surface. At low latitudes of the Northern Hemisphere at height $z = 4$ km, the eddy flux divergence of zonal momentum has significant anomalies with eastward momentum forcing on top of westward momentum forcing in upward/equatorward tilt. The magnitudes of momentum forcing in the meridional and vertical components are comparable but their spatial patterns are quite different in this region. In order to compare the eddy flux divergence of zonal momentum, Fig.3.5g-i shows

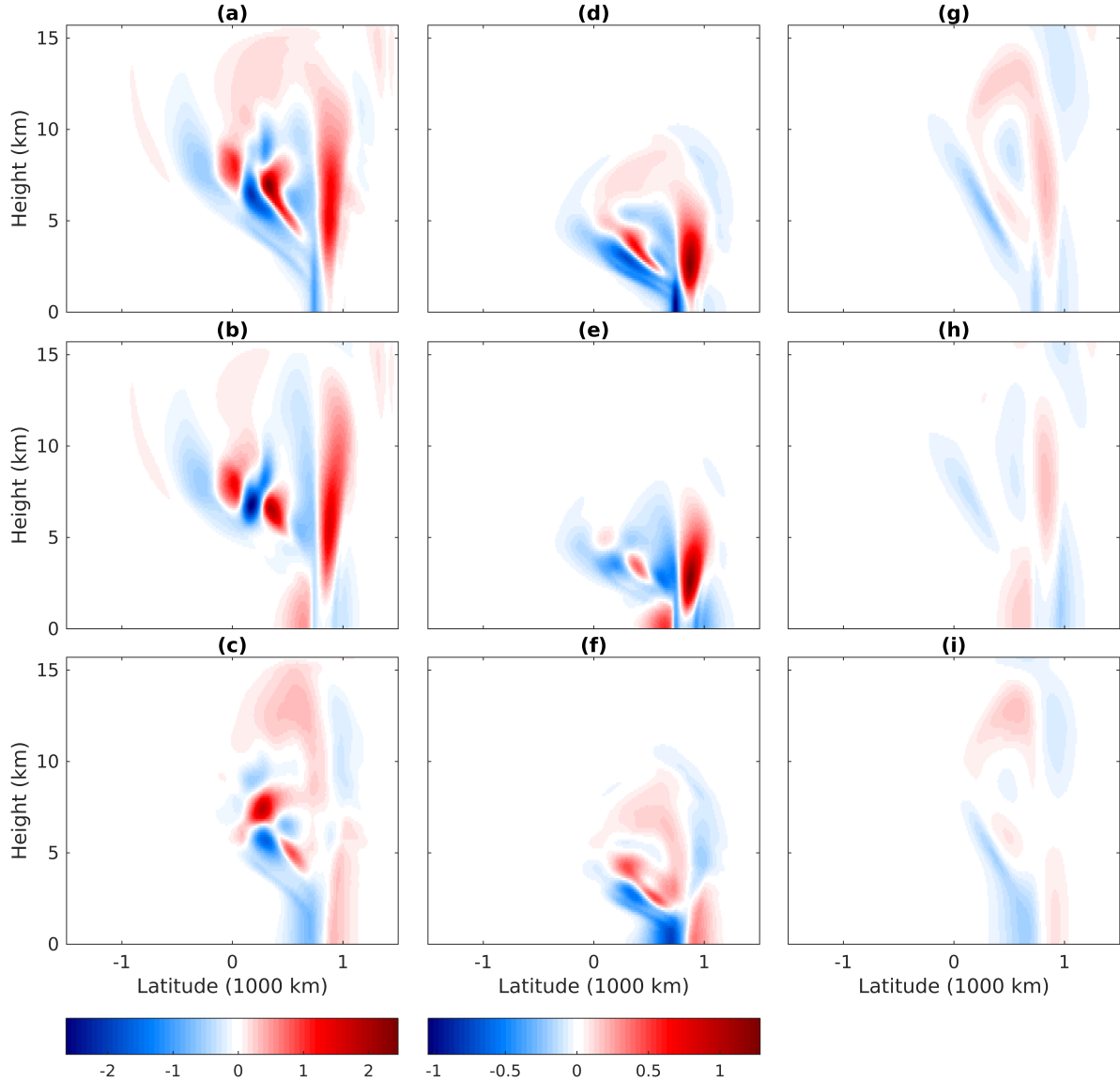


Figure 3.5: Eddy flux divergence of zonal momentum F^U in the latitude-height diagram at day 4. The columns from left to the rights are for *deep2*, shallow and *deep1* heating cases. The second column share the same color bar at the bottom with the third column. The three panels from top to bottom are for (a) F^U , (b) its meridional component $-\frac{\partial}{\partial y} (\bar{v}'\bar{u}')$ (c) its vertical component $-\frac{\partial}{\partial z} (\bar{w}'\bar{u}')$. The dimensional unit of F^U is $ms^{-1}day^{-1}$.

the same fields in the *deep1* heating case. The magnitudes of total eddy flux divergence of zonal momentum and its meridional and vertical components are much weaker than those in the shallow heating case in Fig.3.5d-f, highlighting the significant upscale impact in the shallow heating case.

As indicated by Eq.3.15, eddy flux divergence of zonal momentum arising from the mesoscale dynamics further forces the planetary-scale circulation and induces zonal jet anomalies. Its impact can be illustrated through the comparison between numerical solutions with and without the eddy momentum forcing F^U . Instead of utilizing the mesoscale zonally localized diabatic heating in Fig.3.1a, a mesoscale zonally uniform heating profile is prescribed in the same expression in Eq.3.13, but its horizontal envelope function $H(y)$ is replaced by the one in Fig.3.1b with the same zonal mean. The differences of mesoscale zonal mean of zonal velocity reflect the impact of eddy flux divergence of zonal momentum on the planetary-scale circulation. Fig.3.6a-b shows mean zonal velocity \bar{u} in the latitude-height diagram at day 4 in the zonally localized and uniform *deep2* heating case. The mean zonal velocity fields in both these two cases share several common features, which are consistent with a strong overturning circulation cell around the equator and a weak circulation cell in the Northern Hemisphere. In particular, the horizontal profiles of velocity and vorticity fields at different levels in the zonally uniform heating case are shown in panels (d,h,l) of Fig.3.2. Although the maximum magnitude of zonal wind anomalies due to eddy flux divergence of zonal momentum in Fig.3.6c is about $\frac{1}{10}$ of that in Fig.3.6a-b, most of these zonal wind anomalies are localized in places where the mean zonal wind is relatively weak, resulting in significant rectification of zonal jets. Particularly, there are westerly wind anomalies along the latitude of the positive vortex (see Fig.3.4i), which matches well with the eastward momentum forcing in the same region in Fig.3.5a. Due to the advection effect of the mean meridional circulation (\bar{v}, \bar{w}) , such eastward zonal wind anomalies extend to the upper troposphere, the equator and the Southern Hemisphere. Besides, meridionally alternate zonal wind anomalies in the middle troposphere and low latitudes of the Northern

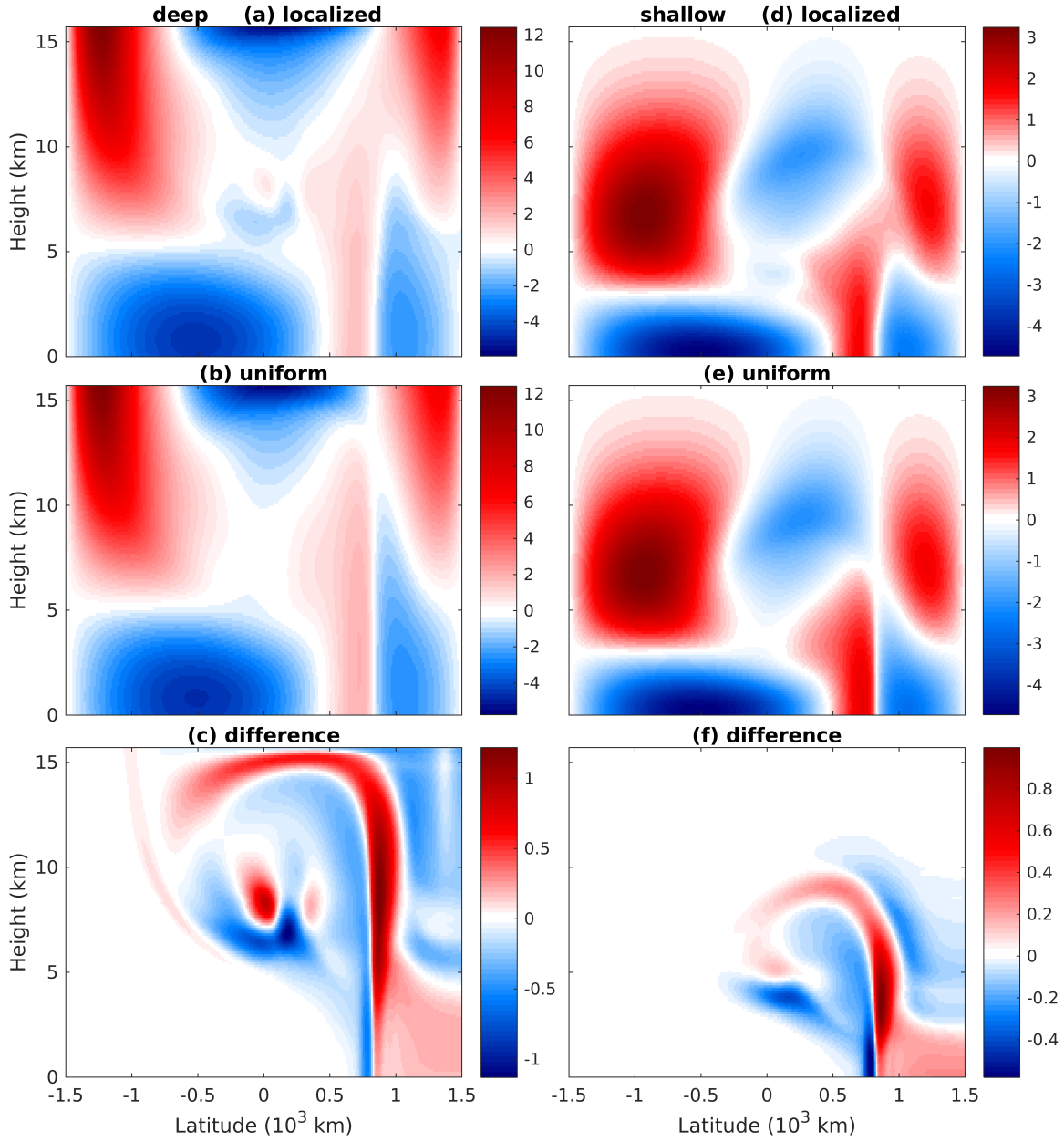


Figure 3.6: Mean zonal velocity \bar{u} in the latitude-height diagram at day 4. The left panels from top to bottom show the solutions for (a) zonally localized heating, (b) zonally uniform heating, (c) their difference (a)-(b) in the *deep2* heating case. The right panels (d-f) show the same fields but for the shallow heating case. The dimensional unit of mean zonal velocity is $m s^{-1}$.

Hemisphere match well with the spatial pattern of the eddy flux divergence of zonal momentum in Fig.3.5a. Fig.3.6d-f shows the same fields in the shallow heating case. The overall spatial patterns of mean zonal velocity and zonal velocity anomalies are mostly confined in the shallower levels. The mean zonal velocity in Fig.3.6d shares many common features as that in the mesoscale zonally uniform heating case in Fig.3.6e. The spatial pattern of mean zonal wind anomalies in Fig.3.6f is consistent with that of eddy flux divergence of zonal momentum in Fig.3.5d. There are westerly wind anomalies along the latitude $y = 800$ km where the positive vortex is located (see Fig.3.4l) and easterly wind anomalies to the south of the westerly wind anomalies in the lower troposphere. Zonal wind anomalies with westerlies on top of easterlies occur at low latitudes of the Northern Hemisphere.

The eddy flux divergence of zonal momentum in Eq.3.16 is a crucial quantity, because it not only significantly modifies the zonal momentum budget as momentum forcing, but also involves energy transfer across multiple spatial scales and induces acceleration/deceleration effects on the planetary-scale mean flow. Here the acceleration and deceleration of eddy flux divergence of zonal momentum is investigated through the kinetic energy of zonal winds in Eq.3.9 instead of the total kinetic energy in Eq.3.11. One essential reason is that only the mesoscale mean zonal velocity is coupled with the planetary-scale gravity waves in Eqs.3.6a-3.6f, while the mean meridional velocity is directly balanced by the diabatic heating through Eqs.3.6b-3.6c. The equation for kinetic energy of mean zonal velocity is reduced from Eq.3.9,

$$\frac{\partial K^u}{\partial t} + \frac{\partial}{\partial y} (\bar{v} K^u) + \frac{\partial}{\partial z} (\bar{w} K^u) = y \bar{v} \bar{u} - 2dK^u + F^u \bar{u}, \quad (3.17)$$

where $K^u = \frac{\bar{u}^2}{2}$ represents kinetic energy of planetary-scale zonal winds.

The eddy energy transfer term $F^u \bar{u}$ in Eq.3.17 is a product of eddy flux divergence of zonal momentum F^u and mean zonal velocity \bar{u} , which can be interpreted as acceleration/deceleration effects of F^u on the mean zonal winds. If the sign of the term $F^u \bar{u}$ is positive (negative), the kinetic energy of zonal winds tends to increase (decrease) and the

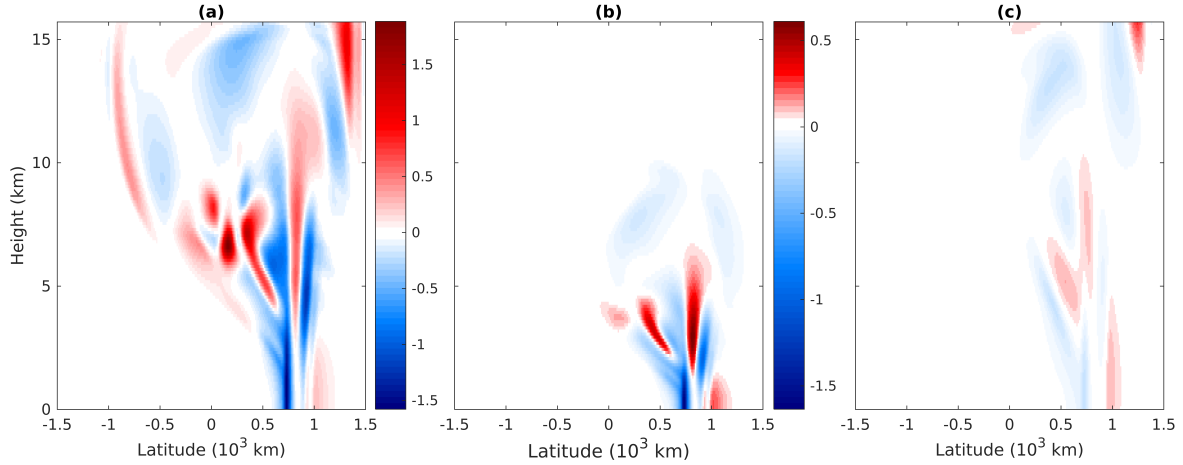


Figure 3.7: Acceleration and deceleration of mean zonal velocity due to eddy flux divergence of zonal momentum in the latitude-height diagram at day 4. The color indicates the value of the quantity $F^U \bar{u}$ with positive anomalies for acceleration effects and negative anomalies for deceleration effects. The panels from left to right are for the cases (a) *deep2*, (b) *shallow*, (c) *deep1*. The dimensional unit is $m^2 s^{-2} day^{-1}$

eddy energy transfer term $F^u \bar{u}$ induces acceleration (deceleration) effects. Besides, the magnitude of acceleration/deceleration effects of the eddy energy transfer $F^u \bar{u}$ depends on the magnitudes of both eddy flux divergence of zonal momentum F^u and mean zonal velocity \bar{u} . Fig.3.7a shows acceleration/deceleration effects of eddy flux divergence of zonal momentum at day 4 in the *deep2* heating case. Along the latitude where the positive vortex is located (see Fig.3.4i), the acceleration effects are induced by eastward momentum forcing F^u on the westerly mean flows \bar{u} . To both the northern and southern sides of that acceleration effects, the deceleration effects with narrow meridional extent is mostly significant in the lower troposphere, which decelerate the westerly (easterly) winds to the south (north) of the positive vortex. At low latitudes of the Northern Hemisphere, acceleration effects are also significant in the middle troposphere where mean zonal winds are weak in Fig.3.6b and modified mainly by eddy flux divergence of zonal momentum in Fig.3.5a. Fig.3.7b shows the acceleration/deceleration effects due to eddy flux divergence of zonal momentum in the shallow heating case. The most significant acceleration/deceleration effects are confined in the lower troposphere. Besides the acceleration effects at high latitudes, there are also decel-

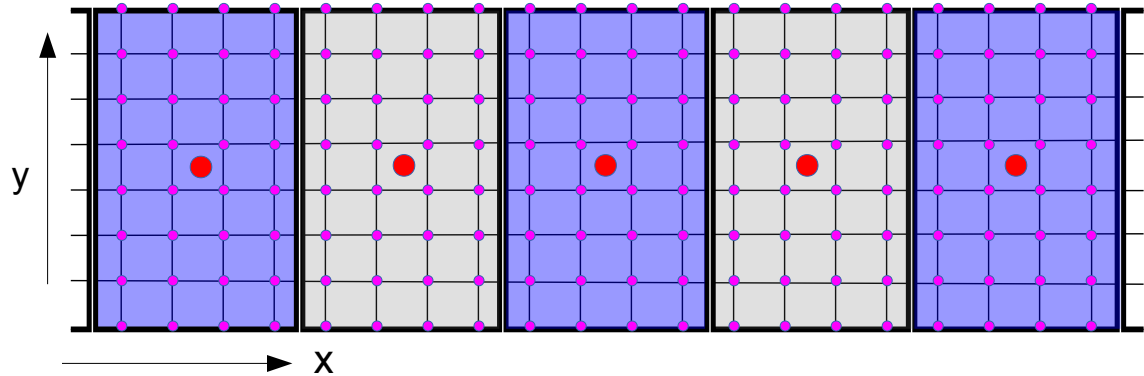


Figure 3.8: A schematic depiction of the multi-scale domain with nested grids. The large red dots are the coarse grids on the planetary scale. Each coarse grid corresponds to a single mesoscale domain characterized by a mesoscale box in thick lines. The fine grids in each mesoscale domain are shown by pink dots.

eration effects of westward (eastward) eddy flux divergence of zonal momentum on the mean westerly (eastward) winds to the south (north) of the latitude $y = 800$ km. Such lower-level deceleration effects in the diabatic heating region is typically seen in other studies about CMT (Majda and Stechmann, 2008, 2009). As a clear comparison, the eddy energy transfer $F^u \bar{u}$ in the *deep1* heating case in Fig.3.7c is much weaker than that in the shallow heating case in Fig.3.7b, highlighting the significant upscale impact of mesoscale fluctuations in the shallow congestus heating in terms of kinetic energy budget.

3.4 ITCZ Breakdown in Zonally Varying Planetary-Scale Flow

In this section, the M-ITCZ equations are utilized to simulate the ITCZ breakdown process over the eastern Pacific involving both the mesoscale and planetary-scale dynamics. In each mesoscale cell, periodic boundary conditions are imposed in the zonal direction and rigid-lid boundary conditions are imposed in the meridional and vertical directions. On the planetary scale, the zonal periodic boundary condition is naturally consistent with the belt

of tropics around the globe. In addition, the model setup and numerical details such as mesoscale and planetary-scale domain size, spatial and temporal resolutions are exactly the same as Sec.3.3. Lastly, the whole model is driven by diabatic heating on both mesoscale and planetary scale, and all physical variables are initialized from a background state of rest. The whole domain is discretized with nested coarse and fine grids as shown in Fig.3.8. In the numerical simulations, the MEWTG equations in Eqs.3.4a-3.4d are only valid on each mesoscale box with the zonally periodic boundary conditions. After taking zonal averaging of physical variables in each mesoscale domain, the planetary-scale physical quantities on each coarse grid is obtained and further involved in the planetary-scale gravity waves. More numerical details are summarized in Appendix.

In the ITCZ, the diabatic heating can be released during tropical precipitation in cloud clusters. In order to model the ITCZ over the eastern Pacific, diabatic heating S^θ is modulated by a planetary-scale zonally localized envelope. In general, such a two-scale diabatic heating S^θ in dimensionless units reads as follows,

$$S^\theta = cF(X)H(x, y)G(z)\phi(t), \quad (3.18)$$

where $F(X) = 1.2e^{-(X-4)^2}$ is the planetary-scale envelope function , $H(x, y)$ is the horizontal heating profile, which can be either mesoscale zonally localized heating in Fig.3.1a or uniform heating in Fig.3.1b. $G(z)$ is the vertical heating profile, which can have either deep or shallow vertical extent in Fig.3.1c. The magnitude parameter c and the time series $\phi(t)$ are the same to those in Sec.3.3.

3.4.1 Cross section of mean zonal velocity in the heating region

In order to assess the upscale impact of mesoscale fluctuations, two numerical simulations with either mesoscale zonally localized or uniform *deep2* heating are implemented for comparison. The difference of zonal velocity anomalies indicates the impact of eddy flux di-

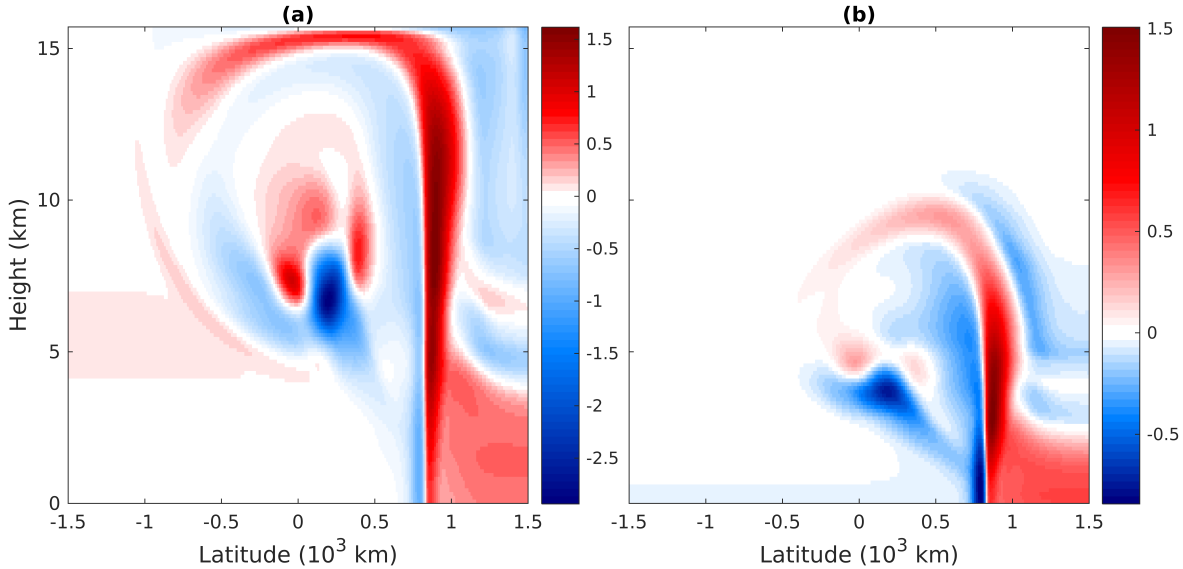


Figure 3.9: Cross section of mean zonal velocity anomalies in the center of heating region (longitude $X = 19.51 \times 10^3$ km) at day 4. The left panel is for *deep2* heating case and the right panel is for shallow heating case. The dimensional unit is ms^{-1} .

vergence of zonal momentum on the planetary-scale circulation. Fig.3.9a shows the cross section of planetary-scale zonal velocity anomalies in the center of the heating region at day 4 in the *deep2* heating case. The overall spatial pattern of zonal velocity anomalies here is quite similar to that in the planetary-scale zonal symmetric case in Fig.3.6c, including westerly wind anomalies in deep vertical extent near the latitude $y = 800$ km with its maximum strength in the middle troposphere and alternate mean zonal velocity anomalies in the middle troposphere near the equator. In contrast, Fig.3.9b shows the cross section of planetary-scale zonal velocity anomalies in the shallow heating case. Compared with the deep convective heating case in Fig.3.9a, the zonal velocity anomalies on the planetary scale are mostly confined in the lower troposphere, which is consistent with the limited vertical extent of the shallow congestus heating. Meanwhile, the spatial pattern of zonal velocity anomalies is quite similar to the planetary-scale zonally symmetric case in Fig.3.6f.

3.4.2 Mean zonal velocity in the lower, middle and upper tropospheres

The zonal velocity anomalies due to the eddy flux divergence of zonal momentum have different spatial patterns at different levels in Fig.3.9. Fig.3.10a-c shows planetary-scale zonal velocity anomalies at three different levels at day 4 in the *deep2* heating case. Firstly, the significant zonal velocity anomalies are confined in the longitudes between $X = 15 \times 10^3 km$ and $X = 25 \times 10^3 km$, which is the same as the zonal extent of the convective envelope in Eq.3.18. Secondly, the zonal velocity anomalies due to eddy flux divergence of zonal momentum have different spatial patterns at different levels. In the lower troposphere in Fig.3.10c, westerly wind anomalies are localized in the northern of the diabatic heating and weak easterly wind anomalies are to the south. In the middle troposphere in Fig.3.10b, the westerly wind anomalies at high latitudes of the Northern Hemisphere has stronger magnitude and broader zonal extent. Besides, there are easterly wind anomalies at low latitudes of the Northern Hemisphere and westerly wind anomalies to their south and north. Since the mean zonal winds in the middle troposphere near the equator are relatively weak, such significant zonal wind anomalies can dramatically change the zonal wind direction and magnitude. The zonal velocity anomalies in the upper troposphere in Fig.3.10a is dominated by westerly winds with broad meridional extent, including low latitudes of both the Northern and Southern Hemisphere as well as the equator. Such broad meridional extent of zonal velocity anomalies is related with the advection effects by the upper branch of the circulation cell in northerly returning flows. In contrast, planetary-scale zonal velocity anomalies at these three levels at day 4 in the shallow heating case are shown in Fig.3.10d-f. Similarly, the most significant planetary-scale zonal velocity anomalies are confined in the diabatic heating region between $X = 15 \times 10^3 km$ and $X = 25 \times 10^3 km$. At the surface in Fig.3.10f, there are westerly wind anomalies at high latitudes of the Northern Hemisphere and easterly wind anomalies to the south, whose spatial pattern is quite similar to the deep

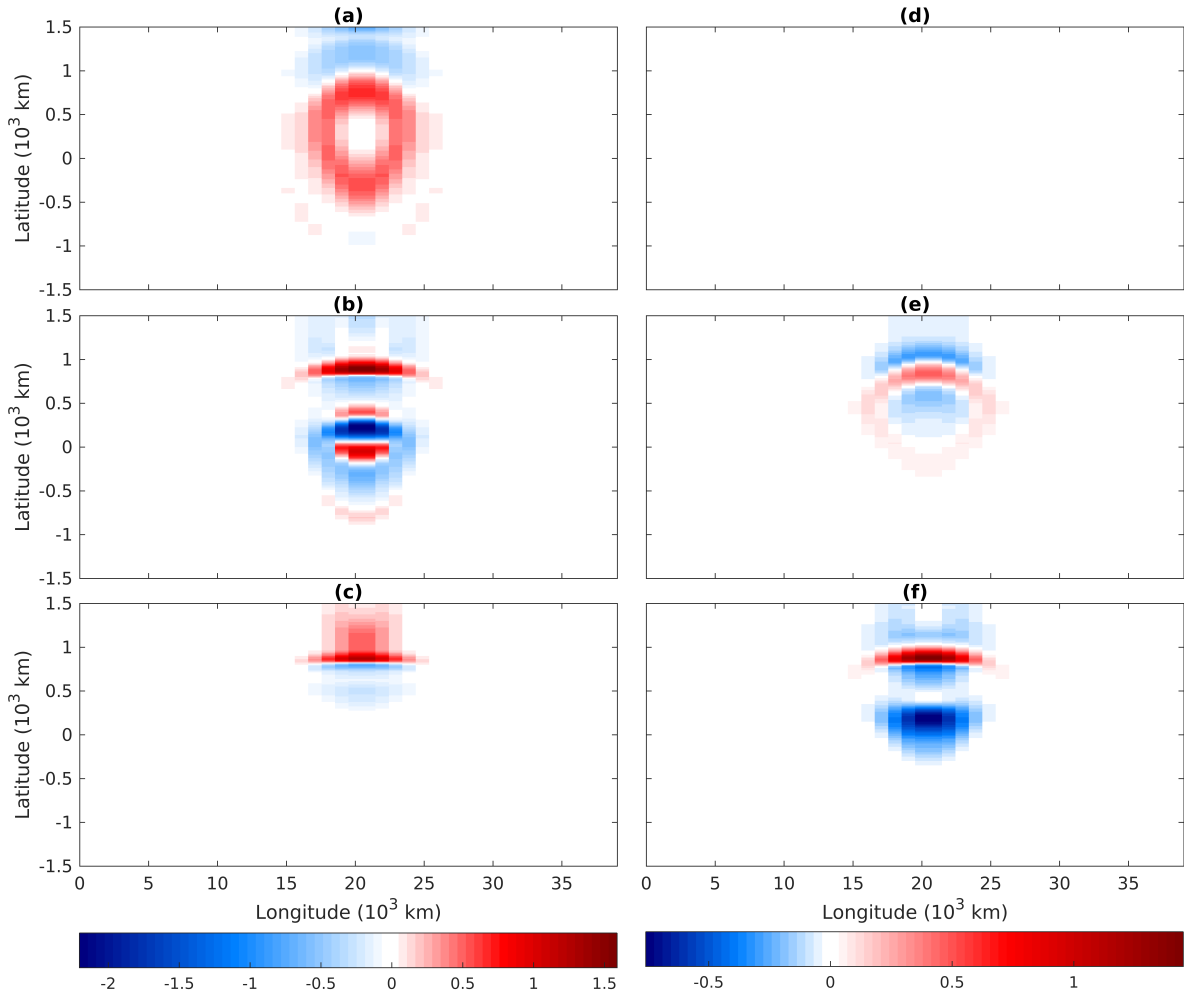


Figure 3.10: Mean zonal velocity anomalies at different heights at day 4 in the longitude-latitude diagram. The left column (a-c) is for *deep2* heating case and the right column (d-f) is for shallow heating case. The panels from top to bottom are for heights 14.84 km, 7.48 km and 3.62 km respectively. The dimensional unit is ms^{-1} .

convective heating case in Fig.3.10c. In the middle troposphere in Fig.3.10e, easterly wind anomalies are found to the north of the westerly wind anomalies in the Northern Hemisphere, whose magnitudes are much weaker than those in lower levels. In the upper troposphere in Fig.3.10d, the magnitude of zonal velocity anomalies is negligible.

In the M-ITCZ equations, the planetary-scale physical variables including large-scale zonal velocity $\langle \bar{u} \rangle$, pressure perturbation Π , potential temperature anomalies Θ and secondary vertical motion W do not depend on meridional coordinate y , representing a planetary-scale gravity wave with uniform meridional profile. Therefore, the meridional mean of zonal velocity and potential temperature anomalies (not shown) can be used to characterize planetary-scale gravity waves. It turns out that the meridional mean of planetary-scale zonal velocity and potential temperature has few discrepancies with/without mesoscale fluctuations in both deep and shallow heating cases, meaning that little upscale impact of mesoscale fluctuations are transported away from the diabatic heating region by planetary-scale gravity waves.

3.5 Concluding Discussion

The ITCZ over the eastern Pacific is a narrow band of cloudiness, which is accompanied by low-level convergent winds and warm sea surface temperature below. Unlike the western Pacific ITCZ that migrates between the Northern and Southern Hemispheres in the seasonal cycle, the eastern Pacific ITCZ persistently remains in the Northern Hemisphere between the latitudes $5^{\circ}N$ and $15^{\circ}N$ throughout the whole year. Instead of being a steady state, the eastern Pacific ITCZ is sometimes observed to undulate and break down into several vortices, some of which become tropical cyclones and others dissipate and die out. As these tropical cyclones in great strength move to high latitudes, a new band of ITCZ cloudiness reforms in the original place. Capturing the flow fields in the baroclinic modes during the ITCZ breakdown including the undulation of a positive vorticity strip and the formation of

a strong positive vortex is one of the main motivations in this chapter. Using a multi-scale model to incorporate both the mesoscale and planetary-scale dynamics during the ITCZ breakdown and assessing the upscale impact of mesoscale fluctuations on the planetary-scale circulation is the other one of the main motivations.

Here a multi-scale model (M-ITCZ equations) is used to achieve those motivations as mentioned above. The M-ITCZ equations were first derived in (Biello and Majda, 2013) by starting from the primitive equations on an equatorial β plane and following systematic multi-scale asymptotic methods (Majda and Klein, 2003; Majda, 2007). Two zonal spatial scales arise naturally from the physically scaling about atmospheric flow field in the ITCZ (mesoscale $L_m = 500$ km and planetary-scale $L_p = 5000$ km). The M-ITCZ equations describe atmospheric flows on both the planetary scale and mesoscale, and the corresponding governing equations across these two scales are nonlinearly coupled to each other. Specifically, the undulation of a positive vorticity strip and formation of a strong positive vortex are simulated on the mesoscale dynamics of the M-ITCZ equations, which resembles the formation of tropical cyclones during the ITCZ breakdown. The planetary-scale circulation is governed by the planetary-scale gravity wave equations in the M-ITCZ equations.

In the first scenario, the planetary-scale flow is assumed to be zonally symmetric, which suppresses planetary-scale gravity waves in the M-ITCZ equations. Such an idealized assumption isolates the upscale impact of mesoscale fluctuations from the planetary-scale gravity wave and provides a suitable scenario to model the ITCZ breakdown over several hundred kilometers in the mesoscale domain. Deep convective heating is prescribed as the mesoscale zonally localized heating in the Northern Hemisphere and uniform cooling elsewhere in the first baroclinic mode. First, after the flow field is initialized from a background state of rest, a positive vorticity strip forms at the surface in the northern side of the diabatic heating region, surrounded by negative vorticity anomalies. As the diabatic heating remains persistent, the positive vorticity strip has increasing magnitude and starts to undulate, which resembles the undulation of the ITCZ as observed in (Ferreira and Schubert, 1997). Later, a strong

positive vortex is generated in the middle of the positive vorticity strip, which mimicks tropical cyclogenesis in the baroclinic modes during the ITCZ breakdown. Since upward motion prevails in the diabatic heating region, positive vorticity anomalies are advected by upward motion and stretched vertically to the middle and upper troposphere. In the middle troposphere, a pair of vorticity dipoles are generated at low latitudes of the Northern Hemisphere, which also means cyclonic (anticyclonic) flows to the west (east) of the diabatic heating region. As the counterpart of the positive vorticity strip at the surface, negative vorticity anomalies with broad meridional extent are induced at the upper troposphere. Secondly, the eddy flux divergence of zonal momentum is characterized by mid-level (low-level) eastward (westward) momentum forcing with deep vertical extent at high latitudes of the Northern Hemisphere and mid-level alternate momentum forcing anomalies at low latitudes. Such eddy flux divergence of zonal momentum tends to induce westerly wind anomalies at high latitudes of the Northern Hemisphere, which are further advected by upper-level northerly winds to the Southern Hemisphere. Besides, mid-level easterly and westerly wind anomalies are also induced at low latitudes of the Northern Hemisphere, which provide extensive features for the zonal jets in this region. As far as the kinetic energy budget is concerned, acceleration effects are induced in the region where the positive vorticity anomalies are vertically stretched, while deceleration effects are mainly located in the lower troposphere to the north and south of the positive vorticity strip. Besides, strong acceleration effects are also induced in the middle troposphere at low latitudes of the Northern Hemisphere, where the wind directions and strength are changed dramatically.

Compared with deep convective heating, shallow congestus heating is prescribed in a vertical profile with its maximum in the lower troposphere. After initialization from a background state of rest, a positive vorticity strip forms at the surface of the Northern Hemisphere, which undulates and generates a strong positive vortex in the middle. A direct comparison between the deep and shallow heating cases with the same maximum heating magnitude indicates that shallow congestus heating induces stronger vorticity anomalies and

wind strength at the surface, which is related with the larger horizontal wind convergence there. In fact, such stronger cyclonic flows driven by shallow congestus heating is also discussed in a canonical balanced model to simulate “how towers” in the hurricane embryo (Majda et al., 2008). In the three-dimensional simulation for ITCZ breakdown of (Wang and Magnusdottir, 2005) using a primitive equation model, shallow heating tends to induce stronger lower-tropospheric potential vorticity response than the deep heating while the upper-tropospheric potential vorticity response vanishes. Here, as upward motion prevails in the diabatic heating region, positive vorticity anomalies in the Northern Hemisphere is advected by upward motion and lifted up to the middle troposphere. The resulting large-scale circulation response is confined in the low and middle troposphere and vanishes in the upper troposphere, which resembles shallow meridional circulation as observed over the eastern Pacific. As far as the eddy flux divergence of zonal momentum is concerned, its spatial pattern in the shallow heating case is mostly confined in the lower and middle troposphere with eastward momentum forcing at high latitudes of the Northern Hemisphere and alternative eastward/westward momentum forcing anomalies at low latitudes. Shallow congestus heating also induces stronger eddy flux divergence of zonal momentum on the planetary-scale zonal winds. As for the kinetic energy budget, there are stronger acceleration effects in the region where the positive vorticity anomalies are vertically stretched and deceleration effects to its north and south. Besides, acceleration effects are also significant in the lower troposphere at low latitudes of the Northern Hemisphere.

In the second scenario, the two scales (planetary scale and mesoscale) are set to interact with each other and the diabatic heating is modulated by a planetary-scale zonally localized convective envelope to mimic the eastern Pacific ITCZ; The fully coupled M-ITCZ equations that allow zonal variation of flow fields on both the mesoscale and planetary scale are used. As studied in (Biello and Majda, 2013), in the mean deep heating case, the resulting overturning circulation consist of the deep meridional circulation and zonal jets due to the Coriolis force. The meridional mean of planetary-scale zonal velocity is in the first baro-

clinic mode and propagates away with the planetary-scale gravity wave, which also brings negative (positive) potential temperature anomalies and upward (downward) motion to the west (east), providing favorable (unfavorable) conditions for convection. After replacing the mean heating by the mesoscale zonally localized heating, significant zonal velocity anomalies are induced in the diabatic heating region, which mainly consist of deep westerly wind anomalies at high latitudes of the Northern Hemisphere and several easterly/westerly wind anomalies in the middle troposphere near the equator. As modulated by the planetary-scale convective envelope, the flow fields in all the mesoscale domains are characterized by cyclonic flow in the same direction in the Northern Hemisphere. In the shallow heating case, most of significant zonal velocity anomalies induced by eddy flux divergence of zonal momentum are confined in the lower troposphere, although the spatial pattern in the corresponding levels are similar to that in the deep convective heating case. Lastly, the eddy flux divergence of zonal momentum has weak impact on the meridional mean of zonal velocity and potential temperature in both deep and shallow heating cases, thus small upscale impact of mesoscale fluctuations are transported away from the diabatic heating region by the planetary-scale gravity waves.

This study based on a multi-scale model has several implications for physical interpretation and comprehensive numerical models. First, the MEWTG equations in the idealized scenario with zonally symmetric planetary-scale flow successfully capture several key features of the ITCZ breakdown in the baroclinic modes, including the undulation of the positive vorticity strip and formation of a strong positive vortex. Secondly, the M-ITCZ equations model both the ITCZ breakdown and planetary-scale circulation in a self-consistent framework and provide assessment of the upscale impact of mesoscale fluctuations in a transparent fashion. Thirdly, compared with the deep convective heating, shallow congestus heating tends to have more significant upscale impact on the planetary-scale circulation including stronger eddy flux divergence of zonal momentum and acceleration/deceleration effects. Lastly, the resulting eddy flux divergence of zonal momentum significantly modifies planetary-scale zonal

velocity, resulting in the rectification of the ITCZ over the eastern Pacific. Such assessment of the upscale impact of mesoscale fluctuations associated with the ITCZ breakdown can help to improve the convective parameterization in more complex numerical models. The M-ITCZ equations under the current model setup can also be generalized in several ways and used to model other phenomena in the ITCZ. For example, as suggested in (Biello and Majda, 2013), instead of prescribing the diabatic heating, an active heating coupling the M-ITCZ equations with moisture will introduce new realistic features of tropical flows. As planetary-scale gravity waves propagate westward, negative potential temperature anomalies and upward motion are also carried westward, which provides favorable conditions for convection. The recently triggered convection through the active heating induces mesoscale fluctuations and generates upscale impact on the planetary-scale gravity wave in return. Such mesoscale Rossby wave coupled with planetary-scale gravity wave through an active heating can be a good candidate for westward moving disturbances as observed in the eastern Pacific ITCZ (Yang et al., 2003; Serra et al., 2008). In addition, coupling an equation for the atmospheric boundary layer can further elaborate the M-ITCZ equations and provide realistic features of tropical phenomena over the eastern Pacific. The resulting model should be useful to model the convective instability in the ITCZ and flow fields during the ITCZ breakdown.

3.6 Numerical Scheme

Once again, the M-ITCZ equations consist of two zonal spatial scales (planetary-scale and mesoscale), and the corresponding dynamics on these scales are coupled to each other in complete nonlinearity. A suitable numerical scheme is required to simulate this model and satisfy the following properties. First of all, the M-ITCZ equations are derived by using multi-scale asymptotic methods, which assume these two zonal spatial scales are independent when the small parameter (Rossby number ϵ) goes to zero in the asymptotic limit. Secondly,

the MEWTG equations in Eqs.3.4a-3.4d are totally nonlinear with the advection term in three-dimensional flows. Thirdly, although both mesoscale and planetary-scale dynamics are coupled to each other, a suitable averaging method need to be used so that large-scale physical variables can be obtained and updated in each time step. Lastly, the hydrostatic balance is valid on the planetary scale in Eq.3.1e, which requires a vertical boundary condition for the planetary-scale pressure perturbation.

3.6.1 Nested grids in the multi-scale domain

There are two zonal spatial scales in the M-ITCZ equations. One is the planetary scale X ($L_p = 5000$ km) and the other is the mesoscale x ($L_m = 500$ km). Therefore, the whole domain can be discretized with nested coarse and fine grids, as shown in Fig.3.8. In the numerical simulations, the MEWTG equations in Eqs.3.4a-3.4d are only valid on each mesoscale box with some suitable boundary conditions. After taking zonal averaging of physical variables in each mesoscale box, the planetary-scale quantities on each coarse grid can be obtained.

During the derivation of M-ITCZ equations by using the multi-scale asymptotic method, the sublinear growth condition is imposed to avoid secular growth Majda and Klein (2003). In details, the sublinear growth condition requires that the zonal averaging of mesoscale zonal derivatives of physical variables vanish when the small parameter (Rossby number ϵ) goes to zero and the size of the mesoscale domain goes to infinity in the asymptotic limit. However, in the numerical simulations, the size of the mesoscale domain is finite due to nonzero small parameter (Rossby number ϵ). In order to be consistent with the sublinear growth condition, the local periodicity boundary condition in zonal direction is imposed, which requires that the numerical solutions are zonally periodic in each mesoscale box.

3.6.2 Fractional step method

The numerical scheme for solving the M-ITCZ equations can be split into two alternative steps as time goes on. The first step is to solve the MEWTG equations in each mesoscale box and the second step is to solve the planetary-scale gravity wave equations in the full domain after calculating mean value of all physical variables in each mesoscale box. In order to solve the MEWTG equations, the Helmholtz decomposition is utilized to decompose horizontal velocity with stream function and velocity potential, which turn out to be governed by two coupled Poisson's equations. Besides, the horizontal vorticity is governed by a forced advection equation in three-dimensional flows, which can be solved by using the Corner-Transport-Upwind (CTU) scheme LeVeque (2002). In addition, the predictor-corrector scheme is utilized to improve temporal accuracy with two stages. A cheap first-order upwind scheme is implemented in the first stage. After estimating the velocity field at half time step in the first stage, the second-order piecewise linear CTU scheme is applied to calculate the horizontal vorticity in the second stage. As for solving the planetary-scale gravity wave equations, all physical variables are decomposed into different baroclinic modes and numerical solutions in each baroclinic mode are solved by using the Fast Fourier Transform.

In each time step, the fractional step method is applied on the M-ITCZ equations. The full numerical routine is organized as shown in the following box.

Step 1: solve the MEWTG equations in each single mesoscale box,

$$\frac{Du}{Dt} - yv = -p_x - du, \quad (3.19a)$$

$$\frac{Dv}{Dt} + yu = -p_y - dv, \quad (3.19b)$$

$$w = S_\theta, \quad (3.19c)$$

$$u_x + v_y + w_z = 0, \quad (3.19d)$$

and compute zonal and meridional averaging of u in each mesoscale box,

$$u \longrightarrow \langle \bar{u} \rangle. \quad (3.20)$$

Step 2: solve the planetary-scale gravity wave equations,

$$\langle \bar{u} \rangle_t + \Pi_X = 0, \quad (3.21a)$$

$$\Pi_x = \Pi_y = 0, \quad \Pi_z = \Theta, \quad (3.21b)$$

$$\Theta_t + W = 0, \quad (3.21c)$$

$$[\langle \bar{u} \rangle - U]_X + W_z = 0, \quad (3.21d)$$

and update u in each mesoscale box by adding the increment of $\langle \bar{u} \rangle$,

$$u + \Delta \langle \bar{u} \rangle \longrightarrow u. \quad (3.22)$$

In the end of step 1, the mesoscale zonal and meridional average of zonal velocity $\langle \bar{u} \rangle$ is calculated so that the planetary-scale mean zonal velocity can be plugged into the gravity wave equations in step 2. Specifically, the trapezoidal rule for meridional averaging is used since it is consistent with the centered difference scheme used in solving the coupled Poisson equation for velocity potential and stream functions in Sec.3.6.3.2. In the end of step 2, the zonal velocity anomalies $\Delta \langle \bar{u} \rangle$ between two time steps are calculated. According to Eq.3.1a,

such zonal velocity anomalies are applied to the total zonal velocity variables u through the large-scale pressure perturbation Π_X , which is independent of the mesoscale zonal and meridional coordinates (x, y) . Therefore, the total zonal velocity u in each mesoscale box is updated by adding the increment of $\langle \bar{u} \rangle$ as Eq.3.22. Besides, such large-scale zonal velocity anomalies do not modify the vorticity $\xi = v_x - u_y$ but the mean zonal velocity at the meridional boundaries.

3.6.3 Solving the MEWTG equations

In this section, the numerical scheme for solving the MEWTG equations (Eqs.3.19a-3.19d) is included.

According to the Helmholtz theory, the horizontal velocity field (u, v) can be decomposed into the stream function ψ and velocity potential ϕ as follows

$$u = -\psi_y + \phi_x, \quad (3.23)$$

$$v = \psi_x + \phi_y. \quad (3.24)$$

After plugging Eqs.3.23-3.24 into Eq.3.19d, the Poisson's equation for the velocity potential ϕ is obtained,

$$u_x + v_y = \phi_{xx} + \phi_{yy} = -w_z = -\frac{\partial}{\partial z} S_\theta. \quad (3.25)$$

Besides, the vorticity equation for $\xi = v_x - u_y$ can be obtained by manipulating Eqs.3.19a-3.19b,

$$\begin{aligned} \xi_t + u\xi_x + v\xi_y + w\xi_z &= -(\xi + y)(u_x + v_y) - w_x v_z + w_y u_z - v - d\xi \\ &= (\xi + y) \frac{\partial}{\partial z} S_\theta - v_z \frac{\partial}{\partial x} S_\theta + u_z \frac{\partial}{\partial y} S_\theta - v - d\xi. \end{aligned} \quad (3.26)$$

According to the definition of the vorticity ξ , the Poisson's equation for the stream function

ψ is also obtained,

$$\xi = v_x - u_y = \psi_{xx} + \psi_{yy}. \quad (3.27)$$

3.6.3.1 The corner-transport upwind scheme for the unforced vorticity equation

As shown in Eq.3.26, the horizontal vorticity in the MEWTG equations is governed by a three-dimensional advection equation as follows,

$$\xi_t + u\xi_x + v\xi_y + w\xi_z = (\xi + y) \frac{\partial}{\partial z} S_\theta - v_z \frac{\partial}{\partial x} S_\theta + u_z \frac{\partial}{\partial y} S_\theta - v - d\xi. \quad (3.28)$$

In this section, a second-order non-oscillatory corner-transport upwind (CTU) method with piece-wise linear approximation LeVeque (2002) is described. To be brief, all terms on the right hand side of Eq.3.28 are denoted by f . The numerical scheme for the unforced advection equation is first discussed here, which will be extended to the forced case in Sec.3.6.3.3. The unforced vorticity equation is as follows,

$$\xi_t + u\xi_x + v\xi_y + w\xi_z = 0. \quad (3.29)$$

According to the method of characteristics, ξ does not change along characteristics line, thus

$$\dot{x} = u(x(s), y(s), z(s), s), \quad (3.30)$$

$$\dot{y} = v(x(s), y(s), z(s), s), \quad (3.31)$$

$$\dot{z} = w(x(s), y(s), z(s), s), \quad (3.32)$$

$$\dot{\xi} = 0. \quad (3.33)$$

A finite-volume type description is used to derive the CTU scheme. Let $\Omega_{i,j,k} = [x_{i-\frac{1}{2}}, x_{i+\frac{1}{2}}] \times [y_{j-\frac{1}{2}}, y_{j+\frac{1}{2}}] \times [z_{k-\frac{1}{2}}, z_{k+\frac{1}{2}}]$ denotes a generic control volume and $t^n = n\delta t$ be

a time discretization. Then the volume average of ξ at t^{n+1}

$$Q_{i,j,k}^{n+1} = \frac{1}{\Delta X \Delta Y \Delta Z} \int \int \int_{\Omega_{i,j,k}} \xi(x, y, z, t^n + \delta t) dx dy dz, \quad (3.34)$$

satisfies

$$Q_{i,j,k}^{n+1} = \frac{1}{\Delta X \Delta Y \Delta Z} \int \int \int_{\tilde{\Omega}_{i,j,k}} \xi(x, y, z, t^n) dx dy dz, \quad (3.35)$$

where $\tilde{\Omega}_{i,j,k}$ is the original copy of the control volume $\Omega_{i,j,k}$.

Suppose the flow field at half time step $u^{n+\frac{1}{2}}, v^{n+\frac{1}{2}}, w^{n+\frac{1}{2}}$ is approximated as discussed in Sec.3.6.3.3, then the corresponding displacement can also be approximated by the midpoint integration formula:

$$\delta x = u^{n+\frac{1}{2}} \delta t, \quad (3.36)$$

$$\delta y = v^{n+\frac{1}{2}} \delta t, \quad (3.37)$$

$$\delta z = w^{n+\frac{1}{2}} \delta t. \quad (3.38)$$

Therefore, the original copy of the control volume can be approximated as follows:

$$\tilde{\Omega}_{i,j,k} = \left[x_{i-\frac{1}{2}} - \delta x, x_{i+\frac{1}{2}} - \delta x \right] \times \left[y_{j-\frac{1}{2}} - \delta y, y_{j+\frac{1}{2}} - \delta y \right] \times \left[z_{k-\frac{1}{2}} - \delta z, z_{k+\frac{1}{2}} - \delta z \right]. \quad (3.39)$$

The corner-transport upwind scheme (CTU) can be applied in such scenario. The essential idea in this numerical scheme is illustrated by Fig.3.11. In Fig.3.11, the gray rectangle is the original copy of the control volume $\tilde{\Omega}_{i,j,k}$, which can be separated into several small rectangle areas A1, A2, A3, A4, meaning that the mean value on the control volume has contributions from the neighbor cells. Usually, the first-order CTU scheme assumes the conserved quantity ξ is constant in each cell. In order to achieve second-order accuracy, the piece-wise linear reconstruction of the solution ξ^n given its volume average is introduced as

follows,

$$\xi(x, y, t^n) = P_{i,j,k}^n(x, y, z) = Q_{i,j,k}^n + S_{i,j,k}^x(x - x_i) + S_{i,j,k}^y(y - y_j) + S_{i,j,k}^z(z - z_k). \quad (3.40)$$

Here $S_{i,j,k}^x, S_{i,j,k}^y, S_{i,j,k}^z$ are slope limiters defined as follows

$$S_{i,j,k}^x = \frac{1}{\Delta X} \Upsilon \left(Q_{i,j,k}^n - Q_{i-1,j,k}^n, Q_{i+1,j,k}^n - Q_{i,j,k}^n, \frac{1}{2} (Q_{i+1,j,k}^n - Q_{i-1,j,k}^n) \right), \quad (3.41)$$

$$S_{i,j,k}^y = \frac{1}{\Delta Y} \Upsilon \left(Q_{i,j,k}^n - Q_{i,j-1,k}^n, Q_{i,j+1,k}^n - Q_{i,j,k}^n, \frac{1}{2} (Q_{i,j+1,k}^n - Q_{i,j-1,k}^n) \right), \quad (3.42)$$

$$S_{i,j,k}^z = \frac{1}{\Delta Z} \Upsilon \left(Q_{i,j,k}^n - Q_{i,j,k-1}^n, Q_{i,j,k+1}^n - Q_{i,j,k}^n, \frac{1}{2} (Q_{i,j,k+1}^n - Q_{i,j,k-1}^n) \right), \quad (3.43)$$

$$\Upsilon(a, b, c) = \begin{cases} \min(|a|, |b|, |c|) \operatorname{sign}(a) & \text{if } a, b, c \text{ have same sign} \\ 0 & \text{otherwise} \end{cases}. \quad (3.44)$$

The numerical scheme for updating $Q_{i,j,k}^n$ (the volume average of ξ) involves its value in all neighboring cells as well as the slope limiters in Eqs.3.41-3.44. The exact expression is quite long and ignored here. More details can be found in LeVeque (2002).

3.6.3.2 The coupled Poisson's equations for velocity potential and stream function

As shown in Eq.3.25 and Eq.3.27, both the velocity potential ϕ and the stream function ψ are governed by Poisson's equations. Besides, the physical boundary conditions are expressed in terms of flow field instead of velocity potential and stream function , thus these two Poisson's equations are coupled to each other. Two boundary conditions at both the northern and southern boundaries are imposed as follows,

Boundary Condition 1: meridional velocity vanishes at the meridional boundaries $y = \pm L_*$,

$$v(\pm L_*) = 0, \quad (3.45)$$

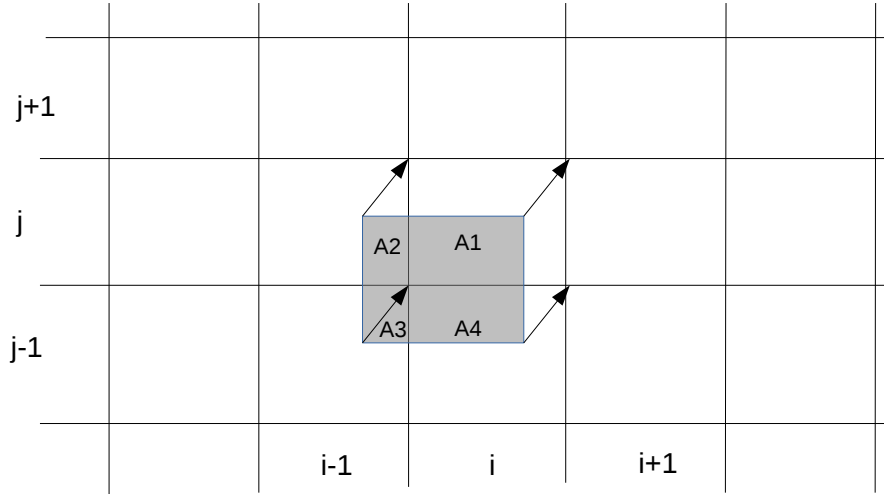


Figure 3.11: A schematic depiction of the essential idea behind the corner transport upwind scheme. The gray box denotes the original copy of the control volume (i, j) , which moves in the direction as indicated by the arrows. This gray box overlaps the neighboring cells and can be divided into as denoted into 4 small rectangles as denoted by A1, A2, A3, A4. Such two-dimensional case can be extended to three-dimensional case with 8 neighboring cells.

which states that there is neither inflow nor outflow through meridional boundaries. Although in reality the tropical flows can interact with the mid-latitude atmospheric flows, this boundary condition is chosen so that the meridional circulation in the tropics is closed and isolated. As already mentioned in Biello and Majda (2013), the meridional component of the flows in the M-ITCZ theory can be matched to meridional flows from higher latitudes ultimately.

Boundary Condition 2: zonal velocity fluctuation u' vanishes at the meridional boundaries $y = \pm L_*$,

$$u = \bar{u} \equiv \frac{1}{P} \int_0^P u(X, x, y, z, t) dx \quad \text{at } y = \pm L_*, \quad (3.46)$$

which amounts to assuming the turbulent flow is zero at $y = \pm L$. This boundary condition makes physical sense if the artificial boundaries are far away from the region of convection ($S_\theta \neq 0$) and that the turbulent flow gets attenuated quickly by dissipation before it reaches the two meridional boundaries.

To sum up, the coupled Poisson's equations can be obtained, along with the zonal and meridional boundary conditions as follows,

$$\phi_{xx} + \phi_{yy} = -\frac{\partial}{\partial z} S_\theta \quad (3.47)$$

$$\psi_{xx} + \psi_{yy} = \xi \quad (3.48)$$

BC1: ϕ, ψ are periodic in x

BC2: $\psi_x + \phi_y = 0$ at $y = \pm L_*$

BC3: $-\psi_y + \phi_x = \bar{u}$ at $y = \pm L_*$

The coupled Poisson's equations above need an extra equation for \bar{u} at meridional boundaries to get closure. After taking zonal averaging in each mesoscale box, Eq.3.19a at meridional boundaries can be reduced to

$$\bar{u}_t + \overline{u\bar{u}_x} + \overline{v\bar{u}_y} + \overline{w\bar{u}_z} - y\bar{v} = -\overline{p_x} - d\bar{u}, \quad (3.49)$$

where the second term on the left hand side vanishes due to the boundary condition in Eq.3.46, the third and fifth terms vanish due to the boundary condition in Eq.3.45 and the first term on the right side is zero due to local periodicity assumption as explained in Sec.3.6.1. Then Eq.3.19a at meridional boundaries is rewritten as follows,

$$\bar{u}_t + \overline{w\bar{u}_z} = -d\bar{u}. \quad (3.50)$$

This equation can be further simplified by using the boundary condition in Eq.3.46,

$$\bar{u}_t + \bar{w}\bar{u}_z = -d\bar{u}. \quad (3.51)$$

Eq.3.51 is a one-dimensional advection equation, which can be solved simultaneously with

the vorticity equation in Eq.3.28 by using a semi-Lagrangian scheme. The details about the numerical scheme are as follows,

Firstly, the departing position of each \tilde{z}_j is calculated,

$$\tilde{z}_j = z_j - \delta t \bar{w}_j, \quad (3.52)$$

where time step δt is chosen to be small enough so that $\delta t \bar{w}_j \ll \delta z$, thus $\frac{|\tilde{z}_j - z_j|}{\delta z} \leq \frac{1}{2}$.

Secondly, quadratic interpolation method is used to estimate $\tilde{\bar{u}}(\tilde{z}_j, t_{n+1})$ (let $\alpha = \frac{\delta t \bar{w}_j}{\delta z}$),

$$\tilde{\bar{u}}(\tilde{z}_j, t_{n+1}) = \left(\frac{\alpha^2}{2} - \frac{\alpha}{2} \right) \bar{u}_{j+1} + (1 - \alpha^2) \bar{u}_j + \left(\frac{\alpha^2}{2} + \frac{\alpha}{2} \right) \bar{u}_{j-1}, \quad (3.53)$$

Lastly, the quantity \bar{u} is damped along each characteristic line, which is governed by an ordinary differential equation $\frac{d}{dt} u(z(t), t) = -du$. The analytical solution is used for the last damping step:

$$\bar{u}(z_j, t_{n+1}) = e^{-d\delta t} \tilde{\bar{u}}(\tilde{z}_j, t_{n+1}). \quad (3.54)$$

In order to increase both efficiency and accuracy when solving the coupled Poisson's equations in Eqs.3.47-3.48, the fast Fourier transform (FFT) subroutine written in Fortran 77 is utilized. In this Fortran subroutine, all real functions (e.g. $f(x)$) are transformed into the following form (In the numerical simulation, the x-grid number N_x is set to be an odd number for simplicity)

$$f(x) = \sum_{k=1} \left[f_k^A \cos \left(\frac{2\pi kx}{L} \right) - f_k^B \sin \left(\frac{2\pi kx}{L} \right) \right] + f_0. \quad (3.55)$$

By using Fourier series expansion for all physical variables ϕ, ψ, ξ, f (here f denotes

$-\frac{\partial}{\partial z} S_\theta$), the coupled Poisson's equations can be decomposed into different wavenumber modes along with the corresponding boundary conditions as follows,

#1, wavenumber $k = 0$

$$\phi_{0,yy} = f_0 \quad (3.56)$$

$$BC1 : \phi_{0,y} = 0 \quad y = \pm L_* \quad (3.57)$$

$$\psi_{0,yy} = \xi_0 \quad (3.58)$$

$$BC2 : -\psi_{0,y} = \bar{u} \quad y = \pm L_* \quad (3.59)$$

#2, wavenumber $k \neq 0$

$$-\frac{4\pi^2 k^2}{L^2} \phi_k^A + \phi_{k,yy}^A = f_k^A \quad (3.60)$$

$$-\frac{4\pi^2 k^2}{L^2} \psi_k^B + \psi_{k,yy}^B = \xi_k^B \quad (3.61)$$

$$BC1 : \frac{2\pi k}{L} \psi_k^B - \phi_{k,y}^A = 0 \quad y = \pm L_* \quad (3.62)$$

$$BC2 : \psi_{k,y}^B - \frac{2\pi k}{L} \phi_k^A = 0 \quad y = \pm L_* \quad (3.63)$$

#3, wavenumber $k \neq 0$

$$-\frac{4\pi^2 k^2}{L^2} \phi_k^B + \phi_{k,yy}^B = f_k^B \quad (3.64)$$

$$-\frac{4\pi^2 k^2}{L^2} \psi_k^A + \psi_{k,yy}^A = \xi_k^A \quad (3.65)$$

$$BC1 : \frac{2\pi k}{L} \psi_k^A + \phi_{k,y}^B = 0 \quad y = \pm L_* \quad (3.66)$$

$$BC2 : \psi_{k,y}^A + \frac{2\pi k}{L} \phi_k^B = 0 \quad y = \pm L_* \quad (3.67)$$

In order to solve the coupled 1D Poisson's equations above, the centered difference scheme

is used to discretize the solution in meridional direction. At the northern and southern boundary, ghost cells are used to enforce the boundary conditions and each set of equations (#1,#2,#3) is reduced into a linear system of the form

$$AX = B. \quad (3.68)$$

One notable feature in the case #1 for wavenumber $k = 0$ is that both the velocity potential ϕ and the stream function ψ are unique up to a constant. In order to uniquely determine their value, the mean zero condition ($\sum_{j=1}^N \varphi_j = 0$) is enforced. Here the constant on the right hand side is arbitrary since the velocity field is determined by the gradient of the velocity potential ϕ and the stream function ψ . The coefficient matrix A and vector B in Eq. 3.68 for each wavenumber mode are listed below.

#1 wavenumber $k = 0$

(1) velocity potential ϕ

$$X = \begin{pmatrix} \phi_1 & \phi_2 & \cdots & \phi_{N-1} & \phi_N \end{pmatrix}^T \quad (3.69)$$

$$B = \begin{pmatrix} f_1 & f_2 & \cdots & f_{N-1} & 0 \end{pmatrix}^T \quad (3.70)$$

$$A = \frac{1}{(\delta y)^2} \begin{bmatrix} -2 & 2 & 0 & 0 & 0 \\ 1 & -2 & 1 & 0 & 0 \\ 0 & \dots & \dots & \dots & 0 \\ 0 & 0 & 1 & -2 & 1 \\ 1 & 1 & 1 & 1 & 1 \end{bmatrix} \quad (3.71)$$

(2) stream function ψ

$$X = \begin{pmatrix} \psi_1 & \psi_2 & \cdots & \psi_{N-1} & \psi_N \end{pmatrix}^T \quad (3.72)$$

$$B = \begin{pmatrix} \xi_1 - \frac{2\bar{u}}{\delta y} & \xi_2 & \cdots & \xi_{N-1} & 0 \end{pmatrix}^T \quad (3.73)$$

$$A = \frac{1}{(\delta y)^2} \begin{bmatrix} -2 & 2 & 0 & 0 & 0 \\ 1 & -2 & 1 & 0 & 0 \\ 0 & \dots & \dots & \dots & 0 \\ 0 & 0 & 1 & -2 & 1 \\ 1 & 1 & 1 & 1 & 1 \end{bmatrix} \quad (3.74)$$

The ones on the last row of the matrix A enforce the mean zero condition and recover uniqueness.

#2 wavenumber $k \neq 0$, $a = \frac{1}{(\delta y)^2}$, $b = \frac{4\pi^2 k^2}{L^2}$, $c = \frac{4\pi k}{L\delta y}$

$$X = \begin{pmatrix} \phi_1 & \phi_2 & \cdots & \phi_N & \psi_1 & \psi_2 & \cdots & \psi_N \end{pmatrix}^T \quad (3.75)$$

$$B = \begin{pmatrix} f_1 & f_2 & \cdots & f_N & \xi_1 & \xi_2 & \cdots & \xi_N \end{pmatrix}^T \quad (3.76)$$

$$A = \begin{bmatrix} -2a - b & 2a & & & & & & \\ a & -2a - b & a & & & & & \\ \dots & \dots & \dots & & & & & \\ & a & -2a - b & a & & & & \\ & & 2a & -2a - b & & & & \\ & & & -2a - b & 2a & & & c \\ & & & a & -2a - b & a & & \\ & & & \dots & \dots & \dots & & \\ & & & a & -2a - b & a & & \\ & & & & 2a & -2a - b & & \\ & & & & & & & \end{bmatrix} \quad (3.77)$$

#3 wavenumber $k \neq 0$, $a = \frac{1}{(\delta y)^2}$, $b = \frac{4\pi^2 k^2}{L^2}$, $c = \frac{4\pi k}{L\delta y}$

$$X = \begin{pmatrix} \phi_1 & \phi_2 & \cdots & \phi_N & \psi_1 & \psi_2 & \cdots & \psi_N \end{pmatrix}^T \quad (3.78)$$

$$B = \begin{pmatrix} f_1 & f_2 & \cdots & f_N & \xi_1 & \xi_2 & \cdots & \xi_N \end{pmatrix}^T \quad (3.79)$$

$$A = \begin{bmatrix} -2a - b & 2a & & & & & & c \\ a & -2a - b & a & & & & & \\ \dots & \dots & \dots & & & & & \\ & a & -2a - b & a & & & & \\ & & 2a & -2a - b & & & & \\ & & & -2a - b & 2a & & & -c \\ & & & a & -2a - b & a & & \\ & & & \dots & \dots & \dots & & \\ & & & a & -2a - b & a & & \\ & & & & 2a & -2a - b & & \\ & & & & & & & \end{bmatrix} \quad (3.80)$$

3.6.3.3 The predictor-corrector scheme for the forced vorticity equation

As mentioned in Sec.3.6.3.1, the displacement $(\delta x, \delta y, \delta z)$ is required to be approximated at the half time step. In the numerical simulations, this displacement is approximated by a first-order upwind scheme in the first stage of the predictor-corrector scheme.

The whole numerical routine in the first stage is as follows. First, the first-order upwind scheme is used to solve the vorticity equation in Eq.3.28 at half time step, from t_n to $t_n + \frac{\delta t}{2}$, and all the forcing terms on the right hand side are assumed to be constant. Since this is a first-order explicit scheme, the computation expense is relatively cheap. At the end of this step, the vorticity $\xi^{n+\frac{1}{2}}$ at half time step is obtained. Then, the flow field $(u^{n+\frac{1}{2}}, v^{n+\frac{1}{2}})$ at half time step is recovered by solving the coupled Poisson's equations as explained in Sec.3.6.3.2. Meanwhile, the mean zonal velocity \bar{u} at the southern boundary condition in Eq.3.51 is updated at half time step . The vertical velocity $w^{n+\frac{1}{2}}$ at half time step is obtained by taking averaging of its value at t_n and t_{n+1} . Finally, the displacement $(\delta x, \delta y, \delta z)$ is calculated by using the formulas in Eqs.3.36-3.38. The estimated displacement $(\delta x, \delta y, \delta z)$ completes the numerical scheme for solving the unforced vorticity equation in Eq.3.29.

As for the vorticity Equation 3.29 with nonzero forcing, the solution has the following general form,

$$\xi(x(t), y(t), z(t), t) = \xi(x_0, y_0, z_0, t_0) + \int_{t_0}^t f(x(s), y(s), z(s), s) ds, \quad (3.81)$$

where the integral on the right hand side is approximated by the mid-point approximation formula

$$\xi(x(t), y(t), z(t), t) = \xi(x_0, y_0, z_0, t_0) + \delta t f\left(x^{n+\frac{1}{2}}, y^{n+\frac{1}{2}}, z^{n+\frac{1}{2}}, t_{n+\frac{1}{2}}\right). \quad (3.82)$$

Similarly, the mid-time displacement can also be evaluated by using the estimated velocity

field at the half time step,

$$x^{n+\frac{1}{2}} = x_i - u^{n+\frac{1}{2}} \frac{\delta t}{2}, \quad (3.83)$$

$$y^{n+\frac{1}{2}} = y_j - v^{n+\frac{1}{2}} \frac{\delta t}{2}, \quad (3.84)$$

$$z^{n+\frac{1}{2}} = z_k - w^{n+\frac{1}{2}} \frac{\delta t}{2}. \quad (3.85)$$

However, the half-time flow field in Eqs.3.83-3.85 at the location $(x^{n+\frac{1}{2}}, y^{n+\frac{1}{2}}, z^{n+\frac{1}{2}})$ won't typically be on a grid point,, while the first-order upwind scheme in the first stage only provide approximated half-time flow field on fixed grid points. Therefore the tricubic interpolation in three dimensions Lekien and Marsden (2005) are implemented to approximate the forcing term $f(x^{n+\frac{1}{2}}, y^{n+\frac{1}{2}}, z^{n+\frac{1}{2}}, t_{n+\frac{1}{2}})$ at the location $(x^{n+\frac{1}{2}}, y^{n+\frac{1}{2}}, z^{n+\frac{1}{2}})$ using the provided grid point values.

3.6.4 Solving the planetary-scale gravity wave equations

The gravity wave equations, on the planetary scale in Eqs.3.21a-3.21d, only involve large-scale variables $\Pi, \Theta, W, \langle \bar{u} \rangle$, which have dependence on the planetary-scale zonal coordinate X and vertical coordinate z . In the numerical simulations, the belt of tropics around the equator with zonal length 40000 km is chosen as the full domain. Thus the solutions should be periodic in the zonal direction. In order to focus on the atmospheric dynamics in the troposphere, rigid-lid boundary conditions at both the top and bottom are imposed by assuming no inflow/outflow through the vertical boundaries,

$$W|_{z=0,\pi} = 0, \quad (3.86)$$

where W represents a residual vertical circulation that involves both secondary vertical velocity and high order diabatic heating Biello and Majda (2013).

3.6.4.1 Decomposition into barotropic and baroclinic modes

It is well known that such linear equations in Eqs.3.21a-3.21d with rigid-lid boundary conditions can be solved with explicit solution formulas in both barotropic and baroclinic modes Majda (2003). In particular, the harmonic functions (sine and cosine functions) are a complete set of basis functions, which also satisfy the rigid-lid boundary conditions in Eq.3.86. Thus all these physical variables can be decomposed into barotropic and baroclinic modes as follows,

$$\langle \bar{u} \rangle = U + \sum_{q=1}^{\infty} u_q \cos(qz), \quad (3.87)$$

$$\Pi = \Pi_0 + \sum_{q=1}^{\infty} \Pi_q \cos(qz), \quad (3.88)$$

$$\Theta = \sum_{q=1}^{\infty} \Theta_q [-q \sin(qz)], \quad (3.89)$$

$$W = \sum_{q=1}^{\infty} W_q [-q \sin(qz)], \quad (3.90)$$

where the barotropic mode of vertical velocity W and potential temperature anomalies Θ vanishes due to the rigid-lid boundary conditions in Eq.3.86.

By using the ansatz for all large-scale physical variables in Eqs.3.87-3.90, the original large-scale gravity wave equations in Eqs.3.21a-3.21d can be separated into equations on each specific vertical mode,

#1, barotropic mode $q = 0$:

$$U_t + (\Pi_0)_X = 0, \quad (3.91)$$

where the barotropic mode of pressure perturbation Π_0 does not appear in other equations. Suppose the pressure perturbation at the surface Π_s is prescribed as boundary condition, then Π_0 can be determined by enforcing Eq.3.88 at $z = 0$,

$$\Pi_0 = \Pi_s - \sum_{q=1}^{\infty} \Pi_q. \quad (3.92)$$

#2, baroclinic modes $q > 0$

$$(U_q)_t + (\Pi_q)_X = 0, \quad (3.93a)$$

$$\Pi_q = \Theta_q, \quad (3.93b)$$

$$(\Theta_q)_t + W_q = 0, \quad (3.93c)$$

$$(u_q)_X - q^2 W_q = 0. \quad (3.93d)$$

In the numerical simulations, the barotropic mode of pressure perturbation Π_0 is assumed to be a constant so that the barotropic mode of zonal velocity U does not change in the planetary-scale gravity wave equation according to Eq.3.91. Such zonally uniform assumption for barotropic mode of planetary-scale pressure perturbation is used to simplify the discussion and emphasize gravity waves in the baroclinic modes, which are thought to be more relevant in nature Kiladis et al. (2009).

3.6.4.2 Gravity waves in the baroclinic modes

The set of linear equations in Eqs.3.93a-3.93d for the baroclinic modes are simplified by getting rid of the variables Π_q and W_q :

$$(U_q)_t + (\Theta_q)_X = 0, \quad (3.94)$$

$$(\Theta_q)_t + \frac{1}{q^2} (U_q)_X = 0, \quad (3.95)$$

which can be further reduced into the wave equation, although Eqs.3.94-3.95 are easier to solve numerically.

Considering the fact that both U_q and Θ_q are zonally periodic in the whole domain, they can be expanded in Fourier series with respect to wavenumber k ,

$$U_q = \sum_k u_q^k e^{\frac{i2\pi kx}{L_p}}, \quad (3.96)$$

$$\Theta_q = \sum_k \theta_q^k e^{\frac{i2\pi kx}{L_p}}, \quad (3.97)$$

where $L_p = 40000$ km denotes the length of the tropics around the equator, q is the vertical index for different baroclinic modes.

For each specific baroclinic mode q and zonal wavenumber k , Eqs.3.94-3.95 can be rewritten in vector form as follows,

$$\mathbf{X}_t + A\mathbf{X} = 0, \quad (3.98)$$

where the vector \mathbf{X} denotes $\begin{pmatrix} u_q^k \\ \theta_q^k \end{pmatrix}$ and the coefficient matrix A denotes $\begin{bmatrix} 0 & \frac{i2\pi k}{L_p} \\ \frac{i2\pi k}{q^2 L_p} & 0 \end{bmatrix}$.

3.6.5 Code validation

As shown in Sec.3.6.2, the M-ITCZ equations are split into two steps by the numerical scheme via the fractional step method. The first step is to solve the three-dimensional nonlinear

MEWTG equations in Eqs.3.19a-3.19d and the second step is to solve the two-dimensional linear planetary-scale gravity wave equations in Eqs.3.21a-3.21d. After implementing the numerical scheme described in the above sections, the code written in Fortran 77 is validated in this section. However, instead of validating the code for the M-ITCZ equations directly, the two steps in the fractional step method are validated separately, which can provide necessary conditions for the accuracy and convergence of the numerical scheme.

The MEWTG equations are three-dimensional fully nonlinear equations with the rigid-lid boundary conditions in meridional and vertical boundaries and the periodic boundary condition in the zonal direction. It is difficult to find such an analytical solution that satisfies both the equations and boundary conditions. An alternative method to validate the code is to prescribe a specific analytical solution which satisfies boundary conditions but not the equations. In order to guarantee that this prescribed analytical solution satisfies the equations, some extra forcing terms must be added on the right hand side of the equations, which can serve as extra forcing in the numerical scheme. Then by doubling the spatial and temporal resolutions, the convergence and accuracy of the numerical scheme can be investigated.

Each mesoscale domain in dimensionless units is $0 \leq x < 2$, $-1 \leq y \leq 1$, $0 \leq z \leq \pi$ for longitude x , latitude y and height z . In order to study the convergence rate of the numerical scheme, 5 numerical experiments in doubling spatial and temporal resolutions have been examined. The numerical experiment in the lowest spatial and temporal resolution has grid numbers $N_x = 11$, $N_y = 11$, $N_z = 17$, which corresponds to grid spacing $\Delta x = 0.18$, $\Delta y = 0.20$, $\Delta z = 0.20$. The total time length is 2 in dimensionless units and there are $N_t = 50$ time steps in the lowest resolution numerical experiment.

The example for code validation is prescribed to satisfy zonal periodic boundary condition and meridional and vertical rigid-lid boundary conditions. The exact expressions of velocity

field in dimensionless units read as follows,

$$u = \cos\left(\frac{\pi y}{L_y}\right) \cos(z) \sin(t), \quad (3.99)$$

$$v = -\sin\left(\frac{2\pi x}{L_x}\right) \sin\left(\frac{\pi y}{L_y}\right) \cos(z) \sin(t), \quad (3.100)$$

$$w = \frac{\pi}{L_y} \sin\left(\frac{2\pi x}{L_x}\right) \cos\left(\frac{\pi y}{L_y}\right) \sin(z) \sin(t), \quad (3.101)$$

where L_x, L_z denote the zonal and vertical extents of the domain and L_y denotes half meridional extent of the domain.

Here differences between the true solution as prescribed in Eqs.3.99-3.101 and the numerical solution in L^∞ norm are used to estimate accuracy and convergence of the numerical scheme. Fig.3.12 shows the numerical error for the horizontal flow field of 5 numerical experiments at time $t = 2$ in different spatial resolutions. Firstly, the numerical error of both zonal velocity and meridional velocity decreases as spatial and temporal resolutions increases, which indicates the convergence of the numerical scheme. Secondly, as demonstrated in Sec.3.6.3, the numerical scheme for solving the MEWTG equations is expected to reach second-order accuracy while the numerical error in Fig.3.12 decreases slower than the second-order convergence but faster than first-order convergence. One possible reason for this behavior is using the first-order tricubic interpolation for estimating three-dimensional forcing in Sec.3.6.3.3. In order to let the prescribed flow field satisfy the MEWTG equations, several extra forcing terms are added in the numerical scheme. The way of linearly adding extra forcing terms into the numerical scheme can be another possible reason for the loss of accuracy. Besides, in the piecewise corner-transport upwind (CTU) scheme, slope limiters are used to approximate the slope of quantities in each cell. Such limiters will also destroy the accuracy of the numerical scheme near shocks and large gradients.

The planetary-scale domain in dimensionless units is $0 \leq x < 8$, $0 \leq z \leq \pi$ for longitude X and height z . In order to validate the FFT code in a variety of cases, several solutions

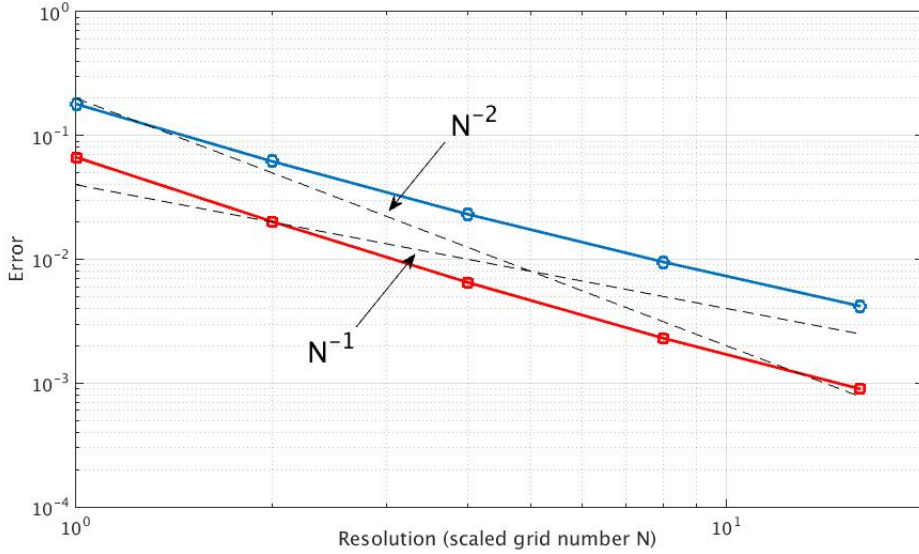


Figure 3.12: The L_∞ norm numerical errors of the horizontal flow field in the logarithmic diagram. The blue line is for zonal velocity and red line is for meridional velocity. The two dashed black lines denote first-order and second-order convergence rate separately. The horizontal axis shows the scaled grid number of these 5 numerical experiments in increasing resolutions and $N=1$ corresponds to the lowest resolution numerical experiment.

in different zonal wavenumber and baroclinic modes are chosen and compared with the numerical solutions. In these numerical experiments, the grid number along the longitudes is $N_{xp} = 41$ and that in height is $N_z = 65$, which correspond to grid spacing $\Delta X = 0.20$ in longitude and $\Delta z = 0.05$ in height. The total time length is 2 in dimensionless units and here time step number $N_t = 200$ is chosen to avoid violating the CFL condition.

In order to validate the accuracy of the numerical scheme for solving the planetary-scale gravity wave equations, a set of linear solutions involving zonal velocity U and potential temperature anomalies Θ are prescribed as follows,

$$U = \sin \left(\frac{2\pi k \left(X - \frac{t}{q} \right)}{L_p} \right) \cos (qz), \quad (3.102)$$

$$\Theta = - \sin \left(\frac{2\pi k \left(X - \frac{t}{q} \right)}{L_p} \right) \sin (qz), \quad (3.103)$$

Case	1	2	3	4
(k, q)	(1, 0)	(1, 1)	(1, 2)	(2, 2)
$\left U - \tilde{U} \right _{L^\infty}$	4.86×10^{-8}	4.51×10^{-8}	3.71×10^{-8}	4.51×10^{-8}
$\left \Theta - \tilde{\Theta} \right _{L^\infty}$	0	4.53×10^{-8}	1.68×10^{-8}	2.27×10^{-8}

Table 3.2: Numerical errors in L_∞ norm in 4 cases with different zonal wavenumber and baroclinic modes. The parameter k denotes zonal wavenumber and q is the vertical index for different baroclinic modes. (U, Θ) are true solutions and $(\tilde{U}, \tilde{\Theta})$ are numerical solutions.

where $L_p = 8$ denotes the zonal extent of the full domain. The parameter k denotes zonal wavenumber and q is the vertical index for different baroclinic modes.

The numerical error is calculated in the L^∞ norm for estimating accuracy of the numerical scheme. The details for the examples and numerical errors are summarized in Table 3.2. The numerical errors for both planetary-scale zonal velocity and potential temperature are in the order of 10^{-8} , which is in the same order as the variables declared in the Fortran code. Such efficiency and accuracy of the numerical scheme is due to the zonal periodicity of the true solutions and linearity of the equations as well as the implementation of the fast Fortran transform method.

Bibliography

- Albright, M. D., D. R. Mock, E. E. Recker, and R. J. Reed, 1981: A diagnostic study of the diurnal rainfall variation in the gate b-scale area. *Journal of the Atmospheric Sciences*, **38** (7), 1429–1445.
- Benedict, J. J., and D. A. Randall, 2011: Impacts of idealized air–sea coupling on madden–julian oscillation structure in the superparameterized cam. *Journal of the Atmospheric Sciences*, **68** (9), 1990–2008.
- Biello, J. A., and A. J. Majda, 2005: A new multiscale model for the madden-julian oscillation. *Journal of the atmospheric sciences*, **62** (6), 1694–1721.
- Biello, J. A., and A. J. Majda, 2006: Modulating synoptic scale convective activity and boundary layer dissipation in the ipesd models of the madden–julian oscillation. *Dynamics of atmospheres and oceans*, **42** (1), 152–215.
- Biello, J. A., and A. J. Majda, 2010: Intraseasonal multi-scale moist dynamics of the tropical atmosphere. *Communications in Mathematical Sciences*, **8** (2), 519–540.
- Biello, J. A., and A. J. Majda, 2013: A multiscale model for the modulation and rectification of the itcz. *Journal of the Atmospheric Sciences*, **70** (4), 1053–1070.
- Chen, S. S., and R. A. Houze, 1997: Diurnal variation and life-cycle of deep convective systems over the tropical pacific warm pool. *Quarterly Journal of the Royal Meteorological Society*, **123** (538), 357–388.

- Dai, A., and K. E. Trenberth, 2004: The diurnal cycle and its depiction in the community climate system model. *Journal of Climate*, **17** (5), 930–951.
- Deser, C., 1993: Diagnosis of the surface momentum balance over the tropical pacific ocean. *Journal of climate*, **6** (1), 64–74.
- Ferreira, R. N., and W. H. Schubert, 1997: Barotropic aspects of itcz breakdown. *Journal of the atmospheric sciences*, **54** (2), 261–285.
- Frenkel, Y., B. Khouider, and A. J. Majda, 2011a: Simple multicloud models for the diurnal cycle of tropical precipitation. part i: Formulation and the case of the tropical oceans. *Journal of the Atmospheric Sciences*, **68** (10), 2169–2190.
- Frenkel, Y., B. Khouider, and A. J. Majda, 2011b: Simple multicloud models for the diurnal cycle of tropical precipitation. part i: Formulation and the case of the tropical oceans. *Journal of the Atmospheric Sciences*, **68** (10), 2169–2190.
- Frenkel, Y., B. Khouider, and A. J. Majda, 2011c: Simple multicloud models for the diurnal cycle of tropical precipitation. part ii: the continental regime. *Journal of the Atmospheric Sciences*, **68** (10), 2192–2207.
- Frenkel, Y., B. Khouider, and A. J. Majda, 2011d: Simple multicloud models for the diurnal cycle of tropical precipitation. part ii: The continental regime. *Journal of the Atmospheric Sciences*, **68** (10), 2192–2207.
- Frenkel, Y., A. J. Majda, and B. Khouider, 2013: Simple models for the diurnal cycle and convectively coupled waves. *Theoretical and Computational Fluid Dynamics*, **27** (3-4), 533–559.
- Gill, A., 1980: Some simple solutions for heat-induced tropical circulation. *Quarterly Journal of the Royal Meteorological Society*, **106** (449), 447–462.

- Grabowski, W. W., and M. W. Moncrieff, 2001: Large-scale organization of tropical convection in two-dimensional explicit numerical simulations. *Quarterly Journal of the Royal Meteorological Society*, **127 (572)**, 445–468.
- Gray, W. M., 1979: Hurricanes: Their formation, structure and likely role in the tropical circulation. *Meteorology over the tropical oceans*, **77**, 155–218.
- Gruber, A., 1972: Fluctuations in the position of the itcz in the atlantic and pacific oceans. *Journal of the Atmospheric Sciences*, **29 (1)**, 193–197.
- Gu, G., and C. Zhang, 2002: Westward-propagating synoptic-scale disturbances and the itcz. *Journal of the atmospheric sciences*, **59 (6)**, 1062–1075.
- Hack, J. J., W. H. Schubert, D. E. Stevens, and H.-C. Kuo, 1989: Response of the hadley circulation to convective forcing in the itcz. *Journal of the Atmospheric Sciences*, **46 (19)**, 2957–2973.
- Haertel, P. T., and G. N. Kiladis, 2004: Dynamics of 2-day equatorial waves. *Dynamics*.
- Hanson, K., A. F. Hasler, J. Kornfield, and V. E. Suomi, 1967: Photographic cloud climatology from essa iii and v computer produced mosaics. *Bulletin of the American Meteorological Society*, **48**, 878–883.
- Hartmann, D. L., H. H. Hendon, and R. A. Houze Jr, 1984: Some implications of the mesoscale circulations in tropical cloud clusters for large-scale dynamics and climate. *Journal of the atmospheric sciences*, **41 (1)**, 113–121.
- Hendon, H. H., and B. Liebmann, 1994: Organization of convection within the madden-julian oscillation. *Journal of Geophysical Research: Atmospheres*, **99 (D4)**, 8073–8083.
- Hendon, H. H., and M. L. Salby, 1994: The life cycle of the madden-julian oscillation. *Journal of the Atmospheric Sciences*, **51 (15)**, 2225–2237.

Hendon, H. H., and K. Woodberry, 1993: The diurnal cycle of tropical convection. *Journal of Geophysical Research: Atmospheres (1984–2012)*, **98** (D9), 16 623–16 637.

Holton, J. R., and G. J. Hakim, 2012: *An introduction to dynamic meteorology*, Vol. 88. Academic press.

Houze, R. A., 2004: Mesoscale convective systems. *Reviews of Geophysics*, **42** (4).

Houze, R. A., and A. K. Betts, 1981: Convection in gate. *Reviews of Geophysics*, **19** (4), 541–576.

Houze Jr, R. A., and C.-P. Cheng, 1977: Radar characteristics of tropical convection observed during gate: Mean properties and trends over the summer season. *Monthly Weather Review*, **105** (8), 964–980.

Hubert, L., A. Krueger, and J. Winston, 1969: The double intertropical convergence zone-fact or fiction? *Journal of the Atmospheric Sciences*, **26** (4), 771–773.

Inness, P. M., and J. M. Slingo, 2003: Simulation of the madden-julian oscillation in a coupled general circulation model. part i: Comparison with observations and an atmosphere-only gcm. *Journal of Climate*, **16** (3), 345–364.

Jiang, X., and Coauthors, 2015: Vertical structure and physical processes of the madden-julian oscillation: Exploring key model physics in climate simulations. *Journal of Geophysical Research: Atmospheres*, **120** (10), 4718–4748.

Johnson, R. H., T. M. Rickenbach, S. A. Rutledge, P. E. Ciesielski, and W. H. Schubert, 1999: Trimodal characteristics of tropical convection. *Journal of climate*, **12** (8), 2397–2418.

Khairoutdinov, M., D. Randall, and C. DeMott, 2005: Simulations of the atmospheric general circulation using a cloud-resolving model as a superparameterization of physical processes. *Journal of the Atmospheric Sciences*, **62** (7), 2136–2154.

- Khouider, B., and Y. Han, 2013: Simulation of convectively coupled waves using wrf: a framework for assessing the effects of mesoscales on synoptic scales. *Theoretical and Computational Fluid Dynamics*, **27** (3-4), 473–489.
- Khouider, B., Y. Han, and J. A. Biello, 2012: Convective momentum transport in a simple multicloud model for organized convection. *Journal of the Atmospheric Sciences*, **69** (1), 281–302.
- Khouider, B., and A. J. Majda, 2006a: Model multi-cloud parameterizations for convectively coupled waves: Detailed nonlinear wave evolution. *Dynamics of atmospheres and oceans*, **42** (1), 59–80.
- Khouider, B., and A. J. Majda, 2006b: Multicloud convective parametrizations with crude vertical structure. *Theoretical and Computational Fluid Dynamics*, **20** (5-6), 351–375.
- Khouider, B., and A. J. Majda, 2006c: A simple multicloud parameterization for convectively coupled tropical waves. part i: Linear analysis. *Journal of the atmospheric sciences*, **63** (4), 1308–1323.
- Khouider, B., and A. J. Majda, 2007: A simple multicloud parameterization for convectively coupled tropical waves. part ii: Nonlinear simulations. *Journal of the atmospheric sciences*, **64** (2), 381–400.
- Khouider, B., and A. J. Majda, 2008a: Equatorial convectively coupled waves in a simple multicloud model. *Journal of the Atmospheric Sciences*, **65** (11), 3376–3397.
- Khouider, B., and A. J. Majda, 2008b: Multicloud models for organized tropical convection: Enhanced congestus heating. *Journal of the Atmospheric Sciences*, **65** (3), 895–914.
- Kikuchi, K., and B. Wang, 2008: Diurnal precipitation regimes in the global tropics. *Journal of Climate*, **21** (11), 2680–2696.

- Kiladis, G. N., K. H. Straub, and P. T. Haertel, 2005: Zonal and vertical structure of the madden-julian oscillation. *Journal of the Atmospheric Sciences*, **62** (8), 2790–2809.
- Kiladis, G. N., M. C. Wheeler, P. T. Haertel, K. H. Straub, and P. E. Roundy, 2009: Convectively coupled equatorial waves. *Reviews of Geophysics*, **47** (2).
- Larson, K., and D. L. Hartmann, 2003a: Interactions among cloud, water vapor, radiation, and large-scale circulation in the tropical climate. part i: Sensitivity to uniform sea surface temperature changes. *Journal of climate*, **16** (10), 1425–1440.
- Larson, K., and D. L. Hartmann, 2003b: Interactions among cloud, water vapor, radiation, and large-scale circulation in the tropical climate. part ii: Sensitivity to spatial gradients of sea surface temperature. *Journal of climate*, **16** (10), 1441–1455.
- Lekien, F., and J. Marsden, 2005: Tricubic interpolation in three dimensions. *International Journal for Numerical Methods in Engineering*, **63** (3), 455–471.
- LeVeque, R. J., 2002: *Finite volume methods for hyperbolic problems*, Vol. 31. Cambridge university press.
- Lin, J.-L., 2007: The double-itcz problem in ipcc ar4 coupled gcms: Ocean-atmosphere feedback analysis. *Journal of Climate*, **20** (18), 4497–4525.
- Lin, J.-L., M. Zhang, and B. Mapes, 2005: Zonal momentum budget of the madden-julian oscillation: The source and strength of equivalent linear damping. *Journal of the atmospheric sciences*, **62** (7), 2172–2188.
- Lin, X., and R. H. Johnson, 1996: Kinematic and thermodynamic characteristics of the flow over the western pacific warm pool during toga coare. *Journal of the atmospheric sciences*, **53** (5), 695–715.
- Majda, A., 2003: *Introduction to PDEs and Waves for the Atmosphere and Ocean*, Vol. 9. American Mathematical Soc.

Majda, A. J., 2007: New multiscale models and self-similarity in tropical convection. *Journal of the atmospheric sciences*, **64** (4), 1393–1404.

Majda, A. J., and J. A. Biello, 2004: A multiscale model for tropical intraseasonal oscillations. *Proceedings of the National Academy of Sciences of the United States of America*, **101** (14), 4736–4741.

Majda, A. J., and R. Klein, 2003: Systematic multiscale models for the tropics. *Journal of the Atmospheric Sciences*, **60** (2), 393–408.

Majda, A. J., M. Mohammadian, and Y. Xing, 2008: Vertically sheared horizontal flow with mass sources: a canonical balanced model. *Geophysical and Astrophysical Fluid Dynamics*, **102** (6), 543–591.

Majda, A. J., and S. N. Stechmann, 2008: Stochastic models for convective momentum transport. *Proceedings of the National Academy of Sciences*, **105** (46), 17614–17619.

Majda, A. J., and S. N. Stechmann, 2009: A simple dynamical model with features of convective momentum transport. *Journal of the Atmospheric Sciences*, **66** (2), 373–392.

Majda, A. J., Y. Xing, and M. Mohammadian, 2010: Moist multi-scale models for the hurricane embryo. *Journal of Fluid Mechanics*, **657**, 478–501.

Majda, A. J., and Q. Yang, 2016: A multiscale model for the intraseasonal impact of the diurnal cycle over the maritime continent on the madden–julian oscillation. *Journal of the Atmospheric Sciences*, **73** (2), 579–604.

Mapes, B., S. Tulich, J. Lin, and P. Zuidema, 2006: The mesoscale convection life cycle: Building block or prototype for large-scale tropical waves? *Dynamics of atmospheres and oceans*, **42** (1), 3–29.

Mapes, B. E., and R. A. Houze Jr, 1993: Cloud clusters and superclusters over the oceanic warm pool. *Monthly Weather Review*, **121** (5), 1398–1416.

- Mapes, B. E., and R. A. Houze Jr, 1995: Diabatic divergence profiles in western pacific mesoscale convective systems. *Journal of the atmospheric sciences*, **52** (10), 1807–1828.
- Matsuno, T., 1966: Quasi-geostrophic motions in the equatorial area. *J. Meteor. Soc. Japan*, **44** (1), 25–43.
- McGarry, M. M., and R. J. Reed, 1978: Diurnal variations in convective activity and precipitation during phases ii and iii of gate. *Monthly Weather Review*, **106** (1), 101–113.
- Moncrieff, M. W., D. E. Waliser, M. J. Miller, M. A. Shapiro, G. R. Asrar, and J. Caughey, 2012: Multiscale convective organization and the yotc virtual global field campaign. *Bulletin of the American Meteorological Society*, **93** (8), 1171–1187.
- Nakazawa, T., 1988: Tropical super clusters within intraseasonal variations over the western pacific. *J. Meteor. Soc. Japan*, **66** (6), 823–839.
- Neale, R., and J. Slingo, 2003: The maritime continent and its role in the global climate: A gcm study. *Journal of Climate*, **16** (5), 834–848.
- Nesbitt, S. W., and E. J. Zipser, 2003: The diurnal cycle of rainfall and convective intensity according to three years of trmm measurements. *Journal of Climate*, **16** (10), 1456–1475.
- Nolan, D. S., C. Zhang, and S.-h. Chen, 2007: Dynamics of the shallow meridional circulation around intertropical convergence zones. *Journal of the atmospheric sciences*, **64** (7), 2262–2285.
- Peatman, S. C., A. J. Matthews, and D. P. Stevens, 2014: Propagation of the madden–julian oscillation through the maritime continent and scale interaction with the diurnal cycle of precipitation. *Quarterly Journal of the Royal Meteorological Society*, **140** (680), 814–825.
- Philander, S., D. Gu, G. Lambert, T. Li, D. Halpern, N. Lau, and R. Pacanowski, 1996: Why the itcz is mostly north of the equator. *Journal of climate*, **9** (12), 2958–2972.

- Ramage, C. S., 1968: Role of a tropical "maritime continent" in the atmospheric circulation
1. *Monthly Weather Review*, **96** (6), 365–370.
- Randall, D. A., and D. A. Dazlich, 1991: Diurnal variability of the hydrologic cycle in a general circulation model. *Journal of the atmospheric sciences*, **48** (1), 40–62.
- Rauniar, S. P., and K. J. Walsh, 2011: Scale interaction of the diurnal cycle of rainfall over the maritime continent and australia: Influence of the mjo. *Journal of Climate*, **24** (2), 325–348.
- Raupp, C. F., and P. L. Silva Dias, 2009: Resonant wave interactions in the presence of a diurnally varying heat source. *Journal of the Atmospheric Sciences*, **66** (10), 3165–3183.
- Raupp, C. F., and P. L. Silva Dias, 2010: Interaction of equatorial waves through resonance with the diurnal cycle of tropical heating. *Tellus A*, **62** (5), 706–718.
- Ray, C., 1928: Diurnal variation of rainfall at san juan, pr 1. *Monthly Weather Review*, **56** (4), 140–141.
- Romps, D. M., 2014: Rayleigh damping in the free troposphere. *Journal of the Atmospheric Sciences*, **71** (2), 553–565.
- Rui, H., and B. Wang, 1990: Development characteristics and dynamic structure of tropical intraseasonal convection anomalies. *Journal of the Atmospheric Sciences*, **47** (3), 357–379.
- Sato, T., H. Miura, M. Satoh, Y. N. Takayabu, and Y. Wang, 2009: Diurnal cycle of precipitation in the tropics simulated in a global cloud-resolving model. *Journal of Climate*, **22** (18), 4809–4826.
- Schneider, E. K., and R. S. Lindzen, 1977: Axially symmetric steady-state models of the basic state for instability and climate studies. part i. linearized calculations. *Journal of the Atmospheric Sciences*, **34** (2), 263–279.

- Serra, Y. L., G. N. Kiladis, and M. F. Cronin, 2008: Horizontal and vertical structure of easterly waves in the pacific itcz. *Journal of the Atmospheric Sciences*, **65** (4), 1266–1284.
- Slingo, J., P. Inness, R. Neale, S. Woolnough, and G. Yang, 2003: Scale interactions on diurnal to seasonal timescales and their relevance to model systematic errors. *Annals of Geophysics*.
- Sobel, A. H., J. Nilsson, and L. M. Polvani, 2001: The weak temperature gradient approximation and balanced tropical moisture waves*. *Journal of the atmospheric sciences*, **58** (23), 3650–3665.
- Sorooshian, S., X. Gao, K. Hsu, R. Maddox, Y. Hong, H. Gupta, and B. Imam, 2002: Diurnal variability of tropical rainfall retrieved from combined goes and trmm satellite information. *Journal of climate*, **15** (9), 983–1001.
- Sperber, K. R., J. M. Slingo, P. M. Inness, and W.-M. Lau, 1997: On the maintenance and initiation of the intraseasonal oscillation in the ncep/ncar reanalysis and in the gla and ukmo amip simulations. *Climate Dynamics*, **13** (11), 769–795.
- Stratton, R., and A. Stirling, 2012: Improving the diurnal cycle of convection in gcms. *Quarterly Journal of the Royal Meteorological Society*, **138** (666), 1121–1134.
- Sui, C., and K. Lau, 1992: Multiscale phenomena in the tropical atmosphere over the western pacific. *Monthly weather review*, **120** (3), 407–430.
- Sui, C., X. Li, K. Lau, and D. Adamec, 1997: Multiscale air-sea interactions during toga coare. *Monthly weather review*, **125** (4), 448–462.
- Takayabu, Y. N., 2002: Spectral representation of rain profiles and diurnal variations observed with trmm pr over the equatorial area. *Geophysical research letters*, **29** (12).

Tian, B., B. J. Soden, and X. Wu, 2004: Diurnal cycle of convection, clouds, and water vapor in the tropical upper troposphere: Satellites versus a general circulation model. *Journal of Geophysical Research: Atmospheres*, **109** (D10).

Tian, B., D. E. Waliser, and E. J. Fetzer, 2006: Modulation of the diurnal cycle of tropical deep convective clouds by the mjo. *Geophysical research letters*, **33** (20).

Toma, V. E., and P. J. Webster, 2010a: Oscillations of the intertropical convergence zone and the genesis of easterly waves. part i: diagnostics and theory. *Climate dynamics*, **34** (4), 587–604.

Toma, V. E., and P. J. Webster, 2010b: Oscillations of the intertropical convergence zone and the genesis of easterly waves part ii: numerical verification. *Climate dynamics*, **34** (4), 605–613.

Tung, W.-w., D. Giannakis, and A. J. Majda, 2014: Symmetric and antisymmetric convection signals in the madden–julian oscillation. part i: basic modes in infrared brightness temperature. *Journal of the Atmospheric Sciences*, **71** (9), 3302–3326.

Tung, W.-W., and M. Yanai, 2002a: Convective momentum transport observed during the toga coare iop. part i: General features. *Journal of the atmospheric sciences*, **59** (11), 1857–1871.

Tung, W.-W., and M. Yanai, 2002b: Convective momentum transport observed during the toga coare iop. part ii: Case studies. *Journal of the atmospheric sciences*, **59** (17), 2535–2549.

Waliser, D., and W. K.-M. Lau, 2005: Intraseasonal variability in the atmosphere-ocean climate system. *Intraseasonal Variability in the Atmosphere-Ocean Climate System, by D. Waliser and WK-M. Lau. 2005 XVIII, 474 p. 80 illus. 3-540-22276-6. Berlin: Springer, 2005.*, **1**.

Waliser, D. E., and C. Gautier, 1993: A satellite-derived climatology of the itcz. *Journal of Climate*, **6** (11), 2162–2174.

Wang, C.-c., and G. Magnusdottir, 2005: Itcz breakdown in three-dimensional flows. *Journal of the atmospheric sciences*, **62** (5), 1497–1512.

Wang, C.-c., and G. Magnusdottir, 2006: The itcz in the central and eastern pacific on synoptic time scales. *Monthly weather review*, **134** (5), 1405–1421.

Wheeler, M., and G. N. Kiladis, 1999: Convectively coupled equatorial waves: Analysis of clouds and temperature in the wavenumber-frequency domain. *Journal of the Atmospheric Sciences*, **56** (3), 374–399.

Winston, J. S., 1971: The annual course of zonal mean albedo as derived from essa 3 and 5 digitized picture data. *Mon. Wea. Rev*, **99** (11), 818–827.

Wu, C.-H., and H.-H. Hsu, 2009: Topographic influence on the mjo in the maritime continent. *Journal of Climate*, **22** (20), 5433–5448.

Wu, Z., 2003: A shallow cisk, deep equilibrium mechanism for the interaction between large-scale convection and large-scale circulations in the tropics. *Journal of the Atmospheric Sciences*, **60** (2), 377–392.

Wyrtki, K., and G. Meyers, 1976: The trade wind field over the pacific ocean. *Journal of Applied Meteorology*, **15** (7), 698–704.

Yanai, M., B. Chen, and W.-w. Tung, 2000: The madden–julian oscillation observed during the toga coare iop: Global view. *Journal of the atmospheric sciences*, **57** (15), 2374–2396.

Yang, G.-Y., B. Hoskins, and J. Slingo, 2003: Convectively coupled equatorial waves: A new methodology for identifying wave structures in observational data. *Journal of the atmospheric sciences*, **60** (14), 1637–1654.

Yang, G.-Y., and J. Slingo, 2001: The diurnal cycle in the tropics. *Monthly Weather Review*, **129** (4), 784–801.

Yang, Q., and A. J. Majda, 2014: A multi-scale model for the intraseasonal impact of the diurnal cycle of tropical convection. *Theoretical and Computational Fluid Dynamics*, **28** (6), 605–633.

Yang, S., and E. A. Smith, 2006: Mechanisms for diurnal variability of global tropical rainfall observed from trmm. *Journal of climate*, **19** (20), 5190–5226.

Zhang, C., 2001: Double itczs. *Journal of Geophysical Research*, **106** (D11), 11 785–11 792.

Zhang, C., 2005: Madden-julian oscillation. *Reviews of Geophysics*, **43** (2).

Zhang, C., M. McGauley, and N. A. Bond, 2004: Shallow meridional circulation in the tropical eastern pacific. *Journal of climate*, **17** (1), 133–139.

Zhang, C., D. S. Nolan, C. D. Thorncroft, and H. Nguyen, 2008: Shallow meridional circulations in the tropical atmosphere. *Journal of Climate*, **21** (14), 3453–3470.